Optical Calibration of the Sudbury Neutrino Observatory and Determination of the ^{8}B Solar Neutrino Flux in the Salt Phase

by

Darren R. Grant, B.Sc., M.Sc.

A thesis submitted to
the Faculty of Graduate Studies and Research
in partial fulfillment of
the requirements for the degree of
Doctor of Philosophy

Ottawa-Carleton Institute for Physics
Department of Physics

Carleton University
Ottawa, Ontario, Canada

January 10

The undersigned recommend to
the Faculty of Graduate Studies and Research
acceptance of the thesis

Optical Calibration of the Sudbury Neutrino Observatory and Determination of the ^{8}B Solar Neutrino Flux in the Salt Phase

submitted by **Darren R. Grant, B.Sc., M.Sc.**
in partial fulfillment of the requirements for
the degree of Doctor of Philosophy

Chair, Department of Physics

Thesis Supervisor

External Examiner

Carleton University

Date _____

Abstract

An improved measurement of the ^{8}B solar neutrino flux has been made at the Sudbury Neutrino Observatory (SNO). This measurement has an increased sensitivity to the neutral current reaction. This is due to an enhanced neutron capture efficiency, accomplished by adding salt, NaCl, to the heavy water in the detector. The data set analyzed in the salt phase consists of approximately 254 days of neutrino data. The data set has been analyzed using independently developed probability density functions (PDFs) in an extended maximum likelihood calculation. The final ^{8}B model-constrained results of this analysis are given by the fluxes (in units of 10^6 neutrinos/(cm^{2}s)):

- $\Phi_{CC}^{Sun} = 1.69 \pm 0.07(\text{stat}) \, ^{+0.08}_{-0.09}(\text{syst})$
- $\Phi_{NC}^{Sun} = 4.91 \pm 0.23(\text{stat}) \, ^{+0.28}_{-0.35}(\text{syst})$
- $\Phi_{ES}^{Sun} = 2.11 \, ^{+0.29}_{-0.27}(\text{stat}) \, ^{+0.11}_{-0.15}(\text{syst})$

These fluxes give a CC/NC ratio of $0.344 \pm 0.021(\text{stat}) \, ^{+0.024}_{-0.035}(\text{syst})$.

The results clearly demonstrate that solar neutrinos are oscillating from one flavor to another, and therefore must have a mass. The total solar neutrino flux, Φ_{NC}^{Sun}, is in good agreement with the expectations from the standard solar model.

The results are also consistent with previous SNO results in the pure D_2O phase. There are improved statistical uncertainties, due to the enhancement of the NC signal by the chlorine. There are also improvements in the systematic uncertainties of these results over previous measurements. This is partially a result of extensive

calibration efforts that have been able to reduce the uncertainties in the detector optical properties.

For Samantha Sarah Nova

Acknowledgments

To be completed...

Statement of Originality

The work presented in this thesis is the author's own and is original except where noted here. The use of other's work is cited in the text where appropriate.

The Sudbury Neutrino Observatory is the result of the efforts of hundreds of scientists and engineers over a period of 20 years. It is therefore a natural process in such an experiment to participate in a number of collaborative efforts while completing a doctorial degree.

The contributions of the author have extended into almost all aspects of the SNO experiment. As a M.Sc. student, the author designed, constructed and commissioned a monitor degasser system for the D_2O water systems. The degasser is a critical element of the SNO assay systems, providing the background measurement of uranium content in the D_2O volume.

As a Ph.D. student, the author participated in the calibration program by taking responsibility for the salt phase optical calibrations. This responsibility included the construction and commissioning of the Mark-II laserball source, originally designed by Bryce Moffat. The optics code used to analyze the salt phase optical data is an evolution of the original QOCA code developed by Bryce Moffat. The final salt optical parameters are generated with this evolved code, with final adaptations and

"bug" fixes applied by Ranpal Dosanjh.

The signal extraction process described in this thesis uses as its foundation the work of Mark Boulay's Ph.D. thesis, in particular the application extended maximum likelihood fitter routines. The signal extraction code (sig-ex), used in the thesis analysis, is an independent program developed to provide verification of the SNO default analysis code. Sig-ex was produced as a collaborative effort between the author, Pierre-Luc Drouin, and Kathryn Miknaitis, with valuable input from Mark Boulay and Alain Bellerive. The probability density functions, used in the signal extraction for the thesis results, were generated independently from parameterizations of the SNOMAN MC distributions. The author was the first in the collaboration to apply the Gaussian-correlated joint probability method, used to include correlations in the signal extraction when using 1D PDFs. This method was first introduced to the author by Alain Bellerive.

Finally, the MSW physics interpretation of the default SNO results, presented in chapter 7, are generated using the QPhysics code developed by Fraser Duncan and Mark Chen. The interpretation represents years of effort by the members of the SNO Physics Interpretation group, and extends beyond the scope of the extraction of the ^{8}B fluxes presented here. The default interpretation is expected to be consistent with what one would extract with the independent fluxes from this thesis, due to the excellent agreement between these results and those of the default SNO analysis.

Contents

List of Tables

List of Figures

Chapter 1

Introduction

The neutrino is among nature's most abundant fundamental particles. Billions of neutrinos are incident on each square cm of the Earth every second. However, because neutrinos interact very weakly, all but a few pass through the Earth without interacting with matter. This makes the detection of neutrinos, and the determination of many of its properties, very difficult.

Neutrinos are produced on the Earth in nuclear reactors and particle accelerators. The first neutrinos were detected in 1955 at a nuclear reactor. However, the largest source of neutrinos for the Earth is the Sun. The fusion reaction energy cycles in the Sun produce neutrinos. These neutrinos are the primary means for the Sun to release the energy it produces. A very detailed model of the reactions in the Sun, known as the Standard Solar Model (SSM), allows for predictions of the expected neutrino flux from the Sun on Earth. It was almost 15 years after the first neutrinos were detected that the first measurement of solar neutrinos was achieved. However, the measured solar neutrino flux was very different from the value predicted by the SSM. Larger and improved solar neutrino experiments, as well as more precise model predictions, have been developed over the 40 years since the first solar neutrino flux measurement.

Despite these developments, there remained a discrepancy between the measured and predicted fluxes. This became known as the Solar Neutrino Problem (SNP). It was uncertain if the problem was due to inaccuracies in the model predictions or difficulties with the experimental measurements. If the solar model proved to be correct, it would require new physics for the neutrino, beyond the Standard Model (SM) of Particle Physics, to explain the measured discrepancy.

The Standard Model assumes neutrinos exist in three families, are massless, neutral and have no magnetic moment. Measurements by the LEP experiments at CERN have demonstrated there are three active flavours of neutrinos: electron, muon and tau, with masses below the Z^0 threshold. Previous solar neutrino experiments were sensitive only to electron neutrinos, the type of neutrino produced in solar fusion reactions. If neutrinos have properties beyond those in the SM, some neutrinos could change flavour and these would not be detected in the previous experiments.

The Sudbury Neutrino Observatory (SNO) is the most recent neutrino experiment studying the SNP and other properties of neutrinos. The detector is located approximately 25 km north of Sudbury, Ontario, Canada. The primary detector volume is approximately 1000 tonnes of ultra-pure reactor grade heavy water (D_2O) located 2 km under the Canadian Shield. The extra neutrons in the deuteron give the SNO detector a unique ability to measure the total solar neutrino flux, independent of neutrino flavour. If neutrinos change flavour after production in the Sun, the SNO experiment has the ability to detect them. SNO may also independently measure the electron-neutrino flux. Therefore SNO has the ability to definitively observe neutrino oscillations.

The impact of the SNP solution will be far reaching in the particle and astrophysics communities. If the total solar neutrino flux is found to be equal to the value measured by previous experiments, the SSM would have to be to re-evaluated. However, if the flux is found to be consistent with the SSM prediction, then new

physics related to the neutrino will have been discovered. The most popular theory to explain the required new physics is to extend the SM so that neutrinos have mass, thus permitting the neutrinos to oscillate from one flavour to another. A massive neutrino also has broad implications for cosmologists. Since the neutrino is very abundant in the universe, even if the neutrino masses are very small, massive neutrinos could contribute significantly to the missing dark matter. This, in turn, affects the models determining the rate of expansion of the universe, the formulation of structure in the universe, and the possible future expansion or collapse of the universe.

This thesis details the measurements of the solar neutrino fluxes during the second (salt) phase of the SNO experiment. In Chapter 2, the reader will find a detailed historical background of neutrinos, from first postulation and detection to the results from the most recently developed neutrino detectors. Chapter 2 also contains detailed information of neutrino physics, including the necessary components for understanding neutrino oscillations and how they fit with experimental results. A complete description of the SNO detector, including discussion of the relevant detector backgrounds and information on the calibration sources used to understand the properties of the experiment, may be found in Chapter 3. Chapter 4 gives the full details of determining the optical properties of the detector for the second phase of the experiment using the laserball calibration source. Discussion of the preliminary steps involved in the analysis of SNO data is contained in Chapter 5. This includes the details of cleaning the data set of backgrounds and development of signal probability distribution functions (PDFs). Chapter 6 provides the full details of the signal extraction process and presents the measured solar neutrino fluxes from the salt phase data set. Finally, Chapter 7 gives a summary of the results in the thesis with a look at the physics implications of the results. It also provides the reader with some suggestions for possible future improvements in the data analysis.

Chapter 2

Neutrino Physics

Neutrino physics has been a topic of discussion for approximately 70 years, since the neutrino was first postulated. This chapter provides a summary of the historical background of the neutrino, and includes discussions of all the solar neutrino experiments and their results, up to the present time. The chapter concludes with a description of the physics necessary to interpret the results of the experiments.

2.1 Historical Background

The neutrino, meaning "little neutral one", was first postulated in 1930 by Wolfgang Pauli to explain the apparent missing momentum, and varying proton and electron energies, from the reconstruction of β decays (see equation 2.1).

$$n \Rightarrow p + e^{-} + \bar{\nu}_e \tag{2.1}$$

Without the neutrino, the reaction products follow 2-body kinematics and should have well defined final state energies and momenta. This was not observed. The observed spectra could only be explained by 3-body kinematics, suggesting the existence of an unseen particle in the final state. This idea opened a new era in particle

and astro-physics.

In 1939, Hans Bethe released his theory of hydrogen fusion as the principle energy source for the Sun [10]. From Bethes' work, it was determined that, due to the rate of energy production in the Sun, the fusion reactions (Figure 2.1) should generate a very large flux of electron-type neutrinos (ν_e). Similarly, the fission reactions occurring in Earth-based nuclear reactors were predicted to produce a large number of electron anti-neutrinos ($\bar{\nu}_e$).

In the 1950s, experiments were being developed to make measurements of solar and reactor neutrinos. In 1955, Clyde Cowan Jr. and Frederick Reines led an effort to construct a neutrino detector consisting of 200 L of water and 40 kg of dissolved $CdCl_2$ [17]. The detector was placed near a nuclear reactor. The $\bar{\nu}_e$ from the reactor interact with the water via an inverse beta-decay process (see equation 2.2).

$$\bar{\nu_e} + p \Rightarrow n + e^+ \tag{2.2}$$

The neutrino interactions were detected by identifying a pair of γ rays (from e^+–e^- annihilation) in coincidence with a neutron capture γ ray (from ^{109}Cd decay) 5 ms after the γ ray pair. Although the reactor produced some 10^{13} anti-neutrinos per cm^2 per second, the detector measured only 3 events per hour. However, a low background rate, providing a signal to background ratio of 4:1, gave conclusive confirmation of the detection of neutrinos.

2.2 Solar Neutrino Experiments

Experiments designed to measure solar neutrinos have evolved over the years. They have increased in sensitivity and have differing energy thresholds, allowing them to probe neutrinos from different reactions in the Sun. This section describes the detectors and physics results obtained by the various experiments.

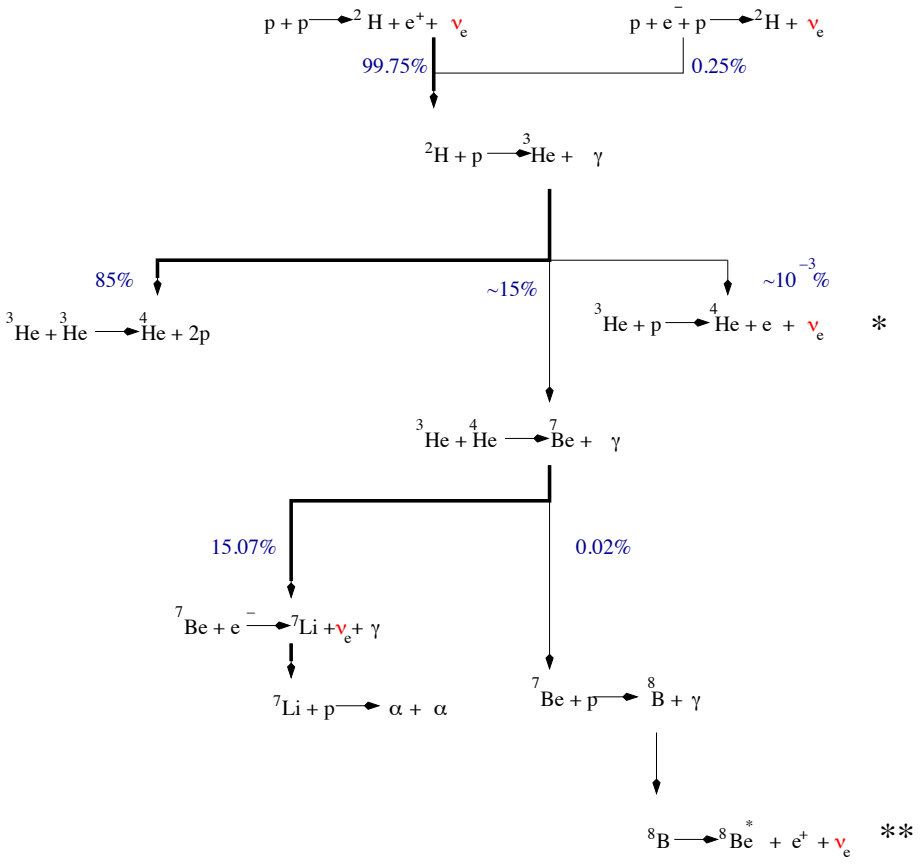

Figure 2.1: The main burning reactions in the Sun; the energy-generating pp chain. Each conversion of four protons to an α-particle is known as a termination of the energy-generating reaction $4p \Rightarrow \alpha + 2e^+ + 2\nu_e + 25$ MeV. Hence, the termination percentage is the fraction of terminations of the pp chain in which each reaction occurs [6]. SNO is sensitive to the higher energy, but relatively rare neutrinos produced in the Hep (*) and ^{8}B (**) reactions.

2.2.1 The First Solar Neutrino Detector

In 1962, Ray Davis Jr. began development of a detector that could detect neutrinos produced in the Sun. At the same time, John Bahcall was developing the foundation for a Standard Solar Model (SSM). This model predicted that solar neutrinos would have a very high flux (see Figure 2.2), but their detection would be

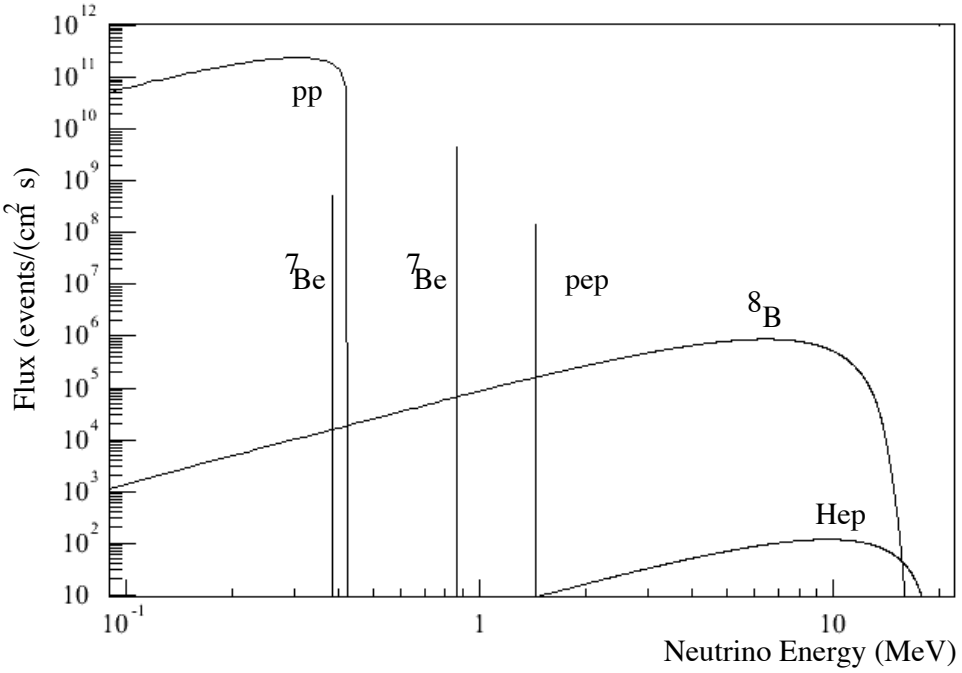

Figure 2.2: Standard solar model predicted rates of solar neutrinos versus neutrino energy. The rates are predicted using the Bahcall-Pinsonneault 2000 Standard Solar Model [75]. Water Cherenkov detectors are sensitive to the neutrino spectra above 5 MeV (^{8}B and Hep). The Cl experiment is sensitive to the spectra above 0.86 MeV, and the gallium experiments are sensitive to neutrinos above 0.23 MeV which includes the pp chain.

complicated by the predicted low neutrino energies, small cross-sections and high potential background levels.

To escape one of the potentially problematic backgrounds, due to cosmic rays, the detector was placed in the Homestake gold mine of South Dakota, 4850 feet below the surface. The detector was a 600 tonne tank filled with C_2Cl_4. Solar neutrinos interacting with the chlorine in the tank produced radioactive ^{37}Ar according to the reaction

$$\nu_e + ^{37}\mathrm{Cl} \Rightarrow ^{37}\mathrm{Ar} + e^-. \tag{2.3}$$

Since ^{37}Ar has a half-life of 35 days, the detector volume was extracted approximately once a month to a counting facility. In the counting facility, the ^{37}Ar atoms were removed from the liquid, and the number of extracted ^{37}Ar atoms amounted to a few per day. The count rate was converted to solar neutrino units (SNU), where 1 SNU = 10^{-36} captures/atom/second. Over a period of more than 30 years of active data-taking, the Homestake experiment has measured the ν_e rate from the Sun to be $2.55 \pm 0.17 \pm 0.18$ SNU [16]. The measured value has been consistently well below the Standard Solar Model (SSM) prediction of 8.0 ± 3.0 SNU [7]. This discrepancy became known as the solar neutrino problem (SNP).

2.2.2 The Next Series of Solar Neutrino Detectors

In the late 1980s, new radio-chemical and water Cherenkov experiments were being designed and constructed.

Radio-chemical Experiments

Two radio-chemical experiments, each using 30 tonnes of Gallium as the detection medium, were constructed. They were the European GALLEX experiment and the Soviet-American Gallium Experiment (SAGE). In these detectors, neutrinos interact via an inverse beta-decay process shown in the reaction

$$\nu_e + ^{71}Ga \Rightarrow ^{71}Ge + e^{-}. \tag{2.4}$$

The neutrino energy threshold for this reaction is 0.233 MeV, much lower than the 0.814 MeV threshold of the Homestake experiment. This threshold gives the Gallium experiments sensitivity to the solar pp neutrinos. The pp neutrinos have the largest predicted production rate (see figure 2.2) and hence are strongly related to the solar luminosity. Theoretical estimates of the pp flux can be calculated to a few percent accuracy.

GALLEX ended active detection in 1997, and is slowly being upgraded to a 100 tonne experiment called GNO. SAGE continues to operate in a configuration consistent with its original design. The results from the Gallium experiments are 71 $\pm$ 6 SNU (GALLEX) and 71 $\pm$ 7 SNU (SAGE), where the statistical and systematic uncertainties have been added in quadrature [63][60]. These results also demonstrate a clear deficit compared to the SSM predictions of 128 $\pm$ 8 SNU.

Water Cherenkov

The Kamiokande water Cherenkov detector was initially designed and built in 1982-83 to search for proton decay. A Cherenkov detector is designed to detect the ultraviolet photons produced when a charged particle exceeds the speed of light in a given medium. Neutrinos may produce a signal in a light water detector by interacting via ν-e scattering, where the scattered e^- produces the Cherenkov light. This permitted the 3000 tonne ultra-pure water Kamiokande detector to also be used as a neutrino detector.

Water Cherenkov detectors differ most distinctly from radio chemical detectors in the available energy thresholds, and in access to the event information in real-time from photomultiplier tubes (PMTs). In 1985-86 the Kamiokande detector was upgraded to enhance its ability to detect neutrinos.

In 1987, the Kamiokande detector was the first experiment to detect neutrinos produced by a supernova (SN1987a – located in the Large Magellanic cloud)[62]. In 1988, Kamiokande released its first results for a measurement of the ^{8}B solar neutrino flux, 2.80 $\pm$ 0.19 (stat) $\pm$ 0.33 (syst) x 10^6 neutrinos/(cm^{2}s) [61]. Comparing the measurement to the SSM prediction of 5.05 $^{+1.01}_{-0.81}$ x 10^6 neutrinos/(cm^{2}s) one finds that even with improvements in the SSM calculations and in detector designs (to improve statistics and reduce systematic uncertainties) the SNP remained

unresolved.

2.2.3 Recently Developed Solar Neutrino Detectors

Two solar neutrino experiments have started operation in the past 10 years. Both are water Cherenkov detectors, one using H_2O and the other, SNO, using heavy water (D_2O) for the primary detection medium. Both experiments have obtained important new physics information, revealing the true nature of the elusive neutrino.

H_2O Cherenkov

In 1995, construction was completed for a new 50000 tonne ultra-pure H_2O Cherenkov detector in the Kamioka mine (named Super-Kamiokande or Super-K). The detector's purpose was to study solar and atmospheric neutrinos, and continue the search, begun by its predecessor, for proton decay. The results from the experiment have proven to be incredibly significant for the particle physics community.

The Super-K experiment produced the first measurement of atmospheric neutrino oscillations. Atmospheric neutrinos are produced when cosmic rays interact with atoms in the atmosphere to produce short-lived particles such as pions and kaons. These particles decay and produce other particles, including muons and neutrinos. The neutrinos are produced in an approximate ratio of two ν_μ for every ν_e. It was assumed the neutrino flux would be symmetric for both upward and downward going particles. A measurement that deviates from this assumption would be evidence for neutrinos changing flavour. In 1998, the Super-K collaboration released results which clearly showed such an up-down asymmetry for muon-like events in the detector (see figure 2.3) [69].

Super-K measures solar neutrinos using ν-e elastic scattering (as the Kamiokande experiment did) that is primarily sensitive to ν_e with a very small sensitivity to ν_μ

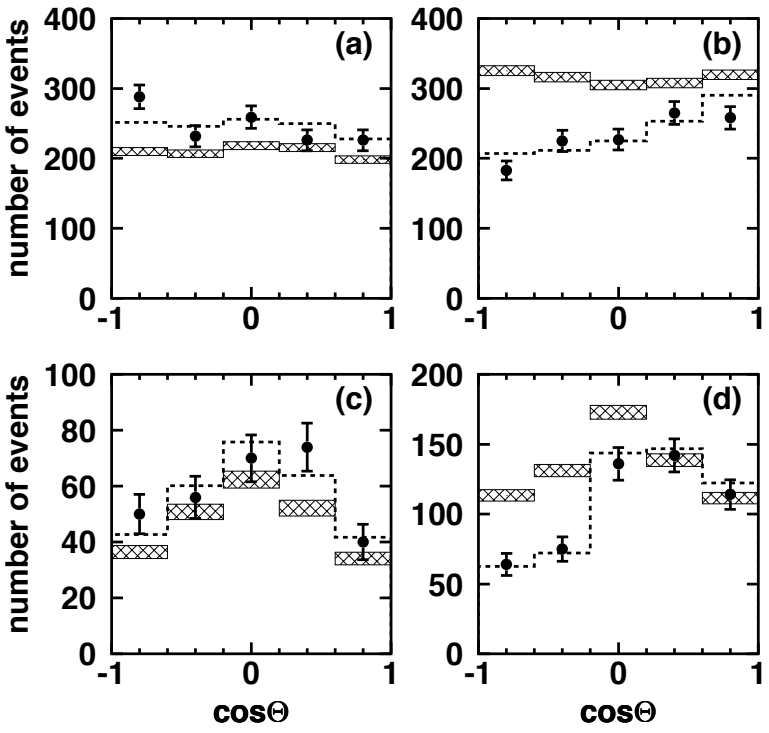

Figure 2.3: Zenith angle (θ) distributions observed in Super-Kamiokande [69]. Here, cos(θ)=1 represents downward going events. Figure (a) shows electron-like events for energies below 1 GeV. Figure (b) shows muon-like events for energies below 1 GeV. Figures (c) and (d) are the multi-GeV electron and muon-like events, respectively. The shaded bins represent the statistical uncertainty of the MC prediction for no oscillations. The dashed line shows the predicted distribution for ν_μ going to ν_τ oscillations with $\sin^2 2\theta$=1 and Δm^2=2.2x10^{-3} eV^2.

and ν_τ. The most recent results from the Super-K experiment, using 1496 days of data, measures the ν_e solar neutrino flux to be 2.35 $\pm$ 0.02 (stat.) $\pm$ 0.08 (syst.) x 10^6/(cm^{2}s) [70]. This result assumes that all solar neutrinos detected by the Super-K detector are only ν_e. The measured solar neutrino flux again falls well short of the SSM predicted flux (5.05 $^{+1.01}_{-0.81}$ x 10^6/(cm^{2}s)).

D_2O Cherenkov

In 1985, Herb Chen released a paper that described how the extra neutron in the deuteron contained in D_2O could be used to detect the total neutrino flux from the Sun [14]. Shortly after the release of this paper, the SNO collaboration was formed with a goal to build a 1000 tonne D_2O solar neutrino detector that could measure, with high accuracy, the total neutrino flux from the Sun [26]. A direct measurement of the total solar neutrino flux would provide a decisive answer to the solar neutrino problem. The persistence of the problem had made it uncertain whether something was happening to neutrinos following production in the solar core, or if the astrophysics of the solar energy production was incorrect.

All previous experiments were essentially sensitive only to the ν_e. In a heavy water detector, there are three possible reactions for detection of solar neutrinos:

$$\nu_e + {}^2H \Rightarrow p + p + e^- \quad \text{Charged Current (CC)} \tag{2.5}$$

$$\nu_x + e^- \Rightarrow \nu_x + e^- \quad \text{Elastic Scattering (ES)} \tag{2.6}$$

and

$$\nu_x + {}^2H \Rightarrow \nu_x + p + n. \quad \text{Neutral Current (NC)} \tag{2.7}$$

In the above equations, ν_x may be any of the active neutrino flavors (e, μ, and τ).

The CC reaction is sensitive only to ν_e, as shown by its Feynman diagram (Figure 2.4). This reaction has the highest statistics of the neutrino-physics interactions in the SNO detector. When a CC reaction occurs in the SNO detector, an electron is produced that has an energy very close to the original neutrino's energy. It is possible to use the energy spectrum of the detected CC events to infer the solar neutrino energy spectrum. The direction of the electron is also slightly correlated with the original neutrino's direction of travel.

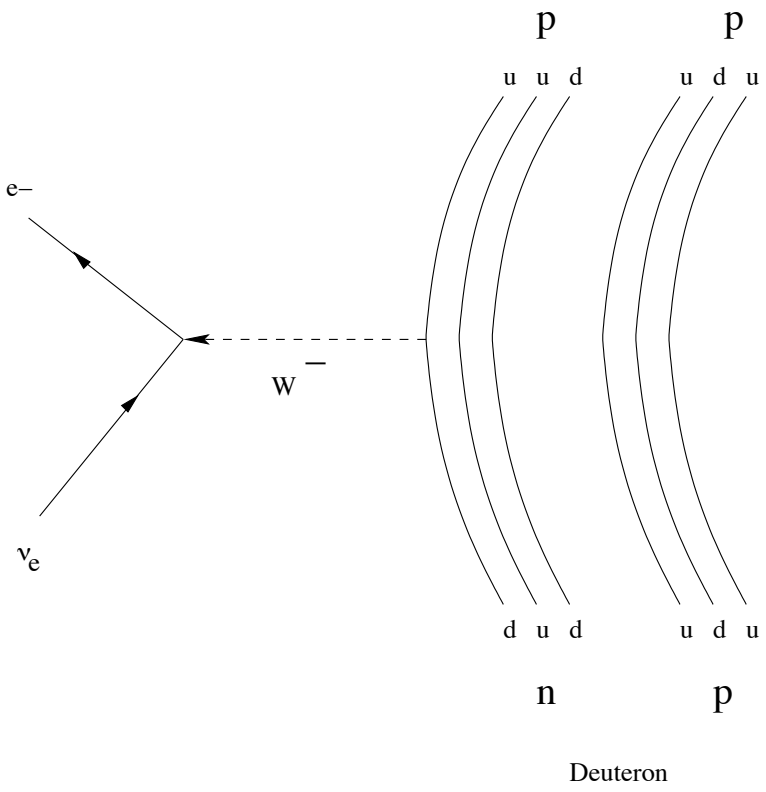

Figure 2.4: The Feynman diagram for the CC reaction. At low energy, the reaction is sensitive to ν_e only.

The NC reaction is equally sensitive to all neutrino types, as shown in it's Feynman diagram (Figure 2.5). With this reaction, SNO has the unique ability to measure the total neutrino flux from the Sun, independent of the neutrino type. The detected particle in the NC reaction is a neutron. In the first phase of the SNO experiment (November 1999 - June 2001), neutrons could re-capture on the D_2O to produce a 6.25 MeV gamma ray. This gamma ray typically produces an electron, which is detected by the Cherenkov light it generates. It is possible to enhance the NC reaction detection efficiency in SNO with, for instance, the addition of chlorine to the D_2O. Chlorine has a higher capture cross-section for neutrons than D_2O, and therefore the detector efficiency for the NC reaction can be greatly improved with

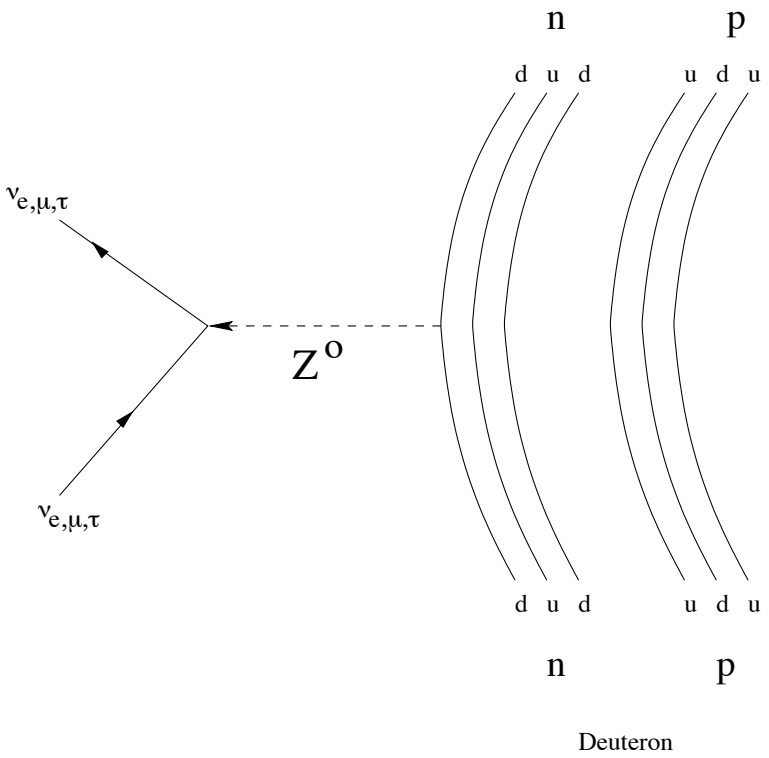

Figure 2.5: The Feynman diagram for the NC reaction. The reaction is equally sensitive to all active neutrino flavors.

its addition. This represented SNO's second experimental phase, from July 2001 to August 2003. SNO is currently being configured for a third phase, involving Neutral Current Detectors (NCDs). In this phase, ^{3}He proportional tube counters are added to the active volume to capture the neutrons produced in the NC reaction.

The ES reaction is most sensitive to ν_e, with the strength of the interaction for the other neutrino flavors approximately 1/6 as strong. Very simply, it is the scattering of a neutrino on an electron in the detector, as shown in its Feynman diagram (Figure 2.6). The electron in this reaction is highly correlated with the incoming neutrino direction. Therefore, the distribution of ES events is peaked away from the position of the source (the Sun for solar neutrinos).

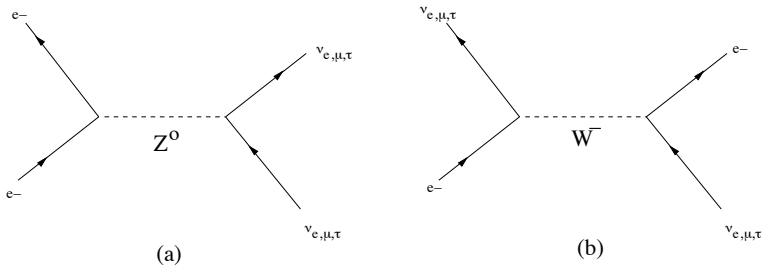

Figure 2.6: The Feynman diagrams for the ES reaction. Figure (a) is sensitive to all three neutrino flavours. Figure (b) is sensitive only to electron-type neutrinos. Therefore, the ES reaction is primarily sensitive to ν_e, with a sensitivity to ν_μ and ν_τ of roughly 1/6 the strength. The ES events are directionally constrained away from the source.

In April 2002 the SNO collaboration released the NC measurement from its first (pure D_2O) phase of the experiment [1]. The SNO experiment measured the total solar neutrino flux to be 6.42 $\pm$ 1.57 (stat.) $\pm$ 0.55 (syst.) x 10^6 neutrinos/(cm^{2}s). The ν_e flux was measured independently through the CC reaction in SNO and was found to be 1.76 $\pm$ 0.05 (stat.) $\pm$ 0.09 (syst.) x 10^6 neutrinos/(cm^{2}s). These results, showing that the ν_e flux was a small fraction of the total flux, were the first direct evidence for solar neutrino oscillations. Combining the results of the total flux with the ν_e flux rules out a null hypothesis of no neutrino oscillations at a 5.3σ level. Hence, the SNO measurement demonstrated neutrinos oscillate following production in the solar core, and that the total neutrino flux is consistent with the SSM prediction (see figure 2.7).

2.3 Neutrino Oscillations

Neutrinos are a part of the electro-weak sector of the Standard Model (SM) in particle physics. The SNO NC results demonstrated that approximately two-thirds of the ν_e produced in the Sun oscillate to another one of the other active neutrino

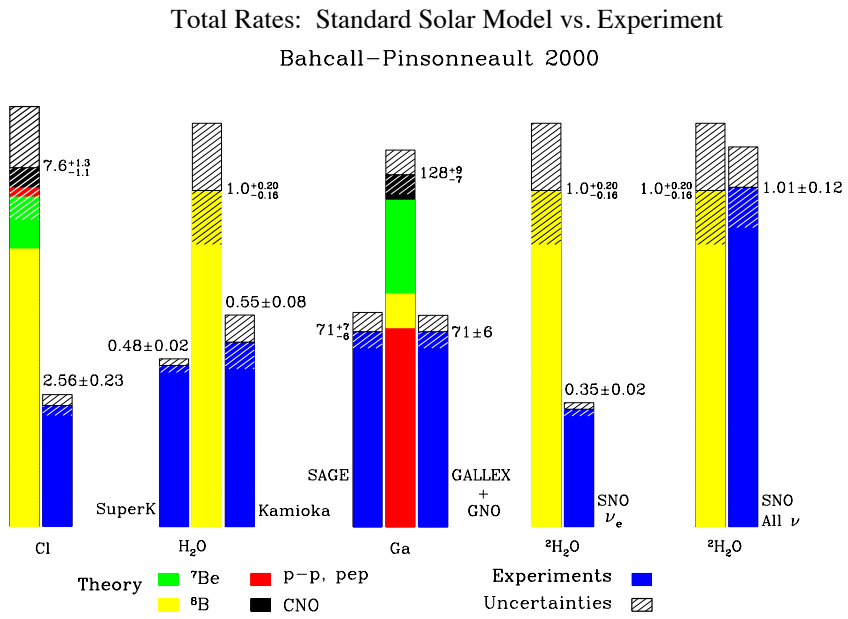

Figure 2.7: Standard solar model predictions compared with results from numerous solar neutrino experiments [75]. Notice the difference between the measured and predicted flux of solar neutrinos in all the experiments except the total flux measured by SNO.

flavours (ν_μ or ν_τ). However, the basic SM assumes the neutrino is massless, and therefore does not provide a mechanism for the neutrino to change flavour. The popular method to incorporate neutrino oscillations is to develop an extension to the SM. In this extension, the neutrino is assumed to be in a mixed mass eigenstate (described below) similar to what was discovered in the K_{Long}-K_{Short} CP-violating meson system. The following sections describe the physics necessary to accommodate neutrino oscillations, and how one may use oscillations to interpret the physical meaning of the experimental results.

2.3.1 Two Neutrino Mixing and Vacuum Oscillations

As a first approximation, we consider two neutrino mixing. In general, the neutrino mass eigenstates are taken to be different from the flavour eigenstates (see equations 2.8 and 2.9) as demonstrated in [6]. The $|\nu_{e,\mu,\tau}\rangle$ terms are the flavor eigenstates, $|\nu_{1,2}\rangle$ are the mass eigenstates and θ is the mixing angle.

$$|\nu_e\rangle = |\nu_1\rangle \cos\theta + |\nu 2\rangle \sin\theta \tag{2.8}$$

$$|\nu_{\mu,\tau}\rangle = -|\nu_1\rangle \cos\theta + |\nu 2\rangle \sin\theta \tag{2.9}$$

In this description, the ν_e flavour state that in observed in interactions is an admixture of two mass eigenstates that represent the fundamental particles. The same two mass eigenstates also make up another neutrino flavour eigenstate (μ or τ). It is therefore possible for an ν_e to undergo oscillations to the other flavour state prior to its interaction and detection. In general, the neutrino will propagate in time as

$$|\nu(t)\rangle = e^{-iHt}|\nu_e\rangle \tag{2.10}$$

where H is the Hamiltonian of the system. For the mass eigenstates

$$H|\nu_1\rangle = |\nu_1\rangle E_1. \tag{2.11}$$

Equation 2.10 can be re-written as

$$|\nu(t)\rangle = |\nu_1\rangle e^{-iE_1 t}\cos\theta + |\nu_2\rangle e^{-iE_2 t}\sin\theta, \tag{2.12}$$

where the energy terms may be represented as

$$E_j = (p^2 + m_j^2)^{1/2}. \tag{2.13}$$

For $m_j << E_j$, equation 2.13 reduces approximately to

$$E_j \approx |p| + \frac{m_j^2}{(2E)}. \tag{2.14}$$

With the above equations, it is possible to develop a survival probability for ν_e as they propagate in time, that is, the probability an ν_e will remain an ν_e after some period of time. The survival probability may be written as

$$P_{ee} = |\langle \nu_e | \nu(t) \rangle|^2. \tag{2.15}$$

Using equations 2.12 and 2.14 above, 2.15 reduces to

$$P_{ee} = 1 - \sin^2(2\theta) \sin^2(\frac{\Delta m^2 t}{4E}) \tag{2.16}$$

where E is the neutrino energy and $\Delta m^2 = m_2^2$ - m_1^2. Neutrino oscillations may occur provided that the mixing angle is non-zero, and at least one of the neutrinos is massive ($\Delta m^2 \neq 0$). The survival probability demonstrates that for specific Δm^2 and $\sin^2(2\theta)$ values, the ν_e flux may be suppressed.

2.3.2 Generalized 3 Neutrino Mixing

The 2 neutrino mixing described above can be expanded to include all three active neutrino flavours. In this case, One may represent the mixing of the neutrino eigenstates with a single mixing matrix, U, known as the Maki-Nakagawa-Sakata-Pontecorvo matrix (Equation 2.17).

$$\begin{bmatrix} \nu_e \\ \nu_\mu \\ \nu_\tau \end{bmatrix} = \begin{bmatrix} U_{e1} & U_{e2} & U_{e3} \\ U_{\mu 1} & U_{\mu 2} & U_{\mu 3} \\ U_{\tau 1} & U_{\tau 2} & U_{\tau 3} \end{bmatrix} \begin{bmatrix} \nu_1 \\ \nu_2 \\ \nu_3 \end{bmatrix} \tag{2.17}$$

It is convenient to parameterize this matrix in the following manner;

$$U = \begin{bmatrix} c_{12} & s_{12} & 0 \\ -s_{12} & c_{12} & 0 \\ 0 & 0 & 1 \end{bmatrix} \text{x} \begin{bmatrix} 1 & 0 & 0 \\ 0 & c_{23} & s_{23} \\ 0 & -s_{23} & c_{23} \end{bmatrix} \text{x} \begin{bmatrix} 1 & 0 & 0 \\ 0 & 1 & 0 \\ 0 & 0 & e^{-i\delta} \end{bmatrix} \text{x} \begin{bmatrix} c_{13} & 0 & s_{13} \\ 0 & 1 & 0 \\ -s_{13} & 0 & c_{13} \end{bmatrix} \text{x} \begin{bmatrix} 1 & 0 & 0 \\ 0 & e^{i\gamma_2} & 0 \\ 0 & 0 & e^{-i\gamma_3} \end{bmatrix} \tag{2.18}$$

where the terms of the form c_{12} and s_{12} are $\cos\theta_{12}$ and $\sin\theta_{12}$ respectively of the specific mixing angle. The δ term represents the CP violating phase for the neutrino sector. If neutrinos are Dirac particles, the final matrix in equation 2.18 becomes the identity matrix. Otherwise, neutrinos would be Majorana particles, and one must include the additional CP violating phases γ_2=e$^{i\alpha_2}$ and γ_3=e$^{i\alpha_3/2+i\delta}$. With this parameterization, the dominant terms in each matrix are closely associated with variables obtained from various experiments. For example, measurements of atmospheric neutrinos predominantly probe $\nu_\mu \rightarrow \nu_\tau$ transitions, which are largely $\nu_2 \rightarrow \nu_3$. Listed in order from the top left of equation 2.18 are matrices that relate closely to solar neutrinos, atmospheric neutrinos, the CP violating phase, reactor-accelerator neutrinos and finally the Majorana Phases from double β decay measurements.

Using this mixing matrix, equation 2.16 for the survival probability can be rewritten as

$$P_{ee} = 1 - \sum_{jk} |U_{ej}|^2 |U_{ek}|^2 e^{-(\frac{i\Delta m^2_{jk} t}{2E})}. \tag{2.19}$$

This represents the probability the ν_e has survived a change to ν_μ or ν_τ, and is a method for describing the probability for neutrino oscillations (see Figure 2.8).

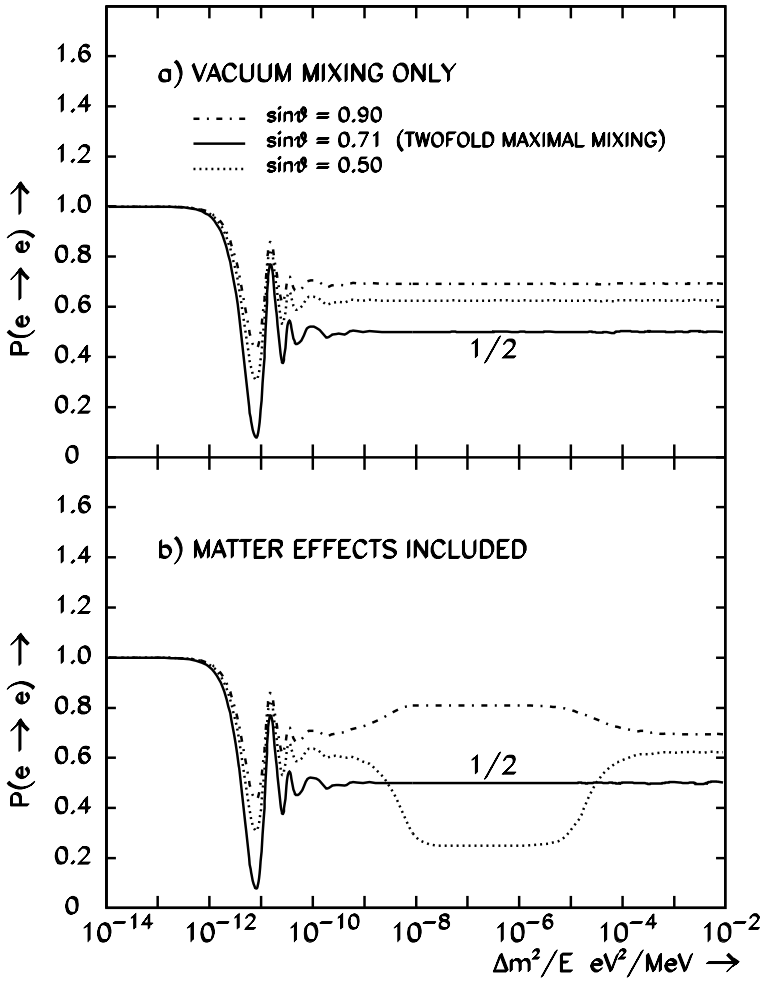

Figure 2.8: The survival probabilities for vacuum mixing oscillations. Shown are the cases for large mixing angle (dot-dashed line), maximal mixing (solid line), and low mixing angle (dotted line). The lower plot shows the effect of including matter effect in the probability calculation. For values of $\Delta m^2/E$ between 10^{-5} and 10^{-9}, there is a clear change in the survival probabilities when matter effects are included [75]. The probability for a large mixing angle ($\sin\theta$=0.90) is enhanced while the small mixing angle ($\sin\theta$=0.50) is suppressed, with the presence of matter effects compared to vacuum mixing.

2.3.3 Matter Enhanced Oscillations- the MSW effect

It has been proposed that neutrino oscillations may be enhanced by the presence of matter. This enhancement is known as the Mikheyev, Smirnov and Wolfenstein

(MSW) effect [74][55]. The principle of the effect is based on the difference between the interaction of ν_e, versus ν_μ and ν_τ, in matter. As discussed earlier, ν_e may interact via a Charge-Current ($W^{\pm}$ exchange) and Neutral-Current (Z^0 exchange), while, at low energies, ν_μ and ν_τ interact only via the Neutral-Current reaction. This difference can be accounted for by adding terms to the Hamiltonian.

The propagation of the neutrino state in matter may be represented as

$$i\frac{d}{dt}|\nu(t)\rangle = (H_o + H_{matter})|\nu(0)\rangle \tag{2.20}$$

where

$$H_{matter} = \sqrt{2}G_F n_e |\nu_e\rangle\langle\nu_e|. \tag{2.21}$$

Here, G_F is Fermi's constant and n_e is the electron density. The effect of the extra term in the Hamiltonian makes the ν_e "heavier" in regions where the electron density is higher, such as the dense regions of the Sun. This is understood as the ν_e obtaining an effective mass through its interactions with electrons in matter. There can therefore exist regions of resonance within the Sun where the ν_e may convert completely to a heavier neutrino (ν_μ or ν_τ). Resonance occurs for an effective mixing angle of

$$\tan 2\theta_M = \frac{\sin 2\theta}{\cos 2\theta - L_V/L_e}. \tag{2.22}$$

In this equation, L_V is the vacuum oscillation length, given by

$$L_V = \frac{4\pi E\hbar}{\Delta m^2 c^3}, \tag{2.23}$$

and L_e is the mass oscillation length

$$L_e = \frac{\sqrt{2}\pi\hbar c}{G_F n_e}. \tag{2.24}$$

The equation is maximized when the denominator of equation 2.22 goes to 0. This occurs when

$$n_e = \frac{\cos 2\theta \Delta m^2}{2\sqrt{2}G_F E}. \tag{2.25}$$

Since the matter enhanced oscillations are also energy dependent, it is clear the ν_e flux may also experience an energy dependent suppression. Therefore, neutrino detectors with different energy thresholds would expect different count rates for the same regions of Δm^2 and $\tan^2(2\theta)$. Comparing the measured detector rates to predictions, from various oscillation regions, can reveal the form of oscillation occurring. The possible oscillation solutions include vacuum versus MSW, or a combination of the two, known as the quasi-vacuum. Figures 2.9 and 2.10 show the contours for the available solutions before and after the first SNO results were included. One observes the SNO data has greatly narrowed the allowed parameter space, particularly in the Low-mixing angle region, which has been eliminated as a possible solution by the SNO data.

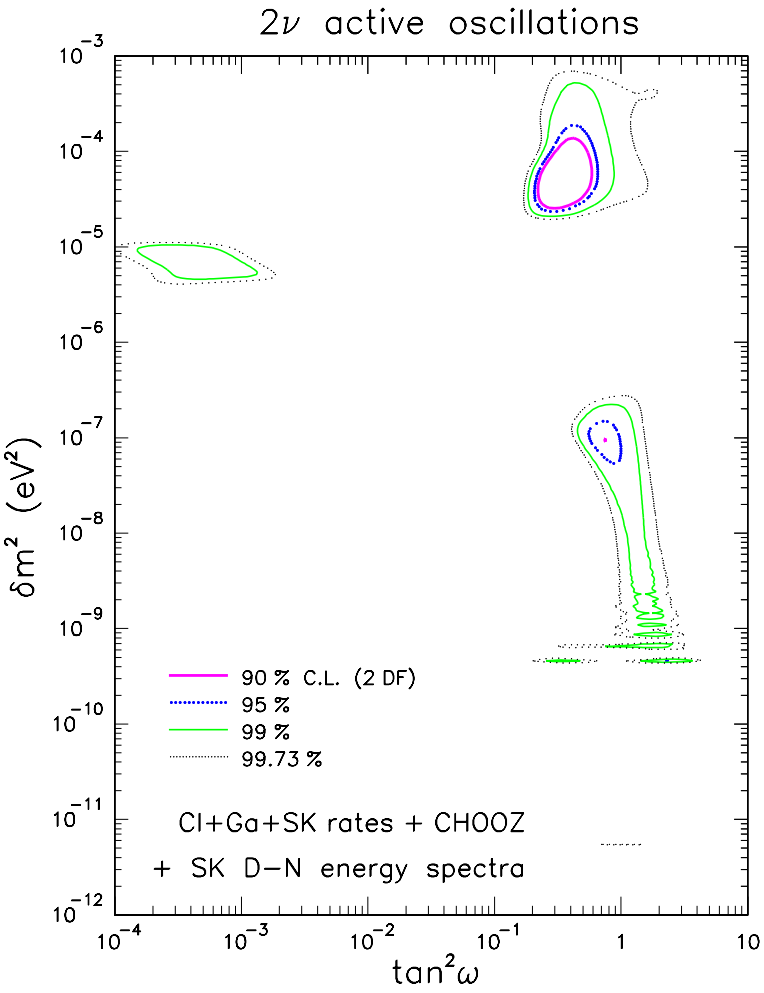

Figure 2.9: The MSW parameter space for a global fit to neutrino experiment results before adding the effect of the first SNO NC measurement [75]. The surviving oscillation regions are the Low mixing angle (top left), the Large mixing angle (top right) and the vacuum-quasi vacuum region (bottom right).

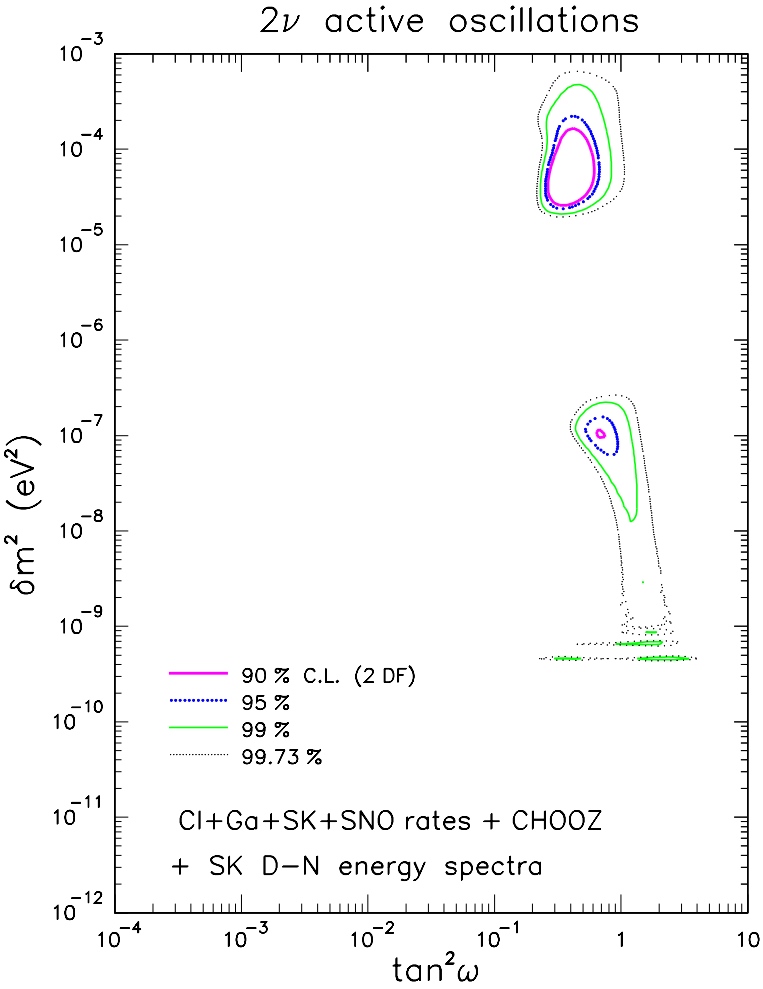

Figure 2.10: The MSW parameter space for a global fit to neutrino experiment results after adding the effect of the first SNO NC measurement[75]. Inclusion of the SNO result has remove the Low mixing angle region from the allowable solutions and eliminated a large amount of the vacuum and quasi-vacuum mixing areas. The Large mixing angle solution space contains the best fit point.

Chapter 3

The SNO Detector

3.1 Detector Overview

The Sudbury Neutrino Observatory (see figure 3.1) is a water Cherenkov detector, located 2 km underground in the Creighton Mine of Inco Ltd. As described in Chapter 2, Cherenkov detectors observe particles through their production of "Cherenkov" light, emitted in a conical geometry along the track of the particle. The SNO detector consists of 1000 tonnes of high purity D_2O contained in a 12 m diameter spherical acrylic vessel (AV). Surrounding the acrylic vessel are approximately 9600 inward facing 20 cm photomultiplier tubes (PMTs) supported on a stainless steel geodesic, the photomultiplier support structure (PSUP). The purpose of the inward looking PMTs is to record the light produced in the detector from neutrino interactions and other sources. To best detect Cherenkov light, the PMTs have been designed to have high efficiency in the UV wavelength region. Further details of the properties of the PMTs and AV are contained in Chapter 4 in the discussion of the optical calibrations of the SNO Detector. Regions of ultra-pure H_2O are located between the AV and PSUP and outside the PSUP, with volumes of

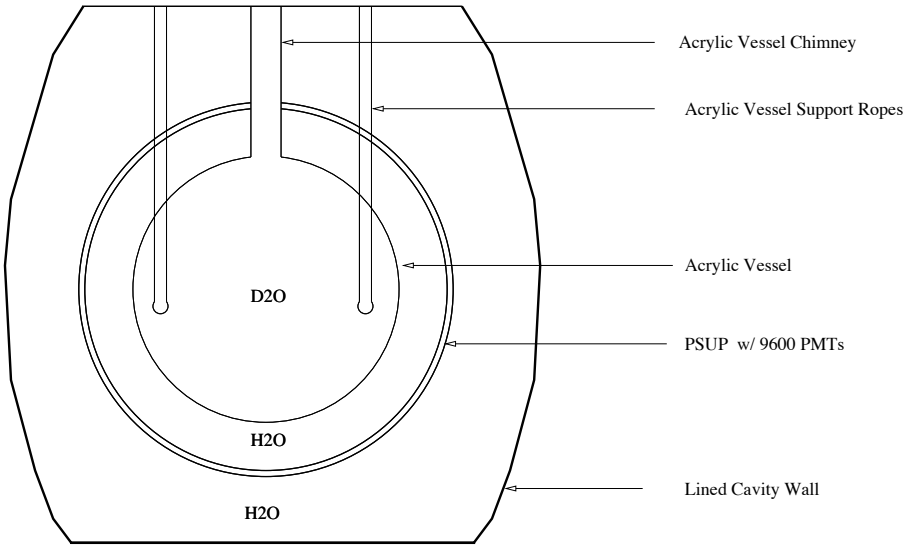

Figure 3.1: A schematic drawing of the SNO detector. The main detector region is the D_2O. This is surrounded by H_2O and is observed by an array of PMTs. The number of PMTs is approximately 9600.

1700 and 5300 tonnes respectively.

Cosmic ray particles and naturally occurring radioactivity in the detector can produce events which mimic the very rare neutrino events. To minimize the impact of this, there are 96 outward-looking PMTs on the PSUP that act as an active veto signal for muons traversing the outer region of the detector. The detector cavity is lined with 9 layers of urylon to act as a radon barrier and provide a water-tight seal. This is also the purpose in locating the detector 2 km underground in order to escape the backgrounds produced by cosmic rays. In addition, each detector component must be as low as possible in uranium and thorium content to maintain low background signals in the detector. The next section describes the low background techniques used to achieve this. The remainder of the chapter is then devoted to describing how SNO generates an event for analysis, and the methods used for calibrating the detector.

3.2 Backgrounds

In the SNO experiment, the term background is used to describe sources of detected events that are not a part of the physics goals of the detector. The background sources include events arising from the electronics, the AV and radioactivity. How we handle the background events in the neutrino data set is discussed in Chapter 5.

The primary source of background in SNO is naturally occurring ^{238}U and ^{232}Th. These elements are found, at some level, in all building materials and liquids. Therefore, each piece of the SNO detector, from the rock in the outer cavity walls, to the glass of the PMTs and steel of the PSUP, and even including the D_2O and H_2O detector media, contain at least traces of these elements. The decay chains for ^{238}U and ^{232}Th are shown in figures 3.2 and 3.3, respectively. In these decay chains, the problem decays for the SNO detector are the daughter isotopes, ^{210}Tl and ^{212}Bi. The decay of these daughters produce gamma rays with energies greater than 2.23 MeV. This energy is large enough to photo-disintegrate the deuteron, and therefore produce neutrons in the detector. The neutrons can mimic the NC neutrino signal and therefore limit the sensitivity of the experiment. Since these backgrounds are associated with the detector components, the only way to limit them is to use materials where the concentrations of U and Th are as low as possible. The most radioactive component of the inner detector are the PMTs. The high rate of β-γ decays of the ^{238}U and ^{232}Th daughters in the PMT glass can limit the the minimum achievable detector energy threshold by causing mis-reconstruction, and coincidental piling-up of events.

To meet the background criteria for the detector media, very complex water systems have been designed and built to purify and assay the H_2O and D_2O for these elements. Purity is achieved principally through the removal of ions via reverse osmosis (RO) processes, degassing systems (to remove radon) and ion exchangers (see

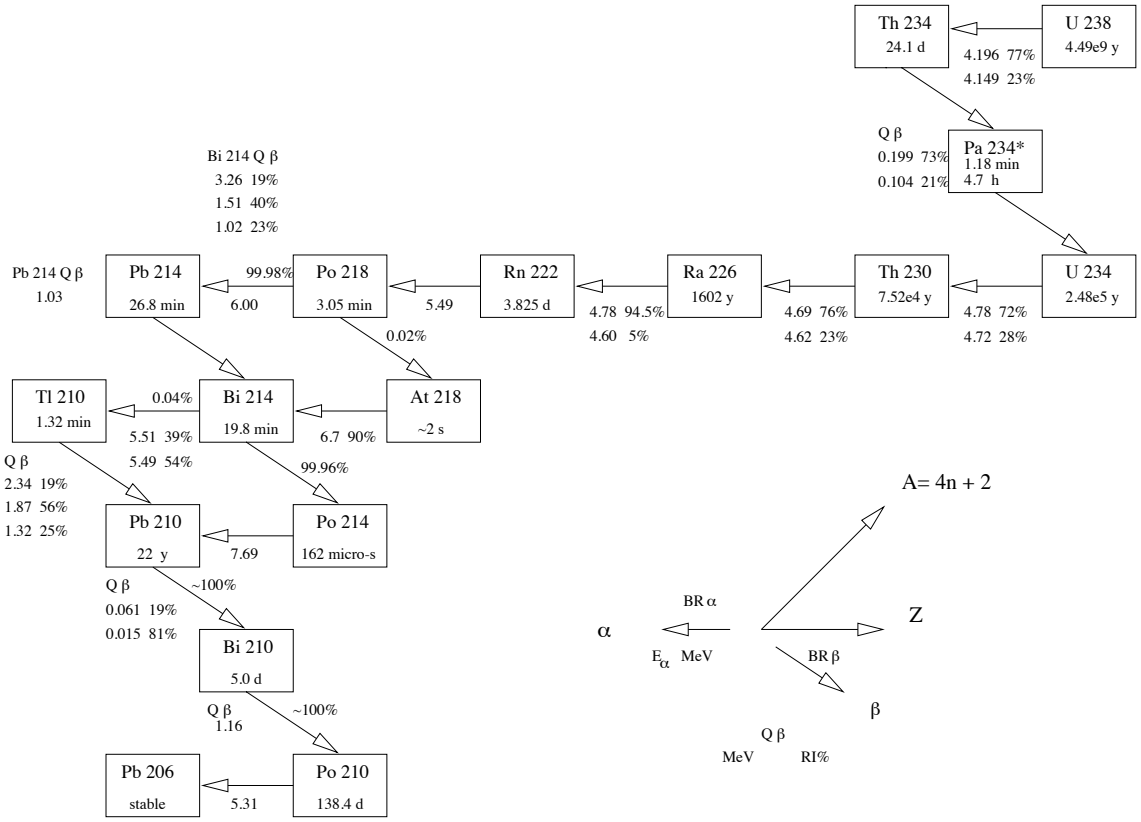

Figure 3.2: A schematic drawing of the ^{238}U decay chain [27]. As shown by the figure in the bottom corner, alpha decays occur when moving to the left, beta decays occur when following arrows down and to the right. Branching ratios for the decays are above the arrow lines, and the energy produced by in the decays are below. Moving to the right, one increases Z, and to the upper-right is an increase in A.

figures 3.4 and 3.5). Furthermore, the water systems filter and cool the water in the detector. The H_2O system uses micro-filters to remove any particles larger than 0.3 microns. The D_2O system uses ultra-filtration devices that have a pore-size of approximately 5000 daltons. The cooling of the detector water provides multiple beneficial effects. The low temperature of the H_2O lowers PMT noise and limits biological growth. The cooling also has the effect of creating a temperature gradient to produce stratification. This limits the ingress of radon into the water to the

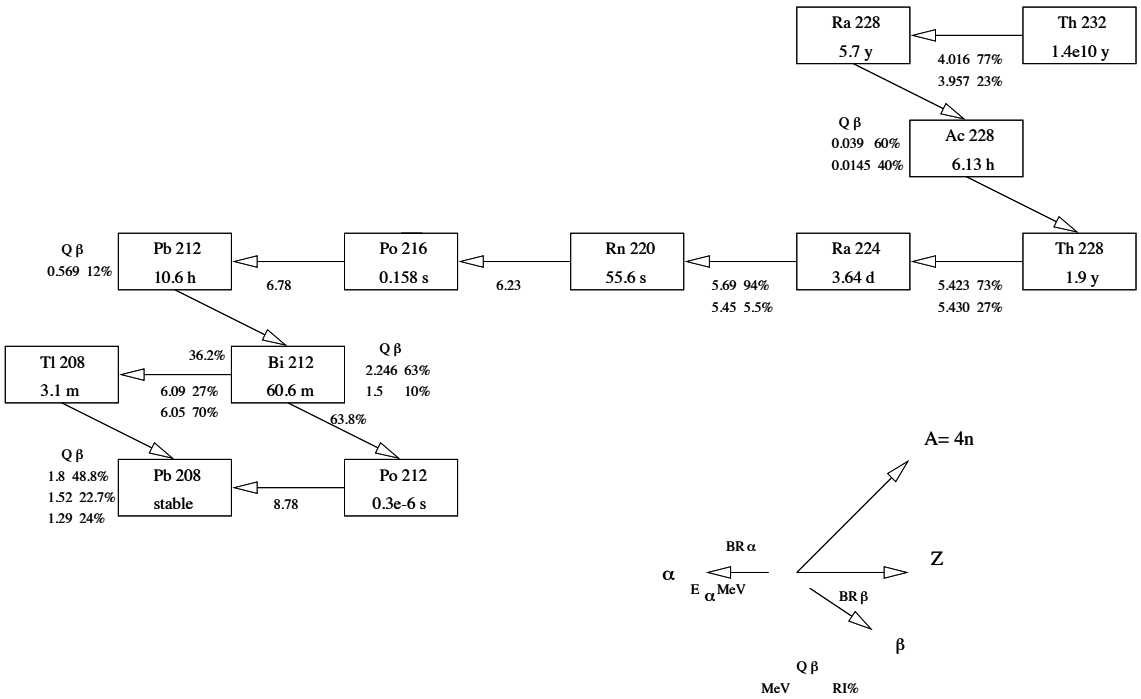

Figure 3.3: A schematic drawing of the ^{232}Th decay chain [27]. Details of the figure are found in 3.2.

upper-most part of the detector. The goal of these systems is to achieve a purity in U and Th (and all of their daughters) that results in less than one background neutron per day. This limit is converted to the ^{238}U and ^{232}Th levels shown in Table 3.1. This is the amount of U and Th allowed if one assumes the decay chains are in secular equilibrium, and is the conventional manner of expressing the chain activity.

It is one issue to design a system to achieve these limits, it is another to produce assay methods which are capable of accurately measuring the traces of U and Th remaining in the water at these levels. Details of the specific assay techniques developed by SNO to perform these measurements are documented in [2], [3] and [4]. Radon from the U chain concentration is measured using the monitor degasser

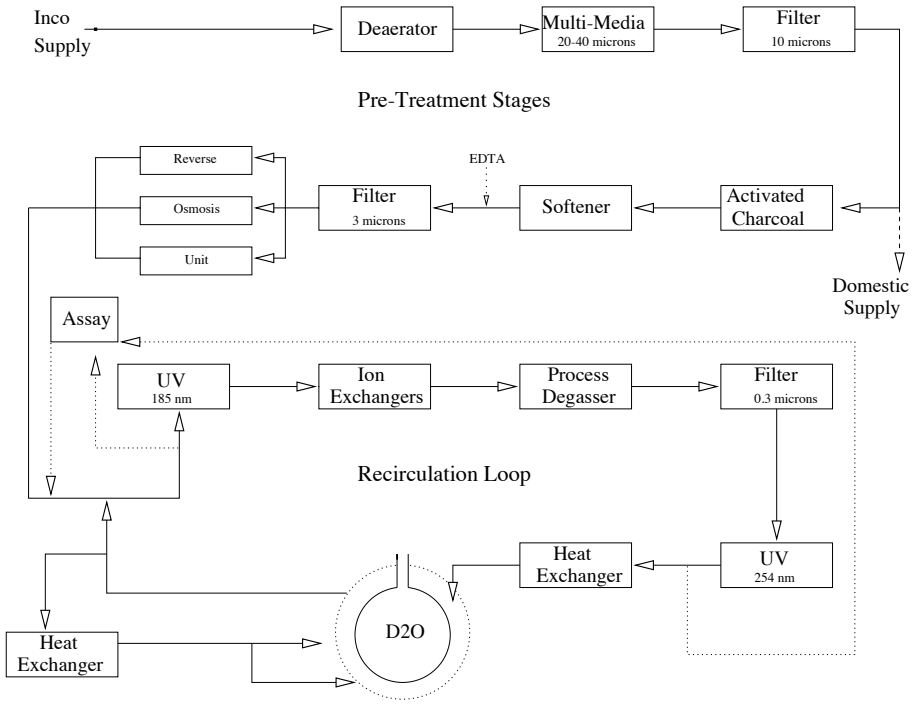

Figure 3.4: A schematic drawing of the SNO H_2O recirculation system. The pre-treatment stages produce water that is usable in the lab for showers, laundry and drinking. The reverse osmosis system removes >99% of metals and organics. The UV stages kill any biological componets in the water. Ion exchangers remove the remaining metals, producing ultra-pure H_2O. The process degasser removes the bulk of gases from the water including radon with >95% efficiency. The heat exchangers remove the process heat from the water, returning H_2O to the cavity at approximately 10° C.

systems. Radium, in both the U and Th chain, is measured with two independent techniques using either MnOx coated beads or HTiO coated filters. Both resins have a very high affinity for heavy metals, such as radium, and effectively clean the water as it is assayed. The results of these assays are seen in figures 3.6 and 3.7. It is observed in these figures that the background levels in the D_2O and H_2O have either met or surpassed the target levels over the life-time of the detector.

The relatively short lived radon daughter of ^{238}U, ^{222}Rn, poses a significant prob-

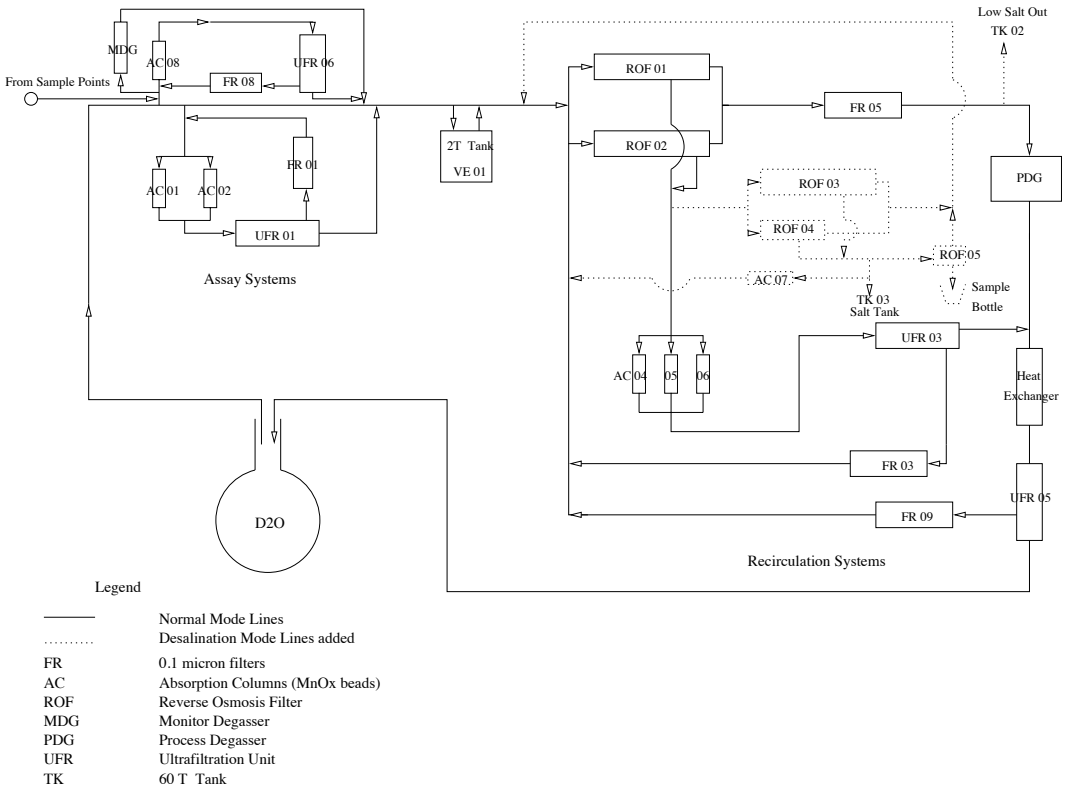

Figure 3.5: A schematic drawing of the SNO D_2O recirculation system. The system is composed of processing and assay components. The reverse osmosis system is multi-stage, allowing very efficient removal of metals, organics and the salt (once that stage of the experiment is complete). Ultra-filtration units remove any particulates of size >5000 daltons. Process degasser systems remove radon gas that may enter due to the recirculation process. Finally, heat exchangers return the D_2O to the AV at a temperature of approximately 8° C.

lem in the underground environment of the detector. Due to the uranium present in the surrounding rock, the level of ^{222}Rn is a factor of 30 greater than that found in the SNO labs on the surface. Radon has the ability to migrate into any system which is not helium leak-tight, and, with a 4 day half-life, can easily diffuse through thin materials. Even small concentrations of ^{222}Rn can produce large backgrounds in the detector. The water systems have been designed to eliminate the possibil-

Water Type	Element	Target Level (g Element/g Water type)
D_2O	^{238}U	4.5 x 10^{-14}
	^{232}Th	3.7 x 10^{-15}
H_2O	^{238}U	4.5 x 10^{-13}
	^{232}Th	3.7 x 10^{-14}

Table 3.1: The target limits for the SNO detector water backgrounds. Note, it is assumed the U and Th chains are in secular equilibrium for the quoted levels. The quoted levels are then the maximum activity for the daughters in terms of the parent elements.

ity for radon to leak or diffuse into them. Degasser units remove and assay the radon present in the detector, and a purified nitrogen covergas is maintained in the airspace above the detector to create a barrier from the radon in the mine air [32] [4]. The urylon liner of the cavity also behaves as a radon barrier, further reducing this background.

The AV that contains the D_2O has the largest exposed surface area in the detector. It is therefore crucial that it also be low in U and Th. The AV was constructed from 125 acrylic panels that were bonded together in the underground cavity. Acrylic has naturally low concentrations of U and Th. The acrylic for the SNO detector was also specifically selected and produced in very clean conditions to ensure minimal contamination. To further maintain the cleanliness of the AV, the SNO underground lab was monitored for mine-dust levels during the construction process in order to keep the total amount of dust on the 10-story tall detector to less than 1 gram.

Like the acrylic of the vessel, the glass for the PMTs was manufactured under controlled conditions to ensure it was as free from backgrounds as possible. The PMT glass, by itself, is relatively free of U and Th contamination. However, the manufacturing process can result in significant contamination. The PMT backgrounds are dominated by β-γ decays at the glass, that can produce a signal in the photocathode. These background events, combined with the U and Th backgrounds described

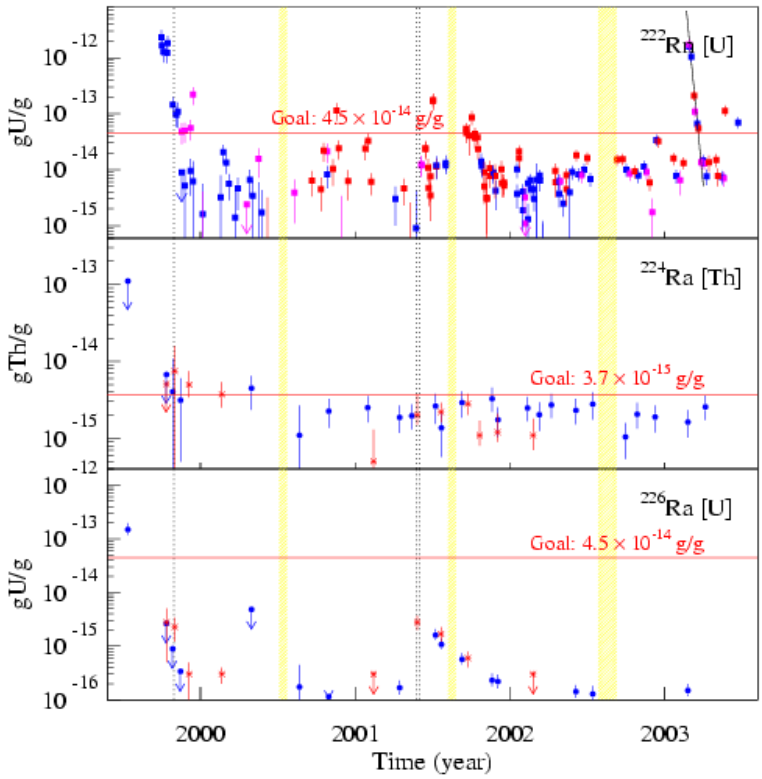

Figure 3.6: Results for radioactivity in the D_2O measured by D_2O assays versus time [66]. The upper-most panel shows the measured radon levels using the monitor degasser. The different colored points represent different sampling locations in the detector. Note the large increase in radon in the detector near the start of 2003. This is due to calibration of the detector using a radon source. The middle and lower panel show the U and Th levels as measured from the MnOx (blue points) and HTiO (red points) assays. The red lines represent the background limit goals for the SNO detector. The single vertical black line shows the start of the pure D_2O data taking phase, and the double vertical black lines represent the start of the salt phase. The yellow bands represent periods of detector shutdown.

previously, create what is known as the background wall for SNO (shown in Figure 3.8). In Figure 3.8, one can see the minimum energy threshold for the detected neutrino events in the experiment is limited by the achieved background levels.

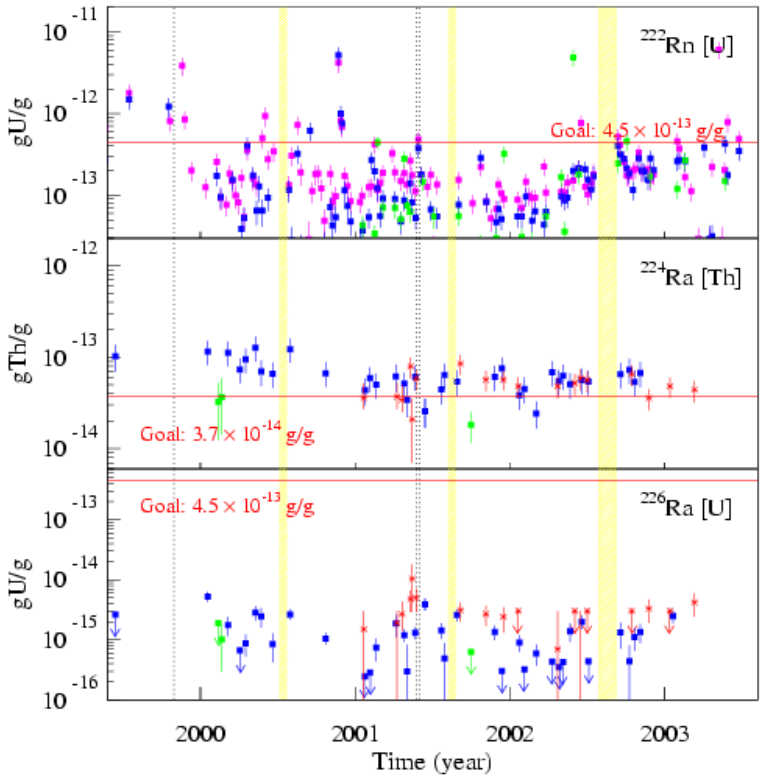

Figure 3.7: Results for radioactivity in the H_2O measured by H_2O assays versus time [66]. Details of the plots are described in 3.6.

3.3 Detector Signals

PMTs consist of a glass dome painted with a photocathode, and a series of anodes which generate a high electric field. The photocathode operates via the photoelectric effect. When a photon strikes the surface of the photocathode, an electron is produced, known as a photoelectron (PE). In accordance with the photoelectric effect, the number of PEs produced is dependent on the energy of each photon. When an interaction occurs in the detector that produces light, the photons which strike the photocathode of the PMTs produce PEs. As the PEs are accelerated in the electric field of the PMT, they shower. The PMT has many internal stages (dynodes) where

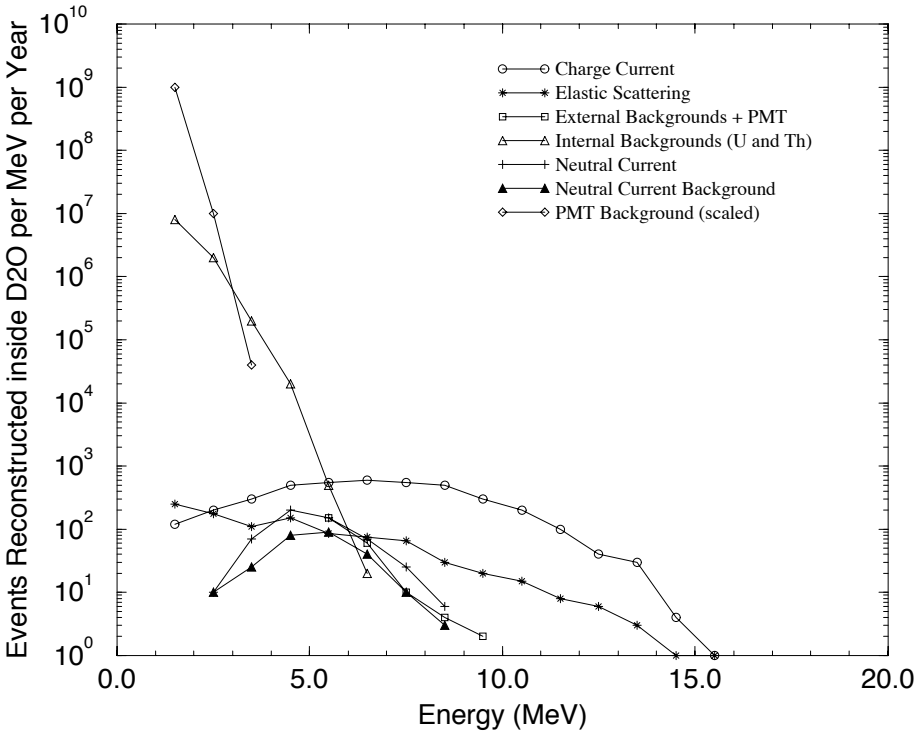

Figure 3.8: A plot of the SNO neutrino spectrum from a simulation representing 1 year of data. The PMT β-γ data has been "scaled" up from a simulation with a shorter time period [32]. External backgrounds are events produced outside of the AV, while internal backgrounds are generated in the D_2O region.

the electrons are multiplied and then accelerated to the next stage. This produces an avalanche of electrons that amplify the PMT signal.

The PMT signal is transmitted by coaxial cable to the electronics crates above the detector. The electronics have an individual channel for each PMT. Once the PMT signal reaches the electronics, the information is translated to time and charge. The charge of the PMTs may be integrated over short and long times, and at low and high gain. This offers four possible measurements of the charge. Three of these are recorded with each "detector event" (high-short, high-long, and low-short). The purpose of the various gains is to have good resolution for low energy events while

still accurately measuring high energy events. The charge for each tube is integrated to give the total charge of an event. This gives an approximate measurement of the amount of energy deposited by a given event.

A trigger system measures the number of tubes that have seen a signal within a global trigger window. The global trigger window has a width of 400 ns. The global trigger is defined once an adequate number of PMTs have produced a signal in the window. The PMT times have a resolution of <1 ns, and are referenced with respect to the start point of the global trigger. The PMTs and electronics are designed to have a very low trigger threshold; sub-single photon range. If more tubes have fired than the defined detector trigger threshold, the PMT information is sent to a builder program which combines all the PMT information for each tube into a single event. The events are then written in CERN ZEBRA (zdab) format and stored for analysis (see Figure 3.9).

A typical SNO neutrino event has an NHIT value (number of hit PMTs) of approximately 50, with the detector trigger threshold set at 18 NHIT. It is possible to use the event information (timing, charge and hit PMT pattern) to reconstruct the event's direction, vertex of interaction, energy, and isotropy. This is typically done using various fitter algorithms on the events. From the PMT information it is not possible to determine on a event-by-event basis the type of neutrino, or even if it was a neutrino, that caused the interaction. One only has the characteristics of event distributions to separate one type of reaction from another in the SNO data. To do this, probability density functions (PDFs) are generated to represent, for instance, the expected energy distribution of NC, CC and ES events. The same can be done for each available parameter. As an example, the PDFs used for the pure D2O phase analysis are shown in Figure 3.10. Note that the ES is easily identified by its forward-peaked $\cos(\theta_{Sun})$ distribution. Likewise, the CC and NC events are discriminated well by their radial distributions. Using these PDFs in a maximum

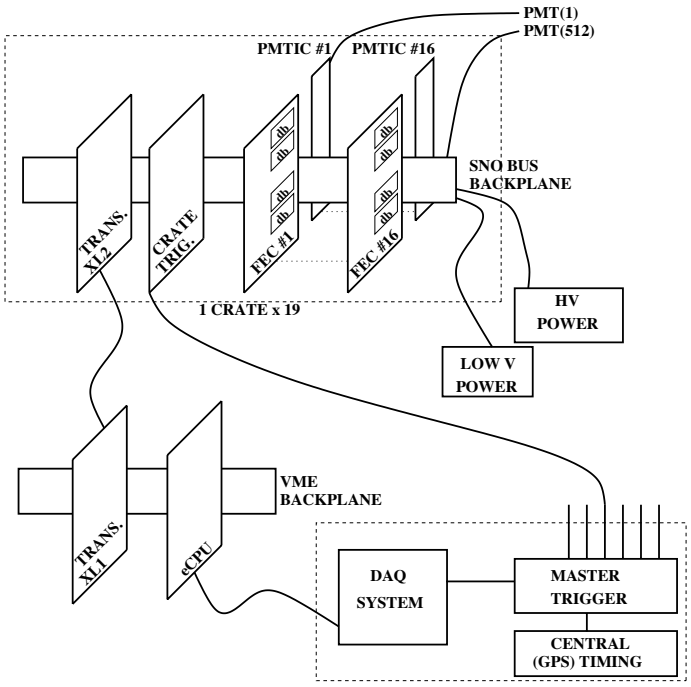

Figure 3.9: A schematic drawing of the custom built SNO trigger electronics system [65]. Signals from the PMTs enter the crates where they are digitized. The initial boards process the PMT information to produce time and charges. The master trigger system combines all the crate information. If the result exceeds the set hardware threshold, the system produces a global trigger. The DAQ electronics then control the readout of the information on the boards to tape storage. The system offers sub single photon thresholds, precision charge linearity, timing resolutions of <1 ns and large memory buffers (to handle the high event rates produced in the event of a supernova).

likelihood or chi-squared minimization, it is possible to determine how many events of each type are present in a given data set.

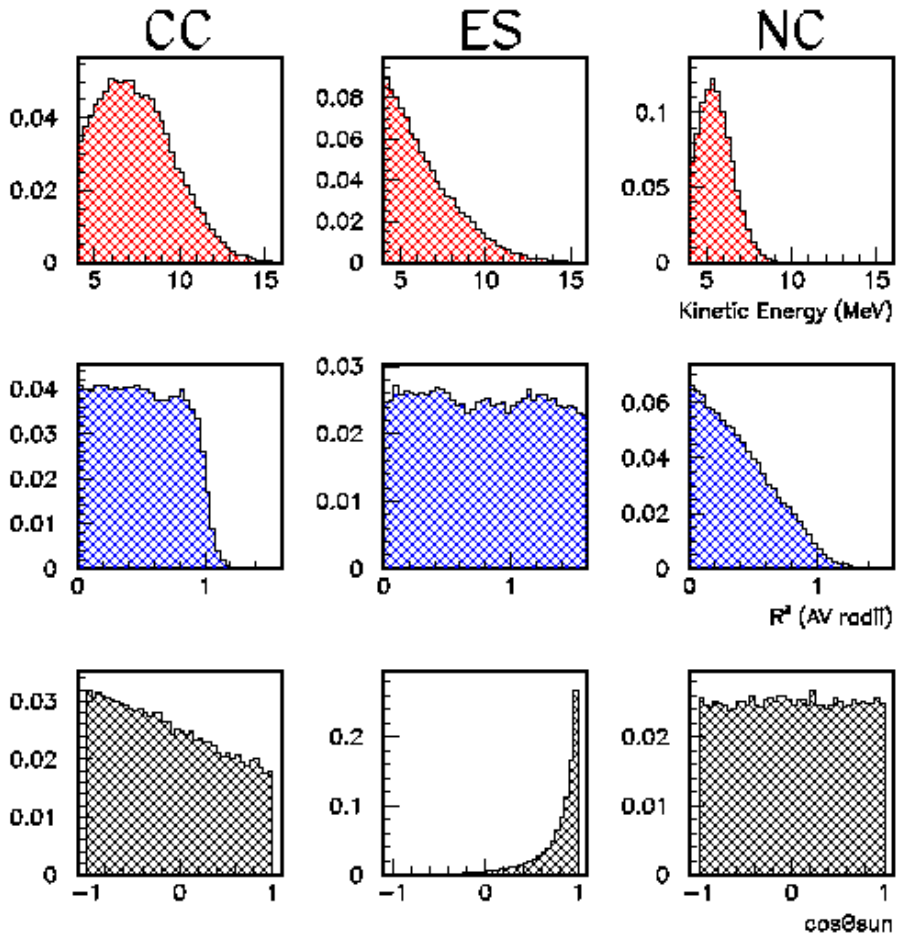

Figure 3.10: An example of the PDFs used for signal extraction during the pure D_2O phase. The differences in the PDFs provide the ability to separate CC, NC and ES events. The kinetic energy is the measured energy of the event assuming it is an electron, and is therefore the total energy of the electron minus 0.511 MeV. The radial term (R^3) is the location of the interaction vertex in units of the AV radius. $Cos(\theta_{Sun})$ is the direction of the event with respect to the direction to the Sun-Earth vector ($\cos(\theta_{Sun})$=1 is in the direction away from the sun.)

3.4 Calibration of the Detector

Calibration is a crucial step of any physics experiment. It is through calibration that a true understanding of the behavior of the detector is obtained. A robust

calibration program has been developed for the SNO detector. The program includes a variety of calibration sources to study various detector properties. The most important properties of the detector are the timing of the PMTs (Phototube Calibrations - PCA) and the electronic channels (Electronics Calibrations - ECA), as well as the detector energy response and optical properties as a function of position and energy. The SNO detector is designed to operate as three independent experiments at different points in its lifetime; during the pure D_2O, salt and NCD phases. Each phase of the experiment has different physical characteristics that change the detector response which need to be understood by extensive calibration. Table 3.2 lists the calibration sources designed and constructed for the SNO detector with the individual properties of each source. The goal of using a variety of sources is to map out the detector's response to photons, electrons, neutrinos and backgrounds at all energies of relevance to the SNO detector.

As an example, figure 3.11, shows the schematic drawing of the ^{16}N source. The ^{16}N source provides the primary measurement of the energy response of the detector. In the source, a gamma-ray of known energy (6.13 MeV) is released, providing a signal typical of what is expected in neutrino interactions. A series of short stability runs at the center of the detector, over the course of one of the experimental phases, provides a measure of the time dependence in the detector energy response. These calibrations are taken on a regular basis (see figures 3.12 and 3.13). The figures show gradual changes in the detector's performance with time due to changes in water transparency and other optical effects. The large change upon introduction of the salt is believed to be related to a change in the performance of the reflectors surrounding the PMTs. The increased slope in the salt phase is believed to be a result of Mn buildup, which could not be removed in the presence of the salt without also removing the salt.

Most of the sources need to be deployed in the D_2O, and often in the H_2O, to

Calibration Device	Quantum	Calibrations
Electronic Pulsers		Time slope/pedestal; Charge slope/pedestal
Laser Ball	Diffuse, approximately isotropic light at various wavelengths (337nm - 620nm)	Common time reference (t_o); D_2O absorp/scattering; Acrylic/H_2O abs/scatter; Reflections/scattering; Single PE response/eff.; Multiple PE resp; Walk
Untagged Sources: ^{16}N ^{252}Cf ^{8}Li Th, U $^{3}H(p,\gamma)^{3}He$ Accelerator	 γ, E=6.13 MeV n β, E_{max}=12.96 MeV γ γ, E=19.8MeV	 Gamma E response; Neutron capture efficiency; Electron E response; Gamma low E response; Gamma High E response
Tagged Sources: ^{16}N ^{252}Cf ^{24}Na ^{228}Th	 γ, E=6.13 MeV n γ γ	 Gamma E response; Neutron capture efficiency; Neutron capture background; Radioactivity response or low E

Table 3.2: Examples of the SNO calibration sources and their uses. Walk is the variation of PMT time with pulse amplitude.

map the detector's response at a representative selection of positions. The sources are similar in design, consisting of a source connected to a weight cylinder. The weight cylinder is then attached to an "umbilical". The umbilical is a long tube that carries all the essential services for the source; such as gases, laser light or electronic signals. Figure 3.14 shows an example of the umbilical for the ^{16}N source. The calibration sources are able to be moved to various positions in the detector using a series of ropes and pulleys, comprising the manipulator system (see figure 3.15). The manipulator system enables position dependent measurements of the detector response to be made.

Full detector scans, with calibrations made at many locations in the detector,

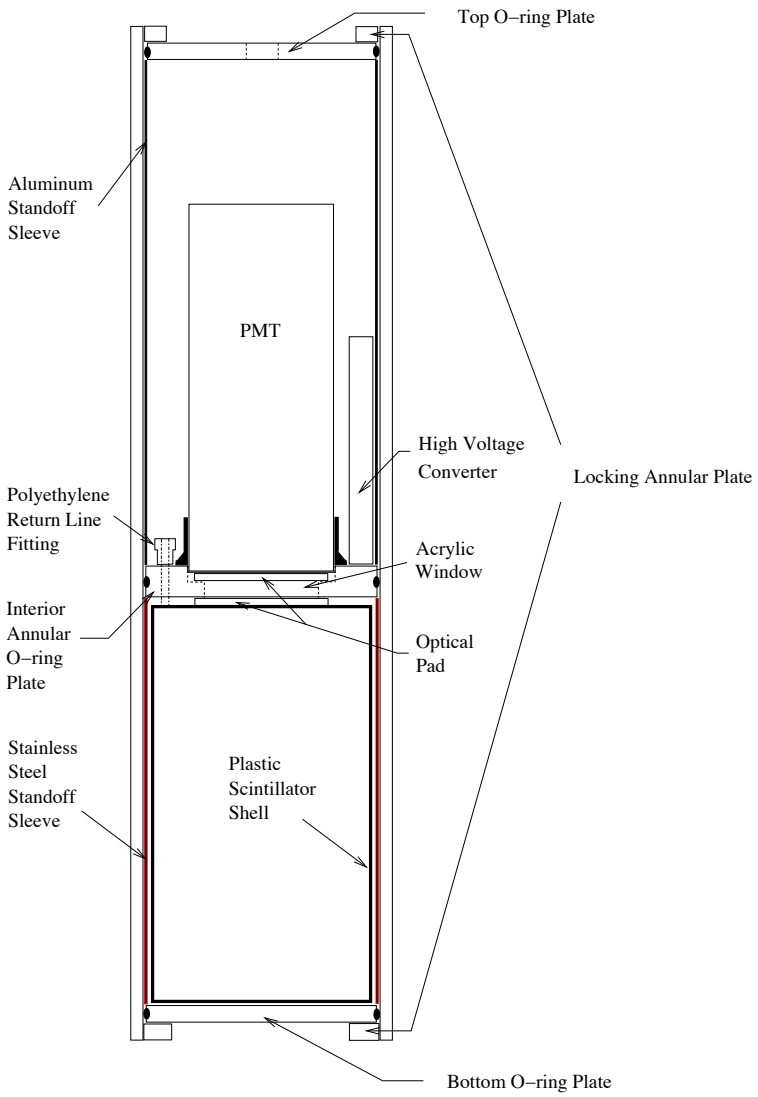

Figure 3.11: Schematic of the ^{16}N calibration source [22]. The^{16}N isotope decays by a β-delayed 6.13 MeV (66%) or 7.12 Mev (4.8%) gamma ray with a 7.13 s half-life. The β is tagged in the plastic scintillator shell, while the gamma ray escapes into the D_2O and produces a Cherenkov electron.

provide a measurement of the radial energy response of the detector. Measurements, similar to those of the ^{16}N source, are made with the other calibration sources. Full details of the development of techniques to make the optical calibrations in the salt

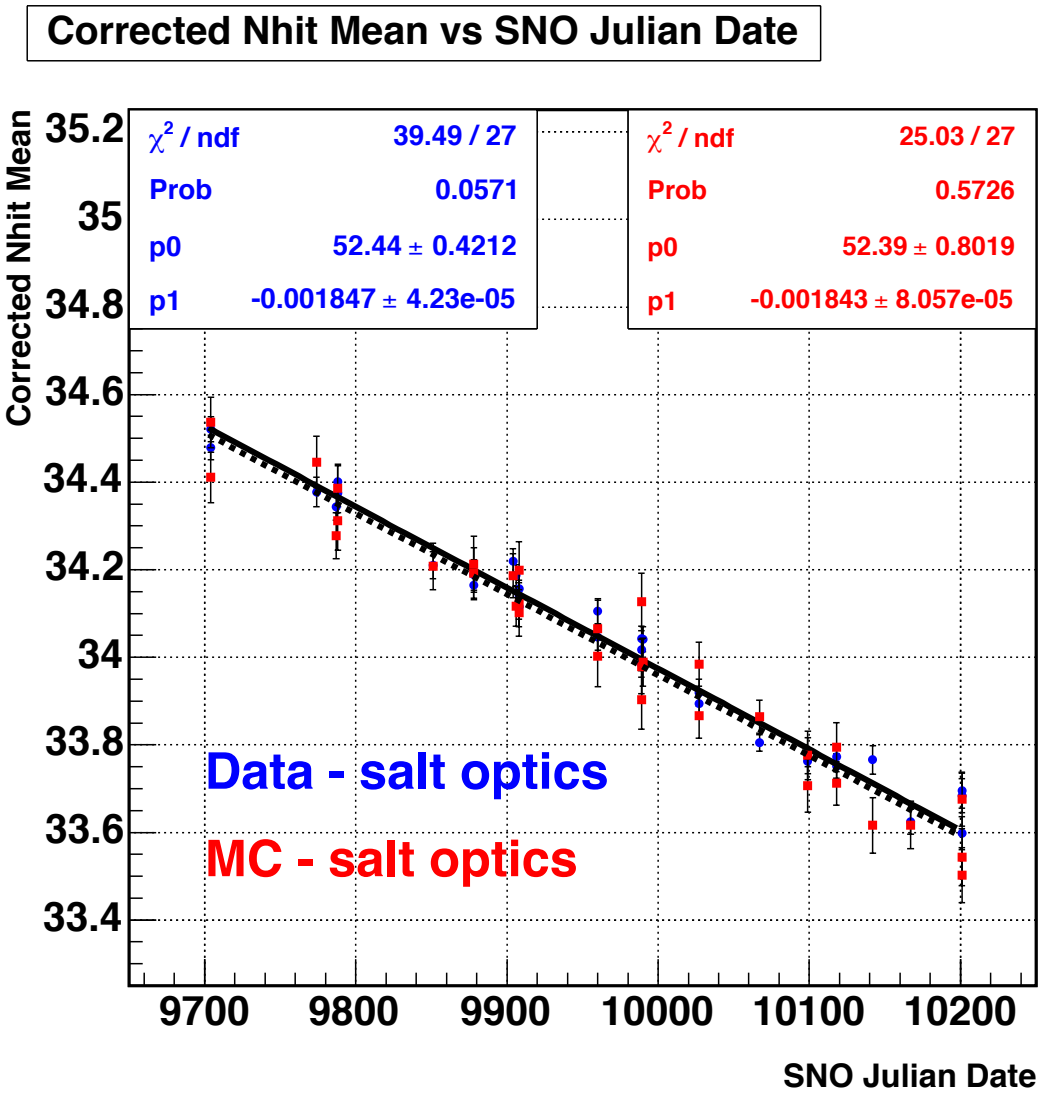

Figure 3.12: Measurement of detector energy stability (in NHIT) for the salt phase, using ^{16}N runs [30]. The line representing the MC data of the ^{16}N runs is in excellent agreement with the calibration data. It is clear the change during the salt phase was a linear decrease.

phase of the experiment are the subject of Chapter 4.

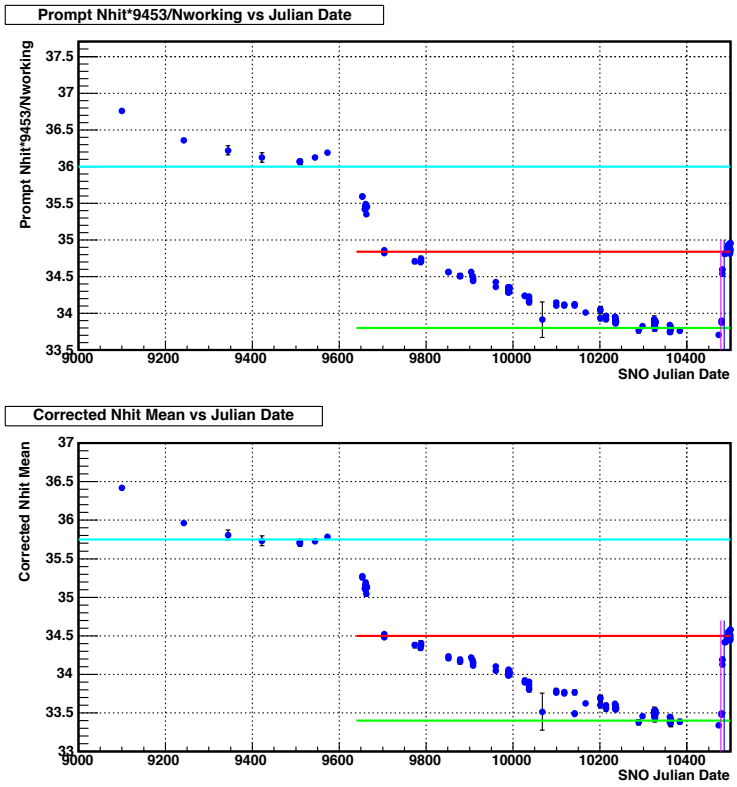

Figure 3.13: Measurement of the SNO energy drift (in NHIT) versus time [30]. The linear drift of the detector energy response is clear in the pure D_2O and salt phases. The large drop near the point of introduction of the salt (approximately Julian date 9600) is attributed to a change in the PMT angular response. The rise at the end of the spectrum is due to the removal of optical contaminants along with the salt at the end of the salt phase. Corrected NHIT represents the effective number of tubes that would have fired in an event if the event had occurred in the center of the detector with a perfect detector state. The correction therefore includes changes due to optics, noise, and the number of working PMTs. The green line is a reference for a unchanging period of the energy response during the salt phase. The red line shows the new energy response for the pure D_2O phase following the removal of the salt. The red line demonstrates that the reverse osmosis process cleaning of the D_2O has returned the detector to an energy response level similar to the pre-salt period.

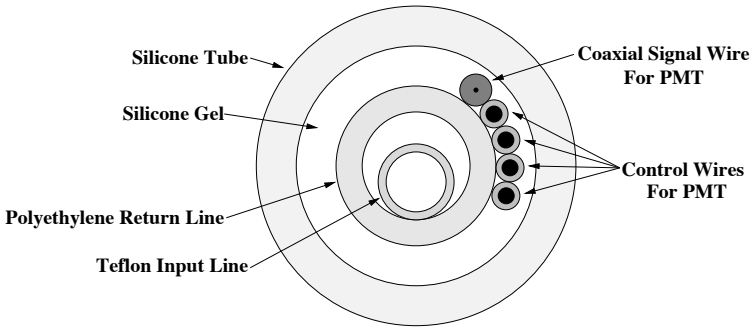

Figure 3.14: Cross section of the ^{16}N umbilical [57]. The input and return lines supply the ^{16}N source with the short-lived ^{16}N gas which is produced in the underground lab with a neutron generator via the reaction ^{16}O(n,p)^{16}N.

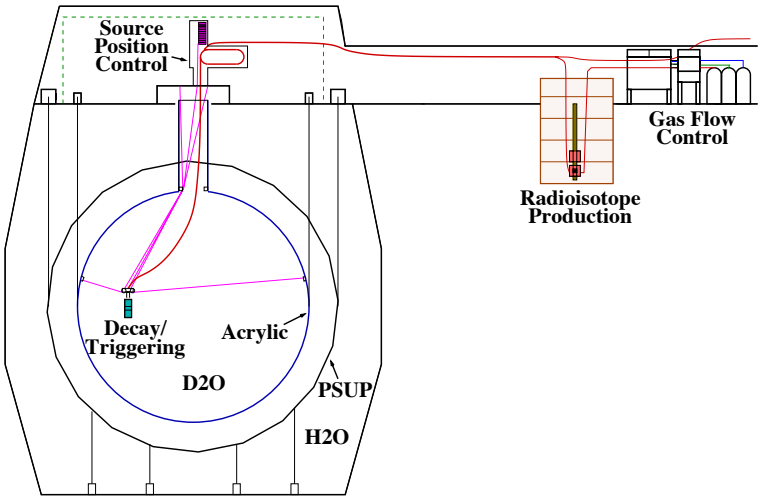

Figure 3.15: Schematic of the calibration manipulator system [57]. The source can be manipulated in a plane by a series of ropes threaded through a series of anchors and pulleys.

Chapter 4

Salt Phase Optical Calibrations

The number of Cherenkov photons generated by the neutrino interactions in the SNO detector are relatively small. SNO has been designed to be an ultra-sensitive optical detector in order to measure as many of these photons, in a given event, as possible. To accurately measure the relatively rare neutrino interactions (approximately 20 per day), one must produce a robust method of determining the optical parameters of each of the detector components. This chapter begins with a detailed description of each of the SNO detector's optical components. The method of collecting the optical data is then discussed, followed by details of the code designed to perform the extraction of the optical parameters. Finally a discussion of how the resultant optical parameters are used in the analysis of the salt phase data set is presented.

4.1 SNO Optical Components

The optical components studied in the SNO detector are part of the inner detector region. This includes, moving outward from the detector center, the D_2O, the acrylic

of the AV, the H_2O and the PMTs. Each of these components are discussed in detail in the sections below.

4.1.1 Photomultiplier Tubes

Photomultiplier tubes (PMTs) are the eyes of the SNO experiment. The SNO detector has 9534 inward-facing 20 cm diameter PMTs (see Figure 4.1). The PMTs provide coverage for 31% of the solid angle of the detector interior. A series of reflective petals, called concentrators, encircle each PMT (see Figure 4.2). Photons that strike the concentrators are focused onto the PMT photocathode. The PMT-concentrator system increases the effective solid angle coverage of the detector interior to 54%. The presence of concentrators around the PMTs also provides a light cut-off angle of 56.4°. This permits the inner detector to be viewed directly by each PMT out to a radius of 7 m measured from the center of the detector. The cut-off ensures that any light produced by a PMT, either by radioactive backgrounds or electronic pulses (known in the analysis as flashers), does not affect neighboring tubes.

Each photon that strikes the PMT photocathode produces approximately 1 photoelectron (PE) inside the PMT. The PMTs have high internal electric fields produced at each dynode stage of the PMT electronics. The photoelectrons are accelerated in the electric fields. At each of the dynodes the electrons shower, multiplying the number of electrons in the chain. After passing through 9 dynode stages, approximately 10^9 electrons are produced in the PMT for every photoelectron generated. The electrons produce an amplified signal that is measured by the SNO electronics. The SNO PMTs have a very high efficiency, with a threshold of half a PE producing a signal in the electronics. The PMTs also have excellent timing characterization, with an average rise-time of 1.7 ns from a single PE.

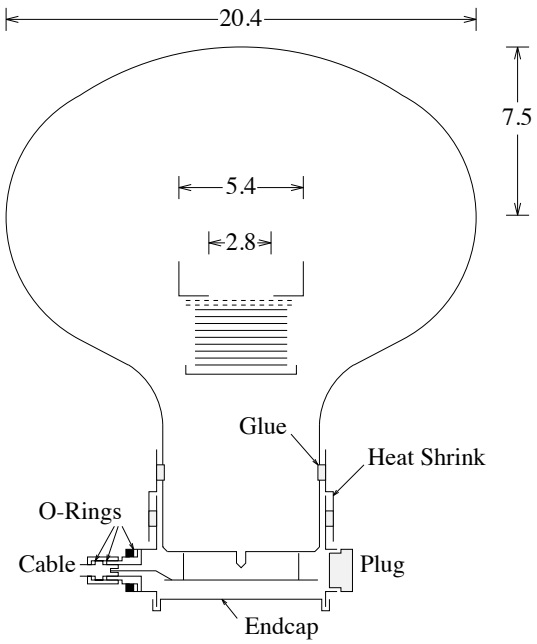

Figure 4.1: A drawing of a SNO PMT [65]. Note the dimensions are given in cm.

An event has a timing distribution dependent on the position of the interaction vertex and the location of the PMTs triggered by the generated light. The time of flight to each PMT is used to locate the vertex and determine the direction of the event. To do this accurately, it is necessary to calibrate the timing of the PMTs. The phototube calibration (PCA) is performed with the laserball source (see section 4.2 for details) at the center of the detector, with the laser light set to a wavelength of 500 nm. The laser is pulsed at a specific frequency, and these pulses set the start time (t_0) of the event trigger. The timing of the PMTs are corrected to agree with the event start time using the distance from the calibration source to the PMT. In this way, all PMTs have the same zero time point, t_0.

The precision of this calibration depends on the accuracy with which one can determine the light path from the source to the PMTs (Figure 4.3) and within the

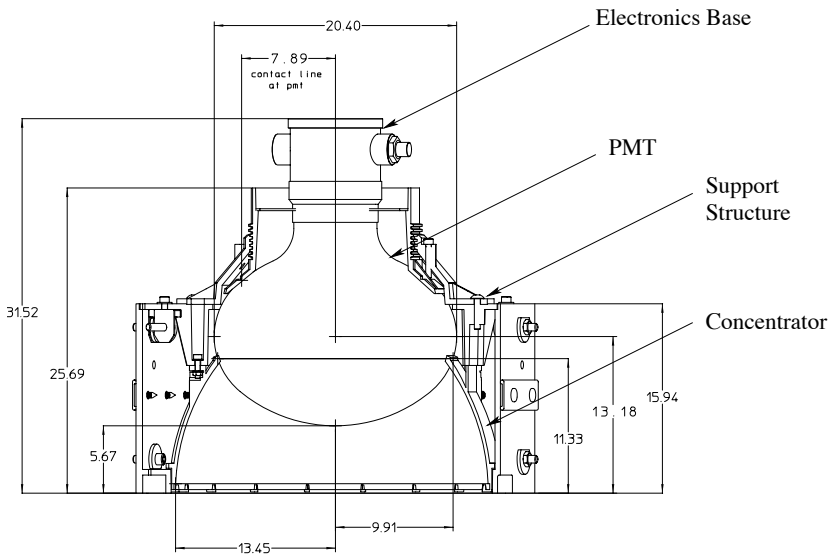

Figure 4.2: A drawing of the SNO PMT and reflector system [65]. The reflector petals are a part of the concentrator, as labeled.

PMT-concentrator system. Large uncertainties may arise due to multiple hits of a photon on the concentrator petals prior to striking the photocathode. This can add tens of centimeters to the path length. Attempts have been made to model the light paths in great detail (3D-PMT models), to ensure the best possible calibrations of the detector are achieved and the models in the MC simulations are as close to reality as possible.

The response of the PMT is also sensitive to the wavelength of the light striking the photocathode. For SNO PMTs, the chosen photocathode has a peak response that overlaps with as much of the Cherenkov light wavelength region as possible (see Figure 4.4). This ensures a high efficiency for detecting a large number of UV wavelength Cherenkov photons.

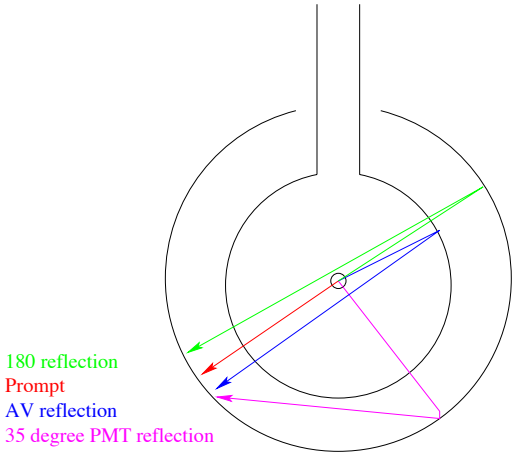

Figure (a)

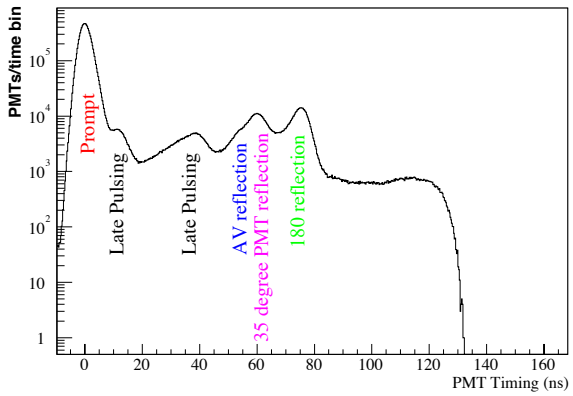

Figure (b)

Figure 4.3: The possible light paths traveled by photons in the SNO detector. Figure (a) shows the prompt light and reflection paths for a light source at the center of the detector. The different path lengths result in time distributed peaks. Figure (b) shows an example of a PMT time distribution for the laserball source located at the center of the detector (Run number 20130, 500 nm wavelength light). Labeled on figure (b) are the corresponding peaks in the PMT time distribution due to the prompt and reflected light. Late pulsing peaks are believed to be due to photons which escape from the dynode stack of the PMT and return to the photocathode to generate a new photoelectron, which then traverses the dynode chain.

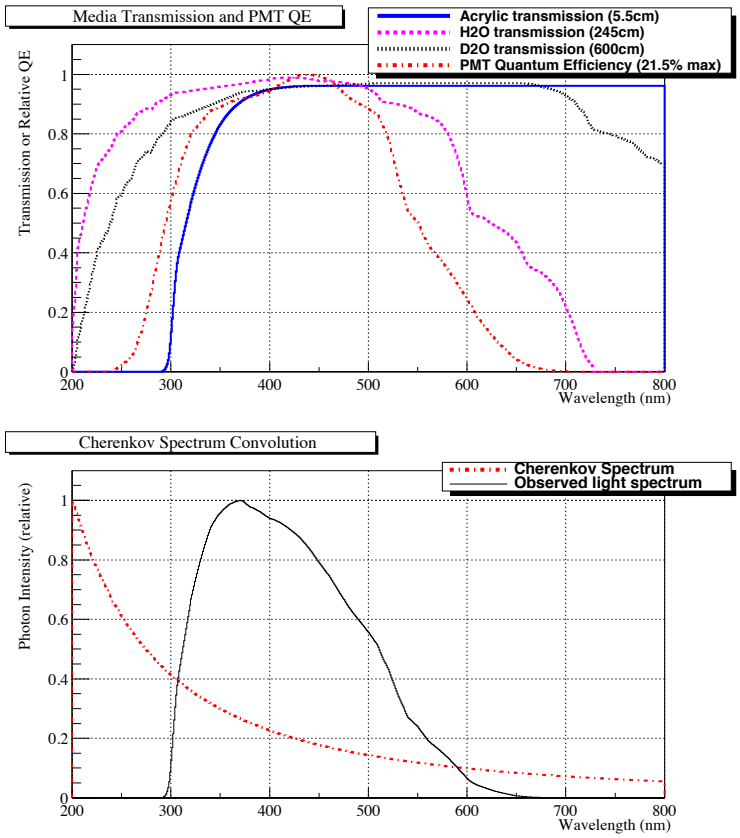

Figure 4.4: PMT efficiency shown folded with the Cherenkov spectrum [57]. The top plot shows the percentage transmission for the various media and the quantum efficiency of the PMTs as a function of wavelength. Each of the media are most sensitive to slightly different wavelength ranges. The bottom figure shows the observed light function (solid line) when each of the upper curves are combined. The Cherenkov light spectrum is shown to increase at the low UV wavelengths. The acrylic transmission defines the "cut-off" for low wavelengths.

4.1.2 Acrylic Vessel

The access to the underground environment is limited to an elevator with dimensions 6 m by 3 m by 4 m. The acrylic vessel (AV) is a 12 m diameter sphere. To produce an acrylic sphere the size of the AV, it was necessary to bond together a series of 125 acrylic panels (see Figure 4.5). Prior to installation, each panel had a 5

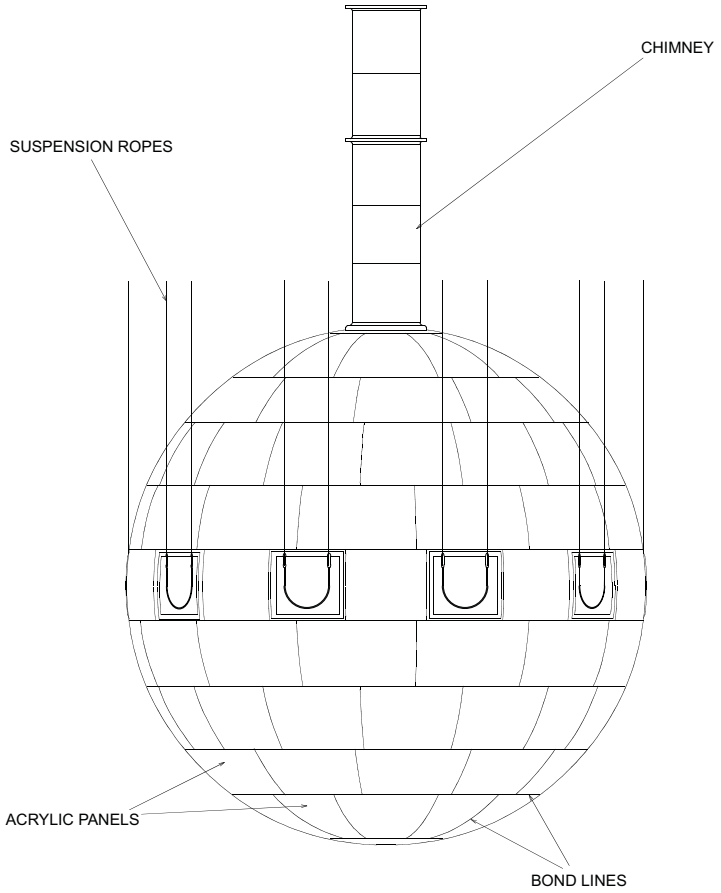

Figure 4.5: The bonded panels of the SNO acrylic vessel. [65]

cm section removed from its top, and the attenuation of the panels were measured in a test facility at AECL Chalk River (see Table 4.1) [25].

Smooth interpolation functions, developed by Bryce Moffat [57], can be used to describe the attenuation at wavelengths falling between the *ex situ* measurements in

Wavelength (nm)	Attenuation (10^{-3} cm^{-1})
300	435. ± 39. (9%)
310	143. ± 27. (19%)
320	100. ± 20. (20%)
330	71.4 ± 15.3 (21%)
340	50.0 ± 7.5 (15%)
350	37.0 ± 5.5 (15%)
360	26.3 ± 4.2 (16%)
380	13.3 ± 1.8 (14%)
400	8.85 ± 1.02 (12%)
450	7.09 ± 0.86 (12%)

Table 4.1: The average acrylic attenuation values for all panels of the AV [57].

Table 4.1,

$$\alpha_a(\lambda) \approx \left\{ \begin{array}{ll} \alpha_{a0} + m_1\lambda, & \lambda < 310 \quad \text{nm} \\ \alpha_{a1} + m_2\lambda + \exp(a + b\lambda), & 310 < \lambda < 450 \quad \text{nm} \\ \alpha_{a2}, & \lambda > 450 \quad \text{nm}, \end{array} \right\} \tag{4.1}$$

where $\alpha_a(\lambda)$ is the acrylic attenuation as a function of wavelength, and the factors α_{ai}, m_i, a and b are fit parameters. The interpolated values shown in Figure 4.6 are used when determining the attenuation coefficients of the detector water sources, described in the optical calibration analysis (OCA) in section 4.3.

4.1.3 D_2O and H_2O

The primary media of SNO, the D_2O and H_2O, must also be taken into consideration when performing a measurement of the detector optical properties. In combination with the absorption of photons by the bulk media, it is also necessary to consider the scattering of the photons from particles in the water and from the dipole molecular structure of the water, known as Mie and Rayleigh scattering respectively. As with the acrylic, the attenuation lengths of D_2O and H_2O are

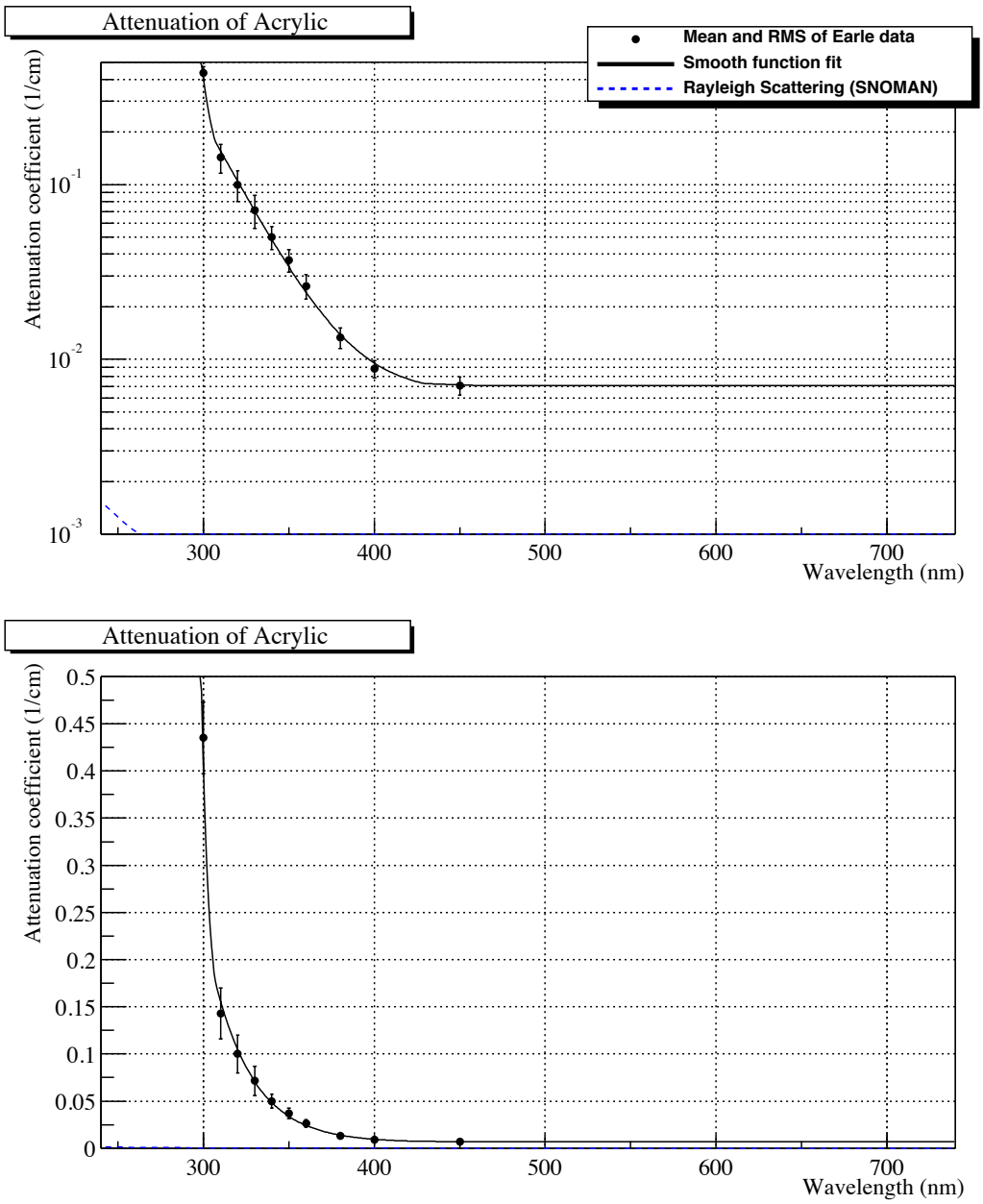

Figure 4.6: The average *ex situ* acrylic attenuation measurements compared to a smooth interpolating function [57].

wavelength dependent (see Appendix A). The SNO detector is most sensitive to wavelengths in the range 370 nm to 450nm, where the attenuation lengths for the D_2O and H_2O remain very long (>100 m). Therefore, the number of photons lost in transit due to the primary media is quite small. However, a significant change in the optical properties of the D_2O or H_2O can produce a large effect on the neutrino analysis because of the long path lengths in the detector. Observed changes to the media are detailed in the OCA description (section 4.3) below.

4.2 Optical Calibration Equipment

Optical calibrations in the SNO detector are performed using a diffusing sphere known as a laserball (see Figure 4.7) . The laserball used in the salt phase consists of a 109 mm diameter quartz sphere filled with micron-sized glass beads suspended in gel. A short length of large diameter (2.5 mm) optical fibre is inserted into the sphere, with the formers tip resting in the center of the latter. Light that enters the laserball through this fibre is diffused by the glass beads as it exits, effectively creating an isotropic light source. The laserball source is mounted on a weight cylinder that is attached to a multi-dye nitrogen laser system (see Figure 4.8) via an 'umbilical' containing fibre-optics. The umbilical fibres are matched to the single fibre of the sphere when the umbilical is attached to the weight cylinder. The natural frequency of the nitrogen laser is 337 nm. By choosing various dye-cells the output frequency of the laser, to the fibre optics, can be varied to 365, 386, 420, 500 and 620 nm. Therefore, with a single calibration source it is possible to map the optical properties of the detector over a broad range of wavelengths.

The laserball source is moved to various positions in the detector using the manipulator system (shown previously in Figure 3.15). Laserball scans are required to sample many positions throughout the detector to produce an accurate measure

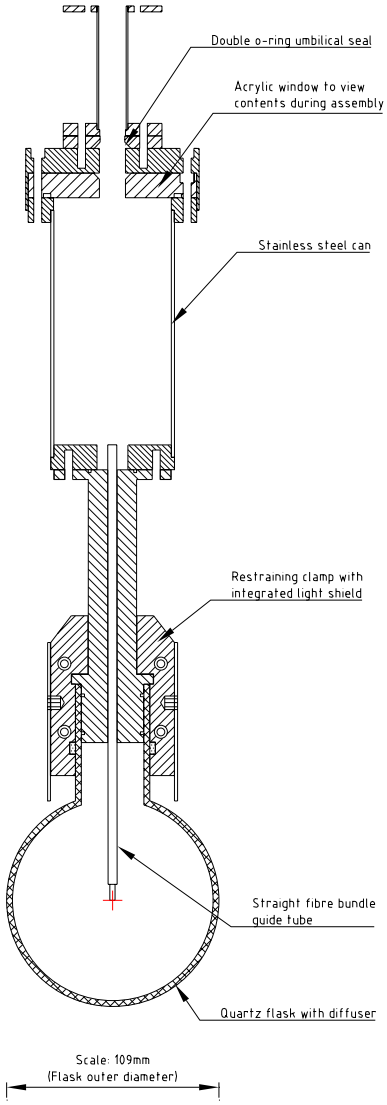

Figure 4.7: A drawing of the SNO salt phase laserball [57].

of the detector's optical parameters (see Figure 4.9). Positions taken at different radii produce varying path lengths, from the laserball to a PMT, through the D_2O, Acrylic and H_2O. Using the SNO optical model, described at the end of this chapter, it is possible to use the different path lengths to extract the attenuation lengths of

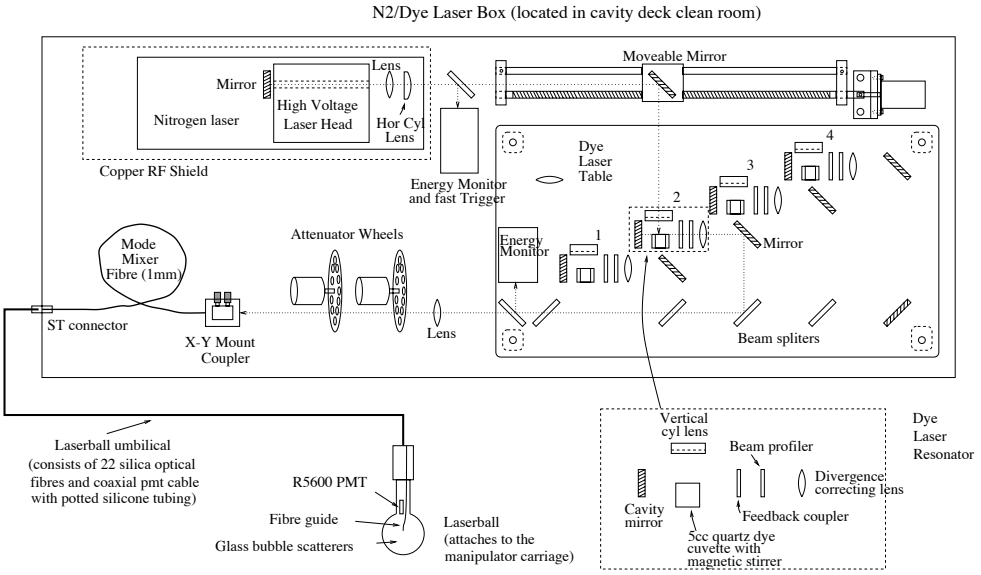

Figure 4.8: A drawing of the SNO nitrogen laser calibration system [29]. By adjusting the position of the movable mirror, one can select which dye laser cell will be used.

these media.

Construction of a Laserball Source

With the detector transition to the salt phase of the experiment, it was decided to construct a new laserball source to improve the design and operation of the Mark-I model (described in Appendix A), and to incorporate a salt conductivity probe as a secondary function of the source. Since the laserball is deployed regularly to perform PCA calibrations, the local salt concentrations in the detector could be measured at the same time to determine the uniformity of the salt mixture. The design and construction of the upgraded calibration source was one of the earlier projects in the course of this thesis.

The Mark-II laserball source is based on the design shown in figure 4.7. This

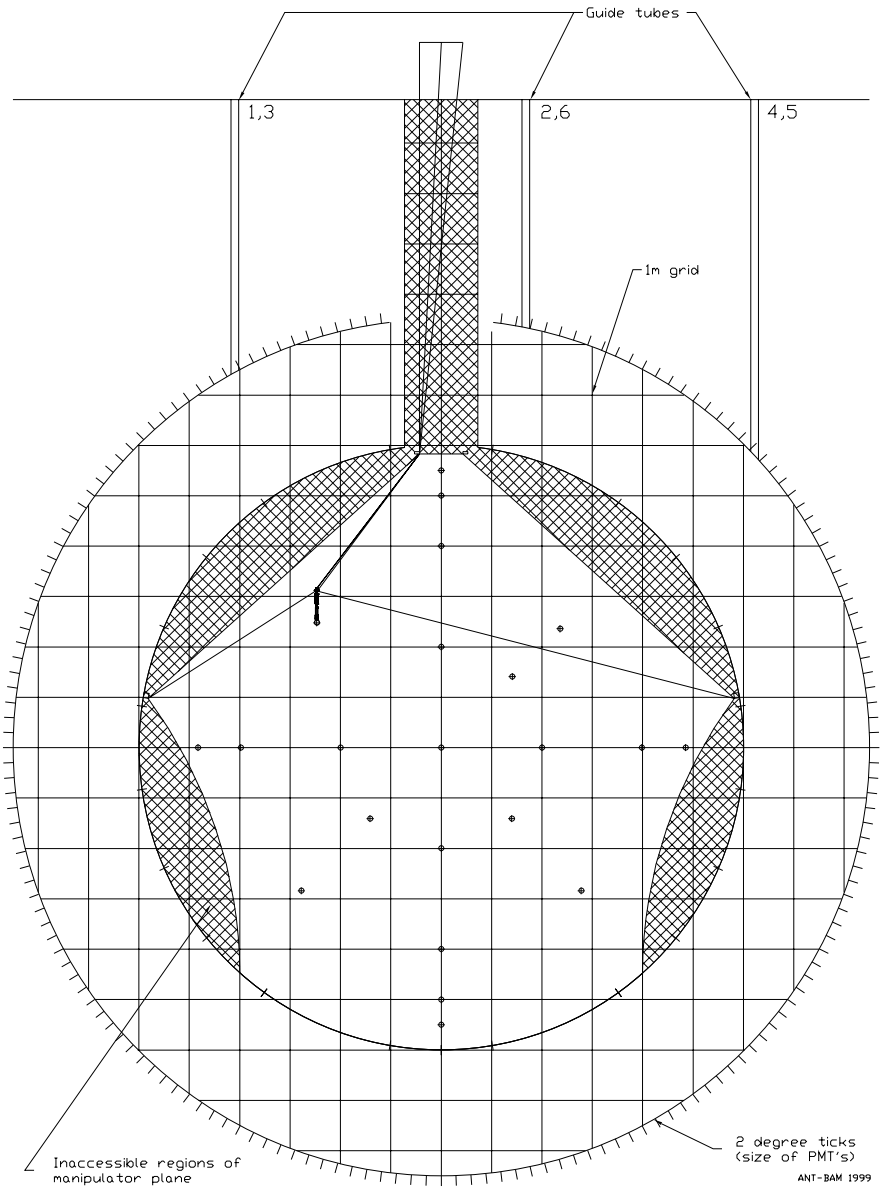

Figure 4.9: An example of the laserball scan performed September 2000 [57]. The marked points represent positions of individual runs in the scan. Note the hatched regions that are inaccessible to the laserball. Also note that all laserball scans performed follow a similar set of positions.

design features a number of improvements over the Mark-I design. The largest change is the use of a stainless steel cylindrical body for the source compared with the acrylic body of the original. This eliminates the need for a mask, which was difficult to correctly model in the Monte Carlo. The restraining clamp design for the connection between the laserball diffusing sphere and the body creates a simple mechanism for assembly of the source. Furthermore, the bundle of fibre optics (from the umbilical) no longer enters the diffusing sphere. Instead, the straight optical fibre is mated with the bundle of fibres from the laser at the restraining clamp. This ensures the exit point of the laser light in the laserball is constant over time, leading to a more stable and reproducible light distribution produced by the source. Breakage of one of the fibres in the bundle inserted in the Mark-I sphere caused significant changes in the light distribution from the source. With the new design, the potential for fibre damage was greatly reduced. The integrated light shield over the neck of the new source was designed to have a much improved fit to the diffusing sphere, effectively eliminating any stray photons from that region.

The Mark-II diffusing sphere was constructed from a quartz flask, carefully chosen to have minimal imperfections in the quartz that could affect the light distribution from the sphere. The flask was ultrasonically cleaned, dried with dust-free cloths, and rinsed with methanol to remove any traces of oils and dust. Two grams of micron-sized glass beads were measured and poured into the dry flask. Approximately half the flask was filled with a gel mixture, and the contents were mixed vigorously. The selected gel (silicon based RTV6196 from GE Silicones) is transparent, low in radioactive backgrounds, and solidifies in approximately 30 minutes. The remainder of the gel was placed in a beaker. The flask and beaker were placed in a bell vacuum chamber and the mixtures were degassed until "boiling" ceased. The beaker and flask were removed from the vacuum chamber and the beaker of gel was poured into the flask until the liquid reached the half-way point of the neck. This was done so

that the diffusive scattering of the light occurs in the spherical shell of the source, not the neck. The flask was shaken vertically to mix the glass beads. Finally the flask was rotated gently at a slight angle to maintain the mixing until the gel set. In total, 3 essentially identical diffusing spheres were created for use in the salt phase.

One of the new diffusing spheres was attached to the Mark-II laserball body and the existing laser umbilical in the SNO underground laboratory environment. First commissioning of the new laserball source involved a standard PCA run and a series of rotation runs to measure the isotropy of the source. The results, shown in Figure 4.10, show a large improvement compared to the asymmetry of the old laserball source (shown in Appendix A). All measurements of the salt phase optical measurements have been carried out with the new laserball source.

4.3 Optical Calibration Analysis

A specific analysis path has been developed for processing the optical calibration analysis (OCA). An "event" from the laserball begins with the generation of a laser pulse. The SNO data acquisition (DAQ) creates a global trigger at the time of the laser pulse, representing time t_0 of the event. Light from the laserball source produces photoelectrons in the detector PMTs, and the PMT pulses are measured with the detector electronics. In a typical laser run, a few hundred PMTs fire for each event. The laser events are written out in the same manner as all detector data, to the data tapes in zdab format. The events are processed with the standard SNO Monte Carlo and analysis software routines (SNOMAN), where the timing and charge of the each PMT are added to ROOT Calibration Histograms (RCH). ROOT is a set of CERN developed analysis routines written in the C++ language. Examples of these histograms are shown in Figure 4.11. The information in these histograms is processed with a program called tdiff that calculates the mean time and the RMS

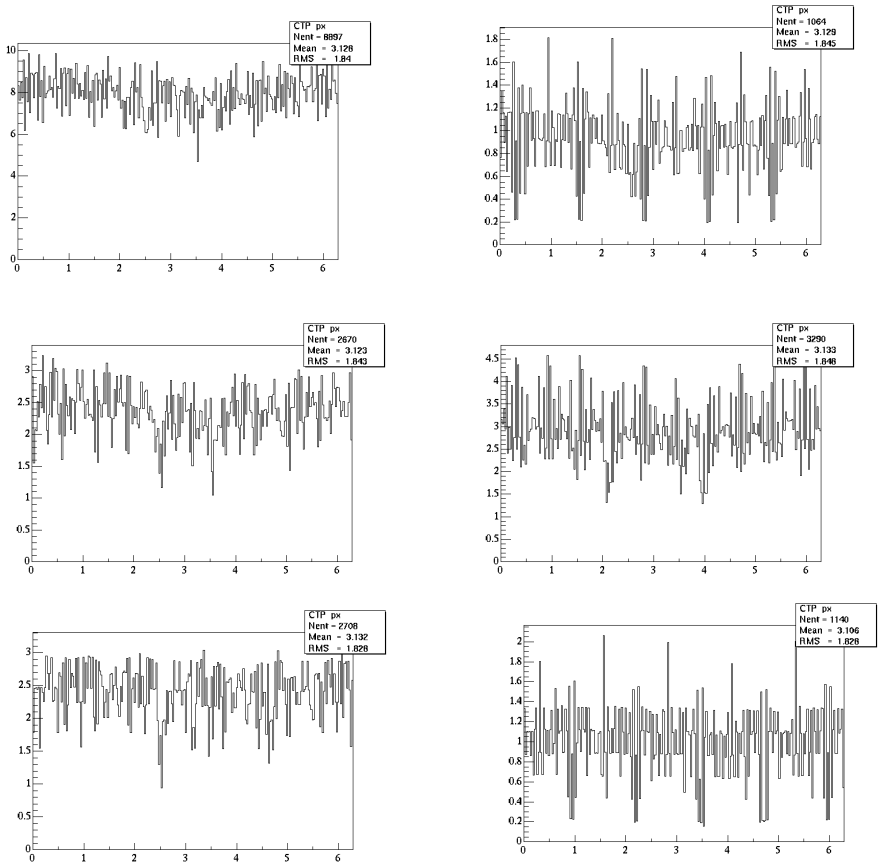

Figure 4.10: The SNO Mark-II laserball asymmetry distribution [31]. Asymmetry is measured by dividing North-facing by South-facing laser runs. Shown are plots of ϕ in θ slices of the detector. From top to bottom, left to right, are cos θ ranges of: -1 to -1, 1 to 0.809, 0.809 to 0.309, 0.309 to -0.309, -0.309 to -0.809, -0.809 to -1. In these plots, the distributions are not normalized to 1 at the center. Note the lack of the dipole asymmetry seen in the Mark-I model calibration source. In each of the θ slices, the ϕ distributions would be well represented with zero-order polynomials.

of the event's timing distributions. This information is used to produce histograms (ROOT Delta Time–RDT) containing the number of times PMTs fire in a given laser run (the occupancy of the PMT), the centroid and the width of the prompt time peak. Examples of these histograms are shown in Figure 4.12.

The RDT histogram showing the laser light time spectrum may be used to mea-

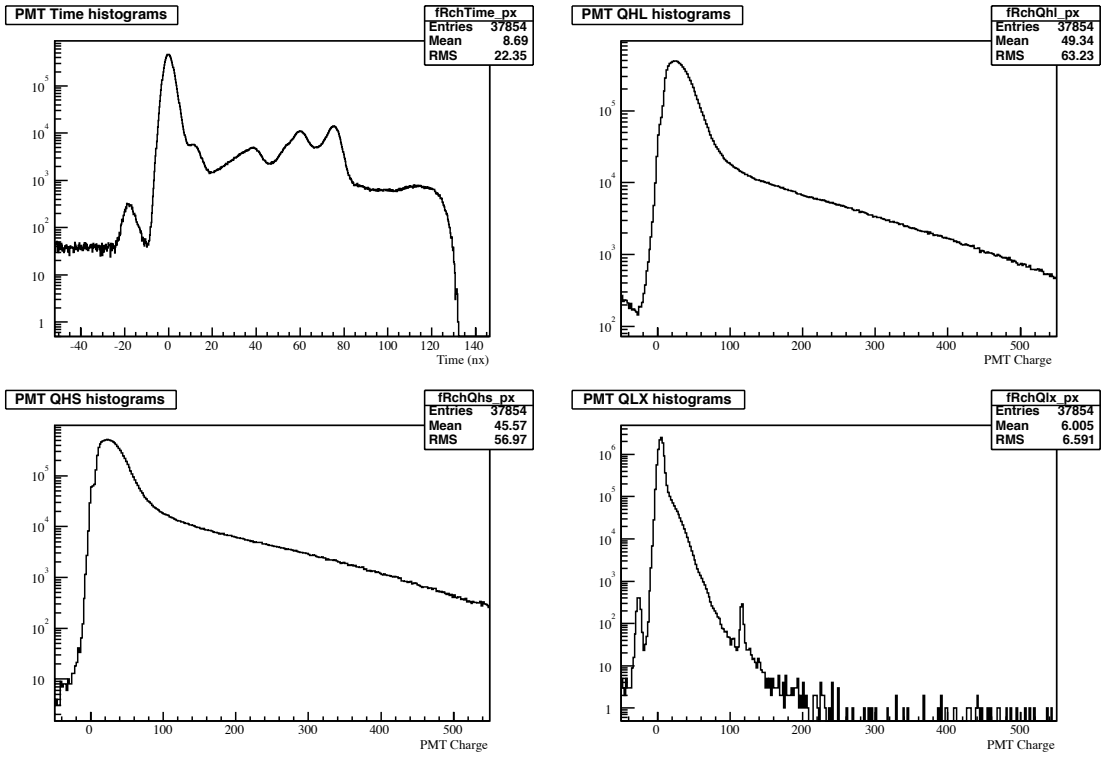

Figure 4.11: Examples of the RCH histograms for laser run 21030 (center of detector at a wavelength of 500 nm). The plots are shown as log scales to show the small scale structure away from the primary peaks. The top left plot shows the projection of the timing of all PMTs. Note that the peaks observed in this plot, from the left, are due to pre-pulsing of the PMTs, the prompt light, late pulsing of the PMTs (shoulder of prompt peak and second peak), the reflection from the AV and 35° reflection from the PMT are combined in the third peak, and the 180° reflection peak from the PSUP in the last peak. The other plots show the charge distributions of the PMTs for the three stored charges, QHL (high-long), QHS (high-short) and QLX (low-short).

sure the speed of light of the laserball at various wavelengths. To do this, one begins by fitting a Gaussian distribution to the prompt peak, ignoring the tails, to determine the "zero" time of the PMTs. A fit of a Gaussian distribution on a falling (exponential) background is then applied to one of the reflection peaks, typically

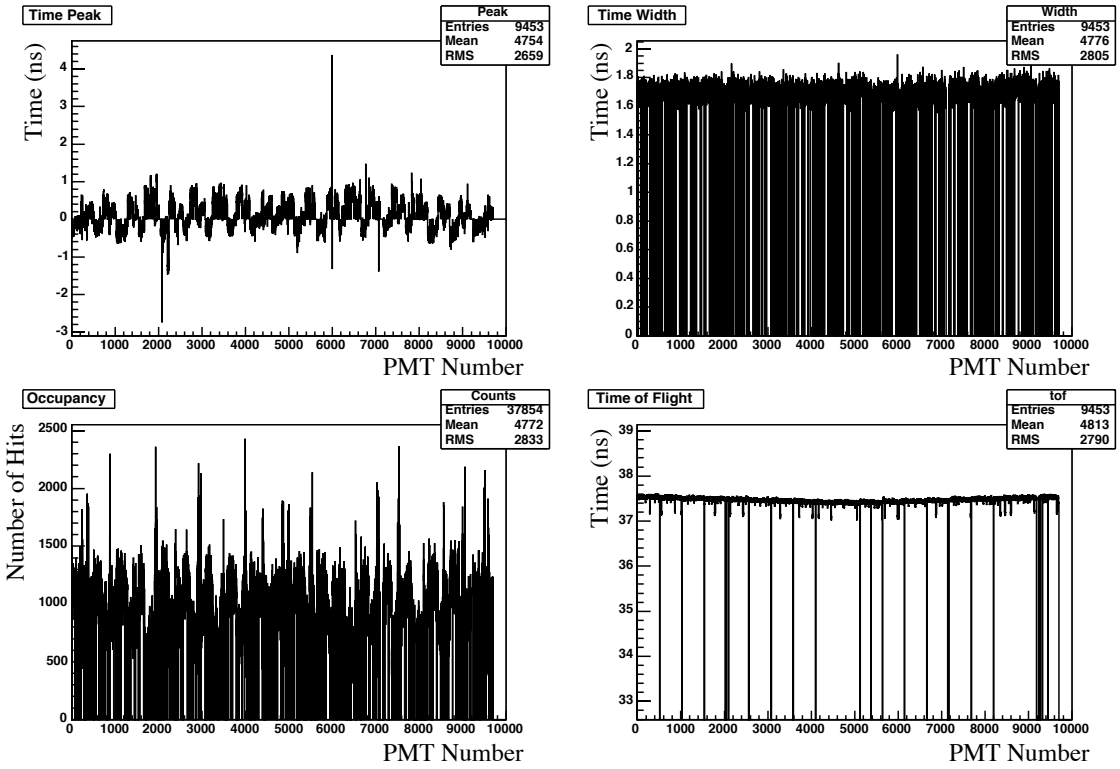

Figure 4.12: Examples of the RDT histograms for laser run 21030. The plots show the time peak, time width, occupancy and time of flight for each PMT in the run. The time peaks for the PMTs are centered around zero, showing good calibration of the PMTs via the PCA. The time width shows a measured average time width for the PMTs of 1.7 ns. The average occupancy per PMT is rather low, demonstrating the intensity of the laserball in the 15 minute run was rather low. A flat distribution for the time of flight as a function of PMT number demonstrates that the laserball source was at the center of the detector during the run.

the direct reflection from the PSUP. Using the manipulator coordinates to provide the position of the laserball source, a path length can be calculated for the prompt and reflected light paths. A knowledge of the light path lengths and PMT timing provides a direct measurement of the average speed of light in the detector. The results of this process are shown in table 4.2. These values, determined from the original salt phase scan, replaced those used in the optics analysis of the pure D_2O

Wavelength (nm)	Pure D_2O (ns)	Salt (ns)	Difference (ns)
337	77.0618	77.5032	0.406
365	77.2197	76.8133	0.044
386	76.5726	76.3300	0.092
420	76.0997	75.9755	0.107
500	75.3974	75.1516	0.143
620	74.6285	74.5364	0.071

Table 4.2: The measured time of flights in the SNO salt phase using the prompt and 180 degree reflection peaks of the PMT timing histograms. Knowing the path length from the laserball source to the PMTs for the prompt and reflected light can be used to convert the time of flight to the speed of light.

phase.

The RDT histograms are also used in the next step of the OCA path. The histogram information is processed with a series of analysis programs, collectively known as qpathrun, that are a part of the QSNO (Q = Queen's University) analysis package. The qpathrun package is a combination of the QOptics and QPath codes. QOptics calculates the light paths to each of the PMTs from the source, taking into account all refractions and reflections as the light travels through the various media. QPath classes use the calculated light paths in combination with the PMT timing to determine the source position, and finally calculate the occupancy ratio. The occupancy ratio (also called the occratio) is the occupancy (the number of prompt hits for the PMT modified by a small multiphoton correction) for PMTs from a given laserball run divided by the occupancy of those tubes from a central run (a long run at the same wavelength at the center of the detector). Therefore, the occratio measures the fractional amount of light seen by a PMT with the laserball in a specific position, normalized to the amount of light seen from the center. The differences between the two run positions result from different path lengths through the various media, and different angles of incidence to the PMTs. The output of the qpathrun code is a

ROOT file containing the QOCATree. The QOCATree contains all the information required (such as the run position, source orientation, and wavelength) to complete the analysis process, by applying the optical model using the QOCAFit class.

The optical model is used to parameterize the prompt light intensity of the PMTs, and has an equation of the form

$$N_{ij} = N_i \Omega_{ij} R_{ij} T_{ij} L_{ij} \epsilon_j e^{-(d_d \alpha_d + d_\alpha \alpha_\alpha + d_h \alpha_h)}. \tag{4.2}$$

Within the model equation, i represents a run number and j represents the PMT number. N_{ij} is the prompt light intensity in phototube j for run i. The factor N_i is the prompt window normalization, given by the number of photons emitted by the laserball in run i. The factor Ω is the solid angle subtended by the PMT. This value may be calculated directly for each PMT based on the laserball's position. By defining rays to the front of the PMT reflectors, a solid angle ellipse can be defined [57]. The solid angle can then be approximated by projecting the area of the PMT onto a sphere with radius equal to the laserball-PMT distance. The factor R is the phototube and reflector assembly angular response, beyond the solid angle. This value is extracted from the laserball data, demonstrated below. The factor T is the Fresnel coefficient for the D_2O/Acrylic/H_2O interfaces. These coefficients may be calculated (for each laserball-PMT path) as the ratio of the amplitude of transmitted to the incident electromagnetic field on an optically smooth interface between 2 homogeneous media [40]. The factor L is the laserball light distribution determined from the flipped laserball runs, previously discussed to measure the isotropy of the source. The other normalization factor, ϵ, is the quantum efficiency of the PMT. The remaining terms in the model, the exponential terms ($\alpha_{d,\alpha,h}$), are the attenuation lengths for the D_2O, acrylic and H_2O, matched with the respective distances through each medium to a given PMT. The attenuation lengths are free parameters in the QOCAFit code. Looking at equation 4.2, it becomes clear how the difference in

the path length, for extensive laserball scans of many different positions, enables the extraction of the attenuation of the media. That is, by applying the model to each PMT, a minimization will generate the attenuation lengths of the media that globally give the best fit of all PMTs to the prediction of the OCA model.

Most of the terms in equation 4.2, such as the solid angle, can be directly calculated for a given PMT. However, the precise quantum efficiency for each PMT remains an unknown. By working with the occratio of the PMTs for each run, rather than the raw occupancies, the unknown terms cancel (see equation 4.3) and the value of the occratio may be predicted very precisely.

$$\mathrm{occ}_{\mathrm{ij}}^{\mathrm{model}} = \left(\frac{\mathrm{N_i}}{\mathrm{N_0}}\right)\frac{\mathrm{R_{ij}}}{\mathrm{R_{0j}}}\frac{\mathrm{L_{ij}}}{\mathrm{L_{0j}}}\mathrm{e}^{-(\delta \mathrm{d_d}\alpha_\mathrm{d}+\delta \mathrm{d_a}\alpha_\mathrm{a}+\delta \mathrm{d_h}\alpha_\mathrm{h})} \tag{4.3}$$

In equation 4.3, the terms δd_d, δd_a and δd_h are the differences in the distance of propagation of light through the D_2O, a specific acrylic panel (according to run position i and PMT j) and the H_2O, respectively. The other factors are the same as defined in equation 4.2, with the 0-subscript referring to the central run used for normalization. We use the minimum of the fit, using the occratios as defined in 4.3, to define the attenuation coefficients of each of the detector media.

The results of the QOCAFit for the pure D_2O phase are compared with the first salt phase optical calibration runs in Figures 4.13 and 4.14. A reduced chi-squared of 2 or less is used as the selection criteria for a "good fit" from the QOCAFit minimization (see Figure 4.15). It is important to point out that the H_2O attenuation lengths are really the addition of the measured acrylic and H_2O attenuation lengths. The *ex situ* acrylic attenuation measurement, for a specific wavelength, is subtracted to give the reported H_2O attenuation length. When only D_2O region scan positions are used in the QOCAFit, it is not possible to break the correlation between these two media.

The error bars in the attenuation plots represent both the statistical and sys-

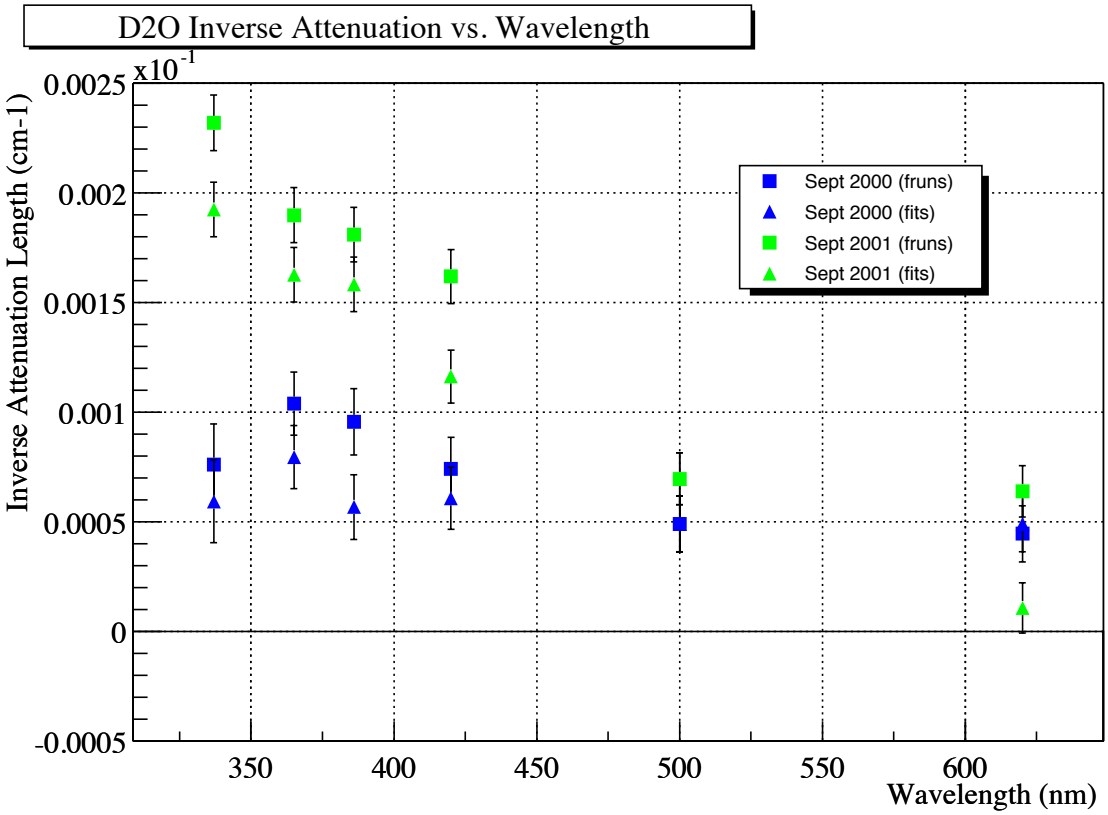

Figure 4.13: The extracted D_2O attenuation from the first salt phase laser calibrations (September 2001) compared to the results from the pure D_2O phase (September 2000). There is an obvious change in attenuation for the lower wavelengths. This change has been attributed to an increase in Mn in the detector due to the MnOx water assays for radium. Note: the "fruns" results show the extracted attenuation assuming the fit position for the (500 nm) laserball run is the same position for each of the other wavelengths. Conversely, the "fits" results use the extracted fit position for each of the wavelengths.

tematics uncertainties from the laserball scans. The statistical errors are small, due to the large quantity of data taken in a laserball run, and therefore the error bars are dominated by the systematic uncertainties. The systematic uncertainty for the laser calibration is determined by shifting certain parameter values in the software, such as the laserball position by a few centimeters, and repeating the QOCAFit.

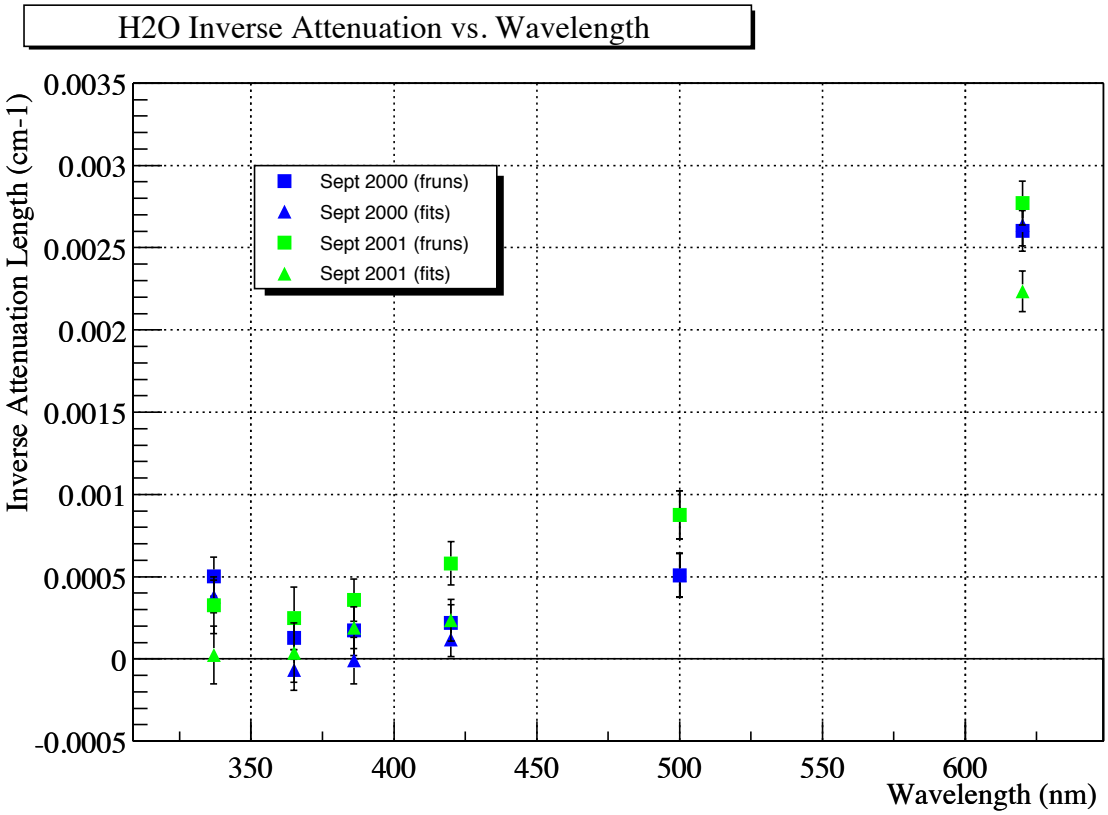

Figure 4.14: The extracted H_2O attenuation from the first salt phase laser calibrations (September 2001) compared to the results from the pure D_2O phase (September 2000). There is no substantial change observed at any wavelength between the two phases. Note that the extracted H_2O attenuation is in fact the combined H_2O and acrylic attenuation. The plotted H_2O attenuation has the *ex situ* acrylic measurement removed from the QOCA extracted value. Other details of the plot are as listed in Figure 4.13.

The attenuation length extracted for each of the varied parameters are compared to the best fit value, and a percentage uncertainty is calculated. The uncertainties are added in quadrature to generate the error on the overall fit (see Table 4.3).

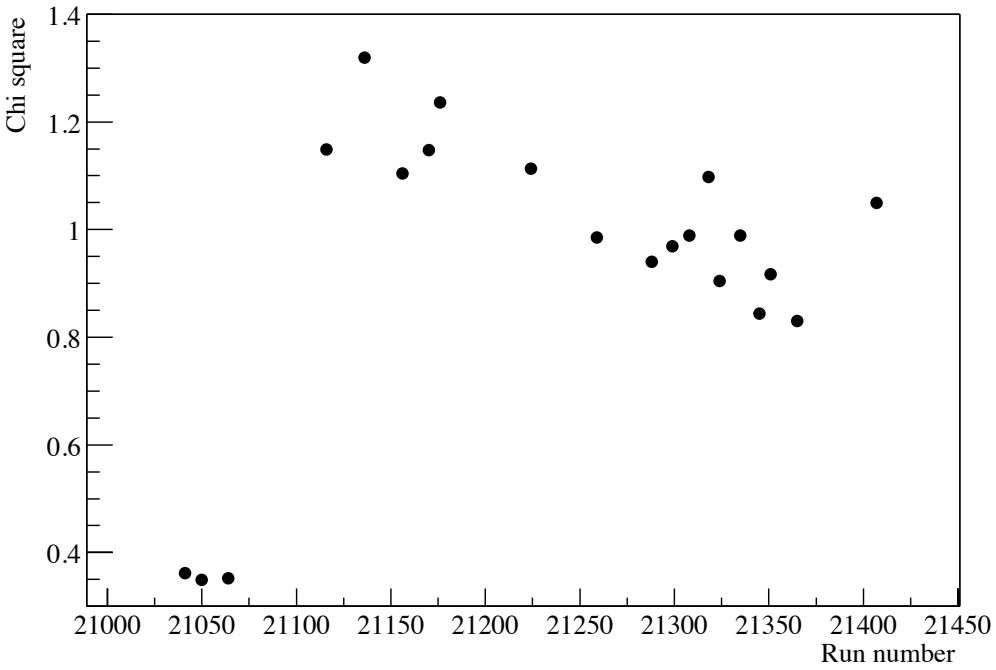

Figure 4.15: The reduced chi-square for fits of individual 500 nm runs in the September 2001 laserball scan. The very low chi-square fits near run number 21050 are for the central runs of the scan.

4.4 Salt Phase Optical Calibration Results

A series of optical calibration scans were performed during the pure D_2O and salt phases of the SNO experiment, (listed in Table 4.4). The full laserball scans typically sample the six wavelengths available from the SNO nitrogen laser and dye system. The full scans also sample multiple rotations of the laserball, to measure the laserball light distribution. It is also possible to measure both the x-z and y-z planes of the detector and to include a full z-scan in the H_2O down one of the available guidetubes (access ports to the H_2O region). A full scan takes typically

Parameter	Attenuation (10^{-3} cm^{-1})
QOCA Attenuation	6.958 x 10^{-5}
Radial scale shift (0.2%)	-5.409 x 10^{-6}
Z-shift (2 cm)	7.763 x 10^{-7}
X-shift (2 cm)	2.075 x 10^{-6}
Radial shift (1 cm)	-1.008 x 10^{-5}
Radial Smear (1 cm)	8.512 x 10^{-7}
Laserball-PMT position shift (1.5 cm)	1.461 x 10^{-6}
Laserball distribution (squared)	4.960 x 10^{-8}
Laserball distribution (flat)	-1.223 x 10^{-7}
PMT to PMT variations (turned off)	-1.256 x 10^{-7}
χ^2 cut at 16 for PMT selection	-4.607 x 10^{-7}
χ^2 cut at 9 for PMT selection	-1.193 x 10^{-6}
Total Systematic	1.175 x 10^{-5}
Statistical Error	8.198 x 10^{-7}
Total Error	1.178 x 10^{-5}

Table 4.3: An example of the QOCA systematic uncertainties for 500 nm data in the September 2001 optics scan. The dominant systematic uncertainties arise from the shifts in the x, z, and radial position of the laserball. The systematic uncertainties are added in quadrature to give the total systematic error. The total systematic error and the statistical error are added in quadrature to produce the total error. For this 500 nm result of the September 2001 laser scan the total error is approximately 17% of the extracted attenuation value.

7 days to complete. While calibrating, we cannot collect neutrino data. Therefore, the amount of time spent on calibrations is a trade off in the statistical error for neutrino events against systematic errors being reduced by calibration. Miniscans have been designed to give very specific optical measurements, for instance attenuation lengths for specific wavelengths, in a short period of time (approximately 2-3 days) to reduce the required amount of calibration time and still achieve the desired level for systematic uncertainties. Prior to the salt phase, the scans were processed with QOCA versions $\leq$6. The code has been developed in the salt phase, but as a cross-check the results from the earlier code is used as a verification analysis. That

Scan Date	Scan Type	Light Water Scan	Analysis
February 2000	Full Scan 365nm, 500nm	None	Pure D_2O
September 2000	Full Scan all wavelengths	Guidetube 1	Pure D_2O
January 2001 I	Miniscan 337nm, 365nm, 500nm	None	Pre D_2O recirc
January 2001 II	Miniscan 337nm, 365nm, 500nm	None	Post D_2O recirc
September 2001	Full Scan all wavelengths	Guidetube 4	Open salt 254.3 days
November 2001	Miniscan	None	Open salt
May 2002	Full Scan all wavelengths	None	Open salt
October 2002	Full Scan all wavelengths	None	Open salt
January 2003	Full Scan all wavelengths	None	Full salt 405 days
May 2003	Full Scan all wavelengths	None	Full salt
August 2003	Full Scan all wavelengths	None	Full salt

Table 4.4: Laserball scans in the SNO experiment

is, when any refinements are included in the QOCA code, the September 2000 data is reprocessed with the new code and the results are compared to ensure no "bugs" have entered the code. In the transition to, and over the course of, the salt phase a number of studies were completed with respect to the QOCA code.

A first step was to study if water chemistry has a significant effect on the optical properties of the detector. The presence of organics and metals in the water increases the amount of scattering and absorption, hence reducing the attenuation length. During the pure D_2O phase it was possible to determine the magnitude of such an effect by performing a laserball scan before and after the running the reverse

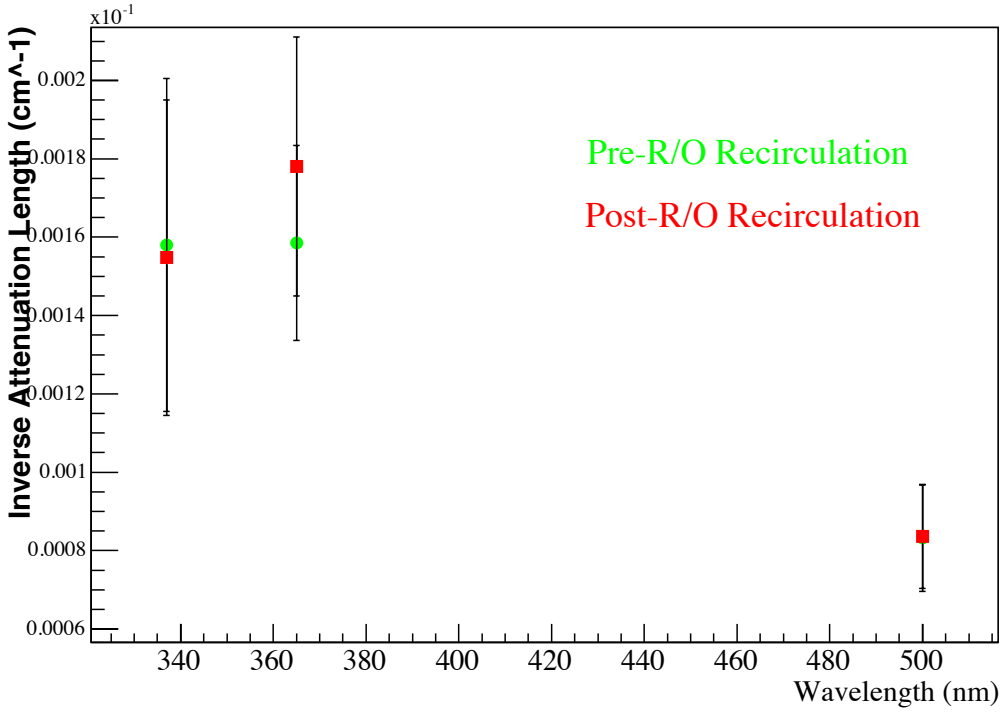

Figure 4.16: The results of a test of the change in attenuation of D_2O following running the D_2O reverse osmosis system. Note the small change in attenuation length at 365nm, although well within the systematic uncertainties. The large uncertainties are due to an incorrect laserball distribution applied to the OCA extraction.

osmosis (RO) system. The RO is very effective at removing organics, metals, and other impurities and is able to turn-over the D_2O volume in approximately 6 days. This experiment is labeled in Table 4.4 as the January 2001 miniscans parts I and II. The OCA process, described above, was completed for each of these scans, and the results are shown in Figure 4.16. There is little observable change in the attenuation of the D_2O at the time of the experiment. This was expected as concurrent multi-element analyses of D_2O samples showed no indication of significant contaminants. It was not possible to perform this experiment during the salt phase of the experiment,

since the RO would have removed the salt from the D_2O. This may be a critical effect since in the pure D_2O phase, the RO had been regularly operated to "clean" the D_2O. During the salt phase, multi-element analyses of water samples measured an increased number of organics and other contaminants in the detector. These contaminants, attributed to the aggressive nature of the salt on the acrylic of the AV and the ion exchange media used for water assays, are most likely the cause of the optical parameter changes measured in the detector.

In the process of running the QOCA code, one has the option of using the manipulator or QOCAFit co-ordinates. If the choice is made to use the QOCAFit co-ordinates, a further choice exists of whether to use 'fruns' or 'fits' values. The 'fits' coordinates are an individual position fit of the laserball (determined using the PMT times) for each run at each wavelength. The 'fruns' coordinates use the 500 nm fit positions for the laserball to represent the position for all other wavelengths at each scan position. In order to optimize the code, a comparison study has been completed for the entire September 2001 full scan. The results obtained using either 'fits' or 'fruns' have been compared for each position (see Appendix A). In general the difference between 'fruns' and 'fits' are found to be small. In an ideal world, there would be no difference between the position determined by the for 'fruns' and 'fits' analyses. However, the light produced by the laser dyes is not perfectly monochromatic, but rather covers a small range around the average values of 337, 365, 387, 420, 500 and 620 nm. Furthermore, at lower wavelengths, fluorescence in the fibre-optics of the laser system umbilical has been observed. This slightly shifts the peak of the wavelength spectrum. It is a reasonable assumption that during the course of taking the laser data, for a particular position in the scan, there is no change in the position in the laserball when the wavelength of the laser is changed. The fit positions (whether 'fruns' or 'fits') are found to have smaller uncertainties than those associated with the manipulator positions. Therefore, in processing of the

laserball calibration data, the 'fruns' positions are chosen to represent the location of the laserball.

Along with the mentioned studies, a number of refinements were made to the QOCA code prior to completing the final optics analyses for the salt phase data set. Included in these refinements were a couple of "bug" fixes for the salt laser data sets. The first problem discovered, and fixed once identified, was to have the code processed using the correct lengths for the laserball cylinder [19]. The laserball had lengths of 66.4 cm prior to June 2001, 76.2 cm for laserball runs between June 2001 and December 2001, and 64.4cm after December 2001. These lengths are held in an information text file, called a titles bank, in the code and are used as the offset value between the manipulator position and the source position. The fix was to ensure that the code obtained the data from the approximate titles bank. It turns out the effect of this bug was small because the analysis has only a small dependence on the z-position of the source (seen in Table 4.3).

The second bug was due to an incorrect time-of-flight (ToF) calculation when processing the laser data [19]. When RCH files are produced, an approximate ToF is used to correct the PMT times so that the time peak for each PMT is near zero. At the QPath stage of the analysis, the ToF is removed from the PMT times. However, the QPath code had a different (hardwired) speed of light compared to that used at the first rootification stage when producing the RCH files. The result was an incorrect ToF being subtracted from the PMT times. Unlike the first bug, the ToF bug had a significant effect on the resulting optical parameters, as shown in the figures of Appendix A.

After completing all the systematic studies, and updating the code to correct for the bugs, all of the data was completely reprocessed. The coordinates used were those determined from 'fruns'. The output of this final QOCAFit are the official parameters for the SNO salt phase data set. The D_2O and H_2O attenuation lengths,

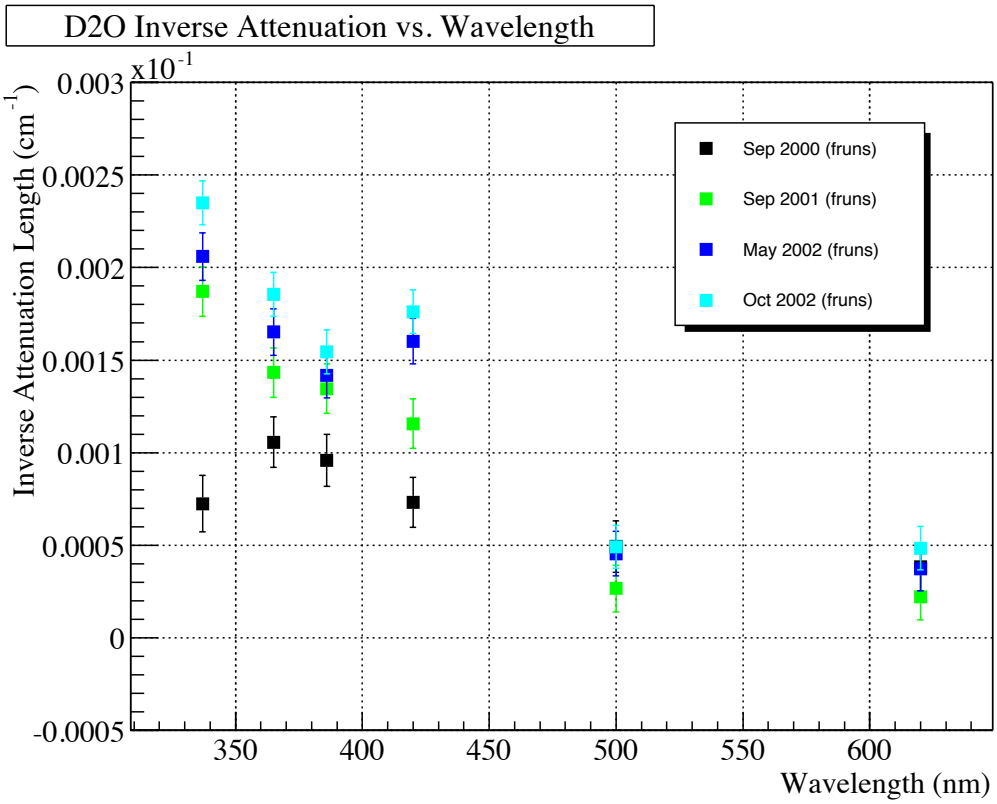

Figure 4.17: The final extracted D_2O attenuation lengths for the salt phase data analysis [9]. The change in attenuation is clear for the lower wavelengths of 337, 365, 387 and 420 nm. This change is due to an increase in Mn in the detector from the MnOx water assays, as mentioned previously.

as a function of wavelength, are shown in figures 4.17 and 4.18 respectively. The attenuation lengths for H_2O remain constant when comparing the results from the pure D_2O phase with the salt phase. However, the D_2O attenuation lengths are seen to change with time in the salt phase. The D_2O attenuation lengths are seen to have increased linearly with time (shown in Figure 4.19 and the plots of attenuation as a function of time in Appendix A) corresponding to the increase in contamination in the detector.

Finally, it is found that the angular response of the PMTs have remained constant

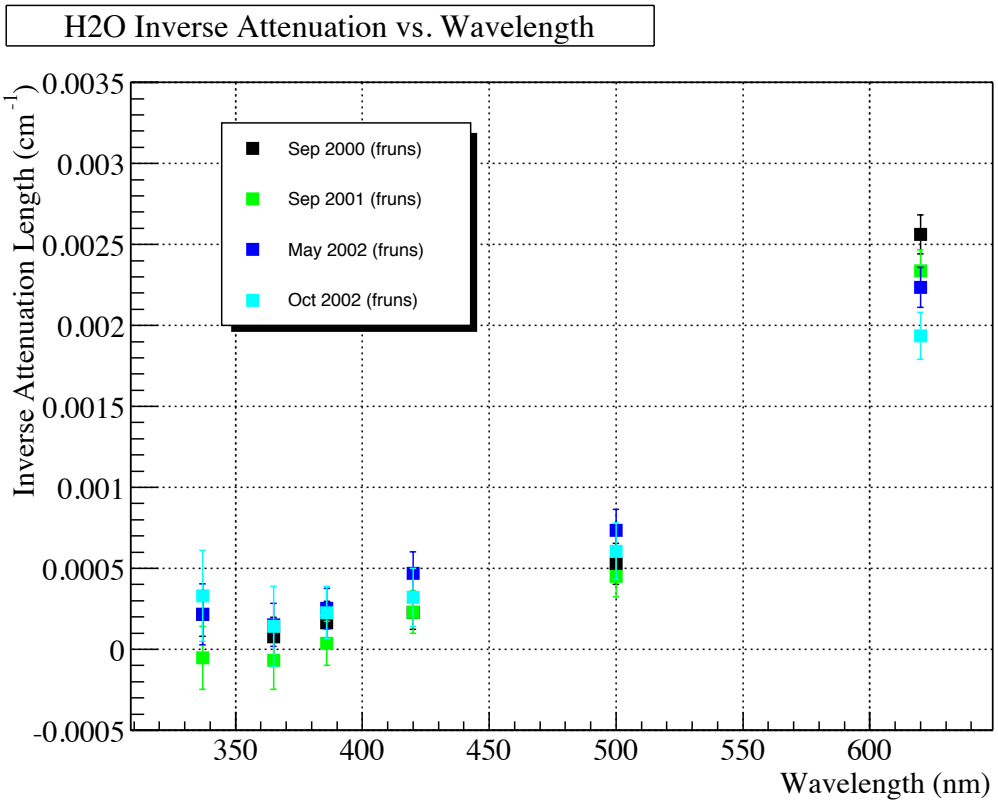

Figure 4.18: The final extracted H_2O attenuation lengths for the salt phase data analysis [9]. There is no apparent change in the H_2O attenuation lengths over the course of the salt phase, and in comparison to the pure D_2O phase.

within the errors of the fit, over the period of the salt phase, with the exception of the 337 nm wavelength measurements. An initial drop between the last scan of the pure D_2O phase and the first scan of the salt phase (see figures 4.20 and Appendix A) is also observed. This has a very large impact on the usability of the neutrino data set. Since neither the optics, nor the energy response, of the detector is understood for the 2 month transition period, the neutrino data from this period has not been analyzed. The change in the angular response is believed to be due to a physical change in the PMT reflectors, either by biological contamination or an increase in

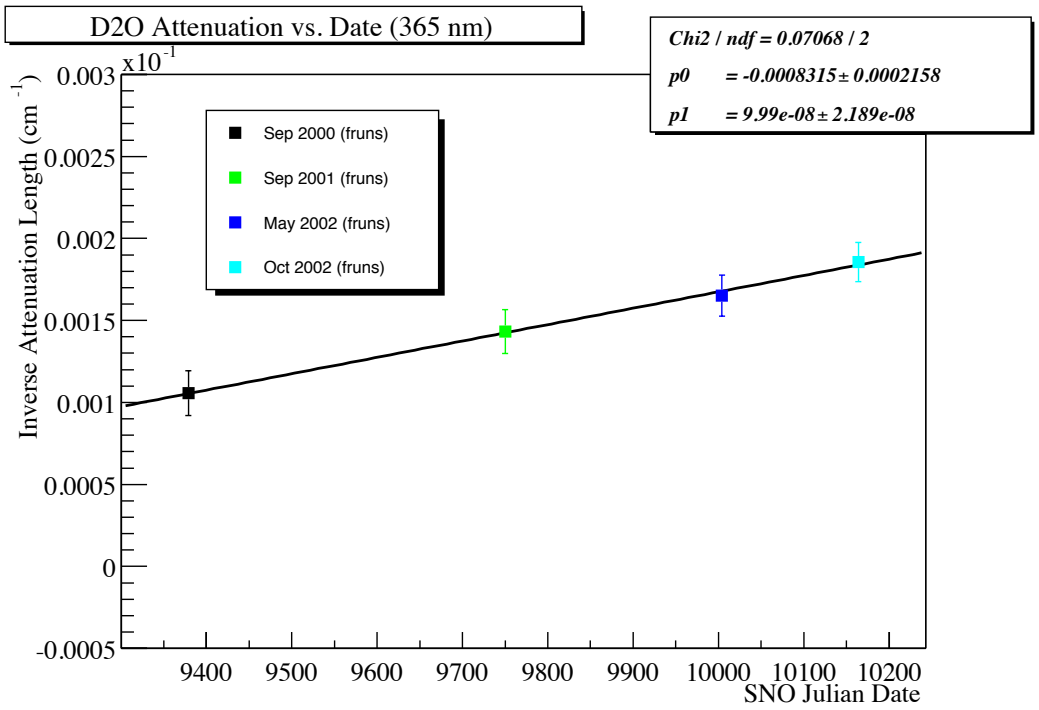

Figure 4.19: A linear fit to the 365 nm D_2O attenuations as a function of time [20].

the water temperature for a short period of time.

The thesis work contributing to the calibration of the detector has been very successful. A new source with much improved uniformity was fabricated and used in the salt calibrations. The optics code has been updated, and several studies have been run to optimize its performance. The original code was largely run manually. The code is now much more automated to reduce errors from handling and version sheer. This automation makes it possible to process new laserball scans in less than 2 days. If any problems enter the laser data due to hardware issues, a new scan can be taken immediately, thus maintaining uniformity of the data in time. The new code has been used to calibrate the optics parameters of the SNO detector in the salt phase. Along the way, we have understood the change in the detector response

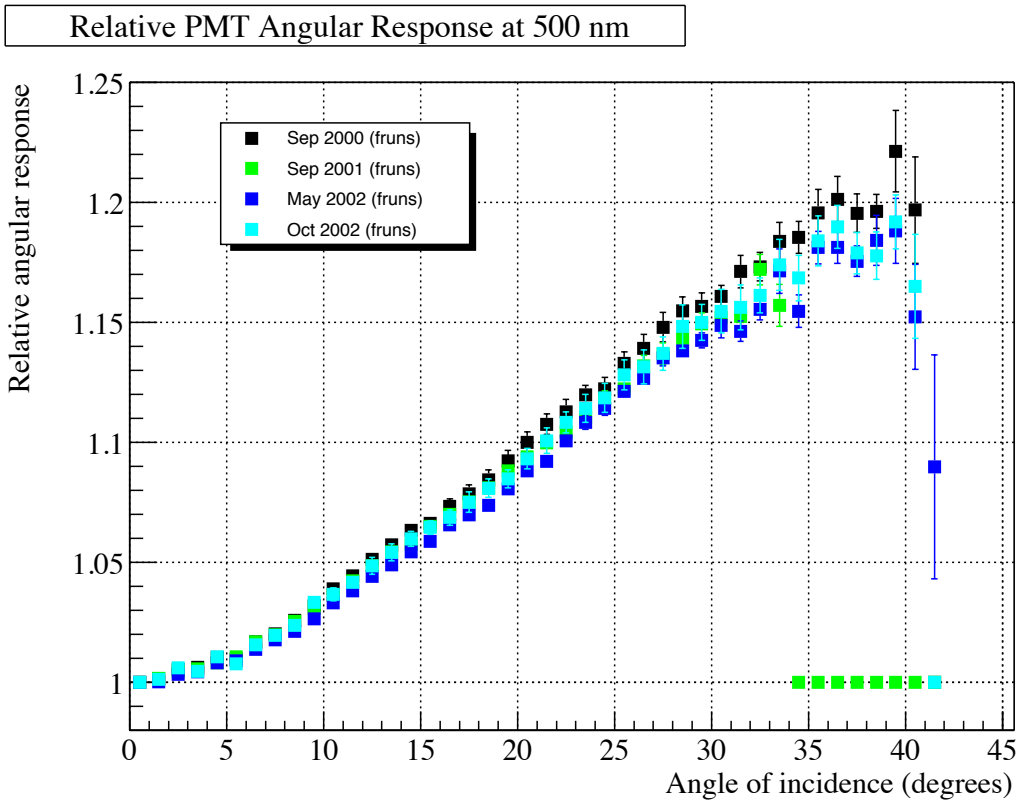

Figure 4.20: The PMT angular response curves for 500 nm laser scans over the course of the salt phase [9]. Note the small change in the angular response from the pure D_2O to the salt phase. This change is attributed to a change in the PMT reflector petals, thus reducing the efficiency of the PMTs at higher incident angles. This change is more clearly shown for the lower wavelengths in the plots in Appendix A.

as a function of time as a gradually increasing amount of contamination entering the heavy water. Although there is some absorbtion on these contaminants, the amount is actually very small and typical attenuation lengths are of order 60 to 100 m!

Chapter 5

Preliminary Steps of the Salt Phase Analysis

There are a number of preliminary steps that must be taken to prepare for the signal extraction of the salt phase data set. These steps include the cleaning of the data, applying the calibration results to the data, generating Monte Carlo data sets (MC) with appropriate optical parameters, and constructing the PDFs needed to complete the signal extraction. Each of these steps are discussed in detail in the sections below.

5.1 Introduction

The salt phase data run numbers range from 20000 to 33782 representing detector operations from May 28, 2001 to September 9, 2003. The average run length is 8 hours. The detector has a live time efficiency of approximately 58% for neutrino data that meets the strict criteria to be included in the analysis. The entire salt phase therefore contains 404 live days of neutrino data. The first analysis data, the

topic of this thesis, includes all salt data up to run number 27000 (October 10, 2002) representing approximately 260 live neutrino days.

5.1.1 Salt Phase Blindness

A blindness criteria was applied to all salt phase data. In doing so, the analysis performed on the data set produced physics results that were hidden or masked from the analyser. A blindness procedure is most often applied in rare event experiments where the possibility of a bias in the data analysis, creating a false result, is quite high. By correctly incorporating blindness into the analysis, it is assured that an analyser's bias will have minimal impact on the final results.

In the pure D_2O phase of the SNO experiment, a statistical blindness was applied to the data set. The full data set was sub-divided into 30 sets. Certain subsets were then selected, such that 20% of the data was open for analysis during the preliminary stages, where PDFs are developed, backgrounds are analyzed and calibrations are completed. The statistical significance of the initial open data set was not high enough to draw physics conclusions. Once the cuts were defined, and all analysis methods were finalized for that phase of the experiment, The process of "opening the box" of the data set occurred. The complete data set was then analyzed using the defined procedures, and the blind and open analysis results were published.

Blindness was even more critical in the salt phase as one did not want to unintentionally bias the physics result to agree with the results obtained during the pure D_2O phase. During the salt phase we were particularly sensitive to NC interactions. With this in mind, an added degree of blindness was included in the data set. Events known as muon followers were used to mask the NC events. Muon followers can include a large number of neutron events that mimic the NC neutrino signal. By including a random number of these events, the true value of the NC signal remained

blind during the analysis. As used for the pure D_2O phase data set, a statistical blindness was also applied to the salt data set to maintain blindness for the CC and ES events. In addition, the cross sections for the neutrino interactions were changed in the Monte Carlo, and the new values were unknown while blindness was in place.

5.1.2 The SNO Analysis Procedure

The analysis of the salt phase data set followed a well defined sequence of steps. The first step was the cleaning of the data. This was followed by the separation of the event types using a set of PDFs. Background levels were determined from radioassays (*ex situ*) and *in situ* measurements (discussed later). The number of each type of event was extracted, and the extracted numbers were used to determine the fluxes of ν_e and ν_x, as well as the solar neutrino parameters, such as neutrino mass differences and mixing angles.

All SNO analyses follow a path very similar to that described above. SNO publishes results from a "default" analysis which uses the best determined values from the collaboration's efforts to generate necessary information like PDFs and background levels. Every effort is made to ensure that each analysis developed by the SNO collaboration also has a verification analysis that is developed using, where possible, independent tools and methods. The work described in this and the next chapter is such an independent analysis for the salt phase signal extraction. The primary differences of this analysis from the default analysis are the way in which the PDFs are generated and the use of an independent analysis code. We will discuss this complementary analysis in detail, noting similarities, differences and comparisons to the default analysis results.

5.2 Details of Data Cleaning

The process of analysing the SNO data began with the neutrino data set. The raw SNO data set was stored in zdab format, and contained neutrino physics, non-neutrino physics and background events. Applying a series of cuts allows one to trim the raw data until all that is left are "good" neutrino events. The cuts are divided into two categories, low-level and high-level. Low-level cuts are designed to remove backgrounds due to the detector electronics and other non-SNO physics events. High-level cuts, applied after the low-level cuts were complete, are used to remove background events which are characteristically similar to neutrino events in the detector. In this case, one selects events in a parameter space where signal events will be favored over background events, for instance, by limiting the fiducial volume or energy threshold, discussed in chapter 6. In this section we discuss each of the cut levels in detail. We begin, however, by introducing how the PMT information is used to characterize each event in terms of energy, isotropy, radius and angle.

PMT Information and Fitters

The basic PMT information, such as timing and charge, was used to develop the low-level cuts (discussed below). These cut types will often look for specific PMT hit patterns, such as the number of PMTs that recorded a hit in a given electronics crate, to identify the background events. However, there is much more information available from the PMTs (to develop high-level cuts) when one combines the raw data of all PMTs in an event. For instance, the knowledge of the PMT locations and their timing, relative to the start time of an event (t_0), provides the means to determine a start vertex for the event. This is the principle behind the time-fitter (ftt) [72]. In this fitter, direct paths are assumed between the hit PMTs and an initial (guess) vertex. The distance from the vertex to each PMT, through the various detector

media and therefore different speeds of light of the media, are minimized until the time for the path length becomes approximately equal to the time represented by the location of the PMT in the event's time distribution. The resultant vertex, from the minimization of all PMT paths, is the point in the detector that best represents the timing for the largest number of hit PMTs. A similar algorithm is used for the PDF-fitter (ftu) [11]. However, in this case a PDF is applied representing the expected PMT hit pattern for an electron in the detector. In almost all SNO detector physics interactions it is an electron that generates the Cherenkov light detected by the PMTs. The electron PDF models the Cherenkov light from electron events which have the shape of a cone, with the tip of the cone located at the interaction vertex and having an opening angle of approximately 41.4°. For the FTU fitter, the event PMT hit pattern is minimized to find the best agreement between the hit PMTs and the expected PDF. The interaction vertex and the direction of travel are inferred from the orientation of the fit cone.

The number of hit PMTs (NHIT) in an event provides information about the energy of the particle producing the initial interaction. The translation of NHIT to energy is performed by the RSP processor [11] [72]. The processor begins by including only those PMTs with prompt light as the PMTs with the late light are caused by reflections. These reflections are poorly modeled in the MC. In doing so, the total number of PMTs in the event is reduced to a corrected NHIT, representing the number of tubes in the prompt light peak, other detector factors and optical properties. This is given by

$$N_{cor} = N_{eff}\frac{1}{\epsilon_{response}}\frac{1}{\epsilon_{hardware}}\frac{1}{\epsilon_{drift}}[11]. \tag{5.1}$$

The N_{eff} factor is the number of PMTs in the prompt time window. The factor $\epsilon_{response}$ contains the detector optical response information obtained from the optical calibration results (given in chapter 4). The factor $\epsilon_{hardware}$ is the ratio of the number

of active PMTs in the detector compared to the number of PMTs present in the MC. Finally, ϵ_{drift} is the correction for the small drift in detector gain as a function of time (as shown in chapter 3). The MC is used to determine the correlation between NHIT and energy, and this calibration is then used to determine the energy of and event with N_{cor} hits in the detector.

Low-level Cuts

A first pass of the data was completed with a series of automated tools known as MCPROD (Monte Carlo and Production data processing). These tools run SNOMAN [72] and QSNO code to apply filter tests on, and move, the events from the zdabs into ntuples and ROOT tree files. The QSNO code is the Queen's University SNO code, designed to interface the FORTRAN code of SNOMAN with the C^{++} analysis code of CERN ROOT. At the completion of the MCPROD processing each event had a series of assigned bits known as a DAMN ID (Data Analysis Mask Number). The ID bits contain the results from the filter tests. At this stage, no events had been removed from the data set but the events were tagged with the filter test results. The user was then free to eliminate events based on these IDs without reprocessing the data. In general, the filter tests, associated with the low-level cuts, can be used to remove events that are due to specific detector backgrounds. Typical backgrounds come from electrical pickup at the electronics which manifests itself by particular patterns in the electronics crates. These patterns are easily identified and may be used to remove the events from the data set. Bursts of events, following the passage of a muon in the detector are more likely to be muon followers than neutrino events, and a burst cut may be used to remove them. This is a useful cut for analysis of solar neutrinos, but may not be useful for other analyses such as a supernova search. The available salt data filter tests are listed in Table 5.1. Table

Test number	Filter Test	Description
5	user defined	NHIT low (<20)
6	two pass cut	event time reordering
7	permanent bank cut	fails header files
8	charge cut	high charge NHIT > $X_{allowed}$
9	cluster cut	NHIT > $X_{allowed\ paddle/crate}$
10	analog measurement board cut	AMB_{event} > AMB_{calib}
11	fitterless time spread (fts) cut	time spread is too broad
12	charge versus time (qvt) cut	removes flashers
13	qcluster cut	identifies PMT breakdowns
14	owl cut	activity in outer detector
15	seismic cut	seismic activity
16	ring of fire cut	removes flashers
17	neck cut	neck tubes
18	junk cut	removes orphans
19	esum cut	ESUMLo trig., no NHIT trig.
20	q-nhit cut	cuts charge/nhit high
21	crate isotropy cut	flashers (crate anisotropy)
22	muon tag	outward PMTs, high charge
23	in time channel (itc) cut	large NHIT out of mean time
24	flasher geometry (fgc) cut	cluster to hits ave. distance
25	owl up cut	backup for neck cut
26	owl ehi cut	removes OWLEHi trig.
27	prescale cut	selects number to pass
28	zero zero cut	tests GTID roll-over problem
29	blind event cut	adds random events

Table 5.1: The SNO filter tests [72]. The filters are designed to identify instrumental background and muon events based on pattern recognition of the hit PMTs geometry, timing and charge. Application of specific combinations of the filters, as shown in Table 5.2, produce different data sets for analysis.

5.2 shows the filter test bit setting and the resulting DAMN IDs applied to the salt data set for this solar neutrino analysis. The blindness mask removed a pre-selected number of events from the data set to maintain the statistical blindness for the CC and ES signal. The blindness mask also passed a pre-selected number of the muon followers into the blind data set to mask the NC events. The open data set analysis mask did not have the blindness filters set, and hence produced a data set free of instrumental backgrounds.

Parameter	Blind Data	Open Data
Filter 5	on	on
Filter 6	on	on
Filter 7	on	on
Filter 8	on	on
Filter 9	on	on
Filter 10	on	on
Filter 11	on	on
Filter 12	off	off
Filter 13	on	on
Filter 14	on	on
Filter 15	off	off
Filter 16	on	on
Filter 17	off	off
Filter 18	on	on
Filter 19	off	off
Filter 20	on	on
Filter 21	on	on
Filter 22	on	on
Filter 23	on	on
Filter 24	off	off
Filter 25	off	off
Filter 26	off	on
Filter 27	off	on
Filter 28	off	off
Filter 29	on	off
DAMN mask	0x20f56fe1	0x0cf56fe1

Table 5.2: The SNO salt phase DAMN masks for both the open and blind data sets. The filter tests from table 5.1 are listed, and the appropriate setting of each is shown for the specific data sets produced. A conversion of the hexadecimal DAMN ID values to binary shows agreement with the bit setting of the filters.

High-level Cuts

The high-level cuts applied to the neutrino data set were developed using the fitter and RSP information. The energy threshold cut used the RSP energy to remove low energy background events. Whether an event was within the analysis fiducial volume, as defined by the radial cut, was dependent on the vertex determined with the ftu fitter. The choice of fiducial volume was also important because it was one of the only means to limit background events that may otherwise leak into the

Event Type/Cuts	Number of Events
Total event triggers	435721068
Neutrino data triggers	196417438
NHIT greater than 20	55446430
Instrumental background cuts	50912120
Muon followers	50030008
High level cuts (Isotropy, ITR)	38113660
Fiducial volume cut	1184211
Threshold cut	3055
Total Events	3055

Table 5.3: The results of the salt phase data reduction resulting from low and high level cuts applied to the raw SNO dataset [50]. Here, the label "high level cuts" is used to describe the application of the isotropy and ITR cuts. Note the large number of events removed using the fiducial volume cut. This is due to the large number of events with NHIT > 20 located near the PSUP and in the H_2O, where backgrounds are much higher than in the D_2O region.

active detector volume from the detector boundaries. From the location of the event vertex, the isotropy of an event may be measured. The isotropy is a measure of the distribution of light in the detector. Very isotropic events generally have multiple sources or backgrounds, where as neutrino events tend to have light focused into a single cone. A set of isotropy cuts were used to remove a class of highly isotropic events (called "Leslie" or "AV" events) that appear to originate from the acrylic vessel. A final high-level cut was developed, known as the in-time-ratio (ITR). The value of ITR represents the number of hit PMTs in a defined prompt time window for an event. Neutrino events will tend to have a large value for ITR, while background events with many hit tubes from reflections will have a lower ITR.

Table 5.3 shows the results of applying the SNO data cleaning process. One observes >90% of the data was in the form of instrumental noise and muon followers, removed by the low level cuts. With such large amounts of data being cut, it is very important to understand how much of the neutrino signal was possibly being cut,

and what residual background was left in the data set.

Sacrifice and Contamination

Whenever events are cut from the data set there is the possibility that the event being cut is actually a "good" neutrino event. Conversely, an event that passes the cut could be some type of background. The "good" events cut from the data set fall into a category known as sacrifice. Similarly, those background events that remain in the final data set represent contamination of the data. The goal in applying any set of cuts to a dataset is to minimize both the contamination and sacrifice.

Sacrifice

Sacrifice was determined independently for the low and high level cuts, although the methods used to calculate sacrifice in each case were similar. For the salt phase data, the sacrifice for electrons was studied independently from the neutron events. It was best to study sacrifice using calibration sources because the high rate for the source signals easily dominates the background contributions. Most of the calibration sources can be tagged or triggered, also increasing the ease of separating the source events from the backgrounds.

The sacrifice for electron events was determined with the ^{16}N calibration source data, with the ^{8}Li source data used as a secondary check. In doing this, one assumes there was very little difference between gamma rays and electrons for the instrumental cuts. If the cross-check between the two sources were to differ, the ^{8}Li source, as an electron source, would be used to provide the only measurement of electron sacrifice for that particular cut. Each of the DAMN cuts used to generate the final dataset were applied to the calibration data. Events that the DAMN filter cuts removed from the calibration data set represented sacrificed electron events in

Electrons (%)	Neutrons (%)
$0.37\ ^{+0.15}_{-0.09}$	$0.40\ ^{+0.15}_{-0.09}$

Table 5.4: The results of the low level cut sacrifice studies [23].

the neutrino data set. In general, the sacrifice of the cuts was found to be stable when studied as a function of NHIT, energy and radius. Sacrifice results using the ^{16}N data were found to be very similar to that of ^{8}Li, although with much higher statistics. The final electron sacrifice was defined by fitting a flat line to the ^{8}Li energy distribution.

The sacrifice for neutron events in the salt phase was determined by applying the DAMN cuts to the ^{252}Cf calibration source data set. Again, events that failed a cut represented the level of sacrifice that particular cut introduced for neutron events in the final neutrino data set. Further details of this work and results may be found in [23]. Table 5.4 shows the values of sacrifice used for low-level cuts in the salt phase. As is clearly shown, only a tiny fraction of real events are removed by the low-level cuts.

As previously mentioned, the high-level cuts involved parameters such as energy threshold, fiducial volume, and isotropy. We note, however, that it is not possible to define a sacrifice for the energy threshold or fiducial volume cuts since these cuts naturally remove large quantities of events outside of their accepted parameter space. Therefore, sacrifice for high-level cuts represents only the isotropy and ITR cuts. In the pure D_2O phase, an isotropy parameter (θ_{ij}) was defined based on the mean angle between PMT pairs in an event. The θ_{ij} parameter was used to remove the highly isotropic Leslie Events from the data set. In the salt phase, neutron events were more isotropic than in pure D_2O, and the tail of the neutron isotropy distribution fell above $\theta_{ij} = 1.45$ (the cut previously used to remove Leslie events). Applying

Signal	Threshold (MeV)	Sacrifice (%)
CC	6.0	0.059 ± 0.023
CC	5.5	0.075 ± 0.029
ES	6.0	0.354 ± 0.136
ES	5.5	0.464 ± 0.179
NC	6.0	$0.144 \pm 0.002(\text{stat}) \pm 0.034(\text{syst})$
NC	5.5	$0.142 \pm 0.002(\text{stat}) \pm 0.033(\text{syst})$

Table 5.5: The results of the high level cut sacrifice studies [23]. There is little change between the sacrifice of events with a change in the energy threshold.

this isotropy cut on the salt phase data set would have generated a unacceptable sacrifice for NC events ($> 8\%$). Instead, the β_{14} isotropy parameter, described later in the chapter, was used to assist in removing Leslie events.

The ^{16}N data was used to model the high-level cut sacrifice for CC and ES events. The effects of the β_{14} and ITR cuts were studied with the ^{16}N dataset, again as a function of various parameters such as NHIT. The same high-level cuts were applied to the ^{252}Cf to determine the sacrifice for NC events. The final results of sacrifice from high-level cuts are shown in Table 5.5. Again only a small fraction of the real events are removed using these cuts.

Contamination

Background events that pass the filter tests are said to contaminate the final dataset. Contamination is measured using a bifurcated analysis. Bifurcated techniques study a single background with two uncorrelated cuts that largely reject the background. The results of the two cuts for removing the background can be compared to one another and, in a manner, can cross-calibrate the efficiency of each other. In SNO, the uncorrelated cut branches are defined by the DAMN and high-level cuts. The response of a background to one cut can be determined by observing

Threshold	Contamination (%)	95% CL Upper Limit (%)
>5.5 MeV	0.0012 ± 0.0003	0.1
6.0 MeV	0.0011 ± 0.0004	0.2

Table 5.6: The level of salt phase contamination after the application of a bifurcated analysis of the high and low level cuts [23].

its behaviour in the uncorrelated branch. The DAMN bank cuts are designed to remove instrumental backgrounds (non-Cherenkov events) using PMT information such as hit geometry, timing and charge. The high-level cuts are designed to accept Cherenkov-like events. The correlation between these branches is studied by loosening the specific cuts (such as energy threshold or fiducial volume) and checking if the background level is constant. Doing this, it is found that correlations between the DAMN and the high-level cuts are negligible [23]. Using these cut branches, the bifurcated analysis gives the contamination levels for the salt phase as shown in Table 5.6.

5.3 Application of the Calibration Results

The information, such as energy, used to analyse the neutrino data set was affected by the results of the detector calibrations. An example of this effect was shown in equation 5.1. The results from the energy and optical calibration sources were used to generate the detector resolution functions (see Table 5.7), and correct the MC events so there was agreement between the calibration source and MC generated events (shown in table 5.8). The MC corrections were necessary due to fundamental differences between the true conditions in the detector and those coded in the MC. For instance, the energy correction factor must be applied due to the difference in the MC modeling of the ^{16}N source compared to the true source. Similarly, a study

Parameter	Resolution Function
Energy	T_{eff} = -0.1681 + 0.4182$T_{eff}^{1/2}$ - 0.03013T_{eff}
Isotropy	$(2.16 + 0.128x - 0.003x^2)\exp\left[-0.5\frac{(y-(0.428+0.00834x-0.000172x^2))}{(0.17-0.00565x+0.000143x^2)}\right]^2$
Vertex	Gaussian, σ=15cm
Angular	Double Exponential

Table 5.7: The SNO detector response functions, as determined by the use of calibration source data (such as ^{16}N). The parameter T_{eff} is the kinetic energy of the detected particle. The value of x in the isotropy response function is the kinetic energy of the particle.

Parameter	Correction Factor
Energy	$T_{eff} = T_{RSP}/(0.985 + (0.09693/T_{RSP}))$ - 0.5109996
Position (data)	z_{fit} shifted up by 5.5 cm
Position (MC)	Radius shifted by -0.5%

Table 5.8: The MC and data correction factors. The energy correction factor represents the fine-tuning of the MC to the mean of the ^{16}N calibration data. The last term is the rest mass of the electron, so that T_{eff} represents the electron energy rather than the neutrino energy. The actual correction term amounts to approximately a 0.5% shift. The correction to position is due to a change in the location of the AV with respect to the PSUP. This is fixed with a 5.5 cm shift in the fit z-position of the data events and a radial shift for the MC events.

of the light reflected from the AV showed the true position of the AV, with respect to the PSUP coordinates, had shifted down approximately 5.5 cm compared to the MC. This translated to a shift in the z position of the data events (up 5.5 cm), and an inward radial shift for the MC events of 0.5%. The corrections were applied to the MC generated data sets for CC, NC, ES and external neutron events. The corrected distributions were used to develop the PDFs (described in the next sections) for the signal extraction process.

5.4 PDF Development

The data analysis has been performed using a variety of techniques by different analysis groups in the SNO collaboration. In particular, there are multiple ways one can derive PDFs such as those previously introduced in Chapter 3. The PDFs characterize the detector response for measurable quantities like energy, position, direction and event isotropy. PDFs may be generated from Monte Carlo studies, determined through measurements with calibration sources, or calculated from first principles. Often one makes use of PDFs from each of these techniques to complete the analysis of the SNO data set, with verification analyses completed using alternate techniques. PDFs generated from first principles are more robust and less dependent on detector parameters than the other methods of determining PDFs. The use of analytic (or parametric) PDFs also removes possible problems associated with binning events into histograms.

During the pure D_2O phase a number of analytic PDFs (for energy, direction with respect to the Sun, and radial position) were developed for the signal extraction data analysis. The addition of salt to the detector, had little effect on the structure of CC and ES events since these reactions were the same from one phase to the next. However, the capture of a neutron on chlorine produced a very different reaction than neutron capture on D_2O. A neutron capture on D_2O generally produces a single γ ray that interacts in the medium to produce an electron which generates Cherenkov light. Neutron capture on chlorine typically produces 2 or 3 γ rays, generating a small electron shower in the detector. More γ rays in an event also produce a more isotropic PMT hit distribution. In addition, the chlorine decay has higher summed energy (8.6 MeV) than the γ ray from the D_2O capture (6.2 MeV) which shifts the mean of the energy distribution higher for NC events. A neutron capture on chlorine also has a much higher capture cross-section than for D_2O that causes the average

distance for neutron capture in the detector to decrease. Therefore, fewer neutrons can wander out of the D_2O region to capture on the acrylic of the AV or escape to the H_2O. With more neutrons capturing at higher D_2O radii, the difference between the electron and neutron radial distributions is reduced. Note, the difference between the CC and NC radial distributions provided a large degree of the separation for the events in the pure D_2O phase. The loss of radial separability in the salt phase created a need for new parameters, such as β_{14}, that could assist with the separation of the CC and NC events.

5.4.1 Energy PDFs

The energy distributions for electrons and neutrons in the SNO detector during the pure D_2O phase were attributed to single γ rays of different energies. Studies showed the detector response to single γ rays, with energies of approximately 6 MeV, were well represented by Gaussian distributions [11]. This information was used to generate parametric PDFs to represent the energy distributions for the CC, NC and ES events. In the salt phase, CC and ES events were again associated with single γ ray interactions in the detector. It therefore remained valid to use Gaussian distributions to represent those events. The full dynamics of the neutron capture on chlorine produced 2 to 3 γ interactions for each NC event. In this reaction, $^{35}Cl^*$ was produced which has a complicated decay scheme of 75 energy levels that range in energy from 0.7 MeV to 8.6 MeV [48].

NC PDFs

The response of the detector must be taken into consideration when determining the energy distribution of the NC events, and it was therefore not possible to generate a purely analytic function based on the physics of the interaction. Rather, some

method must be used to determine the response of the detector to γ rays with an energy range equivalent to that of $^{35}Cl^{*}$. A calibration source was not available to perform this measurement, so we relied on the SNOMAN Monte Carlo to provide the information. SNOMAN includes the EGS4 code to handle the propagation of γ rays in the detector. EGS4 is known to describe photon and electron interactions in materials extremely well, with typical inaccuracies measured to be much less than 1% [72]. We note the MC also used the results from the calibration sources to ensure the correct energy and optics were applied in the modeling of the detector response. In this way, the MC could be tuned to have a detector response that agreed with the true detector.

Due to the complexity of the interaction of neutron capture on chlorine, it was desirable to test that the MC correctly models the reaction. To do this, we studied the behavior of the detector for γ rays of various energies. The γ ray distributions for those energies were then combined using the branching ratios of the decay levels to reproduce the neutron capture interactions. By comparing this quasi-analytic result to the MC distributions for the same interactions, we determined the degree of agreement. Appendix B shows an example of the SNOMAN command files used in this analysis to generate γ rays of various energies. Samples of the γ ray distributions for selected energies are also shown in Appendix B.

From the sample distributions it becomes clear the γ ray detector response was not represented by Gaussian distributions for the lower γ energies. A number of functions, including Maxwell and Chi-distributions [36], were applied to the γ distributions in an attempt to find a single function that would represent the γ ray response for the entire energy range. Each of the individual functions failed to achieve a good fit to the γ distributions over the full energy range. Particular difficulty was experienced in the "transition" energy region (1.8 to 4.0 MeV) where the energy distributions changed from functions that are truncated at the left tail

to Gaussian-like distributions at higher energies. We have determined the convolution of two Gaussian functions, where one is truncated to match the threshold cut at low energy, mapped the γ ray energy distributions across the energy range (see figure 5.1). The truncation of the Gaussian function was achieved by including a step-function in the convolution. The results of these fits are shown in Appendix B, from which we note a small increase of the reduced chi-squared of the fit is observed in the transition range. However, the chi-squared values are found to remain below 5, and the fit is considered good for our purposes.

The parameters of the convolved Gaussian functions involved in the fit were studied as a function of gamma energy (see figures in appendix B). A polynomial was used to interpolate between the energy values, so that it was possible to generate a representative energy distribution for any γ energy, and therefore the entire cascade scheme of $^{35}Cl^{*}$ could be generated in a parametric form. The parametric distributions were combined together for the different possible γ cascades according to the measured branching ratios (BR). Therefore, the parametric distributions were scaled according to the BR of the γ rays in the distribution, and the scaled distributions were convolved together (see figures 5.2 and 5.3). The end result was the combination of all possible gamma cascades, scaled by their BRs, to produce a single distribution that represented the neutron capture on chlorine energy distribution (see figure 5.4).

As previously mentioned, the above development of a NC PDF for the salt phase was not a true analytic method since we began the process by using the detector response, produced by the MC, to represent the γ rays. Starting with the MC predicted response of SNO to single mono-energetic photons, we parameterized the detector response to neutron capture on chlorine. This parameterization agreed well with the overall response predicted by SNOMAN. Hence, we demonstrated the MC can be used to produce the energy distribution of the neutron events for the signal

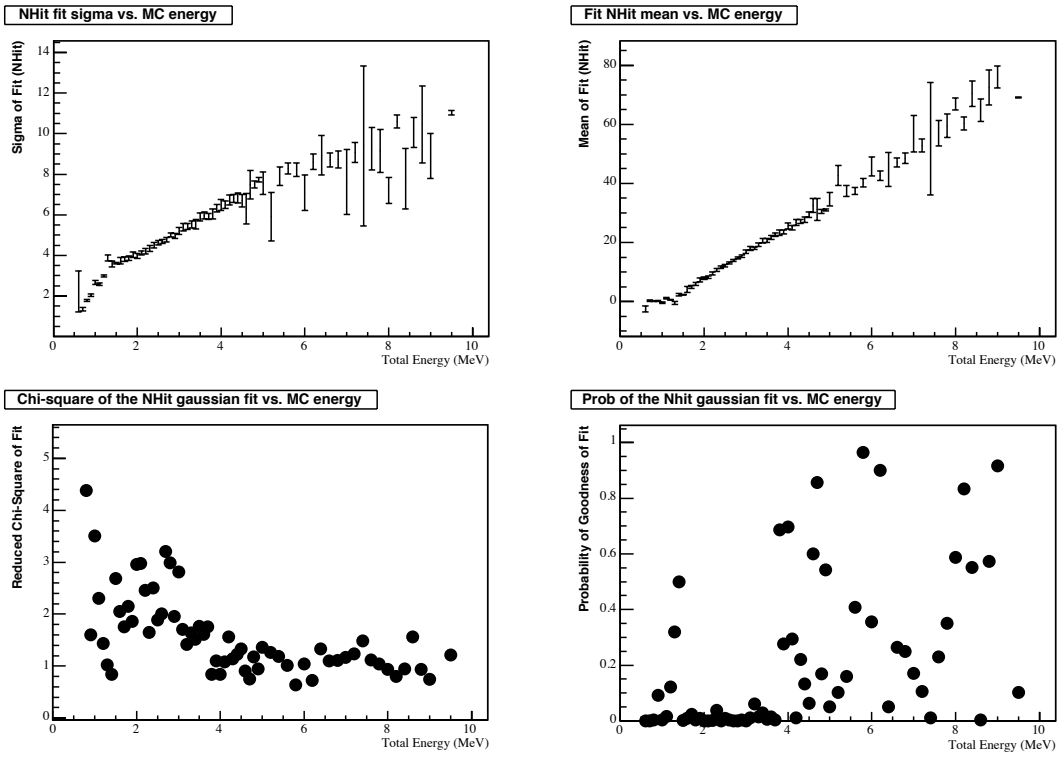

Figure 5.1: The results of the convolved truncated Gaussian fit as a function of energy for the neutron capture on Cl γ ray distributions. The top two plots show the NHIT sigma and mean of the fit versus energy. The bottom two plots show the reduced chi-square and probability of the goodness of the convolved-truncated Gaussian fit to the distributions. The convolved (truncated) Gaussian distributions are seen to provide good fits at all generated γ ray energies.

extraction process. We therefore chose to parameterize the MC energy distribution for NC events in the salt phase to produce the signal extraction PDF. The parameterization function was based upon the work shown above, using a convolution of two Gaussian functions (see figure 5.5).

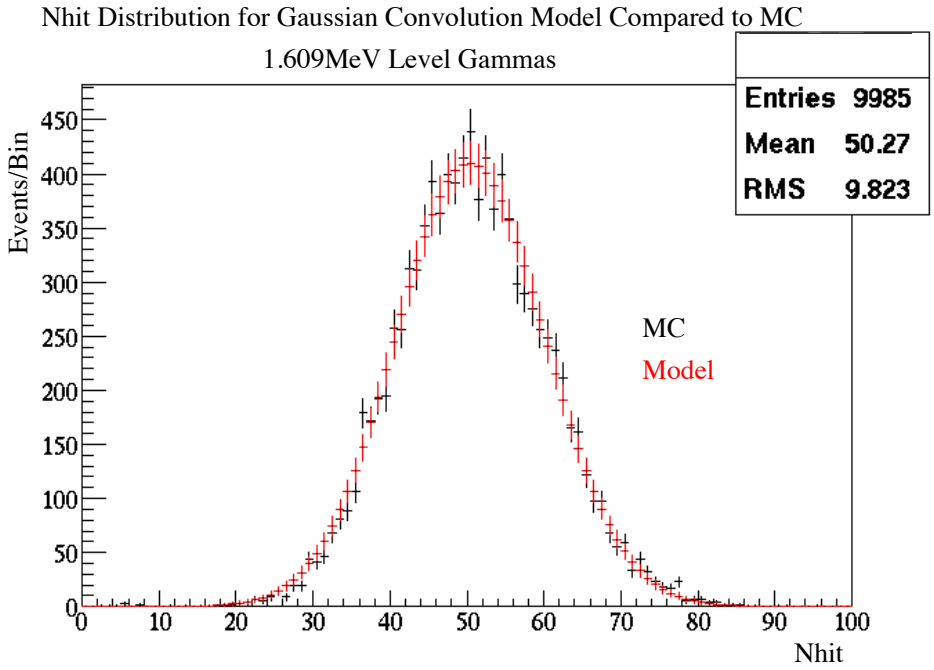

Figure 5.2: Comparison of MC to the convolution model for level 1.601 MeV gamma rays. For this capture level, there is a primary gamma ray produced (6.979 MeV) by the transition from the 8.58 MeV excited level to the bound level of 1.601 MeV. This is followed by decays to the ground state, 0.788 MeV or 1.165 MeV levels with branching ratios of 76%, 1.1% and 23% respectively. The 1.165 MeV level may decay either to the ground state or 0.788 MeV levels with branching ratios of 99.985% and 0.015% respectively. Finally the 0.788 level goes to the ground state 100% of the time. Note the shoulder in the distribution between NHIT 55 and 65 is produced by the high branching ratio of the primary gamma ray to the 1.601 level, and agrees well with the MC distribution.

CC and ES PDFs

For CC and ES events, the principal emission begins with a relativistic electron. Electron and photon interactions in the detector behave very similarly, as demonstrated by the comparison of ^{16}N and ^{8}Li calibration sources to each other and the MC. Therefore, parameterizations that were successful with photons in the NC energy PDF discussion above, may also be applied to these distributions. The CC and

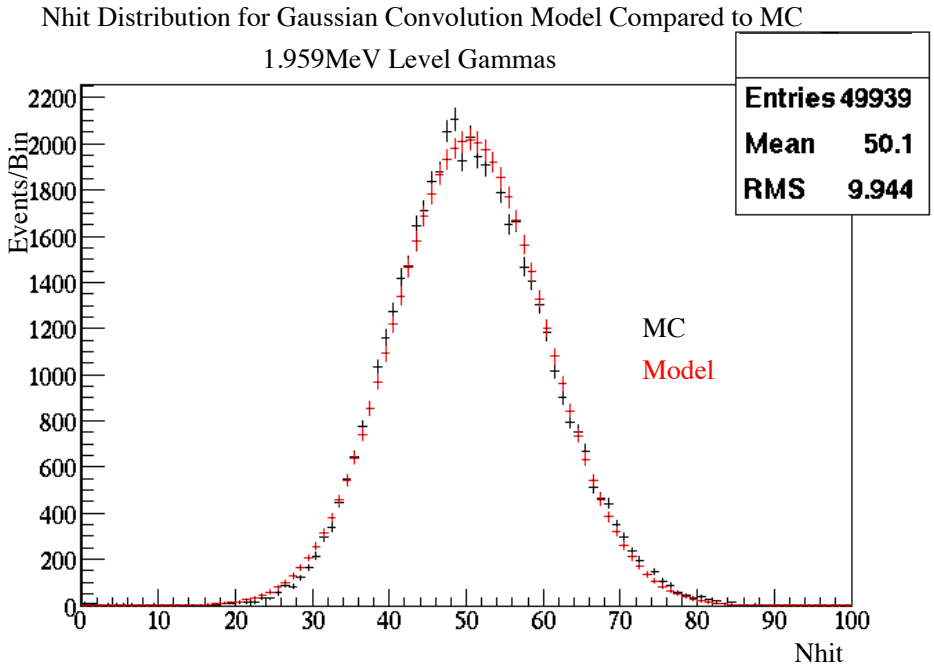

Figure 5.3: Comparison of MC to the convolution model for level 1.959 MeV gamma rays. For this capture level, there is a primary gamma ray with energy of 6.621 MeV. From the 1.959 MeV level, further decays are available to the 1.601 MeV, 0.788 MeV and ground state with branching ratios of 94.7%, 3.7% and 1.6% respectively. The further cascasdes from the 1.601 MeV and 0.788 MeV levels are described in the caption of figure 5.2.

ES energy distributions were fit with Gaussian functions and the results are shown in figures 5.6 and 5.7.

5.4.2 Radial PDFs

We chose in this analysis to parameterize the MC data set for CC, NC and ES events by applying functions that take into consideration the detector geometry to the MC distributions. For example, if the AV did not exist and D_2O filled the volume to the PSUP, one could expect the radial distribution to be a simple polynomial.

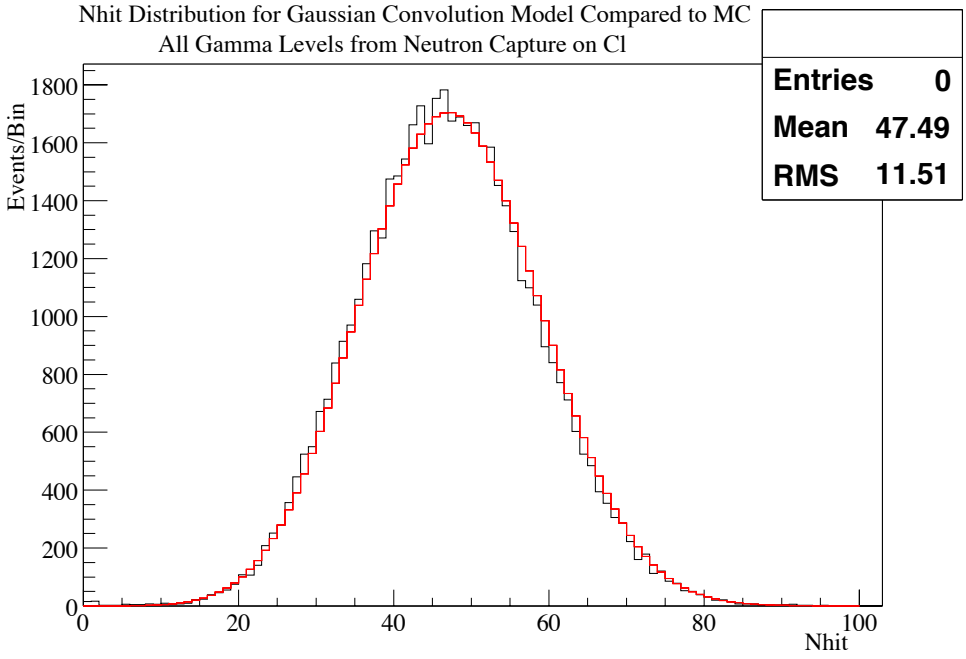

Figure 5.4: Comparison of MC to the convolution model for all levels of gamma rays, including all combinations of cascade paths. A small shift in the mean of the modeled distribution compared to the MC, less than 1/2 a NHIT, is observed. This is of the order of the uncertainty in the parameterization of the mono-energetic gamma ray distributions.

This is similar to the case for the ES events, where the neutrino may scatter off electrons in a D_2O or H_2O molecule to produce a signal in the detector. The CC and NC events take place by interacting with deuterons, and therefore may only occur in the D_2O region. Some neutrons can wander out of the D_2O region and capture on the hydrogen of the H_2O or the acrylic. However, a neutron capture on hydrogen does not produce a signal in the detector, and therefore the event is missed. This created an apparent depletion of neutron events at large radii near the AV. The presence of salt in the D_2O provided a high neutron capture efficiency compared to pure D_2O (see figure 5.8). Hence, more neutron events were observed at higher radii, and the difference between the CC and NC event radial distributions

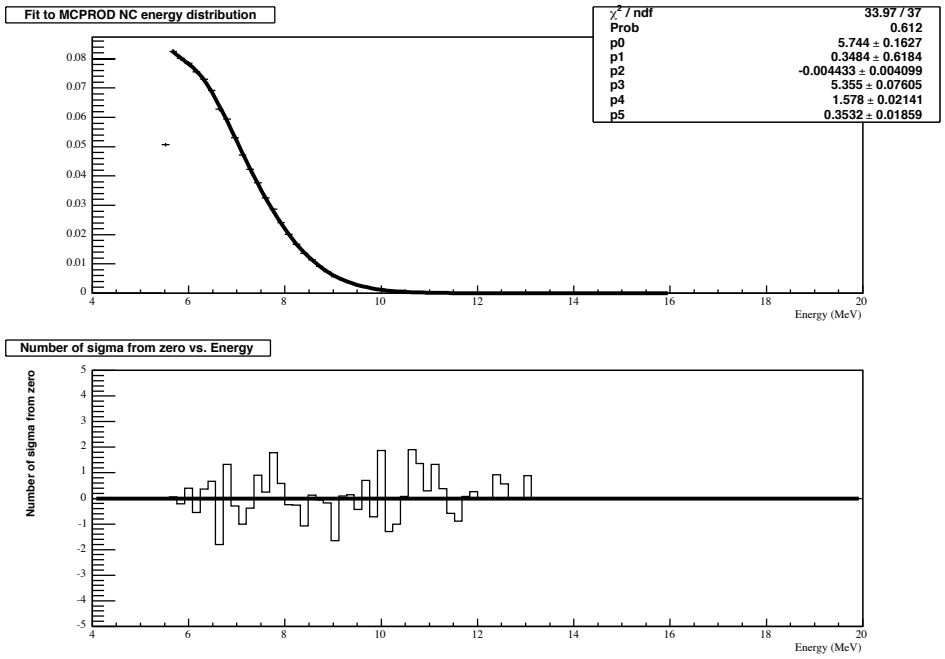

Figure 5.5: The parameterized NC energy distribution using two Gaussian functions. The top plot shows the parameterized function over the MC data prediction. The fit is found to be extremely good, surpassing the fit of analytic functions in the pure D_2O default SNO analysis. The bottom plot shows the goodness of the fit over the relevant energy range. At all energies, the deviation from the parameterization is less than 2 sigma and there are no areas systematically high or low.

was reduced (see table 5.9).

A similar parameterization was therefore used for the CC and NC events. We chose a parameterization function composed of a polynomial convolved with a truncated Gaussian function. The polynomial was used to represent the events away from the AV. The truncated Gaussian function was used to represent the "cut-off" of the events near the AV. The solution of the convolution integral

$$\int_0^n \left[ey^4 + dy^3 - ay^2 - by + c\right] \frac{\sqrt{2}}{\sqrt{\pi}\sigma} \exp\left[\frac{-1}{2}\frac{(x-y)^2}{\sigma^2}\right] dy \qquad (5.2)$$

(with n being the cut-off point at the AV and the integral is evaluated above 0 only)

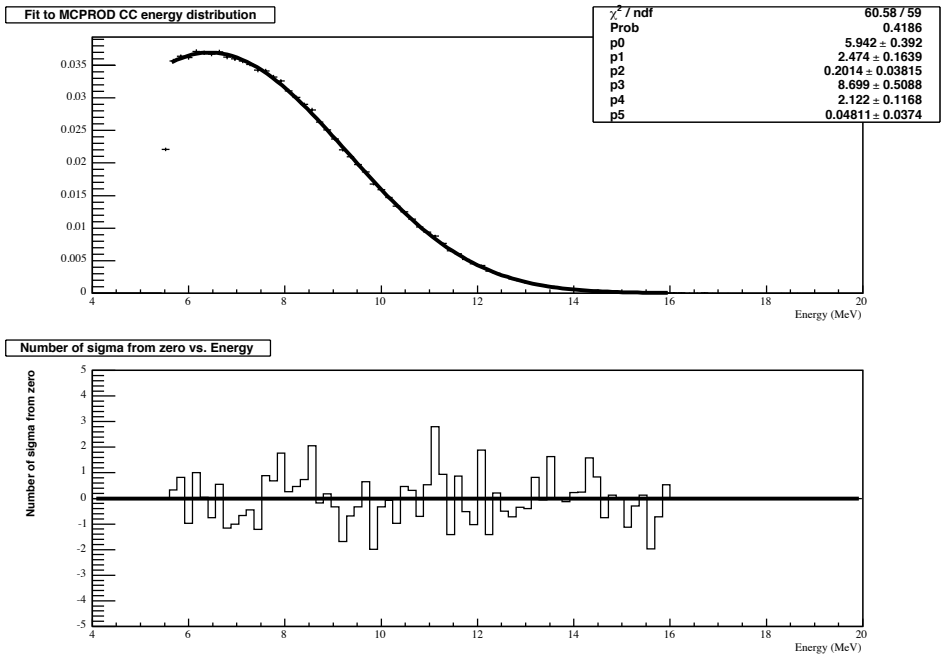

Figure 5.6: The parameterized CC energy distribution using two Gaussian functions. The top plot shows the parameterized fit over the MC predicted data. The bottom plot shows the goodness of parameterized fit for each bin of the energy range. There is excellent agreement between the fit function and the MC at all energies.

has the form

$$\frac{f}{\sqrt{\pi}}(A_1 + B_1 - A_2 - B_2 + A_3 + B_3); \tag{5.3}$$

where f is a free parameter representing the Gaussian height. The terms each have the form

$$\begin{aligned} A_1 =& \sqrt{2}(-asx + bs + dsn^2 + esn^2x + 5es^3x - esn^3 - dsnx - 3ens^3 \\ &+ asn + esx^3 + 2ds^3 + dsx^2 - esnx^2) \exp\left[-\frac{(n+x)^2}{2s^2}\right] \end{aligned} \tag{5.4}$$

$$\begin{aligned} B_1 =& \sqrt{\pi}(-3ds^2x - 6es^2x^2 + as^2 + bx + dx^3 - ex^4 - 3es^4 + ax^2 - c) \\ &\text{Erf}\left[\frac{(-\text{n} + \text{x})}{\sqrt{2}\text{s}}\right] \end{aligned} \tag{5.5}$$

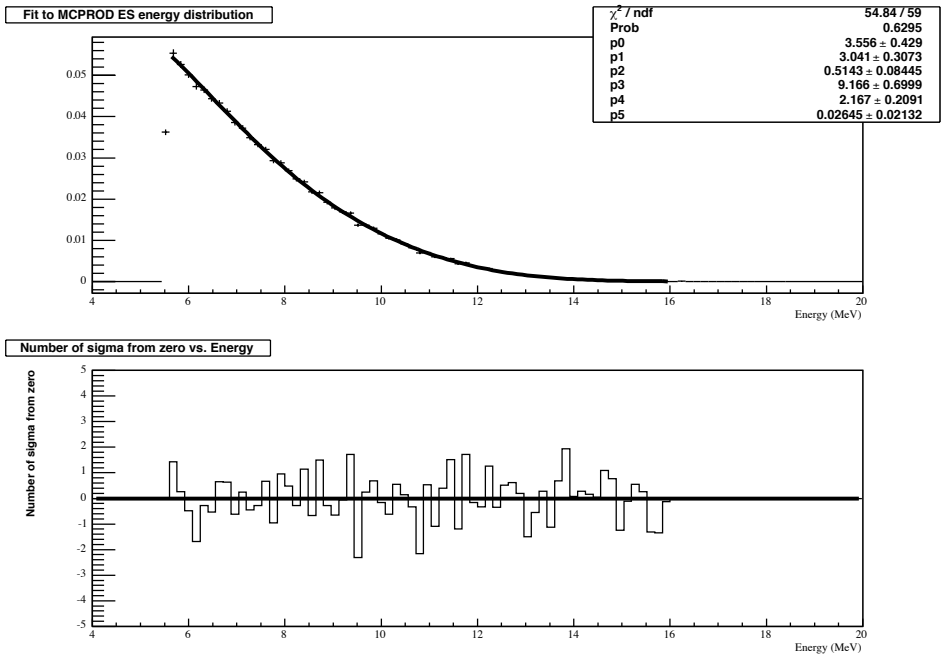

Figure 5.7: The parameterized ES Energy distribution using two Gaussian functions. The top plot shows the parameterized fit over the MC predicted data. The bottom plot shows the goodness of parameterized fit for each bin of the energy range. There is excellent agreement between the fit function and the MC at all energies.

$$A_2 = 2\sqrt{\pi}bs \exp\left[\frac{-x^2}{2s^2}\right] \tag{5.6}$$

$$B_2 = 2\sqrt{\pi}bx\mathrm{Erf}\left[\frac{\mathrm{x}}{\sqrt{2}\mathrm{s}}\right] \tag{5.7}$$

$$\begin{aligned} A_3 =& \sqrt{2}(asx - 3es^3n + bs - 2ds^3 - 5exs^3 - esn^2x - dsnx \\ & - esx^3 - dsx^2 - esnx^2 - esn^3 - dsn^2 + asn)\exp\left[-\frac{(-n+x)^2}{2s^2}\right] \end{aligned} \tag{5.8}$$

$$\begin{aligned} B_3 =& \sqrt{\pi}(dx^3 - ax^2 + ex^4 - as^2 + bx + 3es^4 + c \\ & + 3dxs^2 + 6ex^2s^2)\mathrm{Erf}\left[\frac{\mathrm{n}+\mathrm{x}}{\sqrt{2}\mathrm{s}}\right] \end{aligned} \tag{5.9}$$

In the above equations x is the radius, n is the start point of the step function that truncates the Gaussian function, s is the sigma of the Gaussian function, and

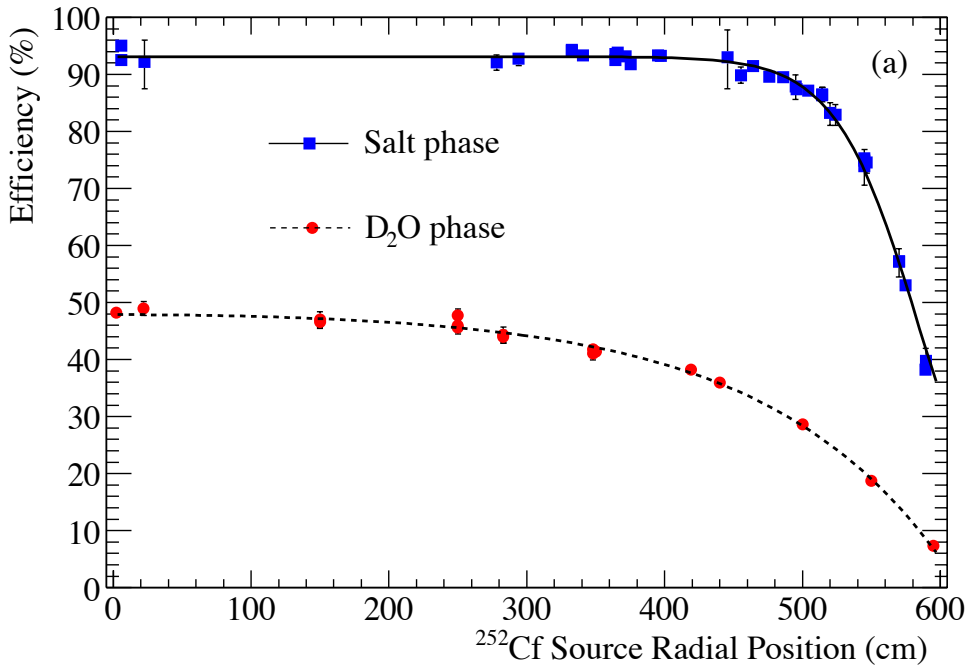

Figure 5.8: Neutron Capture efficiency radial profile [64]. The approximate 95% efficiency shown for neutron capture in salt is for the case where no energy threshold cut has been applied to the data.

the letters e, d, a, b, and c are coefficients of a 4th order polynomial, respectively. Figures 5.9, 5.10 and 5.11 show the results of applying this parameterization to the appropriate MC radial distributions.

5.4.3 Cos(θ_{sun}) PDFs

The PDFs representing angular distributions for CC, NC and ES events, with respect to the position of the Sun, are produced by parameterizing the MC distributions. For each event type, there is an underlying physics interaction that may be used to verify the MC distributions. For example, neutrons drift randomly prior to capture so that the direction of NC events in the detector show no dependence

Parameter	Range	Separation
Energy	4.00 - 20.0 MeV	0.2933
	5.00 - 20.0 MeV	0.3237
	5.25 - 20.0 MeV	0.3295
	5.50 - 20.0 MeV	0.3406
	5.75 - 20.0 MeV	0.3462
	6.00 - 20.0 MeV	0.3496
Radial	0.00 - 1.00	0.0537
	0.00 - 0.95	0.0468
	0.00 - 0.90	0.0374
	0.00 - 0.85	0.0288
	0.00 - 0.80	0.0221
	0.00 - 0.75	0.0172

Table 5.9: Level of separation of CC and NC events using radial distributions. The level of separation is determined by the maximum Kolmogorov-Smirnov distance between the distributions

to the location of the Sun. Therefore, one expects a flat directional distribution for these events as seen in figure 5.12.

For CC events, the weak coupling vertex of the electron, ν_e and W^- produces a current of the form

$$J_e^\mu = \bar{u}_\nu \gamma^\mu \frac{1}{2}(1-\gamma^5)u_e \quad [39]. \tag{5.10}$$

The factor γ^μ is called the vector term, while (1-γ^5) is known as the axial-vector term. Together these two factors form the V-A term of the CC interaction. If one calculates the amplitude for the d-quark to transform to an up-quark for an $\bar{\nu}_e$ scattering on an electron, in the deuteron, the result is consistent with that of neutron β-decay. The differential rate may be written as

$$\begin{aligned} d\Gamma =& G^2 \sum_{spins} \left|\bar{u}(p_\nu)\gamma^0(1-\gamma^5)\nu(p_e)\right|^2 \frac{d^3p_e}{(2\pi)^3 2E_e} \\ & \mathrm{x}\frac{\mathrm{d^3p_\nu}}{(2\pi)^3 2\mathrm{E_\nu}} 2\pi\delta(\mathrm{E_0 - E_e - E_\nu}), \end{aligned} \tag{5.11}$$

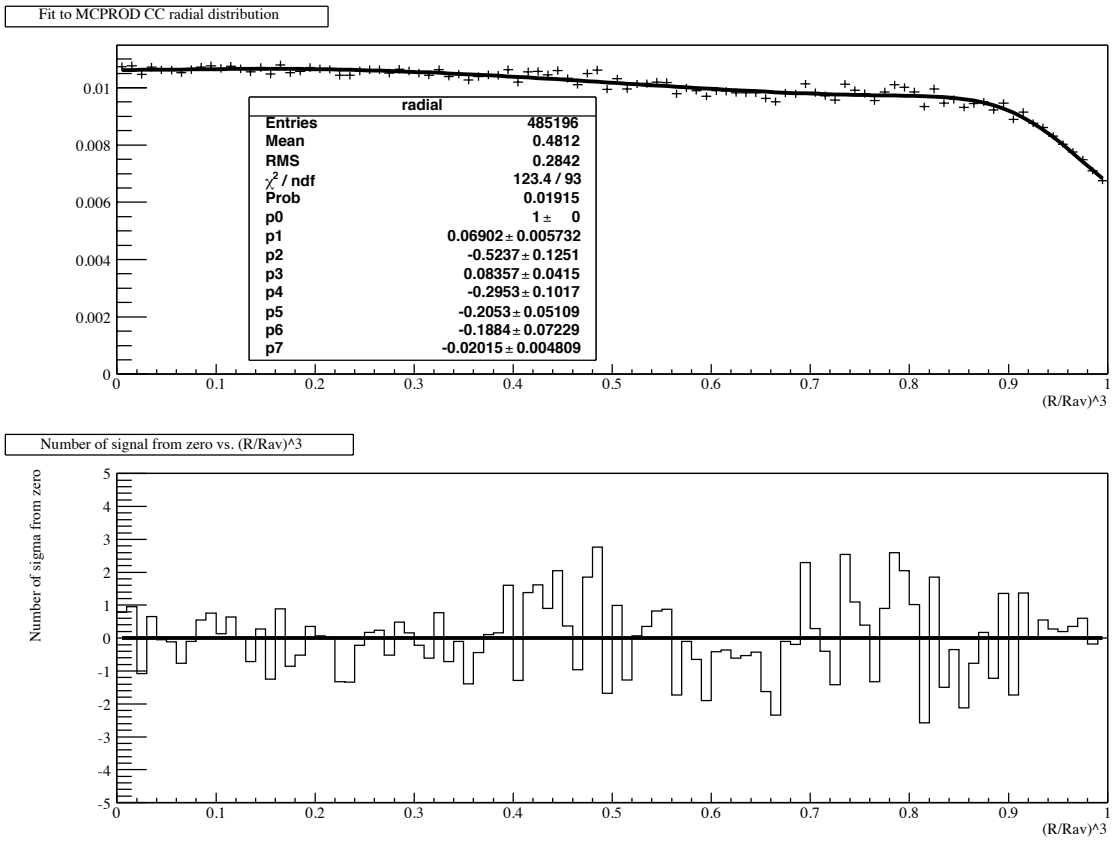

Figure 5.9: The parameterized CC radial distribution using equation 5.3. The top plot shows the parameterized fit over the MC predicted data. The bottom plot shows the goodness of parameterized fit for each bin of the radial range.

where E_0 is the energy of the lepton pair, and we have assumed the d-quark is at rest which changes γ^μ to γ^0. Summing over the spins (if one neglects the mass of

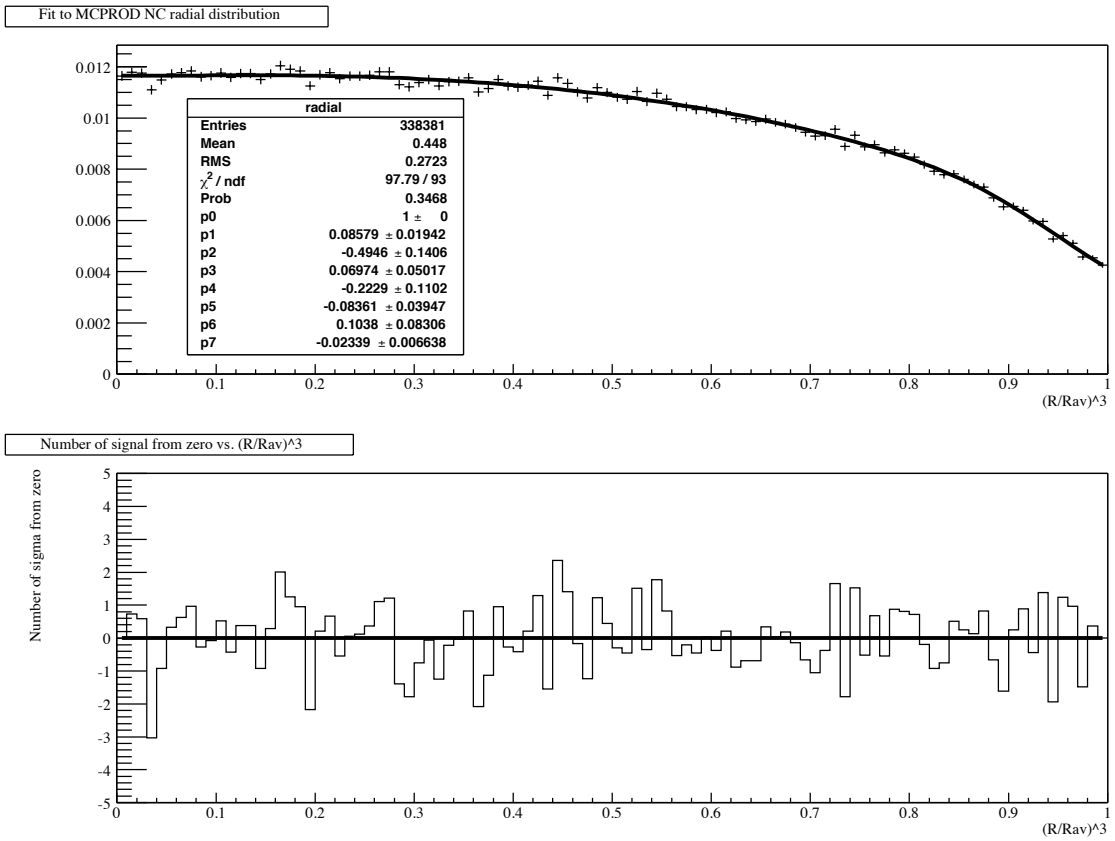

Figure 5.10: The parameterized NC radial Distribution using equation 5.3. The top plot shows the parameterized fit over the MC predicted data. The bottom plot shows the goodness of parameterized fit for each bin of the radial range.

the electron) gives

$$\begin{aligned}\sum_{spins}\left|\bar{u}\gamma^0(1-\gamma^5)v\right|^2 &= \sum(\bar{u}\gamma^0(1-\gamma^5)v)(\bar{v}(1+\gamma^5)\gamma^0u)\\ &= \mathrm{Tr}(\not{p}_\nu\gamma^0(1-\gamma^5)\ \not{p}_e(1+\gamma^5)\gamma^0)\\ &= 2\mathrm{Tr}(\not{p}_\nu\gamma^0\ \not{p}_e(1+\gamma^5)\gamma^0)\\ &= 8(E_eE_\nu+\mathbf{p_e}\cdot\mathbf{p}_\nu)\\ &= 8E_eE_\nu(1+\beta_e\cos\theta)\end{aligned} \tag{5.12}$$

where θ is the opening angle between the electron and neutrino, and β_e is the veloc-

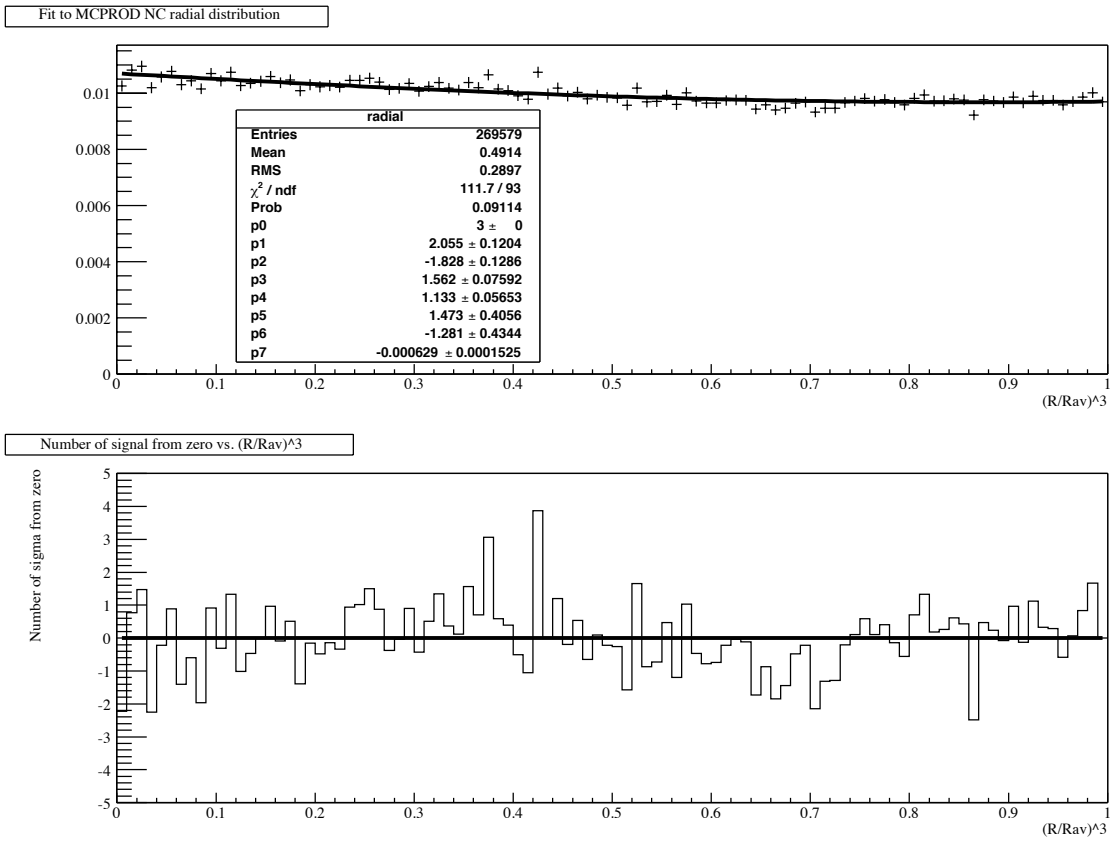

Figure 5.11: The parameterized ES radial distribution using equation 5.3. The top plot shows the parameterized fit over the MC predicted data. The bottom plot shows the goodness of parameterized fit for each bin of the radial range.

ity of the electron (approximately 1). For the above equation, the average cosine, weighted by the differential cross section, is given by

$$\langle \cos\theta \rangle = \frac{1}{3} v_e a(E_\nu) \quad [71]. \tag{5.13}$$

At the neutrino energies associated with detected SNO events, the CC reaction is a pure Gamow-Teller transition and the asymmetry term (a) is therefore equal to -1/3. This produces a small backward slope to the $\cos\theta$ distribution [71] and is the slope shown in the MC distribution in Figure 5.13. Thus, we parameterized the CC angular distribution with a linear function.

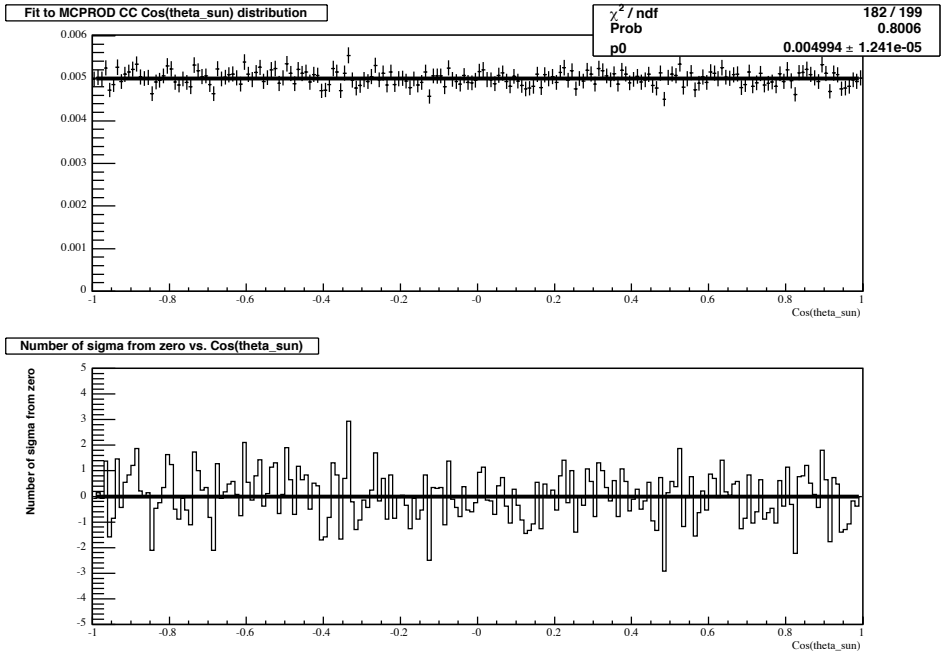

Figure 5.12: The parameterized NC $\cos(\theta_{sun})$ distribution using a zero order polynomial. The top plot shows the parameterized fit over the MC predicted data. The bottom plot shows the goodness of parameterized fit for each bin of the radial range.

The ES events are peaked in the direction away from the Sun. This was expected since the elastic scattering is very forward peaked when a neutrino scatters on an electron. The angular resolution of the detector affects the broadness of the observed peak. The MC distribution for the ES event angular distribution was parameterized using the sum of two Gaussian functions (see Figure 5.14). This parameterization was found to be a better description than the default analysis use of a double exponential.

5.4.4 Isotropy PDFs

For the pure D_2O analysis it was not necessary to include an isotropy parameter as a part of the signal extraction process since the energy and radial PDFs were largely different for CC and NC events. The lack of separation between the CC and

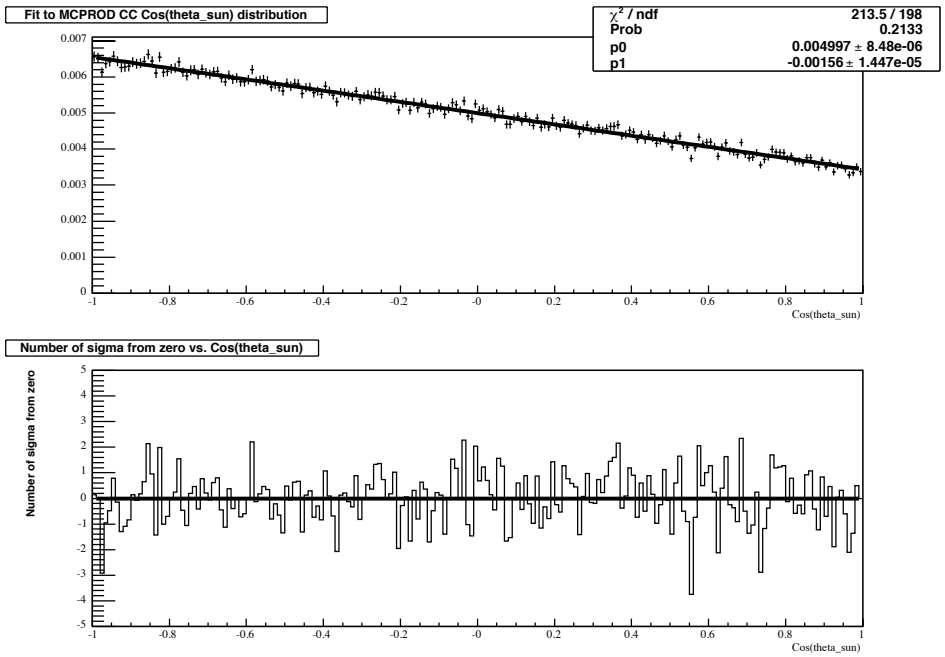

Figure 5.13: The parameterized CC $\cos(\theta_{sun})$ distribution using a first order polynomial. The top plot shows the parameterized fit over the MC predicted data. The bottom plot shows the goodness of parameterized fit for each bin of the radial range.

NC radial distributions in the salt phase made it necessary to develop a new set of PDFs to assist in the signal extraction. It was found different event types produced clearly different and statistically separable isotropic distributions [15], [12]. From these studies, two primary isotropy parameters were extensively developed, θ_{ij} and β.

The term θ_{ij} is the mean angle between all PMTs associated with the event. Well defined single photon or electron rings tend to have a small θ_{ij}, whereas multi-photon events tend to be more isotropic, leading to large average angular separation and a larger θ_{ij}. This parameter was originally developed as an analysis tool to separate the uranium from thorium events in the low energy background data set, called the *in situ* analysis.

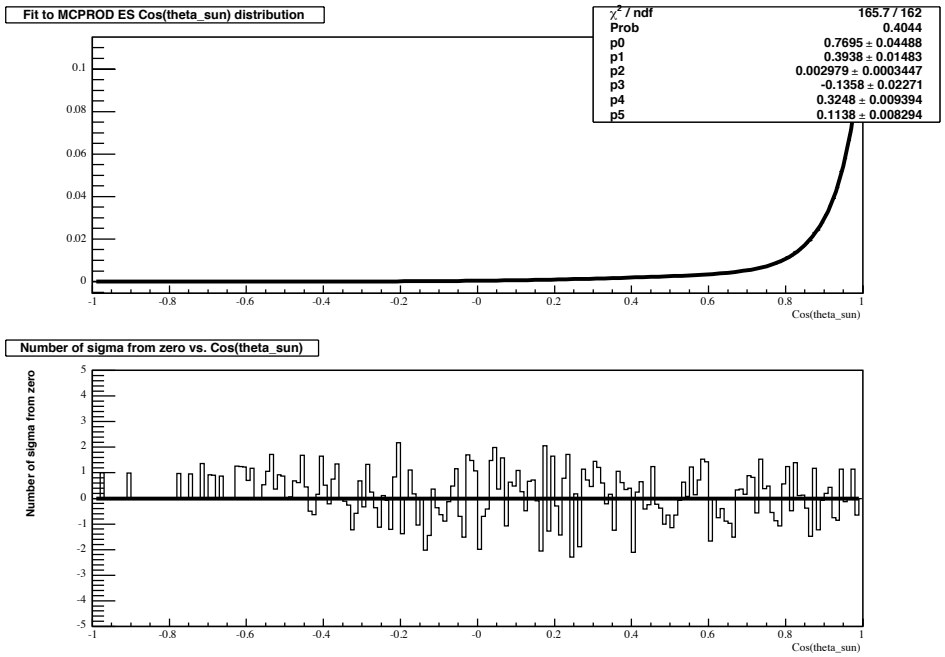

Figure 5.14: The parameterized ES $\cos(\theta_{sun})$ distribution using a sum of two Gaussian functions. The top plot shows the parameterized fit over the MC predicted data. The bottom plot shows the goodness of parameterized fit for each bin of the radial range.

The β parameters were developed from a spatial hit pattern function which contains the polar and azimuthal angle (θ_i, ϕ_i) of each hit PMT with respect to the fit position, and each hit PMT is represented by a delta function as shown in

$$f(\theta,\phi) = \frac{1}{N}\sum_{i=1}^{N}\delta(cos\theta - cos\theta_i)\delta(\phi-\phi_i)[12]. \tag{5.14}$$

The value N runs over all PMTs in an event. Equation 5.14 may be written in spherical harmonic components, giving equation 5.15.

$$f(\theta,\phi) = \sum_{l,m}\alpha_{lm}Y^*_{lm}(\theta,\phi) \tag{5.15}$$

Solving this equation for α_{lm} gives

$$\alpha_{lm} = \frac{1}{N}\sum_{i=1}^{N} Y_{lm}(\theta_i, \phi_i). \tag{5.16}$$

Next one defines the terms β_l, which are rotationally invariant, given by:

$$\beta_l = \sum_m |\alpha_{lm}|^2 \tag{5.17}$$

These terms may be reduced to

$$\beta_l = \frac{2l+1}{2\pi N(N-1)} \sum_{i=1}^{N-1} \sum_{j=i+1}^{N} P_l(cos\omega_{ij}). \tag{5.18}$$

The terms $P_l(\cos\ \omega_{ij})$ are the natural Legendre polynomials, and therefore are a direct representation of the isotropy of an event.

The goal of including an isotropy PDF in the signal extraction was to provide separation between the CC and NC events in the data set. It was necessary to study the different available isotropy parameters to find which would be best suited for use with the salt dataset. First one needed to determine the correct β parameter to use in the study. Certain combinations of the β parameters provided a larger degree of separation between the CC and NC events than others[24]. The combination offering the largest difference between the events was determined to be β_{14} and is given by

$$\beta_{14} = \beta_1 + 4\beta_4 \tag{5.19}$$

where

$$\beta_1 = 4\pi(0.02\beta_1^h + 0.016) \tag{5.20}$$

and

$$\beta_4 = 4\pi(0.034\beta_4^h - 0.002)/9. \tag{5.21}$$

In the above equations, β_i are the Legendre polynomials, and β_i^h are the harmonic parameters. The degree of separability of the β_{14} parameter was compared to θ_{ij}

and other measures of isotropy, including the measured deviation from the standard Cherenkov cone (opening angle = 41.4°) [24], [54]. The results of the study demonstrated a similar degree of separation for each of the parameters. However, the systematic uncertainties for the β_{14} parameter offered a small improvement over the other parameters, and was chosen by the collaboration to be used in the salt phase signal extraction.

With an isotropy parameter chosen, it was desirable to parameterize the distribution to create the PDF for use in the signal extraction process. As mentioned previously, it was possible to parameterize distributions from the MC or calibration source data sets. A comparison of the data sets is desirable to ensure the MC agrees with the true detector response. The comparison of the β_{14} distributions from the ^{16}N and ^{252}Cf sources to the MC distributions showed a clear, albeit small, shift in the mean. When the source of the shift was studied, it was discovered the Mott scattering term was missing in the EGS4 code included in SNOMAN. It should be noted that the EGS4 code is the most recognized code for simulating gammas and electrons in materials. It is used world wide, and has been studied extensively by numerous experiments. The Mott scattering term was a small error in the EGS4 code found by the SNO collaboration. The term was added and the reprocessing of the MC showed excellent agreement with the calibration data [24]. Therefore, it was possible to use the MC dataset to correctly represent the isotropy of neutrino events in the detector.

In this analysis, we chose to parameterize the isotropy distributions using summations of Gaussian distributions. The CC and ES distributions were only slightly asymmetric, and therefore a combination of two similar Gaussian functions produced excellent agreement (see figures 5.15 and 5.16). The NC isotropy distribution, however, clearly required a more asymmetric function (see figure 5.17). In this case we required the use of three Gaussian functions to adequately map the distribution.

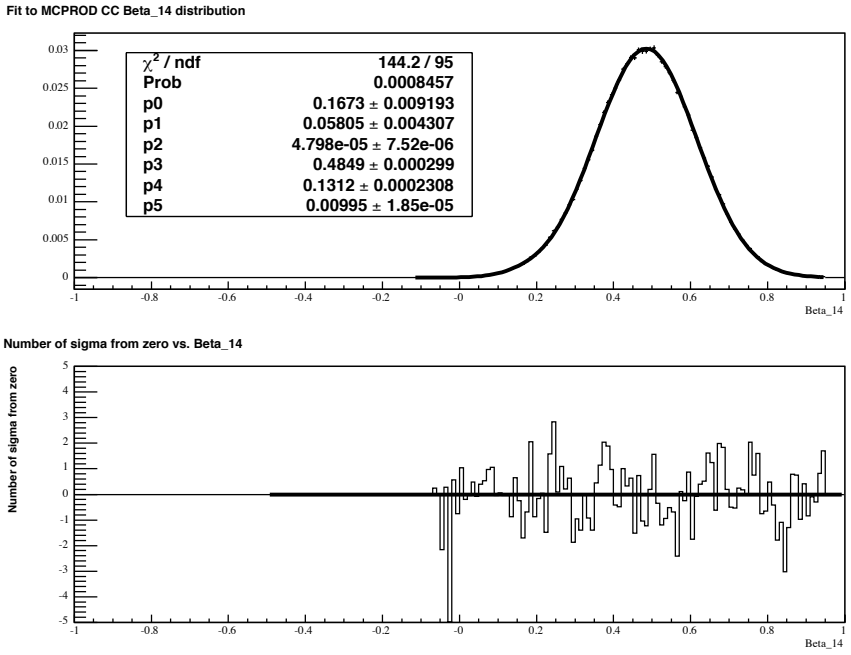

Figure 5.15: The parameterized CC β_{14} distribution using a sum of two Gaussian functions. The top plot shows the parameterized fit over the MC predicted data. The bottom plot shows the goodness of parameterized fit for each bin of the radial range.

5.4.5 Other PDFs

Thus far we have completed the generation of all necessary PDFs for CC, NC and ES events to proceed with the signal extraction process. However, the background events which are best described by fitting must now be considered. The most critical backgrounds are those associated with internal and external neutrons due to the large predicted number of these events. Note, the γ ray backgrounds are predicted to produce less than 5 total events, and therefore have a negligible contribution to this analysis. Internal background neutrons are generated from a number of sources. Decays of U and Th daughters, and activated ^{24}Na are the dominant contributors. Internally produced neutrons are essentially identical to neutrons from solar neutrino

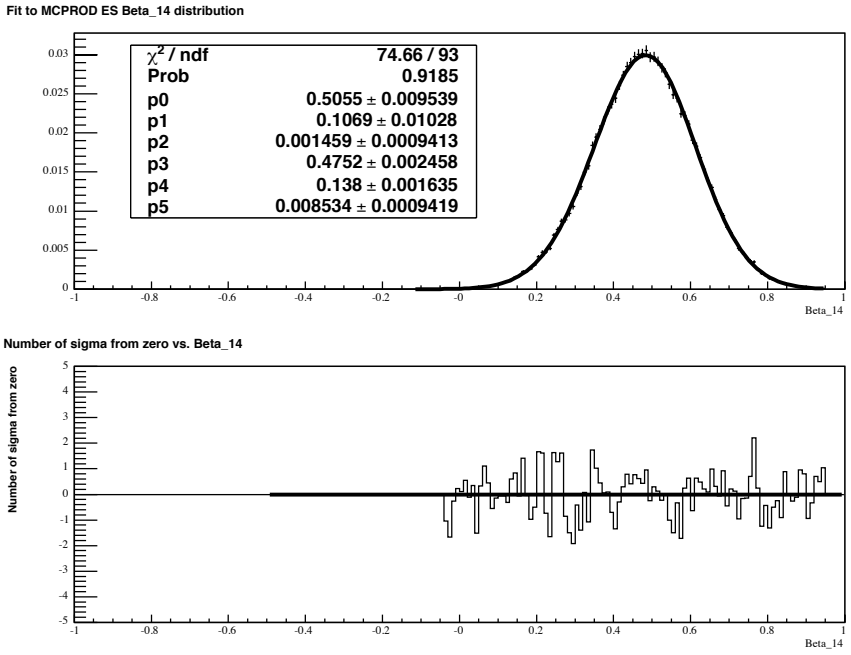

Figure 5.16: The parameterized ES β_{14} distribution using a sum of two Gaussian functions. The top plot shows the parameterized fit over the MC predicted data. The bottom plot shows the goodness of parameterized fit for each bin of the radial range.

interactions and their number has been measured. Therefore, the same PDFs were used to subtract these internal background events directly from the total neutron flux. External background neutrons are believed to be created by alpha decays on the acrylic of the AV. There is no accurate method for determining their number, so they must be determined from the fit. These neutrons have energy, $\cos(\theta_{Sun})$, and isotropy distributions very similar to NC events. Therefore, the same functions as those developed above for NC events were used to parameterize the MC distributions of these events. However, due to the production of these neutrons near the AV, their radial distribution was very different than the NC events. This difference in the radial distributions was used to statistically separate the external background

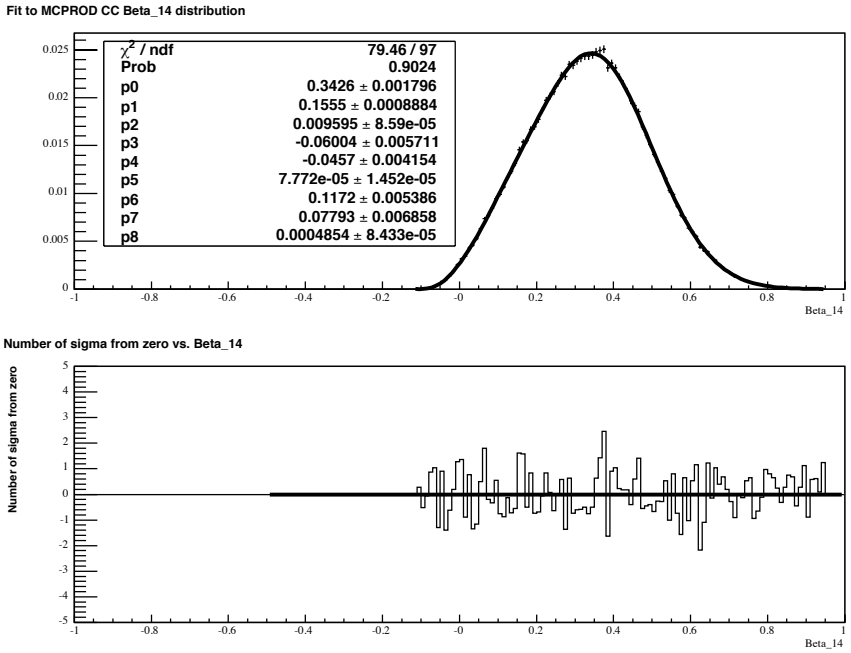

Figure 5.17: The parameterized NC β_{14} distribution using a sum of three Gaussian functions. The top plot shows the parameterized fit over the MC predicted data. The bottom plot shows the goodness of parameterized fit for each bin of the radial range.

neutrons from the NC events in the signal extraction process. The external neutron radial PDF was a parameterization of the MC distribution for these events and used a sum of two Gaussian functions, similar to that used for the ES $\cos(\theta_{Sun})$ distribution (shown in figure 5.18).

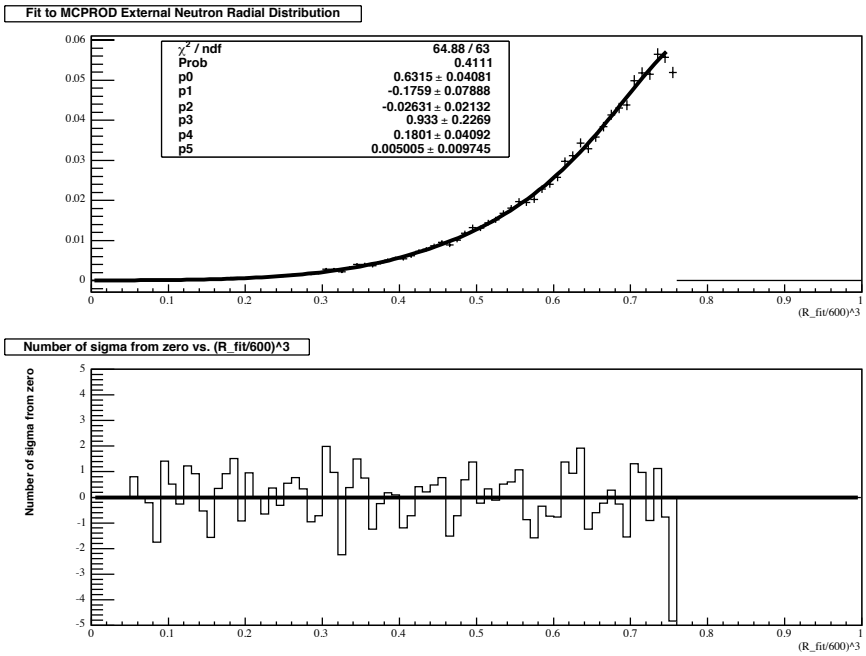

Figure 5.18: The parameterized external neutron radial distribution using a sum of two Gaussian functions. The top plot shows the parameterized fit over the MC predicted data. The bottom plot shows the goodness of parameterized fit for each bin of the radial range.

Chapter 6

Salt Phase Signal Extraction and Results

The ultimate goal of this work was to determine the solar neutrino flux. In this chapter we describe the process whereby the various signal rates are determined in the presence of the background events. The detector backgrounds were either measured or deduced by independent means. We used an extended maximum likelihood minimization to statistically separate the events into one of the four classes (CC, NC, ES or external neutron background). It was possible at this step to choose to perform either an energy constrained or unconstrained signal extraction. The constrained analysis used energy PDFs in the signal extraction, effectively including the expected ^{8}B energy spectrum in the fit, and therefore producing a model dependence in the result. The unconstrained fit did not include the energy PDFs, instead relying on isotropy and $\cos(\theta_{Sun})$ to separate the event types. Without using energy in the extraction, the result was model independent and was therefore a slightly more powerful test for determining the solution to neutrino oscillations. For each of the extracted fluxes, constrained or unconstrained, we needed to determine the sta-

tistical uncertainties coming from the fit, including correlations between the types. Finally, it was necessary to determine the systematic errors for the fit parameters and measured quantities.

Each of these steps are discussed in this chapter, with the final result being a precision constrained measurement of the total solar neutrino flux.

6.1 Detector Backgrounds

There were a number of low rate background sources associated with the detector. For signal extraction, the critical backgrounds were Cherenkov-like events and those associated with neutrons. The background values for the salt phase signal extraction are listed in Table 6.1. The photodisintegration background, one of the dominant sources in the detector, was calculated using the final *in situ* and *ex situ* assay measurements. The *ex situ* measurements determined the levels of U and Th via the water radiaoassay program. The *in situ* measurements determined the levels of U and Th using isotropy studies of the low energy events in the data set. There is a small difference in the isotropy of the events generated by the elements of the U and Th decay chains. One may use this difference to separate the detected low energy events into the contributions from the two chains. The *in situ* and *ex situ* results were combined to provide the best estimate of the U and Th levels in the detector. Knowing these levels, one could calculate the number of neutrons generated by these decays. This gave the largest number of internal background neutrons.

Other internal neutrons were generated by such sources as alpha decays, activated ^{24}Na (created in the D_2O as the water is recirculated through the heavy water systems), atmospheric and anti-neutrinos. In each case the neutron production rate was estimated using the predicted and, where possible, measured rates of each source. The total internal neutron background was approximately 111 events in the total

Background Source	Events
Internal-source Neutrons	
Deuteron photo-disintegration	$73.1^{+24.0}_{-23.5}$
^{2}H(α, α)pn	2.8 ± 0.7
^{17,18}O(α, n)	1.4 ± 0.9
Fission, atmospheric ν (NC + sub-Cherenkov threshold CC)	23.0 ± 7.2
Terrestrial and reactor anti-ν	2.3 ± 0.8
Neutrons from rock	≤ 1
^{24}Na activation	8.4 ± 2.3
n from CNO neutrinos	0.3 ± 0.3
Total internal neutron background	**111.3** $^{+25.3}_{-24.9}$
Internal Gammas	
fission, atmospheric ν	5.2 ± 1.3
^{16}N decays	< 2.5 (68% CL)
External-source neutrons	from the fit
Cherenkov events	
from β-γ decays	< 14.7 (68% CL)
"AV" events	<5.4 (68%)

Table 6.1: The salt phase signal extraction backgrounds. Internal neutrons are directly subtracted from the NC flux. Internal γs are backgrounds produced from spontaneous fission and atmospheric neutrinos. This type of background has been investigated and found to produce an insignificant effect on the extraction results. The external neutrons are permitted to float in the signal extraction, and are separated from the other fluxes primarily with the radial distribution. The Cherenkov and AV events are handled in the calculations of systematics.

data set of 3053 events, or about 3.6%. The internal neutrons must be subtracted from the total NC flux since there is no method available to distinguish between the neutrons produced by neutrinos and those generated by the backgrounds.

The rate of internal γ rays, discussed in chapter 5, was relatively small compared to other sources. These events were primarily produced from three sources in the detector; fission decays, atmospheric neutrinos and ^{16}N decays. The γ rate due to the fission decays was deduced using the measured detector levels of U and Th. Similarly,

the calculated rate of atmospheric neutrinos interactions in the detector was used to estimate the γ events produced. The ^{16}N can be produced in the detector from cosmogenic interactions on nitrogen present in the D_2O. The ^{16}N may then decay, producing γ rays, just as in the calibration source.

Also discussed in chapter 5 were the external neutrons, the number of which are determined in the signal extraction fit. It is believed radon was electro-statically attracted to the AV during the construction stage of the detector. Of the radon that decayed on the AV, some fraction of the long-lived daughter ^{210}Pb (22 year half-life) may have remained attached to the AV after cleaning. The ^{210}Pb may then alpha decay over the lifetime of the SNO experiment. Neutrons can be produced by (α, n) interactions in the acrylic.

The final background dealt with directly in this analysis was the "AV" or "Leslie" events. Although the true source of these events remained unknown, their characteristics were well defined. The light from Leslie events was highly isotropic, and the events were found to reconstruct near the AV. It was therefore possible to isolate the events in the data set and determine their numbers by direct counting. The resulting background value was treated as a systematic uncertainty on the final flux results.

6.2 The Signal Extraction Process

The primary components of the signal extraction for SNO included the set of PDFs to describe the data, the neutrino data set and the signal extraction (sig-ex) code. The development of the PDFs and the neutrino data set have been described above. This section describes the details of the sig-ex code.

The sig-ex code was composed of a series of modules that function together to complete the signal extraction process. The code was written to operate as an addi-

tion to the ROOT C++ analysis package. There were 4 primary modules (described below): the data controller, the PDF controller, the fitter and the control tools. Each module was a series of C++ classes designed to be independent of the others. Any code changes that needed to be adopted to handle changes in the detector could be made to the affected modules without needing to change the others.

Control Tools

The control tools were designed to behave as the interface between the other 3 modules. The primary user information, such as the high-level cuts to apply, the PDFs to use, and the location of the data files, was contained in a single card file. An example of a sig-ex card file is shown in Appendix C. The control tools loaded the information from the card file into a tree-type storage format (datatree). This format provided complete and easy access of the information to the other modules at all times.

Data Controller

The data controller module manipulated the raw data. The module acquired information it needed from the datatree, including the location of the raw datafile, the type of file the raw data was stored in and the cuts to be applied. The module applied the user defined cuts to the events in the datafile. Those events that pass the cuts were added, as histogram information, to the datatree created by the control tools. Again, once a part of the datatree, the event information was available to the other modules.

PDF Controller

The PDF controller module provided the code interface for the user supplied PDFs. This module also had the ability to generate a set of binned PDFs from a set of events when one wanted to include correlations between the event parameters in the signal extraction process. High level cuts were first applied to the PDFs to ensure the range of the functions are equivalent to those of the data set. The module then normalized the PDFs to unity to ensure each had equal total probability.

Fitter Module

The fitter module was designed to apply a user-given fitter function to the data events. The default function included in the sig-ex code was an unbinned extended maximum likelihood calculation. To develop this function, we began by observing the relation between the neutrino signal and the PDFs that represent the parameters for each event type. For each parameter (j), such as energy or isotropy, one could represent the total neutrino signal by summing over the event types,

$$A_j = \sum_{l=1}^{N} F_{l,j}\alpha_{l,j}, \tag{6.1}$$

where N is the number of event types (*eg* N=3 if one is only working with CC, NC and ES event types), F_i is the PDF for event type i, and α_i is the fraction of the total signal for the i^{th} event type.

A likelihood function may then be defined for these PDFs,

$$L = \prod_{k=1}^{n} A_{j,k} \tag{6.2}$$

where k runs through each event in the data set. In this definition, for a specific parameter (*eg* energy), the PDFs for each event type (*eg* CC) are evaluated for each event. This provides a probability for the event to belong to a particular event type.

The product of the probabilities in the equation is known as the joint probability for the PDF. We now define the log likelihood of equation 6.2 to obtain the familiar minimization equation

$$\log L = \sum_{k=1}^{n} \log(A_{j,k}). \tag{6.3}$$

We note here that to include all the available information in the fit, we must also sum over each of the parameter types (j). This alters the minimization equation to become

$$\log L = \sum_{k=1}^{n} \log \left(\sum_{j=1}^{M} A_{j,k} \right) \tag{6.4}$$

where M is the number of parameter types, equal to 4 when we use energy, isotropy, radial and angular PDFs in the fit. Performing a minimization with equation 6.4 returns the coefficients α_i for each event type.

In the situation where the number of events (n) in the data set are also Poisson distributed with a mean value of ϕ (in this case the total neutrino flux), the standard likelihood function (equation 6.2) may be modified to include the Poisson probability of obtaining n events from a flux of ϕ, generating the extended likelihood function

$$L = \frac{\phi^n}{n!} e^{-\phi} \prod_{k=1}^{n} A_{j,k}, \tag{6.5}$$

where both ϕ and A are functions of α. Again we take the logarithm to generate the minimization function

$$\log L = -\phi + \sum_{k=1}^{n} \log(\phi A_{j,k}), \tag{6.6}$$

where we have ignored the terms that are not dependent on α because in the minimization only terms with a first derivative in α will contribute.

Substituting equation 6.1 into equation 6.6, and including the summation over j as we did in equation 6.4 gives the final form for the unbinned extended maximum

likelihood function

$$\log L = -\phi + \sum_{k=1}^{n} \log \sum_{j=1}^{M} \left(\sum_{l=1}^{N} \phi \alpha_{l,j} F_{l,j} \right). \tag{6.7}$$

The resultant α terms, determined by minimizing the extended maximum likelihood function will be equivalent to the values returned using the standard likelihood function. However, the uncertainties on the fit parameters now include an uncertainty due to the Poisson fluctuation of the total number of events in the data set. That is, if the experiment were to be repeated numerous times, we have now included the estimate for the fluctuations in the α if the expected neutrino flux remains the same but the number of events in the data

A similar process may be used to develop a likelihood function for use with binned PDFs. In this case the number of events in a specific bin is ϕ_i,

$$\phi_i = n_{tot} \int_{x_i^{min}}^{x_i^{max}} A_{j,k} dx, \tag{6.8}$$

where ϕ_i and $A_{j,k}$ are functions of α, and the limits of the integral are the bin limits. Therefore, the probability to be in a certain bin is given by $\phi_i / \mathrm{n}_{tot}$. With this probability, the histogram can be represented as an P dimensional random vector, where P is the number of bins and with the joint probability density function given by a multinomial distribution,

$$A_{joint} = \frac{n_{tot}!}{n_1! ... n_P!} \left(\frac{\phi_1}{n_{tot}} \right)^{n_1} ... \left(\frac{\phi_P}{n_{tot}} \right)^{n_P}. \tag{6.9}$$

The logarithm of equation 6.9 gives the binned log-likelihood function

$$\log L = \log \left(\frac{n_{tot}!}{n_1! ... n_P!} \right) + \sum_{i=1}^{P} n_i \log(\phi_i) - n_i \log(n_{tot}). \tag{6.10}$$

As before, only the terms with dependence on α will contribute in the minimization process. Therefore, the log-likelihood function becomes

$$\log L = \sum_{i=1}^{P} n_i \log(\phi_i). \tag{6.11}$$

If the bin sizes are made very small, the result of minimizing equation 6.11 is equivalent to that for equation 6.3 of the unbinned case.

We would now like to extend the binned likelihood function to include the Poisson distribution as previously shown for the unbinned case. We must examine the case where the total number of entries ($n_{tot} = \sum_{i=1}^{P} n_i$) are a random variable for a Poisson distribution with a mean of $\phi_{tot} = \sum_{i=1}^{P} \phi_i$. The joint PDF then becomes

$$\begin{aligned} A_{joint} =& \frac{\phi_{tot}^{n_{tot}}}{n_{tot}!} \frac{n_{tot}!}{n_1!...n_N!} \left(\frac{\phi_1}{\phi_{tot}}\right)^{n_1} ... \left(\frac{\phi_N}{\phi_{tot}}\right)^{n_N} \\ =& \prod_{i=1}^{N} \frac{\phi_i^{n_i}}{n_i!} e^{-\phi_i}. \end{aligned} \tag{6.12}$$

We may then take the logarithm of equation 6.12 to determine the extended log-likelihood function for binned data,

$$\log L = -\phi_{tot} + \sum_{i=1}^{P} n_i \log(\phi_i). \tag{6.13}$$

Again, we have ignored the terms that have no dependence on α and therefore will not contribute to the minimization results. As one might expect, this function has the same form as the unbinned case described above. We also note that once again a summation over each of the parameter types (j), associated with the $A_{j,k}$ term in the definition of ϕ_i, is necessary to include all event information in the fit. A minimization of this function yields the most probable values for α_i, which gives the number of events in each class (CC, NC, ES and background).

Finally, it is possible to perform a chi-squared goodness of fit test on the fitter module results by comparing a summation of the original PDFs, weighted by the number of extracted events for each type, to the true neutrino event distribution.

Parameter	Cut Value
Energy	5.5 MeV <= T_{eff} <= 20 MeV
Radial	R_{fit} <= 550 cm
ITR	ITR >= 0.55
β_{14}	-0.12 <= β_{14} <= 0.95

Table 6.2: The salt phase signal extraction high level cuts. Note that energy is estimated using the RSP processor in SNOMAN.

6.3 Parameters Used in the High-Level Cuts

The high-level cuts, applied to the data set prior to performing the signal extraction process, are shown in Table 6.2. We note that the energy cut is defined by T_{eff} (the kinetic energy of the events), which was determined by subtracting the electron rest mass from the fit RSP energy. The radial, ITR and β_{14} parameters were defined as we discussed in detail in chapter 5.

The selected cuts represent the parameter space where the events were most likely to be neutrino events as opposed to backgrounds. For instance, a higher radial cut allowed a much larger number of external background and Leslie events to enter the dataset. Similarly, a lower kinetic energy threshold provided a larger number of neutrino events, but also placed the cut very close to the fast rising background wall. This made it very difficult to estimate backgrounds in the signal region. The β_{14} cut space was chosen to minimize the loss of neutron events from the data set while limiting the addition of Leslie events. Finally, the ITR cut effectively ensured the passed events have hit PMTs that were primarily a part of the prompt time peak. This is the type PMT timing one expected from Cherenkov events with the typical cone of photons. These cuts, in conjunction with the low level cuts, provided a "clean" neutrino data set containing 3053 events for the salt phase analysis.

6.4 Fit Results

We have developed 1D parametric PDFs for each parameter of each event type to be extracted. There are small correlations between the parameters and these correlations can affect the extracted fluxes and statistical uncertainties. The default SNO analysis used binned 2D PDFs of T_{eff} versus β_{14} to account for the largest of the correlations. An alternate method, that we applied here, was to determine the correlations using the MC data set to build correlation matrices of the parameters. This was done by comparing all parameters event by event.

The correlations between parameters may be included by converting the joint probabilities of the likelihood function (discussed in the previous sections) to Gaussian correlated (GC) joint probabilities. The method to develop the GC joint probabilities begins with a joint PDF, $P(x_1x_2)$, that is defined to be normalized to unity,

$$\int\int P(x_1x_2)dx_1dx_2 = 1. \tag{6.14}$$

One may create marginal PDFs by projecting the joint PDF onto the x_1 and x_2 axes, giving

$$p(x_1) = \int P(x_1x_2)dx_2 \tag{6.15}$$

and

$$p(x_2) = \int P(x_1x_2)dx_1. \tag{6.16}$$

In this definition, x_1 and x_2 are independent if and only if

$$P(x_1x_2) = p(x_1)p(x_2). \tag{6.17}$$

When this condition is true equation, that is when the parameters are uncorrelated, equation 6.17 may be expanded to use any number of PDFs. For the situation where one was performing signal extraction for CC, NC and ES events only, the joint PDF would have the form

$$P(x_1, x_2, x_3) = p(x_1)p(x_2)p(x_3). \tag{6.18}$$

In the original x-space the parameters are correlated. We therefore wish to make a rotation to a coordinate system (y) where the variables are uncorrelated such that we may employ equation 6.18. This may be accomplished in the y-space by using a normal Gaussian distribution function, with

$$g(y)dy = p(x)dx. \tag{6.19}$$

For y being monotonic and invertible, the joint PDF P($\vec{x}$) is related to the $\vec{y}$ joint PDF, G($\vec{y}$), by

$$P(\vec{x}) = G(\vec{y})\,|J|\,. \tag{6.20}$$

where $|J|$ is the absolute value of the Jacobian determinant for the transformation from x to y space,

$$|J| = \prod_{i=1}^{n} \frac{\partial y_i}{\partial x_i} = \prod_{i=1}^{n} \frac{p(x_i)}{g(y_i)}. \tag{6.21}$$

The variable $G(\vec{y})$ in equation 6.20 is the n-dimensional Gaussian probability distribution centered at the origin,

$$G(\vec{y}) = (2\pi)^{-n/2}\,|U|^{-1/2}\,e^{-\frac{1}{2}\vec{y}^T U^{-1}\vec{y}}. \tag{6.22}$$

Here U is an n x n covariance matrix (U_{ij}=cov$[y_i, y_j]$) and $|U|$ is the determinant.

The variables in $\vec{x}$ are not typically Gaussian distributed, while the parameter transformation $y_i(x_i)$ has individual Gaussian distributions (y_i) and therefore the variables for $\vec{y}$ are well approximated. We use this information to create better described joint PDFs for the $\vec{x}$ variables where the new PDF is written as a correction to the original,

$$P'(\vec{x}) = c(\vec{x})P(\vec{x}) \tag{6.23}$$

where $c(\vec{x})$ is a correction factor. $P'(\vec{x})$ is again related to the y-space parameters via the Jacobian of the transformation from x to y,

$$P'(\vec{x}) = G(\vec{y})\,|J|\,. \tag{6.24}$$

With appropriate substitutions, equation 6.23 becomes

$$G(\vec{y}) \prod_{i=1}^{n} \frac{p(x_i)}{g(y_i)} = c(\vec{x}) \prod_{i=1}^{n} p(\vec{x}). \tag{6.25}$$

Simplifying, the correction term $c(\vec{x})$ is the ratio of the Gaussian distributions,

$$c(\vec{x}) = \frac{G(\vec{y})}{\prod_{i=1}^{n} g(y_i)}. \tag{6.26}$$

We note that $g(y_i)$ is a unit Gaussian function with mean of 0 and sigma of 1, represented by

$$g(y_i) = \frac{1}{\sqrt{2\pi}} e^{-x^2/2}. \tag{6.27}$$

Substituting the value for $c(\vec{x})$, $G(\vec{y})$ and $g(y_i)$ into equation 6.23, the final form of the Gaussian-correlated joint PDF becomes

$$P'(\vec{x}) = \frac{e^{-\frac{1}{2}\vec{y}^T(U^{-1}-I)\vec{y}}}{|U|^{1/2}} \prod_{i=1}^{n} p(x_i). \tag{6.28}$$

Using the correlation matrices produced from looking at the MC events, for each flux type, the correlated joint PDFs were used in the extended likelihood minimization. We then had the full correlations of the parameters accounted for, with the use of 1D PDFs. This was especially convenient when working with a limited MC dataset, where the statistics may be insufficient to build the necessary multi-dimensional PDFs to account for all the correlated parameters. We note, however, that this method provided only an approximation, albeit a good approximation, and may only be used when the correlations between the parameters are small. The best possible result will always be achieved when using multi-dimensional PDFs of the parameters.

Using the sig-ex code described above and the 1D binned PDFs (with or without correlations), the number of each event type was extracted (see Table 6.3). The fit produced correlation matrices with values for each of the event types, shown in Tables

Event Type	Number of Events-No Correlations	Number of Events-Correlations
CC	$1413.0\ ^{+53.8}_{-52.9}$	$1420.1\ ^{+54.9}_{-54.0}$
NC	$1283.3\ ^{+60.8}_{-59.7}$	$1268.0\ ^{+60.3}_{-59.3}$
ES	$166.8\ ^{+21.6}_{-20.7}$	$162.5\ ^{+22.2}_{-21.1}$
Ext n	$72.5\ ^{+34.3}_{-33.5}$	$89.5\ ^{+32.9}_{-32.1}$

Table 6.3: The signal extraction results for 1D parameterized binned PDFs. Displayed are the results for the cases of including and not including the correlations between the event types. Only statistical uncertainties are listed.

	NC	CC	ES	Ext-n
NC	1.0	-0.377	-0.070	-0.452
CC	-0.377	1.0	-0.203	-0.050
ES	-0.070	-0.203	1.0	-0.007
Ext-n	-0.452	-0.050	-0.007	1.0

Table 6.4: The correlation matrix as a result of the extended maximum likelihood fit. The fit to the salt data is performed using the correlated 1D parametric PDF method discussed in this thesis. There are strong anti-correlations between CC-NC events and NC-External neutron events. This implies events will tend to be moved in or out of the NC category and into the CC and external neutron categories.

6.4 and 6.5 for the correlated and uncorrelated PDF fits, respectively. The differences in these tables were due to the inclusion of the correlations between the parameter PDFs, using the covariance matrices in Appendix C. For the correlated PDF signal extraction, those covariance matrices were used in equation 6.28 to generate the Gaussian-correlated joint PDFs. When performing the fit, the strong correlations moved events from the NC type to CC and external neutrons. We note that a chi-squared goodness of fit test (discussed later) was applied to ensure the best fit results were obtained.

When working with the PDFs it must be decided whether to use binned or unbinned in the signal extraction. This analysis presents results with PDFs having 1000 bins in the parameter ranges. This was the criteria applied when developing the

	NC	CC	ES	Ext-n
NC	1.0	-0.358	-0.039	-0.505
CC	-0.358	1.0	-0.202	-0.028
ES	-0.039	-0.202	1.0	-0.002
Ext-n	-0.505	-0.028	-0.002	1.0

Table 6.5: The correlation matrix as a result of the extended maximum likelihood fit. The fit is performed using the uncorrelated 1D parametric PDF method discussed in this thesis on the salt data set. Note the large change in correlation between the NC and external neutrons compared to Table 6.4.

Number of Bins	CC Events	NC Events	ES Events	Ext n Events
100	1413.0	1283.3	166.8	72.5
1000	1413.0	1283.3	166.8	72.5
3600	1412.4	1285.6	166.1	74.9
Function	1413.4	1286.7	165.0	74.3

Table 6.6: The signal extraction results with a varying number of bins in the PDFs. For the smooth parametric functions there is very little difference observed between binned and unbinned PDF extracted fluxes.

PDFs for the signal extraction process prior to the time when the blindness criteria was removed from the salt data set. In order to eliminate the possibility of creating a biased result with the open data analysis, the same PDF binning was used for the final results. It is possible, however, that uncertainties may arise in the the analysis based upon the choice of binning. Hence, a study of the number of extracted events as a function of the number of bins, for sets of parameters, was completed, and the results are shown in Table 6.6. It becomes clear that the results for 1000 bins give very small differences to those of unbinned PDF distributions, with a maximum change of 0.4% for NC events, 2.4% for external neutrons and 1% for ES events.

The goodness of the likelihood fit results, including correlations of the PDFs, was determined by comparing the extracted event rates for the appropriate PDFs, to the

Parameter	Reduced Chi-Squared
Energy	1.051
β_{14}	1.456
$\mathrm{Cos}(\theta_{Sun})$	1.165
Radial	1.038

Table 6.7: The comparison of extracted results to neutrino data distributions using a Chi-Squared goodness-of-fit test. Note the reduced chi-squared calculation for the radial distribution does not include the end-point bins (at 0 and 0.77).

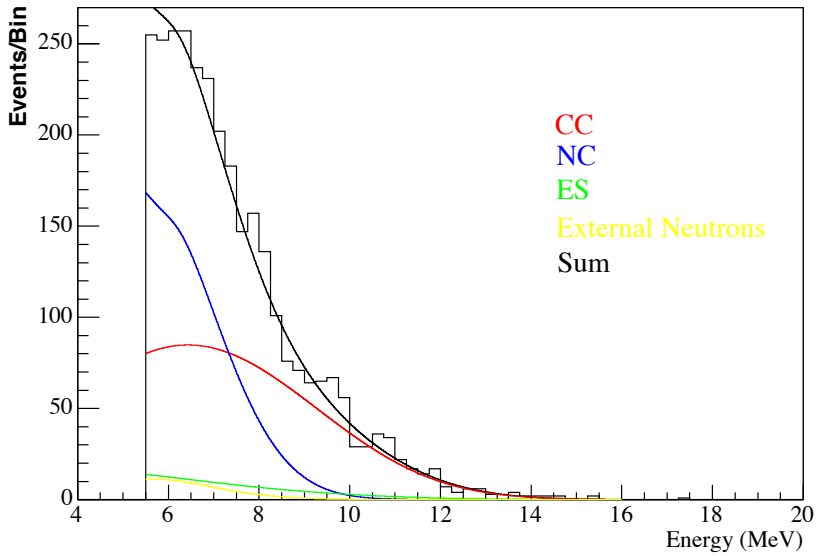

Figure 6.1: A comparison of the extracted energy distributions to the neutrino data. The histogram shows the binned neutrino data. The "Sum" curve is the expected energy distribution from summing the event type PDFs weighted by the fractional contribution to the total signal, as determined by the fit.

neutrino data distributions. The comparisons are shown in Figures 6.1 to 6.4, and the agreement is quite good, as shown by the chi-squared test results in Table 6.7.

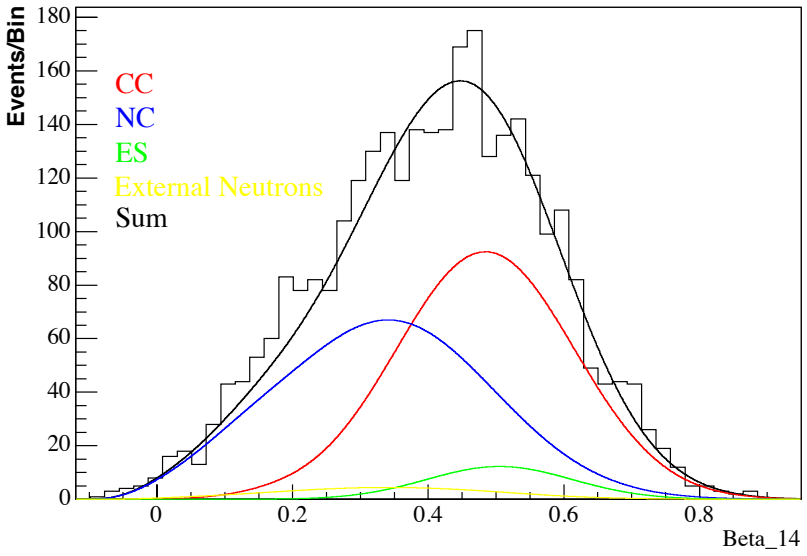

Figure 6.2: A comparison of the extracted isotropy distributions to the neutrino data. See the caption of Figure 6.1 for the details of the plot.

6.5 Systematic Uncertainties

There were a number of systematic uncertainties associated with the signal extraction process, including those generated by parameterizing the MC distributions, and in the determination of the detector response functions. The sections below contain the details of determining each of the systematic uncertainties.

6.5.1 Systematic Error Attributable to Parameterization of PDFs

There were systematic uncertainties associated with the parameterization of the MC distributions, used as the PDFs in the signal extraction. To determine these uncertainties, we began with the best fit parameters of the parameterization functions.

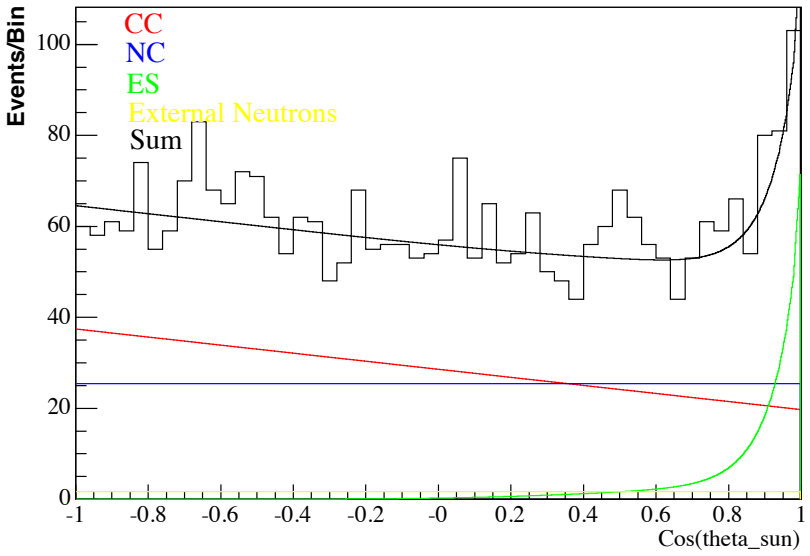

Figure 6.3: A comparison of the extracted angular distributions to the neutrino data. See the caption of Figure 6.1 for the details of the plot.

With uncorrelated parameters, the normal technique to determine the systematic uncertainty would be to determine how much each parameter needs to move in order to shift the χ^2 by 1 (*ie* a change of 1 sigma). For correlated parameters, one needs to shift all values in a way that produces a total shift of 1 sigma.

For each parameterization , such as the CC energy spectrum that used a 2 Gaussian representation, the fit determined a covariance matrix between the parameters. The best fit parameters were stored in a vector and, along with the covariance matrix, submitted to CERNLIB routines called CORSET and CORGEN [42]. These routines are designed to produce correlated Gaussian-distributed random numbers where, in this case, the random numbers are confined to the 1 σ range of each parameters error. The CORSET routine converted the covariance matrix to a square-root matrix (described in [42]) and the square-root matrix was passed to the CORGEN

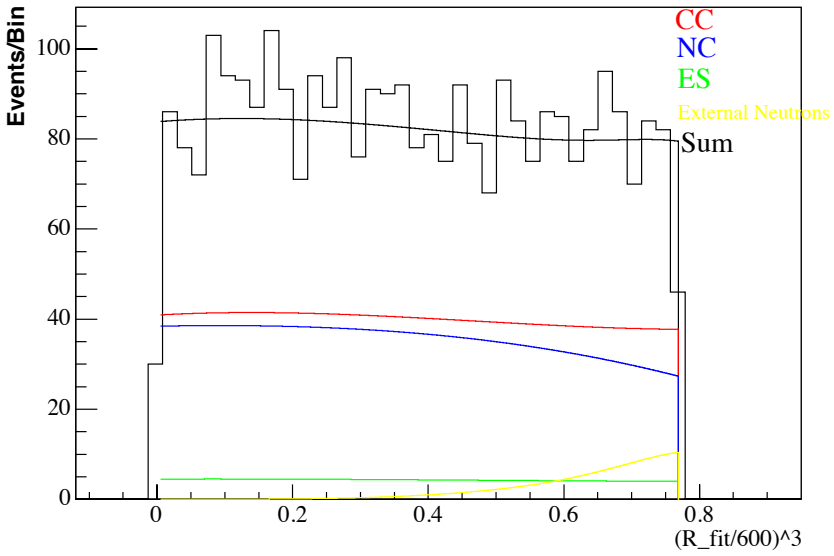

Figure 6.4: A comparison of the extracted radial distributions to the neutrino data. See the caption of Figure 6.1 for the details of the plot.

routine. CORGEN used a Gaussian random number generator to produce a vector, with length the same as the number of parameters, of random numbers between zero and one. The vector was multiplied by the square-root matrix from CORSET, and the result was a vector containing correlated Gaussian-distributed random numbers. This vector was used to shift the parameter values away from the best fit result, producing a new parameterized function.

A set of 750 of these vectors were generated and used to produce a set of "shifted" PDFs. The shifted PDFs were used in place of the original (best fit) PDFs in the signal extraction, producing new values for the number of extracted events. The result of this ensemble test was a set of histograms with an arithmetic RMS that represented the uncertainty in the signal extraction due to the parameterization of the PDFs (see figures in Appendix C). As an example, the systematic uncertainties

Event Type	Parameter	Mean	RMS
CC	β_{14}	1413.0	0.8821
	$\cos(\theta_{sun})$	1412.0	0.6635
	energy	1418.0	8.768
	radius	1413.0	0.1049
NC	β_{14}	1283.0	1.577
	$\cos(\theta_{sun})$	1283.0	0.0001
	energy	1281.0	6.917
	radius	1283.0	2.554
ES	β_{14}	175.2	0.1971
	$\cos(\theta_{sun})$	166.8	0.5234
	energy	166.5	0.6159
	radius	166.9	0.6836

Table 6.8: The PDF systematic uncertainties derived from an ensemble test of shifted parameter PDFs.

for the CC event PDFs are shown in Table 6.8. The values in this table were converted to percentage uncertainties (see Table 6.9) and added in quadrature with the other signal extraction systematic uncertainties.

6.5.2 Systematic Errors Arising from Uncertainties in the Detector Response Functions

There were also systematic uncertainties associated with each of the detector responses listed in table 6.10. To determine the response values and the associated uncertainties, one used calibration sources and the MC. For instance, the uncertainties on the energy scale and resolution were derived from studies of the ^{16}N source [9]. The systematic on the neutron efficiency was determined from the uncertainty associated with the ^{252}Cf source [47]. Uncertainties of the isotropy parameters were obtained by comparing the MC distributions with the data from both the ^{16}N and ^{252}Cf calibration sources [24]. The uncertainty on the event vertex was determined

Parameter	Systematic Uncertainty (%)
CC β_{14}	6.2e-2
CC $\cos(\theta_{sun})$	4.7e-2
CC Energy	0.618
CC Radial	7.4e-3
CC PDF Total	0.623
NC β_{14}	0.123
NC $\cos(\theta_{sun})$	8.9e-6
NC Energy	0.540
NC Radial	0.199
NC PDF Total	0.589
ES β_{14}	0.112
ES $\cos(\theta_{sun})$	0.313
ES Energy	0.370
ES Radial	4.10e-2
ES PDF Total	0.499

Table 6.9: The PDF systematic uncertainties for each of the event types. The total uncertainties for each event type are the sum (in quadrature) of the systematic uncertainties for each PDF parameter.

with MC studies using the difference between the generated and fit positions [56].

To determine the effect of the systematic uncertainties on the signal extraction results, the MC distributions were "adjusted" according to the values in Table 6.10 to generate a new set of PDFs. For example, 2 energy scale uncertainty PDF distributions were generated by shifting the energy of each MC event by $\pm 1.09\%$. The new MC energy distribution were parameterized using the same functions described in chapter 5. Each of the new PDFs were applied in independent passes of the signal extraction process. The difference between the extracted fluxes, using the best fit PDFs, and those associated with the systematic uncertainties was calculated. This gives the systematic error on the flux.

The resolution uncertainties were determined by applying a Gaussian smearing to each of the MC events. The Gaussian smearing used the parameter value of the event

Parameter	Uncertainty
Energy scale	± 1.09 %
Energy non-linearity	± 0.25% at 20 MeV
Energy resolution	± (0.035 + 0.00471(T_{eff} - 5.5 MeV)) for T_{eff}>5.5 MeV ± 0.035 for T_{eff}<5.5 MeV
Radial energy bias	± 1%, linear from 0 to 550 cm
Vertex X accuracy	± 2 cm
Vertex Y accuracy	± 2 cm
Vertex Z accuracy	± 6 cm
Vertex radial accuracy	± 1% of R
Vertex resolution	15%
Angular response (β_S)	9.5%
Angular response (β_M)	4.2%
Angular response (α)	11%
Isotropy mean	0.87%
Isotropy sigma	0.97%
Neutron efficiency	+2.7%, -2.5%

Table 6.10: The flux systematic uncertainties for detector response functions [67]. The size of the uncertainties are obtained from the SNOMAN MC and calibration source data.

as the mean, and shifted the event by a Gaussian-distributed random number with the width of the Gaussian distribution equal to the size of the resolution uncertainty. The smeared events produced a new MC distribution that was parameterized to provide a new PDF for the sig-ex code.

The results for all detector response functions are shown in Table 6.11. These values were converted to percentage uncertainties, based on the deviation from the best fit value, and are listed in Table 6.12. The largest systematics were due to the energy scale (for CC and NC events) and the isotropy mean.

The final systematic uncertainties associated with the signal extraction of the salt phase data set are shown in Table 6.13. Note we made the conservative estimate that the uncertainties associated with the detector parameters were uncorrelated with

Parameter	CC	NC	ES
Best fit	1413.0	1283.3	166.81
Energy scale (high)	1376.1	1319.8	167.2
Energy scale (low)	1448.7	1247.9	166.7
E nonlinearity (high)	1410.3	1285.9	166.9
E nonlinearity (low)	1409.4	1286.8	166.9
E radial bias (high)	1435.1	1261.1	167.1
E radial bias (low)	1389.1	1307.2	166.9
Energy resolution	1393.4	1302.7	167.1
Vertex accuracy X (high)	1412.9	1283.3	166.9
Vertex accuracy X (low)	1413.0	1283.1	166.9
Vertex accuracy Y (high)	1413.0	1283.2	166.9
Vertex accuracy Y (low)	1413.0	1283.2	166.9
Vertex accuracy Z (high)	1413.0	1281.2	167.0
Vertex accuracy Z (low)	1412.8	1286.3	166.9
Vertex resolution	1414.4	1281.7	167.0
Vertex radial acc (high)	1413.0	1281.2	167.0
Vertex radial acc (low)	1411.1	1285.6	167.0
Isotropy mean (high)	1397.9	1291.8	173.5
Isotropy mean (low)	1450.7	1235.3	177.2
Isotropy sigma	1427.7	1260.0	175.6
Angular resolution	1418.2	1284.0	161.0

Table 6.11: The extracted number of events for each event type, for each of the systematic uncertainties in table 6.10. The largest changes are observed in the isotropy parameters and the energy scale.

those associated with the parameterization of the PDFs. Hence, the uncertainties were added in quadrature to determine the total systematic uncertainties for the salt phase fluxes.

Radiative Corrections

At this point, we have determined the number of events of each event type observed by the SNO detector. The flux from the Sun was determined from the number of events through the use of cross sections for the CC, NC and ES neutrino interac-

Parameter	CC (%)	NC (%)	ES (%)
Energy scale	+2.61,-2.53	+2.76,-2.84	+0.066,-0.23
E nonlinearity	+0.25,-0.00	+0.00,-0.27	+0.0,-0.054
E radial bias	+1.69,-1.56	+1.73,-1.86	+0.00,-0.17
Energy resolution	± 1.39	± 1.51	± 0.17
Vertex accuracy X	+0.0071,-0.00	+0.016,-0.00	+0.00,-0.054
Vertex accuracy Y	+0.00,-0.00	+0.0078,-0.00	+0.00,-0.054
Vertex accuracy Z	+0.014,-0.00	+0.16,-0.23	+0.00,-0.11
Vertex resolution	± 0.099	± 0.13	± 0.11
Vertex radial acc	+0.13,-0.00	+0.16,-0.18	+0.00,-0.11
Isotropy (β_{14}) mean	+3.74,-0.66	+0.66,-3.74	+0.00,-6.23
Isotropy (β_{14}) sigma	± 1.82	± 1.82	± 5.27
Angular resolution	± 0.37	± 0.055	± 3.48
Neutron Efficiency	± 0.00	+2.7,-2.5	± 0.00
Internal background n	± 0.00	+1.97,-1.94	± 0.00
Cherenkov backgrounds	+0.00,-1.1	+0.00 -1.1	± 0.00
"AV events"	+0.00,-0.4	+0.00,-0.4	± 0.00
Total	+3.75,-4.53	+6.44,-5.40	+6.32,-8.88

Table 6.12: The flux systematic errors, quoted in terms of percentage errors. Note that this table is an expansion of Table 6.11 to include the percentage uncertainties of the backgrounds from Table 6.1. The total uncertainty on the flux due to the measured detector parameters is the quadrature sum of all entries in this table.

Parameter	CC (%)	NC(%)	ES (%)
Total PDF	± 0.62	± 0.59	± 0.50
Total Detector	+3.75,-4.53	+6.44,-5.40	+6.32,-8.88
Total Systematics	+3.80,-4.57	+6.49,-5.43	+6.34,-8.89

Table 6.13: The total flux systematic error. The detector and PDF systematic uncertainties are assumed to have no correlations and are therefore conservatively added in quadrature.

tions in the SNO detector (shown in the Feynman diagrams in Figures 2.4 to 2.6). The effect on the systematic uncertainties for including these cross sections in the analysis are dealt with later in this chapter. Here we deal with the corrections to

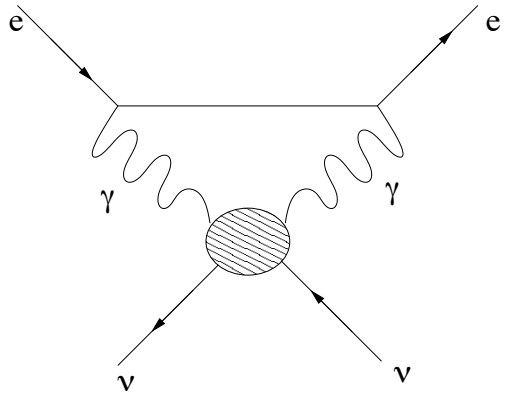

Figure 6.5: ES Feynman Diagram with Radiative Term

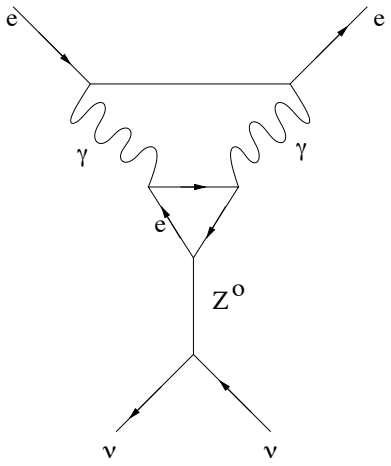

Figure 6.6: ES Feynman Diagram with Radiative Term

these cross sections, known as radiative correction, that arise because of interactions that include virtual γ rays at the vertexes (see examples of these higher-level interactions in the Feynman diagrams 6.5, and 6.6). As a result of the virtual γs, there is a change in the interaction cross-section that leads to different probabilities for detection. This effectively changes the energy spectrum of the observed interactions, although the effect is very small ($\geq 2^{nd}$ order).

Parameter	Correction Factor
CC	1.0318 - 7.45e-4(T_{eff}+0.511) + 4.72e-6(T_{eff}+0.511)^2
ES	0.9764 - 7.81e-4T_{eff} - 1.31e-4T_{eff}^2 + 3.64e-6T_{eff}^3
NC	1.0154

Table 6.14: The radiative correction expressions applicable to the SNO MC events [67].

Parameter	CC	NC	ES
Extracted Events	1376.7	1319.3	167.2
Percentage Uncertainty	2.57%	2.80%	0.18%
Percentage change	0.04%	0.04%	0.06%

Table 6.15: The energy scale (high) systematic uncertainty for applying radiative corrections. The percentage uncertainty listed in the table is the value based on the number of extracted events with the radiative correction applied compared with the best fit value in Table 6.11. The percentage change is the difference between the percentage uncertainty with and without radiative corrections for the energy scale (high) systematic.

The MC events were generated without the higher-level interaction cross-sections included in the calculation of the event rates and energy spectrum. We considered the effect of the radiative corrections by re-weighting the MC distributions with the correction factors given in Table 6.14. The effect on the extracted signal of re-weighting the MC was determined by constructing a new set of PDFs for one of the studied systematic uncertainties, and examining the change in the number of extracted events. This test was carried out for the energy scale (high) systematic uncertainty, and the results are shown in Table 6.15. The change was approximately 0.05% for one of the largest systematic uncertainties and the radiative corrections were considered to have a negligible effect on the calculation of final systematic uncertainties.

Signal Extraction	CC	NC	ES	Ext-n
Constrained Analysis	$1430.3^{+55.5}_{-54.6}$	$1265.8^{+61.3}_{-62.3}$	$163.7^{+22.4}_{-21.5}$	$79.7^{+34.2}_{-33.3}$
Unconstrained Analysis	$1339.6^{+63.8}_{-61.5}$	$1344^{+68.8}_{-69.0}$	$170.3^{+23.9}_{20.1}$	$84.5^{+34.5}_{-33.6}$
Correlated Parametric PDFs	$1420.1^{+54.9}_{-54.0}$	$1268.0^{+60.3}_{-59.3}$	$162.5^{+22.2}_{-21.1}$	$89.5^{+32.9}_{-32.1}$

Table 6.16: The total extracted events for each of the different event types. The constrained and unconstrained results come from the SNO default analysis. The correlated parametric PDFs results are the best fit values obtained from the work described in this thesis. Very good agreement is observed between the constrained analysis using the SNO default method, and the method developed in this thesis.

6.6 Comparison Between the Default and Thesis Analyses

The salt data set was analyzed by the SNO collaboration using what we call the default analysis. That analysis produced both energy constrained and unconstrained results. The energy constrained results were directly comparable to those of the pure D_2O phase. In the salt phase, the default analysis used a 2D PDF for β_{14} and T_{eff}, and 1D PDFs for the radial and $\cos(\theta_{sun})$ distributions. Therefore, the correlations between β_{14} and energy were accounted for, but the small correlations between the other parameters were not taken into account. In the pure D_2O data, there was very little difference between the isotropic distributions of the CC and NC events. Under these conditions it was necessary to use the energy distributions to obtain a good fit with low uncertainties. However, in the salt phase, the isotropy parameter gave better separation between the CC and NC events, and so it was possible to make fits without using the energy spectra. These were the so called unconstrained analyses. In an unconstrained fit, no assumptions about the shape of the ^8B are made. The work in this thesis was limited to a constrained analysis only. The results of the various analyses are shown in Table 6.16.

Variable	Value
^{8}B flux	5.15 x 10^6 cm^{-1}s^{-1} [75]
^{8}B Shape	Ortiz [58]
CC cross section	Butler [13]
Raw Live time	258.792 days

Table 6.17: The SNOMAN MC inputs for determining the predicted SSM event rates.

6.6.1 Flux Determination

The next step was to convert the number of extracted events into a solar neutrino flux. When the MC generated CC, NC and ES events, it used the predicted Standard Solar Model (SSM) flux, the best available measurements of the cross-section, and the ^{8}B shape as inputs (see Table 6.17). The MC therefore produced neutrino events at the same rate, with the same energy spectrum, as the expected solar neutrino flux. By normalizing to the MC data we may determine the solar neutrino fluxes. For this method to accurately predict the expected flux for each neutrino event type, a series of corrections must be applied.

To begin with, the high level cuts were applied to the MC data set. This ensured the events cover the same range of energy and volume (due to the use of energy threshold and fiducial volume cuts) as the neutrino data. The MC data set was many orders of magnitude larger than the neutrino data set, so that one may complete various statistical studies. Hence, the MC data set has to be reduced, so that the size was statistically equivalent to that expected for the neutrino live time. This involved dividing the number of MC events by the MC statistical factor (typically 200 times the expected SSM rate) for CC and ES events, or multiplying the neutron production rate by the correct neutrino data set live time for NC events. The MC was a very complete description of the SNO detector. However, there were a number of parameters that were not known exactly when the code was run, or which had varied

Variable	CC	NC	ES
^{8}B flux	0.9806	0.9806	0.9806
Orbital Eccentricity	1.0	0.99818	1.0
CC on ^{17}O and Na	1.0081	1.0	1.0
Number of deuterons	1.01228	1.0	1.0
Number of electrons	1.0	1.0	1.0151
Sacrifice	0.9943	0.9932	0.9914
Geometry errors	1.00534	1.0	1.004538
coupling constant (g_A=1.267)	1.0111	1.0111	1.0
Radiative corrections	(wCC)	1.0154	(wES)
Weak Axial Exchange Current (L1A)	0.984	0.979	1.0
Live time	0.9821	0.9821	0.9821
ϵ_{cor}	0.9774(wCC)	0.9771	0.9736(wES)

Table 6.18: The corrections to the MC PDFs for the SSM event rate prediction. The correction to the ^{8}B flux is due to the difference between using the flux predicted by Bahcall and Pinsonneault in 2000 (BP2000) [7] and 2002 (BP2002) [75]. The terms wCC and wES are equivalent to the weights for CC and ES PDFs given in table 6.14, and therefore are different for each event based on kinetic energy. These corrections are not a part of the original MC generation and are necessary to produce accurate predictions for the neutrino flux rates in the detector.

since. Small corrections to the MC data set, either due to improved information on the original MC inputs such as the corrected live time or missing information in the MC such as the radiative corrections, were thus required. These corrections are listed in Table 6.18.

Using the above information, we can determine the number of each event type expected from the SSM based on the equations

$$N_{CC}^{model} = \sum_i N_{CC}^{MC}(aftercuts)\frac{1}{f_{CC,i}}\epsilon_{cor}^{CC} \tag{6.29}$$

$$N_{NC}^{model} = R_{NC}L_{ds}\epsilon_{cor}^{NC}\epsilon_n^{cuts} \tag{6.30}$$

$$N_{ES}^{model} = \sum_i N_{ES}^{MC}(aftercuts)\frac{1}{f_{ES,i}}\epsilon_{cor}^{ES}. \tag{6.31}$$

The value of each of the variables in these equations are defined in table 6.19. The

Variable	Value
$f_{CC/ES,i}$	200.0 for i=^{8}B; 2000.0 for i=hep
R_{NC}	13.171489 per day for SSM ^{8}B and hep n rate from SNOMAN
L_{ds}	corrected live time = 254.158 days
ϵ_n^{cuts}	0.399 for neutron detection efficiency after cuts
ϵ_{cor}	PDF scale correction, see table 6.18

Table 6.19: The values of the variables appearing in equations 6.29 to 6.31. The terms $f_{CC/ES,i}$ are the number of SSM rates for which the MC has been generated, *eg* 200.0 for the ^{8}B neutrinos and 2000.0 for the hep neutrinos. Note we assume all neutrinos are ν_e for CC and ES events. R_{NC} is the neutron rate per day as calculated by SNOMAN for one SSM neutrino flux.

Variable	CC	NC	ES
SSM predicted number	4248.90	1304.11	389.18

Table 6.20: The SSM predicted event rates. These rates represent the neutrino flux of each event type, assuming no neutrino oscillations, for the corrected salt phase live time.

expected ^{8}B flux of each interaction type, assuming the full SSM is shown in Table 6.20.

Using the values given in Table 6.20, the measured flux for each event type was determined and compared to the number of extracted events in Table 6.16. Using the BP2000 predicted flux of 5.05 x 10^6, and the ratio of measured to expected events, we calculated the fluxes given in Table 6.21. When calculating the expected rates, we have used the cross sections supplied by Butler *et al*, and therefore have introduced a systematic uncertainty that arises from the uncertainties in the theoretical calculations of the cross section for each of the interactions. The uncertainties (shown in Table 6.22) were added in quadrature with the total systematic uncertainties in Table 6.13 to produce the total systematic error on the flux. Note that the CC and ES rates are low relative to the predictions for the full SSM, in agreement with the

Parameter	Flux (10^6 cm^{-2}s^{-1}) (Default)	Flux (10^6 cm^{-2}s^{-1}) (Thesis)
CC	1.70 ± 0.07(stat) $^{+0.09}_{-0.10}$(syst)	1.69 ± 0.07(stat) $^{+0.07}_{-0.08}$(syst)
NC	4.90 ± 0.24(stat) $^{+0.29}_{-0.27}$(syst)	4.91 ± 0.23(stat) $^{+0.32}_{-0.27}$(syst)
ES	2.13 $^{+0.29}_{-0.28}$(stat) $^{+0.15}_{-0.08}$(syst)	2.11 $^{+0.29}_{-0.27}$(stat) $^{+0.13}_{-0.19}$(syst)

Table 6.21: Comparison of the extracted model-constrained neutrino flux from the SNO default analysis (Default) and the correlated parametric 1D PDF result (Thesis). The thesis results show slightly better statistical and systematic uncertainties when compared with the default analysis.

Variable	CC	NC	ES
Cross Section Uncertainty	1.3%	1.1%	0.5%

Table 6.22: The cross-section systematic uncertainty, from [13].

solar neutrino deficit. On the other hand, one sees already the good agreement of the NC result, showing that the total flux of neutrinos is as expected. Hence, the missing neutrinos are of a different flavour. The results also show excellent agreement between the default SNO results and the results of this independent analysis with parametric 1D PDFs.

6.6.2 CC/NC Flux Determination

The CC/NC ratio was determined by dividing the flux values in Table 6.21 and gave a result of 0.344. The fact this result was not equal to 1 was a clear demonstration that the total solar neutrino flux is different from the ν_e flux. This implies neutrinos change flavor following the production of ν_e in the Sun. The systematic and statistical uncertainties for CC/NC required a new set of calculations. If we include the correlations between the event types, and the correlations were positive, a number of the systematic uncertainties reduce in the ratio.

The statistical uncertainty for the CC/NC ratio was determined using

$$\sigma_q^2 = (\frac{\partial q}{\partial x})^2\sigma_x^2 + (\frac{\partial q}{\partial y})^2\sigma_y^2 + 2\frac{\partial q}{\partial x}\frac{\partial q}{\partial y}\sigma_{xy}. \tag{6.32}$$

Here q is given by $q = x/y = N_{CC}/N_{NC}$, where N_{CC} and N_{NC} are the extracted number of CC and NC events respectively. Substituting for q and equating σ_{xy} to the covariances between CC and NC, determined from the maximum likelihood fit, equation 6.32 becomes

$$\sigma_q^2 = \frac{\sigma_{Ncc}^2}{N_{NC}^2} + \frac{N_{CC}^2}{N_{NC}^4}\sigma_{N_{NC}}^2 - 2\frac{N_{CC}}{N_{NC}^3}cov(N_{CC}, N_{NC}), \tag{6.33}$$

where the value of $cov(N_{CC}, N_{NC})$ is -0.377 from Table 6.4. This produces a statistical uncertainty for CC/NC of +6.13%,-6.03%.

There are 2 primary issues one must consider in calculating the set of systematic uncertainties for the CC/NC ratio, namely the correlations between the event types and dealing with the asymmetric errors. In the constrained analysis we developed, the CC and NC events were strongly anti-correlated. The anti-correlation was attributed to using the energy distributions in the signal extraction. In this constrained analysis we observed an increase in the combined systematic uncertainties due to the negative correlations (see below). The SNO default unconstrained analysis, performed without the energy PDFs, observed a positive correlation between CC and NC events and therefore a reduction in a large number of the systematic uncertainties.

To deal with the asymmetric errors we calculated percentage uncertainties as was done for Table 6.12. To do this we defined a term (R) which was the CC/NC flux ratio ϕ_{CC}/ϕ_{NC}. The systematic uncertainty was then calculated with

$$\sigma_{R_i} = \frac{R_i - R_{best}}{R_{best}} \tag{6.34}$$

where R_i is the ratio of the CC and NC fluxes for a specific error (i), such as the energy scale, and R_{best} is the ratio of the best fit fluxes. Using equation 6.34, in

Systematic	Uncertainty (%)
Energy scale	+5.31,-5.43
E nonlinearity	+0.53,-0.00
E radial bias	+3.49,-3.35
Energy resolution	± 2.86
Vertex accuracy X	+0.0071,-0.016
Vertex accuracy Y	+0.00,-0.0078
Vertex accuracy Z	+0.25,-0.16
Vertex resolution	± 0.22
Vertex radial acc	+0.31,-0.16
β_{14} mean	+1.72,-6.66
β_{14} sigma	± 2.91
Angular resolution	± 0.31
Neutron Efficiency	± 2.6
Internal background n	+1.91,-2.07
Cherenkov backgrounds	+0.14,0.00
"AV events"	± 0.4
Cross section	± 0.6
Total	+7.70,-10.16

Table 6.23: The CC/NC systematic uncertainties. The table contains the same systematics listed in table 6.12 with the inclusion of the cross-section uncertainty for CC/NC. The total systematic uncertainty is obtained from adding each of the entries in the table in quadrature.

conjunction with the error analysis presented in table 6.11, a new set of systematic uncertainties were produced for the CC/NC ratio. These are shown in table 6.23. The statistical and systematic uncertainties were then applied to the value of the CC/NC flux, giving a final result of $0.344 \pm 0.021(\text{stat}) \, ^{+0.026}_{-0.035}(\text{syst})$. The significance of these results are discussed in the following chapter.

Chapter 7

Conclusions and Discussion

This chapter contains a summary of the work presented in the thesis, the physics interpretation of the extracted fluxes and a discussion of the future directions the analysis could take to further explore the data.

7.1 Summary of Results

We have measured the detector optical properties for the salt phase of the SNO experiment. We have understood a number of effects that caused changes in the optical properties compared to the pure D_2O phase.

The salt phase optical calibrations measured a decrease in D_2O attenuation for short wavelengths (<450 nm) which was approximately linear over the data period. The attenuation rate of change was seen to "level off" near the end of the salt phase. The change in attenuation length appeared to be correlated with the MnOx assay schedule during the salt phase, and the measured increase of Manganese in the D_2O. The apparent "leveling-off" for the attenuation in April 2003 coincided with the end of MnOx assays in the salt phase. Furthermore, the removal of the salt at the end

of this phase, using RO filtration, also removed the built-up Manganese from the detector. The measured attenuation levels and detector energy response following this clean-up, were equivalent to values near the start of the salt phase.

During the transition period from the pure D_2O to the salt phase, a large decrease in the detector's energy response was observed. This was coincident with a large change in the angular response of the PMTs. The measured angular response was relatively constant for the salt phase. It is believed that a short period of time during which the water cooling systems were inactive may have resulted in an increase in the detector cavity temperature. The reflector-concentrators that surround the PMTs to focus the high-angle incident light on the PMT photocathode are affected by changes in temperature. A higher temperature in the cavity could have physically affected the reflectors resulting in a decrease of the detector energy response of approximately 3%.

The aggressive calibration schedule maintained over the salt phase produced better understood detector properties. For instance, due to regular optical scans it was possible to track the changes in the detector with both optics and energy. This was a large improvement over the pure D_2O phase that relied solely on the energy scans of the detector to understand changes that were occurring. The improved knowledge of the optical parameters also had a direct impact on the systematic uncertainties associated with the energy scale. For example, the conversion from NHIT to RSP energy used the measured optical properties of the media. We therefore saw an improvement in one of the largest systematic uncertainties of the pure D_2O phase, the energy scale, for the salt data. This was largely due to the optical measurements presented here.

We completed a MC study of the NHIT response from the complicated decay chain of a neutron capture on chlorine. In doing so, we demonstrated the suitability of the distributions generated by the MC. The MC distributions were parameterized

Experimental Phase/Theory	Parameter	Flux (10^6 cm^{-2}s^{-1}
Pure D_2O (constrained)	CC	$1.76\ ^{+0.06}_{-0.05}$(stat) $\pm$ 0.09(syst)
	NC	$5.09\ ^{+0.44}_{-0.43}$(stat) $^{+0.46}_{-0.43}$(syst)
	ES	$2.39\ ^{+0.24}_{-0.23}$(stat) $\pm$ 0.12(syst)
Salt Phase		
(SNO-constrained)	CC	1.70 ± 0.07(stat) $^{+0.09}_{-0.10}$(syst)
	NC	4.90 ± 0.24(stat) $^{+0.29}_{-0.27}$(syst)
	ES	$2.13\ ^{+0.29}_{-0.28}$(stat) $^{+0.15}_{-0.08}$(syst)
(Parametric-constrained)	CC	1.69 ± 0.07(stat) $^{+0.07}_{-0.08}$(syst)
	NC	4.91 ± 0.23(stat) $^{+0.32}_{-0.27}$(syst)
	ES	$2.11\ ^{+0.29}_{-0.27}$(stat) $^{+0.13}_{-0.19}$(syst)
(SNO-unconstrained)	CC	$1.59\ ^{+0.08}_{-0.07}$(stat) $^{+0.06}_{-0.08}$(syst)
	NC	5.21 ± 0.27(stat) $\pm$ 0.38(syst)
	ES	$2.21\ ^{+0.31}_{-0.26}$(stat) $\pm$ 0.10
Theory (BP2000)	NC	$5.05\ ^{+1.01}_{-0.81}$

Table 7.1: A comparison of fluxes obtained during each of the phases of the SNO experiment.

to produce PDFs for use in the signal extraction process. The total ^{8}B solar neutrino flux was measured in the salt phase using the independently developed 1D parametric PDFs. We have included the correlations between the event parameters by applying a method that uses Gaussian correlated joint-probabilities in the maximum likelihood calculation. The results were consistent with the various analyses in the different phases of the SNO experiment, and with the SSM prediction (see Table 7.1). We saw a clear demonstration of the existence of new physics beyond the Standard Model of particle physics. The ratio of CC/NC would be equal to 1 if solar neutrinos did not oscillate into other flavours. This is known as a null hypothesis test, and in this analysis with CC/NC = 0.344 ± 0.021(stat) $^{+0.026}_{-0.035}$(syst), the result differed from the null hypothesis by $>19\sigma$. If we assumed a 2-flavor neutrino oscillation model, then the ratio was also 4.7σ from the case of maximal mixing with CC/NC = 0.5.

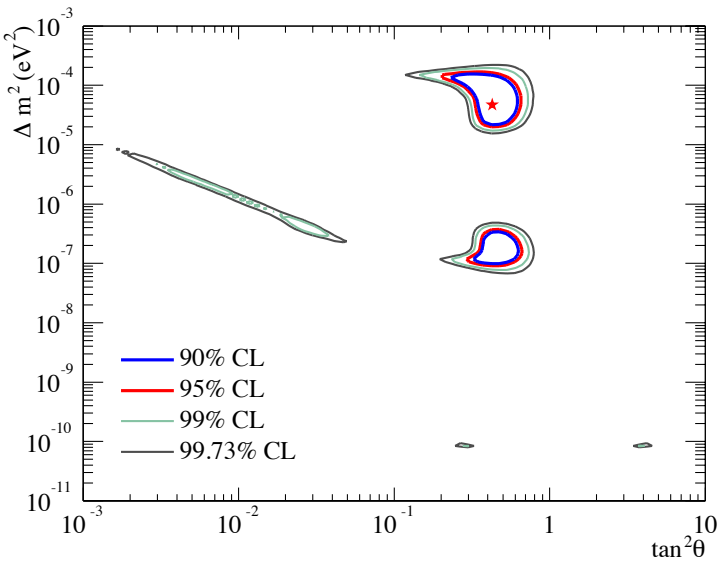

Figure 7.1: The allowable MSW phase-space determined from a fit with using only SNO data [64]. Included is the pure D_2O day and night spectra, the salt CC, NC and ES fluxes with a floating ^{8}B flux and a fixed Hep flux. The best fit point (marked with a star) is Δm^2=4.7 x 10^{-5} and $\tan^2\theta$=0.43.

7.2 MSW Interpretation of the Results

The fluxes determined in the salt phase can be used to constrain the neutrino oscillations. This is of great interest to the neutrino-physics community. MSW phase-space plots show the most probable oscillation solutions and provide the best fit values for oscillation parameters Δm^2 and $\tan^2(\theta)$. The most recent publication from SNO [64] contained a plot showing the remaining allowable MSW regions using all available SNO information (see Figure 7.1). By combining the new salt phase SNO results with measurements from global solar neutrino experiments, one removes all possible oscillation regions with the exception of the Large Mixing Angle (LMA) solution. By adding the latest results from the KamLAND reactor experiment, the combined results begin to constrain the LMA region significantly (see Figure 7.2).

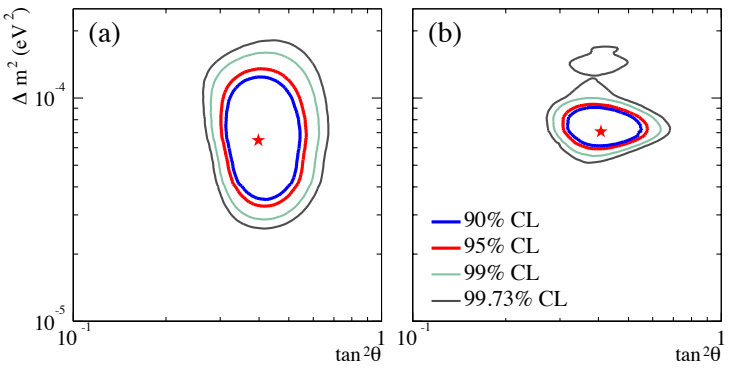

Figure 7.2: The neutrino oscillation contours for a global fit of (a) solar neutrino experiments, and (b) solar global and KamLAND. Figure (a) contains the information of figure 7.1 with the results of Super-Kamiokande, Homestake and the Gallium experiments. Only the LMA region of the phase space remains from the fit, with the best fit point, marked with the star, has $\Delta m^2 = 6.5 \text{ x } 10^{-5}$ and $\tan^2\theta = 0.40$. Figure (b) shows the effect of including the KamLAND result in the fit with the Global solar neutrino experiment information. Much of the LMA region is eliminated and the best fit point has $\Delta m^2 = 7.1 \text{ x } 10^{-5}$ and $\tan^2\theta = 0.41$

Note that due to the excellent agreement between the constrained results of the default analysis compared to this thesis work, one would expect consistent MSW plots to those presented here for physics interpretation calculations with the thesis measurements.

7.3 Future Direction

There are a number of possible upgrades that may be applied to the analysis presented in this thesis. The first of these upgrades, would be to repeat the analysis excluding the energy PDFs. This would require the development of a set of PDFs for the isotropy parameter (β_{14}), each one valid for a specific energy range. In this case, the extraction would produce a ^{8}B model-independent result, directly comparable to the default analysis unconstrained result. It would also be desirable to perform

signal extraction for a grid of varying energy and radial cuts. Such an analysis, however, would require large efforts by the low energy background and calibration groups to provide reliable uncertainties for the extended ranges, particularly for energy thresholds less than 5.5 MeV.

Another possibility is the reduction of the systematic uncertainties using a traditional statistical method, known as the "pull" method, recently applied to neutrino experiment results [28]. In this method, the individual event information, often taken from calibrations, is used in the fit as constraints on the size of the uncertainties. This reduces the possible size of the systematics in the extraction process. In addition, it is possible the combination of results from the pure D_2O and salt phases will reduce a number of the common systematics, thus providing the best measurement of CC/NC.

In the near future the remaining approximately 150 days of the salt neutrino data set will be analysed. This analysis will provide slightly better statistical uncertainties with similar systematic uncertainties, compared to the first salt phase results. Implementing some of the above suggestions in this analysis should improve on the limits of the remaining MSW space. Furthermore, the completion of the day/night analysis for the entire salt phase will add yet another constraint on the shape.

Finally, as this thesis is being completed, SNO is entering a new experimental phase. In this phase, the salt has been removed from the detector and Neutral Current Detectors (NCDs) are being deployed. These detectors are proportional counters filled with ^{3}He, and therefore have a high cross-section for neutron capture. The benefit of this experimental mode is a much better separation of the neutrons from the Cherenkov events. This will break the covariance between the CC and NC events. Thus, in the NCD phase, it may be possible to perform the signal extraction analysis without the use of energy or isotropy PDFs, removing the largest systematics from the final results.

Bibliography

[1] Amhed Q. *et al.* , **Direct Evidence for Neutrino Flavour Transformation from Neutral-Current Interactions in the Sudbury Neutrino Observatory, Phys. Rev. Lett. (2001).**

[2] Anderson T.C *et al.* , **A radium assay technique using hydrous titanium oxide adsorbent for the Sudbury Neutrino Observatory, NIM .**

[3] Anderson T.C. *et al.* , **Measurement of radium concentration in water with Mn-coated bead at the Sudbury Neutrino Observatory, NIM .**

[4] Anderson T.C. *et al.* , **Measurement of 222Rn dissolved in water at the Sudbury Neutrino Observatory, submitted to NIM.**

[5] Bahcall J.N. *et al.* , **Solar Neutrinos: Radiative Corrections in Neutrino-Electron Scattering Experiments**, (February 1995).

[6] Bahcall J.N., **Neutrino Astrophysics, Cambridge University Press, 1989**.

[7] Bahcall J.N. and Pinsonneault M.H., **Solar Models: current epoch and time dependences, neutrinos, and helioseismological properties, Astrophys.J. 555 (2001) 990-1012**

[8] Bellerive A., **Joint Probability Density Functions with Projections and Correlations**, SNO Internal Note (June 2003).

[9] Bellerive A. *et al.* , **Energy and Optics Measurements for the Salt Phase of SNO**,SNO Internal Note (May 2003).

[10] Bethe H.A, **Energy Production in Stars, Phy. Rev. 55, 434-56 (1939).**

[11] Boulay M., PhD Thesis (April 2001), **Direct Evidence for Weak Flavour Mixing with the Sudbury Neutrino Observatory**

[12] Bryce S.J., PhD Thesis (1996), **Monte Carlo and Analysis Techniques for the Sudbury Neutrino Observatory**, Oxford University.

[13] Butler M., **Neutrino-Deuteron Scatterin in Effective Field Theory at Next-to-Next-to Leading Order, Phys.Rev. C63 (2001) 035501.**

[14] Chen H., **Phys. Rev. Lett. 56, 1534 (1985).**

[15] Chen X., PhD Thesis (1997), **Monte Carlo and Analyses of Backgrounds in the Sudbury Neutrino Observatory**, Oxford University.

[16] Cleveland B.T. *et al.* , **Nucl. Phys. (Proc. Supp.) B38, 47 (1995).**

[17] Cowan C.L. Jr., Reines F. *et al.* , **Detection of the Free Neutrino: A Confirmation, Science 124, 103 (1956).**

[18] Cowan G., **Statistical Data Analysis**, Oxford Science Publications, Oxford University Press, 1998.

[19] Dosanjh R., **Problems in 2002 salt-phase optics**, SNO Internal Note (May 2003).

[20] Dosanjh R., **Salt Phase Optics Extraction**, SNO Internal Note (May 2003).

[21] Dosanjh R. and Grant D.R., **Optics During the Salt Phase of SNO**, SNO Internal Note (April 2002).

[22] Dragowsky M.R. *et al.* , **The ^{16}N Calibration Source for the Sudbury Neutrino Observatory,** SNO Internal Note written for NIM (July 2001).

[23] Dunford M. *et al.* , **Updates to Data Cleaning for the Salt Phase, Version 1.1**, SNO Internal Note (August 2003).

[24] Dunmore J.A., **Generation of Energy Dependent Beta Parameter PDFs**, SNO Internal Note (August 2003).

[25] Earle D., Private Communication.

[26] Ewan G.T. *et al* , **Sudbury Neutrino Observatory Proposal, SNO-87-12, (October 1987)**.

[27] Farine J., Phd. Thesis, Neuchatel, (1996).

[28] Fogli G.L. *et al.* , **Getting the most from the statistical analysis of solar neutrino oscillations., Phys.Rev. D66 (2002) 053010.**

[29] Ford R.J., PhD Thesis (December 1998), **Calibration of SNO for the Detection of ^{8}B Neutrinos.**

[30] Graham K., Private Communication.

[31] Grant D.R., **Asymmetry Study of the new Laserball**, SNO Internal Note (July 2001).

[32] Grant D.R., MSc. Thesis, Carleton University, (1998).

[33] Grant D.R., **Optics During Phase II of the SNO**, SNO Internal Note (September 2001).

[34] Grant D.R and Hallin A. **Results from the January Laserball Miniscan**, SNO Internal Note (March 2001).

[35] Grant D.R, Miknaitis K., and Drouin P.L., **TSigEx- The SNO Salt Signal Extraction Code**, SNO Internal Note.

[36] Greeniaus L.G., **TRIUMF Kinematics Handbook, 2nd Edition**, (September 1987).

[37] Greiner W. and Muller B., **Gauge Theory of Weak Interactions**, Springer-Verlag, 1993.

[38] Hallin A., **Diagonal Scan**, SNO Internal Note (April 2000).

[39] Halzen F. and Martin A.D., **Quarks and Leptons: An Introductory Course in Modern Particle Physics**, John Wiley & Sons, 1984.

[40] Hecht E., **Optics, 2^{nd} Edition**, Addison-Wesley Pusblishing, Inc., 1990.

[41] Hime A. for the SNO Neutrons Working Group, **Status Neutron Capture Efficiency Calibration for the Dissolved Salt-Phase in SNO**, (August 2003).

[42] James F., **Correlated Gaussian-distributed Random Number (CORSET and CORGEN)** CERN Program Library (1994).

[43] James F., **Minuit- Function Minimization and Error Analysis Reference Manual**.

[44] Karlen D., **Using Projections and Correlations to Approximate Probability Distributions**, Computers in Physics,12:4 (1998) 380.

[45] Klein J.R. *et al.* , **A Proposal for a Blind Analysis of NC Signal during the Salt Phase of SNO**, SNO Internal Note (May 2001).

[46] Klein J.R., talk given at 4th Tropical Workshop on Particle Physics and Cosmology, Cairns, Austraila (June 2003).

[47] Kos M. *et al.* for the SNO Neutrons Working Group, **Neutron Detection Efficiency During the Salt Phase of SNO**, (May 2003).

[48] Krusche B. *et al.* , **Gamma Ray Energies and ^{36}Cl Level Scheme from the Reaction ^{35}Cl(n,γ).**, Nuclear Physics A386 (1982) 245-268.

[49] Kurylov A. *et al.* , **Radiative Corrections in neutrino-deuteron disintegration**, Phys. Rev. C65 (2002) 055501.

[50] Kyba C., **Data Reduction Table for the Salt Phase (Run 20000-27000)**, SNO Internal Note (August 2003).

[51] Lyons L., **Statistics for Nuclear and Particle Physicists**, Cambridge University Press, 1989.

[52] Maki Z., Nakagawa M., and Sakata S., **Prog. Theor. Phys. 28:870(1962).**

[53] Maneira J., **Optical Calibration Consistency Checks**, SNO Internal Note (May 2003).

[54] Marino A.D., **Studies on the Separation of Signals in Salt by Isotropy Patterns**, SNO Internal Note (February 2002).

[55] Mikheev S. P., Smirnov A. Yu., **Neutrino oscillations in a variable-density medium and nu bursts due to the gravitational collapse of stars, Sov. Phys. JETP 64 (1986) 4-7.**

[56] Miknaitis K. *et al.* , **Checks on Reconstruction Using the AV Location**, (September 2003).

[57] Moffat B.A., PhD Thesis (July 2001), **The Optical Calibration of the Sudbury Neutrino Observatory.**

[58] Ortiz C.E. *et al* , **Phys. Rev. Lett. 85, 2909 (2000).**

[59] Taylor J.R., **An Introduction to Error Analysis**, University Science Books, Oxford University Press, 1982.

[60] The GALLEX Collaboration, **GALLEX solar neutrino observations: results for GALLEX IV, Physics Letters B, 447(1-2) (1999) 127-133**

[61] The KAMIOKANDE-II Collaboration, **Nucl. Phys. B 38, 54 (1995).**

[62] The KAMIOKANDE-II Collaboration, **A Search for High-Energy Neutrinos from SN1987A:First Six Months, Phys. Rev. Lett.59:2604 (1987).**

[63] The SAGE Collaboration, **Measurement of the Solar Neutrino Capture Rate by SAGE and Implications for Neutrino Oscillations in Vacuum, Phy. Rev. Lett. 83, 4686-4689 (1999).**

[64] The SNO Collaboration, **Measurement of the Total Active ^{8}B Solar Neutrino Flux at the Sudbury Neutrino Observatory with Enhanced Neutral Current Sensitivity**, submitted to Phys. Rev. Lett. (September 2003).

[65] The SNO Collaboration, **The Sudbury Neutrino Observatory, NIM.**

[66] The SNO Low Energy Background Analysis Group, **The Low Energy Background in the Salt Phase of the SNO Experiment**, SNO Internal Note (June, 2003).

[67] The SNO Salt Flux Working Group, **SNO Salt Phase Solar Neutrino Flux Analysis**, SNO Internal Note (September 2003).

[68] The SNO Water Group, **Scientific Review of SNO Water Systems**, (April 1996).

[69] The Super-KAMIOKANDE Collaboration, **Atmospheric neutrino results from Super-Kamiokande and Kamiokande-Evidence for ν_μ oscillations, hep-ex/9810001.**

[70] The Super-KAMIOKANDE Collaboration, **Constraints on neutrino oscillations using 1258 days of Super-Kamiokande solar neutrino data," Phys. Rev. Lett., 86(25):5656-60 (2001).**

[71] Vogel P. and Beacom J.F., **The angular distribution of the reaction $\bar{\nu}_e + p \rightarrow e^+ + n$**, (March 1999).

[72] West N. *et al.* , **SNOMAN Companion 5.00**.

[73] Wilkerson J., **Data Division in Salt vs Blind analysis**, SNO Internal Note (May 2002).

[74] Wolfenstein, L., **Neutrino oscillations and stellar collapse, Phys. Rev. D20 (1979) 2634-2635.**

[75] www.sns.ias.edu/ jnb

Appendix A

Optical Calibration Analysis

This appendix contains information the reader may find useful for assisting in the explanation of the analysis of the laserball data and optical calibration results. Included in the sections below are attenuation reference plots for the D_2O and H_2O media, details about the Mark-I laserball design and isotropy distribution, the results of the fits to fruns for the September 2001 scan, the changes in optical properties due to bug fixes, a study of the linearity of the change in attenuation with time, and the PMT angular response curves for each wavelength from the pure D_2O and salt phase laser scans.

A.1 Reference Attenuation Plots- D_2O and H_2O Comparison of Theoretical to Measured Values

This section contains the D_2O and H_2O attenuation plots for measured values in the SNO detector compared to external measurements and theoretical predictions.

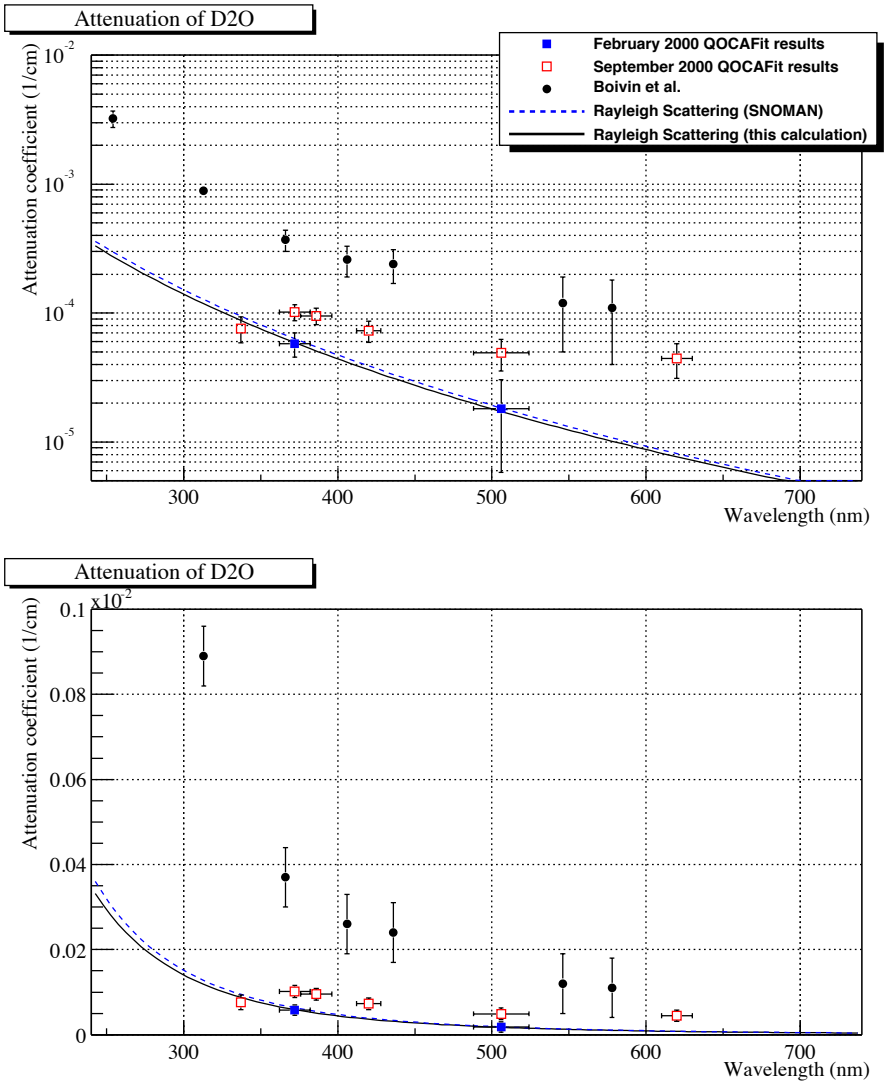

Figure A.1: The expected and measured D_2O attenuation lengths for the pure D_2O phase of the detector [57]. The QOCAFit results are from pure D_2O laserball scans. Points labeled Boivin *et al.* are attenuation lengths measured external to the SNO detector. The predicted attenuation curves due to Rayleigh scattering by the SNOMAN MC and an independent calculation, performed by Bryce Moffat, are shown. There is therefore more attenuation measured in the SNO D_2O than would be caused only by Rayleigh scattering.

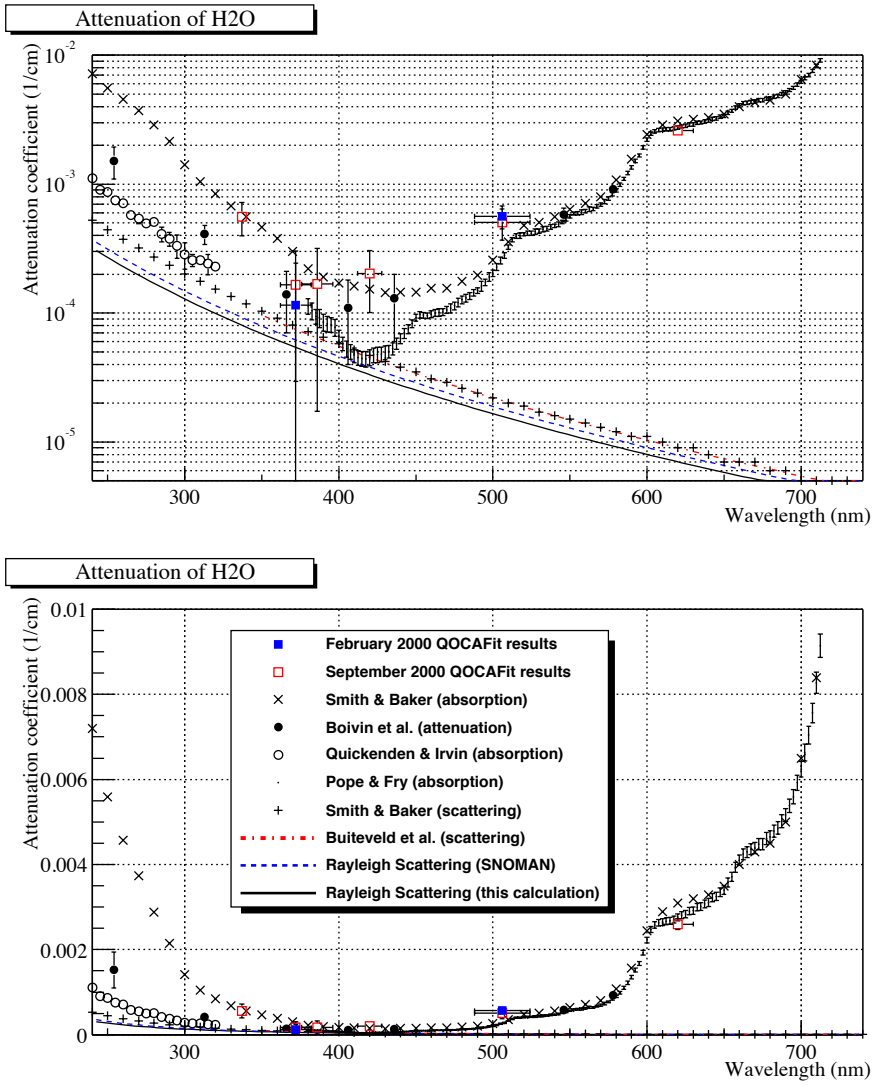

Figure A.2: The expected and measured H_2O attenuation lengths for the pure D_2O phase of the detector [57]. Shown are the measured H_2O attenuation lengths (QOCAFit) in the SNO pure D_2O phase compared to external predictions and measurements. The Rayleigh scattering prediction is shown from the SNOMAN MC, and independent calculation by Bryce Moffat, and Buiteveld *et al.*

A.2 The Mark-I Laserball

The first generation laserball source was composed of a cylindrical acrylic body attached to a quartz flask (see figure A.3). A stainless steel mask was designed to

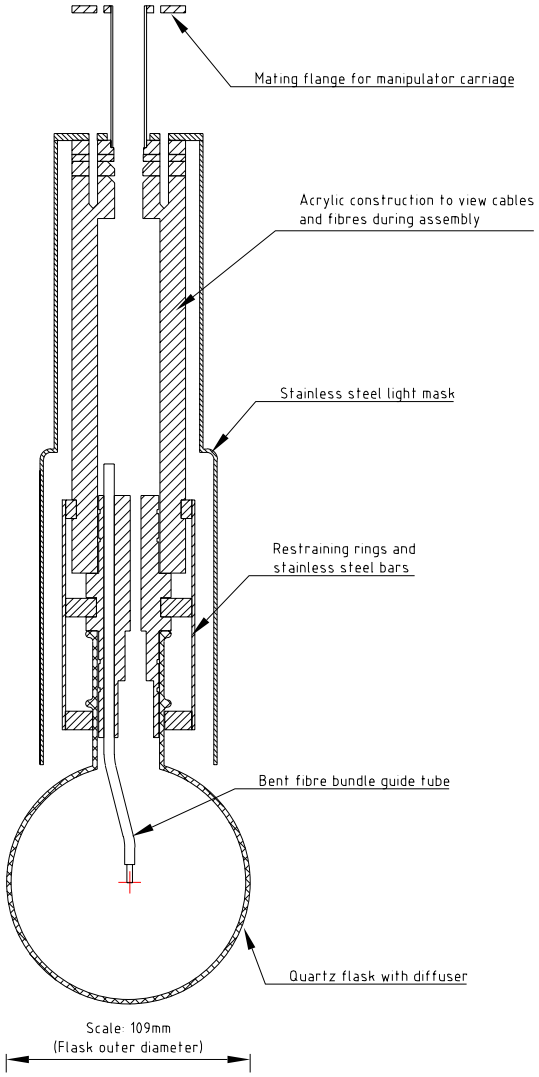

Figure A.3: The SNO Mark-I laserball design with a stainless steel light mask.

cover the neck of the source to eliminate stray photons leaking from the fibre-optics. This design was difficult to assemble, and as a result some water was able to enter the diffusing sphere which caused the light distribution from the laserball to change from approximately isotropic to largely asymmetric (see figure A.4). This shows that, after reassembly, there are a number of θ and ϕ combinations with different

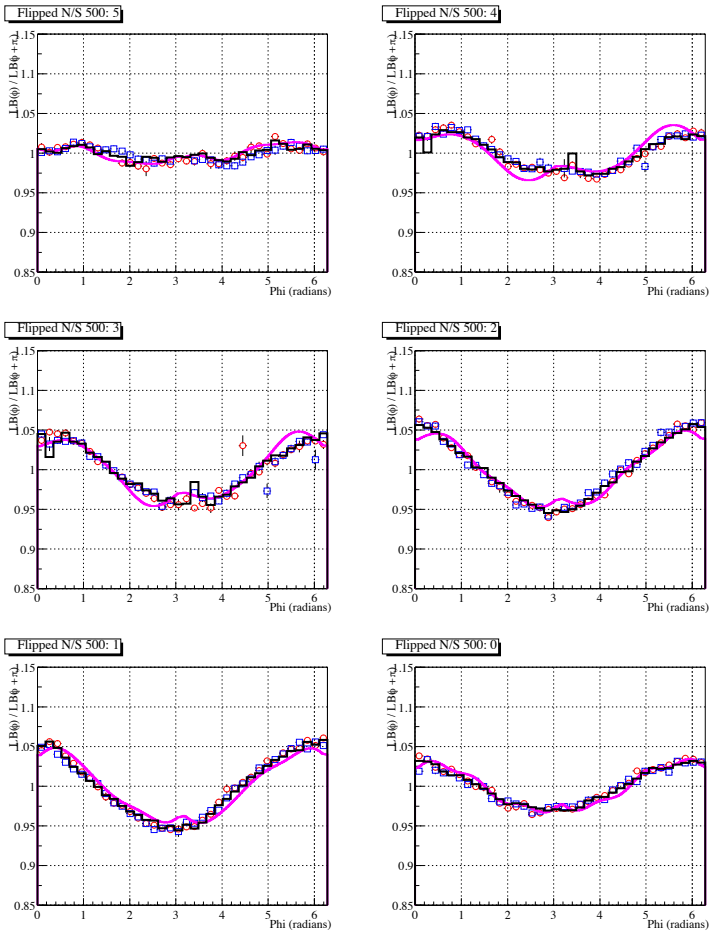

Figure A.4: The SNO Mark-I laserball asymmetry distribution after deployment and reassembly [57]. Asymmetry is measured, for example, by dividing North-facing by South-facing laser runs. Shown are plots of ϕ in θ angular slices (spherical coordinates) of the detector. From top to bottom, left to right, are cos θ ranges of: -1 to -0.809, -0.809 to -0.309, -0.309 to 0.309, 0.309 to 0.809, 0.809 to 1, and -1 to 1. The smallest asymmetry is in the first range at the bottom, and the largest is in the range 0.309 to 0.809. The average asymmetry is approximately $\pm$ 4%. The circles are for North/South data, while the squares are East/West. The black histogram is the ratio for 180° rotations. The magneta curve is the result of the Y_{lm} (harmonics) fit.

amounts of observed light.

A.3 Comparison of 'fits' to 'fruns'

This section contains a comparison of 'fruns' versus 'fits' for all runs in the September 2001. Each table contains the runs for an individual wavelength in the scan. Relatively good agreement is observed between the 'fruns' and 'fits' results at all wavelengths, with the exception of high radius positions (>500cm). The agreement implies the speed of light input for each wavelength in the salt phase is approximately correct. It also demonstrates the QOCA position fitter is not optimized to handle source positions near the AV where complicated reflections from the acrylic may occur.

Run Number	Manipulator Position				Fitted Position				Position from 500nm (fruns)				Difference
	x	y	z	R	x	y	z	R	x	y	z	R	ΔR
21081	0.10	−1.06	9.69	9.75	5.16	−0.43	9.28	10.63	4.61	−0.45	9.10	10.21	0.42
21100	−0.05	−0.87	9.78	9.82	5.59	−0.30	9.36	10.91	5.21	−0.35	9.04	10.44	0.47
21066	−0.10	−0.98	9.78	9.83	3.91	−0.19	9.37	10.15	3.74	−0.28	9.11	9.85	0.30
21052	−1.56	−0.13	9.76	9.88	1.15	3.08	8.30	8.93	0.65	2.95	7.98	8.53	0.40
21035	−1.56	−0.18	9.86	9.98	1.30	1.43	7.03	7.29	1.12	1.48	6.69	6.94	0.35
21539	0.06	−1.03	9.94	9.99	3.40	−1.50	8.88	9.63	3.11	−1.45	8.62	9.28	0.35
21118	0.07	−1.09	−90.26	90.27	5.33	−0.04	−90.34	90.50	5.03	−0.01	−89.42	89.56	0.94
21283	−71.00	−0.00	−71.00	100.41	−65.36	−0.11	−64.07	91.53	−65.47	−0.06	−64.00	91.55	−0.02
21361	69.81	−0.99	79.97	106.16	74.02	−0.32	76.77	106.64	72.71	−0.27	75.55	104.85	1.79
21154	−0.03	−0.95	110.03	110.03	5.38	−0.01	109.22	109.35	5.02	−0.15	107.61	107.72	1.63
21347	138.38	−1.42	−130.29	190.07	142.82	−0.05	−131.66	194.25	140.56	−0.03	−129.88	191.38	2.87
21301	−138.75	−1.09	−130.39	190.41	−132.35	0.27	−131.75	186.75	−131.01	0.35	−130.46	184.89	1.86
21322	−139.43	−0.66	150.01	204.80	−133.98	0.19	146.17	198.28	−132.61	0.06	144.19	195.90	2.38
21363	139.81	−0.84	149.90	204.98	144.01	−0.26	146.11	205.15	141.50	−0.34	143.94	201.85	3.30
21172	0.02	−0.63	259.98	259.98	4.96	−0.09	258.73	258.78	4.61	−0.09	255.04	255.09	3.69
21303	−206.88	−1.13	−200.52	288.11	−200.91	0.97	−202.00	284.90	−198.61	0.98	−199.17	281.28	3.62
21349	207.05	−1.43	−200.54	288.25	211.66	0.27	−201.48	292.22	208.22	0.27	−198.55	287.71	4.51
21409	−298.46	−0.62	9.21	298.60	−291.11	1.11	6.71	291.19	−287.47	1.14	6.61	287.55	3.64
21337	−209.41	−0.35	219.68	303.50	−203.09	0.60	213.05	294.34	−200.68	0.56	210.22	290.63	3.71
21226	219.52	−0.68	225.32	314.58	222.37	−0.33	218.91	312.04	219.08	−0.23	215.86	307.56	4.48
21320	−260.35	−1.13	−255.98	365.12	−254.93	1.06	−257.63	362.44	−251.66	0.96	−253.67	357.33	5.11
21134	−0.46	−1.57	−390.24	390.24	7.04	−0.48	−388.91	388.97	6.61	−0.49	−383.15	383.21	5.76
21174	0.25	−0.33	410.22	410.22	5.37	0.12	408.28	408.32	4.88	0.10	402.19	402.22	6.10
21395	−218.12	−1.30	−490.94	537.22	−213.48	0.92	−492.60	536.87	−210.23	0.88	−484.26	527.92	8.95
21152	−0.04	−1.44	−540.33	540.33	5.96	−0.03	−540.35	540.38	5.65	0.04	−532.14	532.17	8.21
21377	223.60	−0.00	−500.00	547.72	233.57	0.39	−496.85	549.01	227.56	0.35	−484.40	535.19	13.82
21393	−203.77	−1.23	−520.96	559.40	−199.14	1.01	−522.98	559.61	−196.26	0.93	−513.99	550.18	9.43
21190	−4.47	−13.00	559.49	559.66	−0.35	−9.60	552.08	552.16	−0.71	−9.77	547.42	547.51	4.65
21379	221.89	−1.78	−520.81	566.11	229.63	0.44	−522.67	570.89	225.24	0.62	−513.58	560.80	10.09

Table A.1: Comparison of 'fruns' to 'fits' positions for 337 nm laserball runs in the September 2001 laser scan [21].

Run Number	Manipulator Position				Fitted Position				Position from 500nm (fruns)				Difference
	x	y	z	R	x	y	z	R	x	y	z	R	ΔR
21041	−1.49	−0.49	9.00	9.14	1.23	1.40	6.83	7.08	1.12	1.48	6.69	6.94	0.14
21079	0.10	−0.98	9.69	9.74	5.08	−0.41	9.12	10.45	4.61	−0.45	9.10	10.21	0.24
21064	−0.11	−0.95	9.76	9.81	3.76	−0.24	9.22	9.96	3.74	−0.28	9.11	9.85	0.11
21098	0.01	−0.99	9.76	9.81	5.53	−0.39	9.17	10.72	5.21	−0.35	9.04	10.44	0.28
21050	−1.52	−0.22	9.75	9.87	1.04	2.95	8.11	8.69	0.65	2.95	7.98	8.53	0.16
21116	0.12	−1.02	−90.25	90.26	5.43	0.04	−90.08	90.24	5.03	−0.01	−89.42	89.56	0.68
21288	−71.08	−1.01	−61.17	93.78	−64.70	−0.13	−62.76	90.14	−64.42	−0.10	−62.44	89.71	0.43
21259	69.62	−0.87	79.84	105.93	73.41	0.20	75.47	105.28	72.71	−0.27	75.55	104.85	0.43
21156	0.09	−0.85	110.01	110.01	5.28	−0.08	108.58	108.71	5.02	−0.15	107.61	107.72	0.99
21299	−138.86	−1.10	−130.38	190.48	−131.83	0.31	−131.42	186.15	−131.01	0.35	−130.46	184.89	1.26
21345	140.00	−0.00	−140.00	197.99	143.39	−0.05	−132.68	195.36	140.56	−0.03	−129.88	191.38	3.98
21324	−139.52	−0.61	150.06	204.90	−133.44	0.16	145.32	197.29	−132.61	0.06	144.19	195.90	1.39
21365	139.81	−0.92	149.93	205.00	143.21	−0.33	145.35	204.05	141.50	−0.34	143.94	201.85	2.20
21170	0.05	−0.59	259.97	259.97	4.97	−0.17	257.33	257.38	4.61	−0.09	255.04	255.09	2.29
21308	−206.81	−1.04	−200.53	288.07	−200.06	1.05	−201.05	283.63	−198.61	0.98	−199.17	281.28	2.35
21351	207.05	−1.45	−200.54	288.25	210.53	0.28	−200.62	290.81	208.22	0.27	−198.55	287.71	3.10
21407	−298.47	−0.60	9.20	298.61	−289.74	1.16	6.53	289.82	−287.47	1.14	6.61	287.55	2.27
21335	−209.39	−0.35	219.66	303.47	−202.16	0.63	211.97	292.92	−200.68	0.56	210.22	290.63	2.29
21224	219.60	−0.61	225.33	314.64	221.33	−0.30	217.71	310.46	219.08	−0.23	215.86	307.56	2.90
21318	−260.22	−1.07	−256.00	365.04	−253.68	1.04	−256.34	360.65	−251.66	0.96	−253.67	357.33	3.32
21136	−0.39	−1.55	−390.23	390.23	6.91	−0.36	−386.98	387.04	6.61	−0.49	−383.15	383.21	3.83
21176	0.20	−0.27	410.28	410.28	5.35	0.10	406.32	406.36	4.88	0.10	402.19	402.22	4.14
21397	−218.28	−1.36	−490.97	537.31	−212.32	0.99	−490.12	534.13	−210.23	0.88	−484.26	527.92	6.21
21375	223.76	−1.92	−491.13	539.70	230.46	0.39	−490.56	542.00	227.56	0.35	−484.40	535.19	6.81
21150	−0.10	−1.43	−540.32	540.32	6.17	0.04	−538.03	538.07	5.65	0.04	−532.14	532.17	5.90
21391	−203.67	−1.32	−520.96	559.36	−198.06	1.03	−520.40	556.82	−196.26	0.93	−513.99	550.18	6.64
21192	−4.42	−13.01	559.49	559.66	−0.45	−9.71	552.00	552.09	−0.54	−9.73	547.35	547.43	4.66
21381	221.99	−1.86	−520.79	566.13	228.25	0.55	−520.06	567.94	225.24	0.62	−513.58	560.80	7.14

Table A.2: Comparison of 'fruns' to 'fits' positions for 365 nm laserball runs in the September 2001 laser scan [21].

Run Number	Manipulator Position				Fitted Position				Position from 500nm (fruns)				Difference
	x	y	z	R	x	y	z	R	x	y	z	R	ΔR
21037	−1.56	−0.55	9.00	9.15	1.32	1.41	6.74	7.01	1.12	1.48	6.69	6.94	0.07
21269	0.10	−0.90	9.65	9.69	5.51	−0.44	6.87	8.82	5.16	−0.45	6.78	8.53	0.29
21077	−0.00	−1.02	9.68	9.73	5.19	0.03	9.26	10.62	4.61	−0.45	9.10	10.21	0.41
21062	−0.11	−0.95	9.76	9.81	3.79	−0.26	9.23	9.98	3.74	−0.28	9.11	9.85	0.13
21094	0.05	−0.95	9.76	9.81	5.55	−0.34	9.10	10.66	5.21	−0.35	8.92	10.34	0.32
21048	−1.52	−0.22	9.75	9.87	1.04	2.90	8.10	8.67	0.65	2.95	7.98	8.53	0.14
21114	−0.04	−1.05	−90.26	90.27	5.31	0.06	−89.90	90.06	5.03	−0.01	−89.42	89.56	0.50
21291	−71.00	−0.00	−71.00	100.41	−65.27	−0.07	−63.99	91.41	−64.42	−0.10	−62.44	89.71	1.70
21257	69.71	−0.94	79.84	105.99	73.31	0.19	75.32	105.11	72.71	−0.27	75.55	104.85	0.26
21158	0.02	−0.83	110.03	110.03	5.23	−0.11	108.34	108.47	5.02	−0.15	107.61	107.72	0.75
21343	138.30	−1.35	−130.30	190.02	141.88	−0.00	−130.94	193.07	140.56	−0.03	−129.88	191.38	1.69
21297	−140.00	−0.00	−140.00	197.99	−133.27	0.37	−133.33	188.52	−131.01	0.35	−130.46	184.89	3.63
21327	−139.62	−0.68	150.10	205.00	−133.30	0.13	145.10	197.04	−132.61	0.06	144.19	195.90	1.14
21367	139.82	−0.92	149.94	205.02	142.80	−0.39	145.07	203.56	141.50	−0.34	143.94	201.85	1.71
21168	−0.13	−0.62	259.96	259.96	4.91	−0.19	256.87	256.92	4.61	−0.09	255.04	255.09	1.83
21310	−207.10	−1.07	−200.49	288.25	−199.69	0.97	−200.65	283.09	−198.61	0.98	−199.17	281.28	1.81
21353	207.25	−1.54	−200.52	288.38	210.12	0.31	−200.19	290.22	208.22	0.27	−198.55	287.71	2.51
21405	−298.33	−0.55	9.17	298.47	−289.29	1.20	6.56	289.37	−287.47	1.14	6.61	287.55	1.82
21333	−209.45	−0.36	219.61	303.48	−201.93	0.60	211.71	292.57	−200.68	0.56	210.22	290.63	1.94
21222	219.59	−0.71	225.30	314.61	220.75	−0.28	217.29	309.75	219.08	−0.23	215.86	307.56	2.19
21316	−260.36	−1.17	−255.99	365.13	−253.23	1.01	−255.83	359.97	−251.66	0.96	−253.67	357.33	2.64
21138	−0.37	−1.49	−390.23	390.23	6.89	−0.39	−386.24	386.30	6.61	−0.49	−383.15	383.21	3.09
21178	0.27	−0.34	410.35	410.35	5.32	0.16	405.38	405.41	4.88	0.10	402.19	402.22	3.19
21399	−218.38	−1.43	−490.96	537.34	−211.97	0.94	−488.85	532.83	−210.23	0.88	−484.26	527.92	4.91
21373	223.83	−1.86	−491.12	539.72	229.98	0.40	−489.33	540.68	227.56	0.35	−484.40	535.19	5.49
21148	0.21	−1.46	−540.33	540.33	5.97	0.04	−536.77	536.80	5.65	0.04	−532.14	532.17	4.63
21389	−203.92	−1.28	−520.95	559.44	−197.68	1.02	−519.16	555.52	−196.26	0.93	−513.99	550.18	5.34
21188	−4.42	−13.01	559.49	559.66	−0.44	−9.61	550.44	550.52	−0.71	−9.77	547.42	547.51	3.01
21383	222.06	−1.76	−520.78	566.15	227.88	0.54	−518.79	566.63	225.24	0.62	−513.58	560.80	5.83

Table A.3: Comparison of 'fruns' to 'fits' positions for 386 nm laserball runs in the September 2001 laser scan [21].

Run Number	Manipulator Position				Fitted Position				Position from 500nm (fruns)				Difference
	x	y	z	R	x	y	z	R	x	y	z	R	ΔR
21039	−1.56	−0.42	9.00	9.14	1.21	1.45	6.59	6.86	1.12	1.48	6.69	6.94	−0.08
21083	−0.05	−1.04	9.68	9.74	4.99	−0.41	8.87	10.19	4.61	−0.45	9.10	10.21	−0.02
21092	0.02	−1.02	9.76	9.81	5.56	−0.34	9.09	10.66	5.21	−0.35	8.92	10.34	0.32
21060	−0.15	−1.03	9.78	9.84	3.81	−0.29	9.11	9.88	3.74	−0.28	9.11	9.85	0.03
21054	−1.57	−0.13	9.76	9.89	0.92	3.02	7.94	8.54	0.65	2.95	7.98	8.53	0.01
21532	0.15	−1.01	9.95	10.00	3.19	−1.64	8.67	9.38	3.11	−1.45	8.62	9.28	0.10
21110	0.11	−1.02	−90.26	90.27	5.20	0.04	−89.53	89.68	4.89	0.06	−89.41	89.54	0.14
21422	70.00	0.00	70.00	98.99	74.62	0.13	76.28	106.71	73.03	0.14	75.29	104.90	1.81
21285	−71.00	−0.00	−71.00	100.41	−80.19	−39.33	−68.34	112.46	−65.47	−0.06	−64.00	91.55	20.91
21160	−0.11	−0.90	110.04	110.04	5.10	−0.15	108.02	108.14	5.02	−0.15	107.61	107.72	0.42
21429	140.00	0.00	140.00	197.99	144.02	−0.12	145.87	204.99	141.08	−0.14	143.63	201.33	3.66
21451	−140.00	0.00	140.00	197.99	−134.58	0.79	145.53	198.22	−132.24	0.66	143.33	195.01	3.21
21457	140.00	0.00	−140.00	197.99	143.26	0.34	−133.20	195.62	140.49	0.37	−130.42	191.70	3.92
21467	−140.00	0.00	−140.00	197.99	−133.64	0.78	−133.47	188.88	−131.29	0.67	−130.46	185.09	3.79
21166	−0.12	−0.59	259.95	259.95	4.83	−0.26	255.89	255.94	4.61	−0.09	255.04	255.09	0.85
21439	−210.00	0.00	210.00	296.98	−202.15	0.98	212.99	293.65	−198.42	0.93	209.38	288.46	5.19
21465	210.00	0.00	−210.00	296.98	212.27	0.56	−203.15	293.82	208.12	0.46	−198.86	287.85	5.97
21478	−210.00	0.00	−210.00	296.98	−202.82	1.35	−203.64	287.41	−199.15	1.14	−199.14	281.63	5.78
21411	−298.00	0.00	−0.00	298.00	−292.80	1.17	6.17	292.87	−287.57	1.12	6.53	287.64	5.23
21437	213.57	−0.60	226.20	311.09	217.79	0.11	221.03	310.30	213.55	0.17	217.32	304.68	5.62
21480	−260.00	0.00	−266.00	371.96	−251.06	1.49	−260.23	361.60	−246.21	1.27	−254.67	354.23	7.37
21140	−0.47	−1.57	−390.24	390.24	6.70	−0.42	−384.44	384.50	6.61	−0.49	−383.15	383.21	1.29
21180	0.22	−0.34	410.39	410.39	5.10	0.05	403.59	403.62	4.88	0.10	402.19	402.22	1.40
21516	217.43	−1.62	−491.42	537.38	221.41	−0.24	−486.36	534.39	225.96	0.46	−494.63	543.80	−9.41
21146	0.04	−1.47	−540.32	540.32	5.88	−0.03	−533.97	534.00	5.65	0.04	−532.14	532.17	1.83
21186	−4.41	−12.99	559.49	559.66	−0.43	−9.66	549.56	549.65	−0.71	−9.77	547.42	547.51	2.14
21530	−203.70	−1.27	−530.70	568.45	−221.64	0.91	−526.19	570.97	−218.72	0.02	−512.73	557.43	13.54
21518	222.00	−1.70	−530.60	575.17	231.50	0.49	−524.92	573.70	225.06	−0.01	−512.63	559.86	13.84

Table A.4: Comparison of 'fruns' to 'fits' positions for 420 nm laserball runs in the September 2001 laser scan [21].

Run Number	Manipulator Position				Fitted Position				Position from 500nm (fruns)				Difference
	x	y	z	R	x	y	z	R	x	y	z	R	ΔR
21070	−0.00	−1.02	9.67	9.72	4.72	0.22	9.37	10.49	4.61	−0.45	9.10	10.21	0.28
21096	−0.09	−0.97	9.76	9.81	4.85	−0.38	9.05	10.27	5.21	−0.35	8.92	10.34	−0.07
21043	−1.60	−0.23	9.75	9.88	0.53	1.55	−2.05	2.62	1.12	1.48	6.69	6.94	−4.32
21046	−1.60	−0.23	9.75	9.88	0.19	2.72	−1.40	3.07	0.65	2.95	7.98	8.53	−5.46
21068	−1.60	−0.23	9.75	9.88	1.57	0.16	−0.14	1.58	3.74	−0.28	9.11	9.85	−8.27
21534	0.27	−1.04	9.96	10.02	2.84	−1.49	8.56	9.14	3.11	−1.45	8.62	9.28	−0.14
21425	70.00	−0.00	70.00	98.99	74.32	0.05	76.50	106.66	73.03	0.14	75.29	104.90	1.76
21112	−0.00	−0.00	−100.00	100.00	4.86	0.06	−91.34	91.47	5.03	−0.01	−89.42	89.56	1.91
21279	−71.00	−0.00	−71.00	100.41	−65.95	−0.13	−64.00	91.90	−65.47	−0.06	−64.00	91.55	0.35
21427	140.00	−0.00	140.00	197.99	143.84	−0.06	146.22	205.11	141.08	−0.14	143.63	201.33	3.78
21453	−140.00	−0.00	140.00	197.99	−135.21	0.71	146.01	199.00	−132.24	0.66	143.33	195.01	3.99
21455	140.00	−0.00	−140.00	197.99	143.10	0.38	−133.45	195.67	140.49	0.37	−130.42	191.70	3.97
21469	−140.00	−0.00	−140.00	197.99	−134.24	0.81	−133.49	189.32	−131.29	0.67	−130.46	185.09	4.23
21202	−0.00	−0.00	250.00	250.00	4.74	−0.38	259.33	259.37	0.00	0.00	0.00	0.00	259.37
21443	−210.00	−0.00	210.00	296.98	−202.95	0.96	213.53	294.59	−198.42	0.93	209.38	288.46	6.13
21463	210.00	−0.00	−210.00	296.98	211.98	0.54	−203.13	293.59	208.12	0.46	−198.86	287.85	5.74
21476	−210.00	−0.00	−210.00	296.98	−203.47	1.37	−203.64	287.87	−199.15	1.14	−199.14	281.63	6.24
21413	−298.00	−0.00	−0.00	298.00	−293.82	1.23	6.28	293.89	−287.57	1.12	6.53	287.64	6.25
21435	220.00	−0.00	220.00	311.13	217.99	0.18	221.58	310.83	213.55	0.17	217.32	304.68	6.15
21482	−260.00	−0.00	−260.00	367.70	−251.79	1.39	−259.91	361.87	−246.21	1.27	−254.67	354.23	7.64
21200	−0.00	−0.00	400.00	400.00	4.62	−0.30	410.83	410.86	4.70	−0.30	402.57	402.59	8.27
21210	−0.00	−0.00	−400.00	400.00	6.50	−0.19	−391.22	391.27	6.77	−0.36	−383.31	383.37	7.90
21514	−223.60	−0.00	−500.00	547.72	225.64	0.36	−496.78	545.62	225.96	0.46	−494.63	543.80	1.82
21194	−0.00	−0.00	550.00	550.00	−0.73	−9.66	559.64	559.72	−0.54	−9.73	547.35	547.43	12.29
21488	−0.00	−0.00	−550.00	550.00	5.32	0.11	−544.86	544.89	5.59	−0.03	−532.63	532.66	12.23
21526	−203.70	−1.27	−530.70	568.45	−222.15	0.96	−526.10	571.08	−218.72	0.02	−512.73	557.43	13.65
21520	222.00	−1.70	−530.60	575.17	231.38	0.58	−525.63	574.30	225.06	−0.01	−512.63	559.86	14.44

Table A.5: Comparison of 'fruns' to 'fits' positions for 620 nm laserball runs in the September 2001 laser scan [21].

A.4 The Effects of the QOCA Results for "Bug" Fixes

This section contains a series of plots showing the effect of applying the time of flight "bug" fix described in Chapter 4 on the attenuation lengths and angular response extracted from the laserball data with the QOCA code.

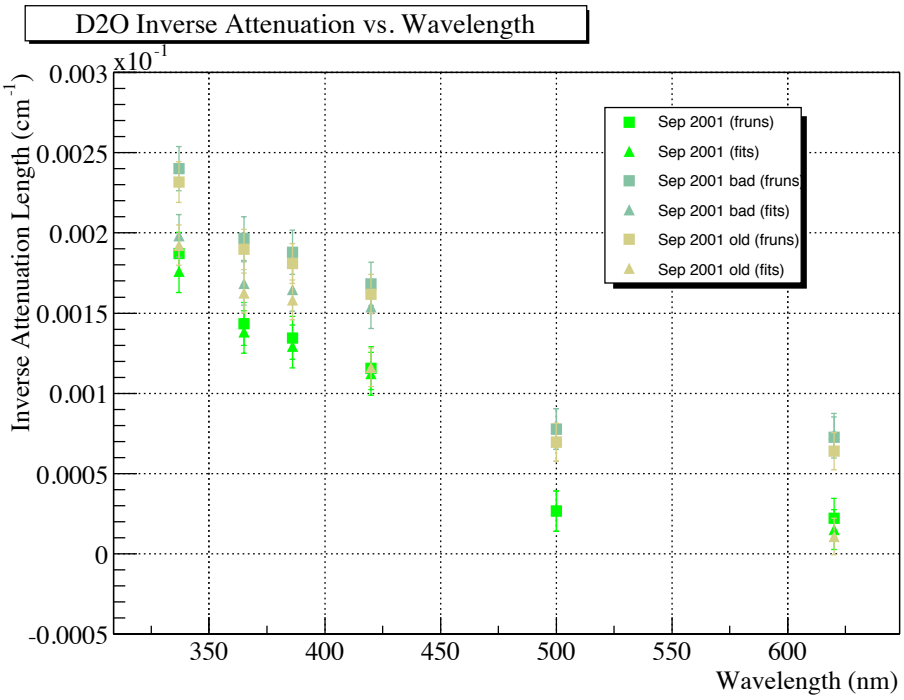

Figure A.5: The effect of the time of flight bug on the September 2001 extracted D_2O attenuation [20]. Shown are the 'fruns' and 'fits' results for the first processing of the September 2001 laser dataset (old), the effect of correcting the first "bug" of an incorrect vertical height for the weight cylinder (bad) and finally the result for the correction of both bugs (green points). The change in the attenuation due to the vertical height of the weight cylinder is seen to be a very small effect.

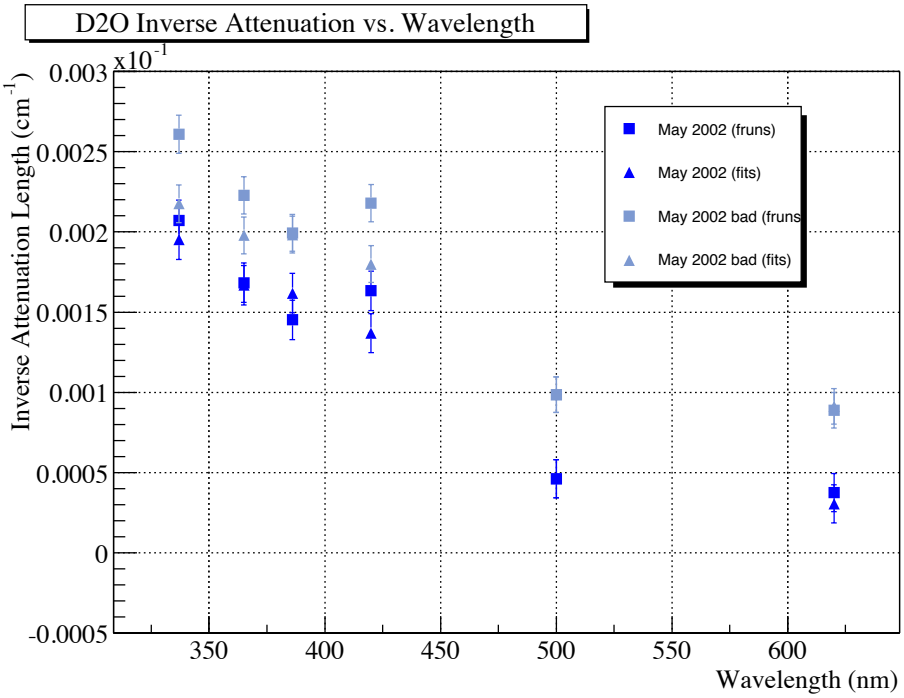

Figure A.6: The effect of the time of flight bug on the May 2002 extracted D_2O attenuation [20]. Shown are the fruns and fits results for the processing of the effect of correcting the first bug of an incorrect vertical height for the weight cylinder (bad) the result for the correction of both bugs.

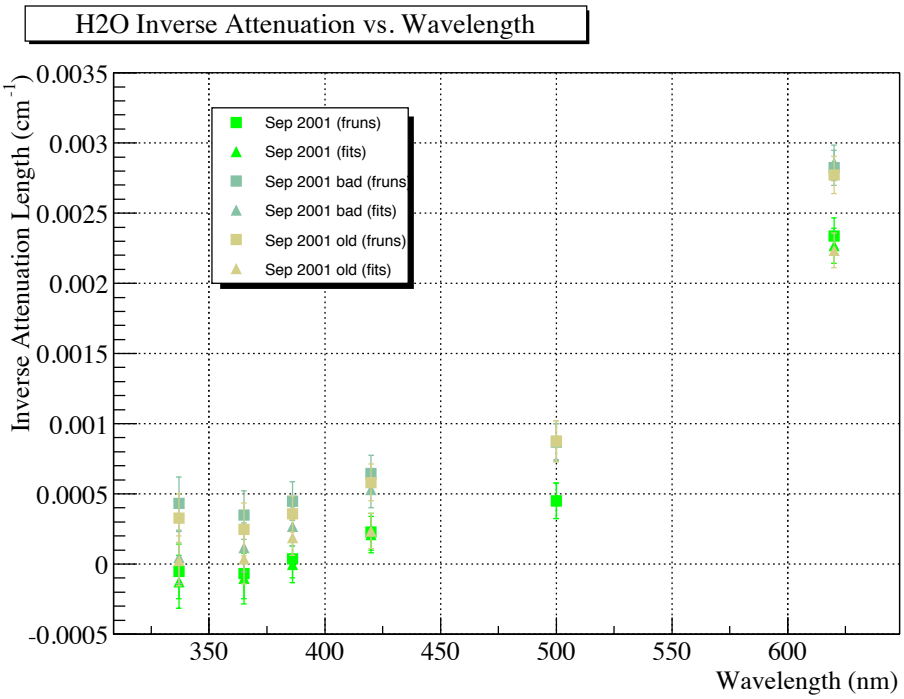

Figure A.7: The effect of the time of flight "bug" on the September 2001 extracted H_2O attenuation [20]. Shown are the 'fruns' and 'fits' results for the first processing of the September 2001 laser dataset (old), the effect of correcting the first "bug" of an incorrect vertical height for the weight cylinder (bad) and finally the result for the correction of both bugs (green points). The change in the attenuation due to the vertical height of the weight cylinder is seen to be a very small effect.

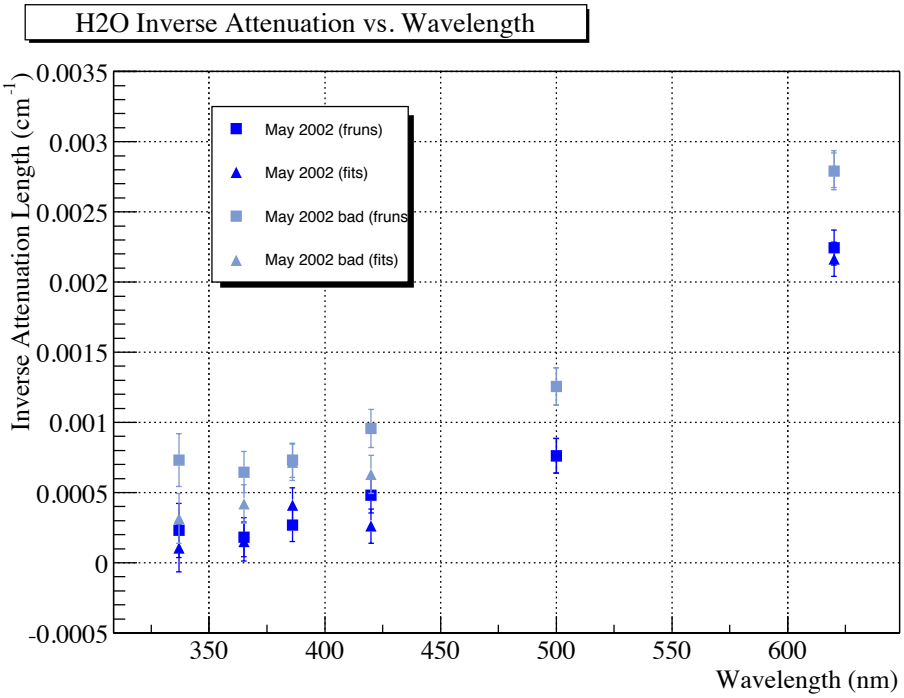

Figure A.8: The effect of the time of flight "bug" on the May 2002 extracted H_2O attenuation [20]. Shown are the 'fruns' and 'fits' results for the processing of the effect of correcting the first "bug" of an incorrect vertical height for the weight cylinder (bad) the result for the correction of both bugs.

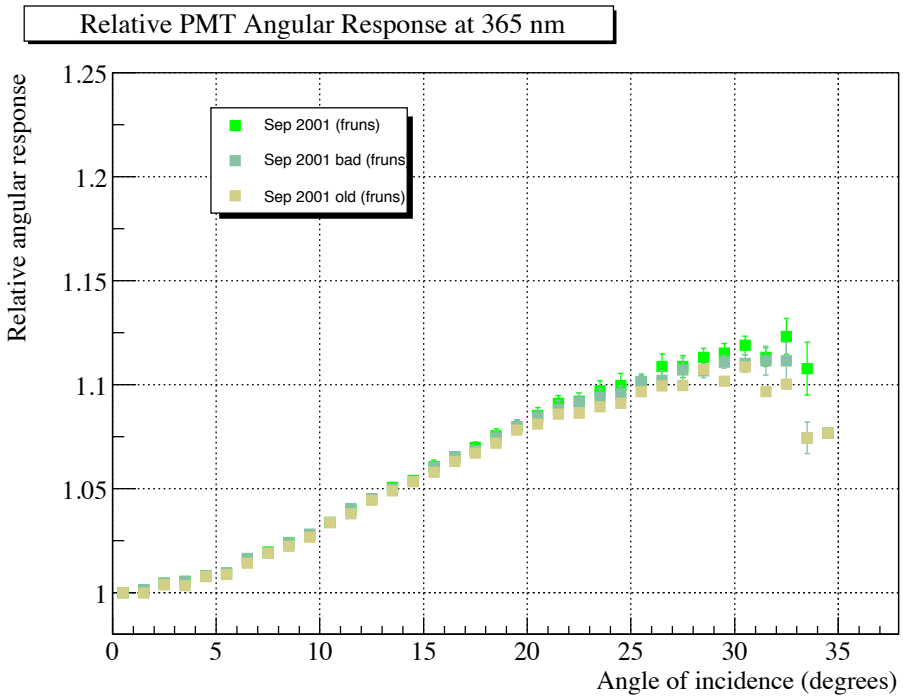

Figure A.9: The effect of the time of flight "bug" on the September 2001 measured PMT angular response for the 365 nm laser data [20]. Shown are the results for the first processing of the September 2001 laser dataset (old), the effect of correcting the first "bug" of an incorrect vertical height for the weight cylinder (bad) and finally the result for the correction of both bugs (green points). There is observed a small change in the response at high incident angles.

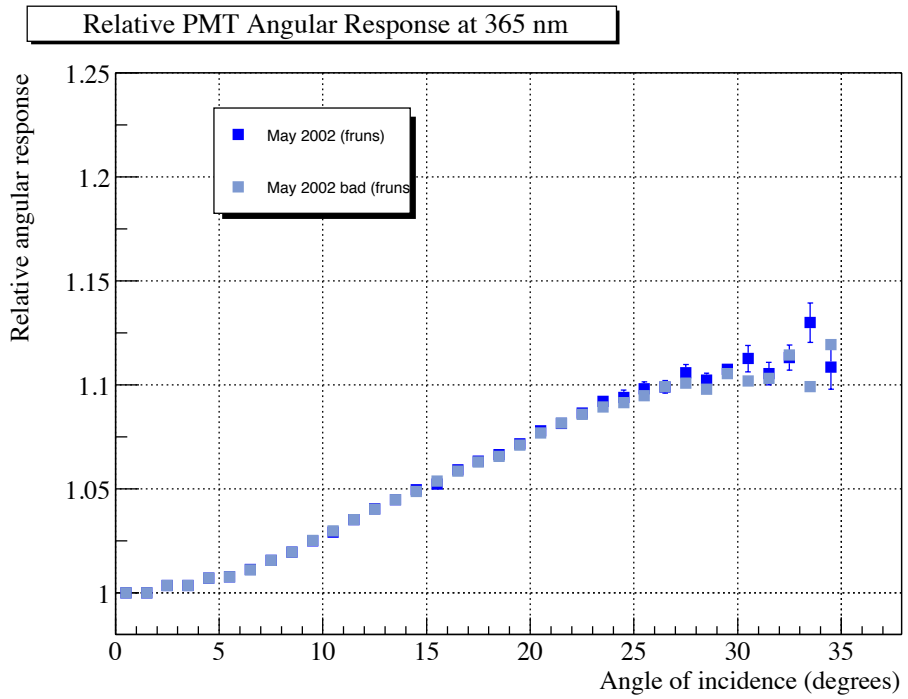

Figure A.10: The effect of the time of flight "bug" on the May 2002 measured PMT angular response for the 365 nm laser data [20]. Shown are the results for correcting the first "bug" of an incorrect vertical height for the weight cylinder (bad) and the result for the correction of both bugs. There is observed a small change in the response at high incident angles.

A.5 Extracted D_2O and H_2O Attenuation Lengths as a Function of Time

This section contains a series of plots showing linear fits to the extracted attenuation lengths (D_2O and H_2O) as a function of time. The linear functions are used to provide time dependent optical constants for the MC. This ensures the detector response calculated in MC agrees with the true detector at any give time in the experimental phase.

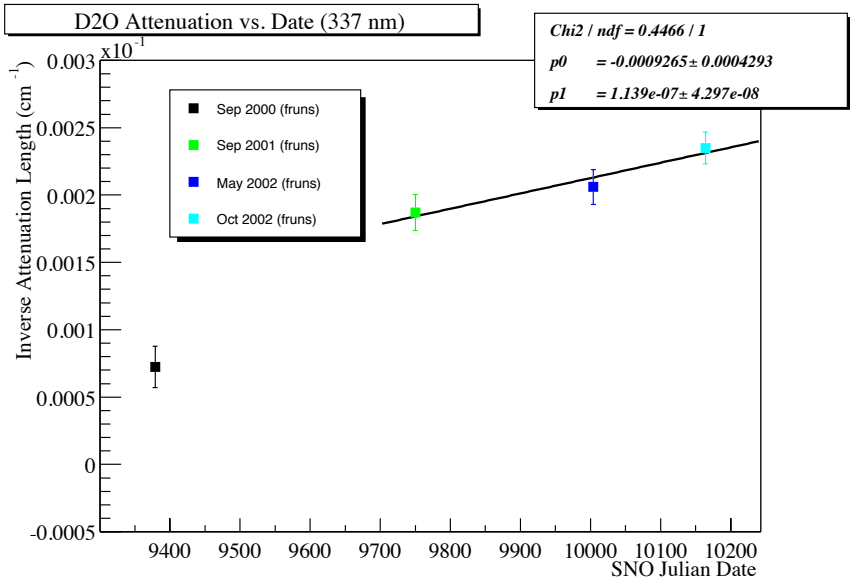

Figure A.11: A linear fit to the measured 337 nm D_2O attenuations as a function of time [20].

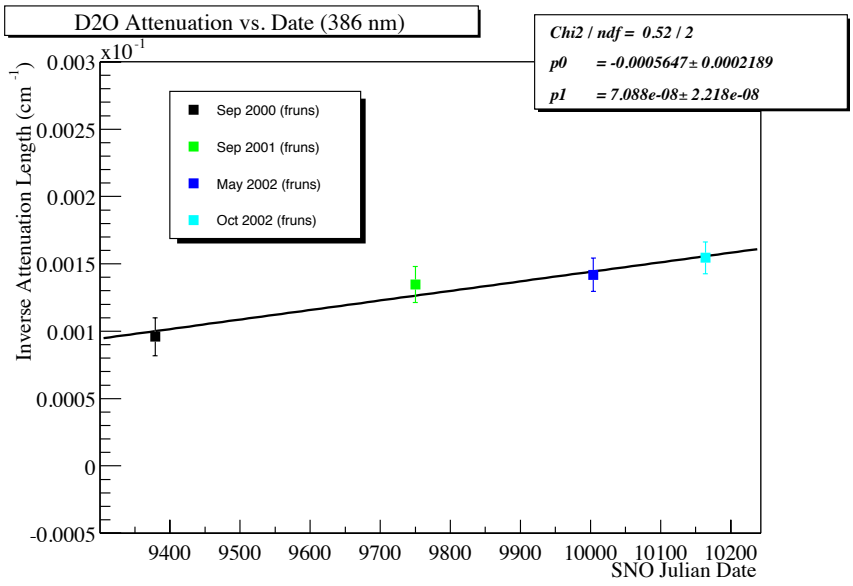

Figure A.12: A linear fit to the measured 386 nm D_2O attenuations as a function of time [20].

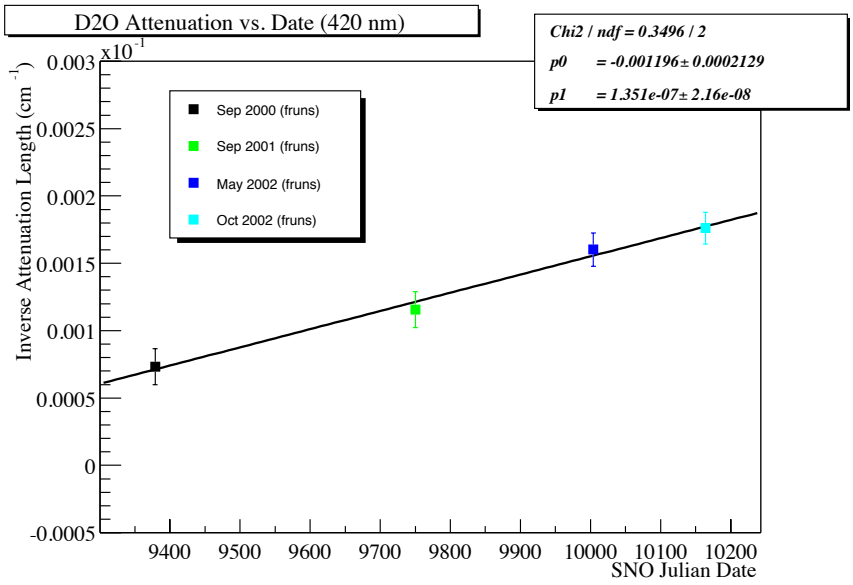

Figure A.13: A linear fit to the measured 420 nm D_2O attenuations as a function of time [20].

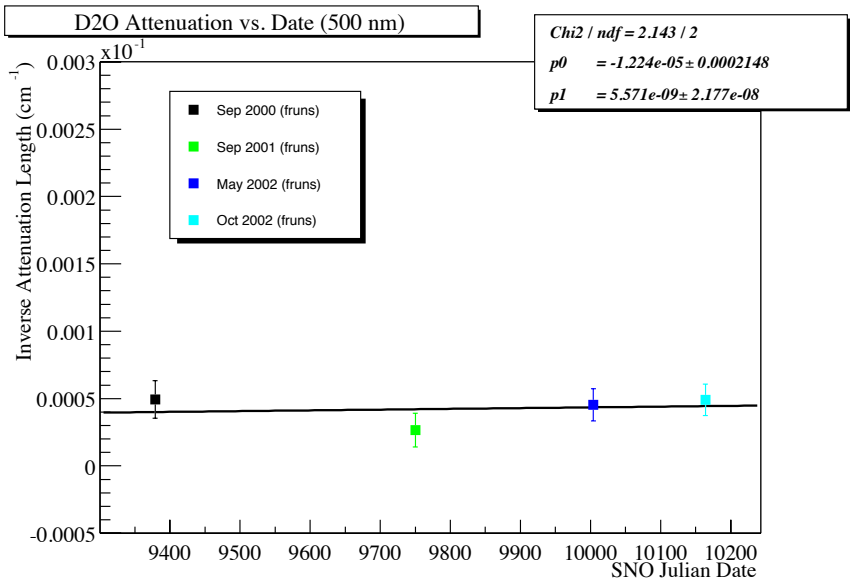

Figure A.14: A linear fit to the measured 500 nm D_2O attenuations as a function of time [20].

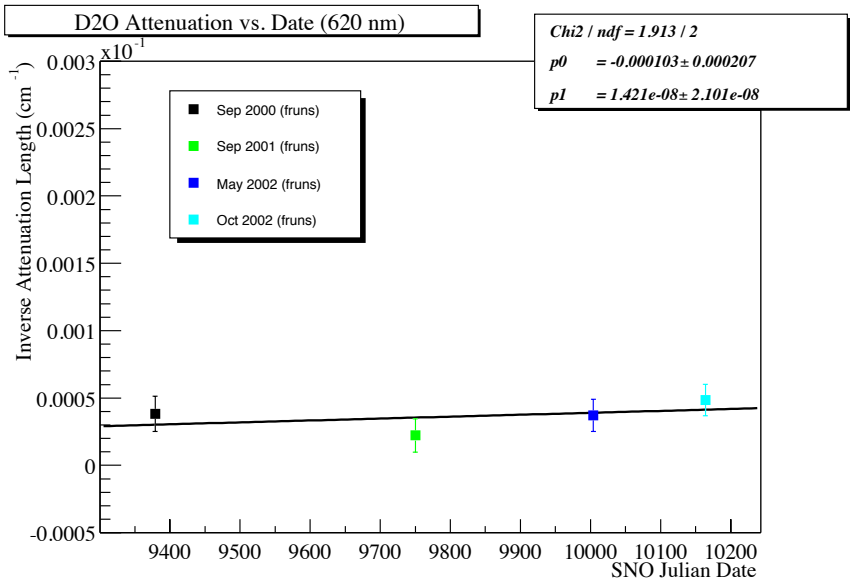

Figure A.15: A linear fit to the measured 620 nm D_2O attenuations as a function of time [20].

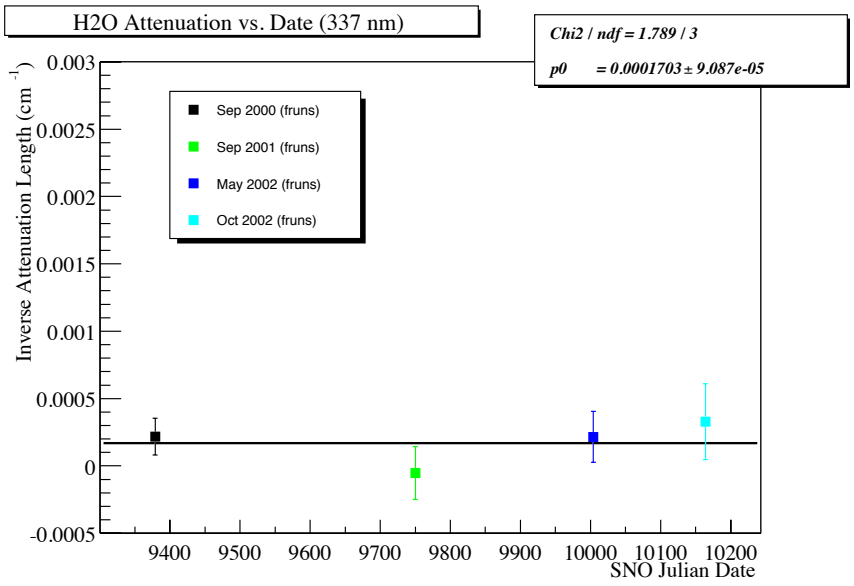

Figure A.16: A linear fit to the measured 337 nm H_2O attenuations as a function of time [20].

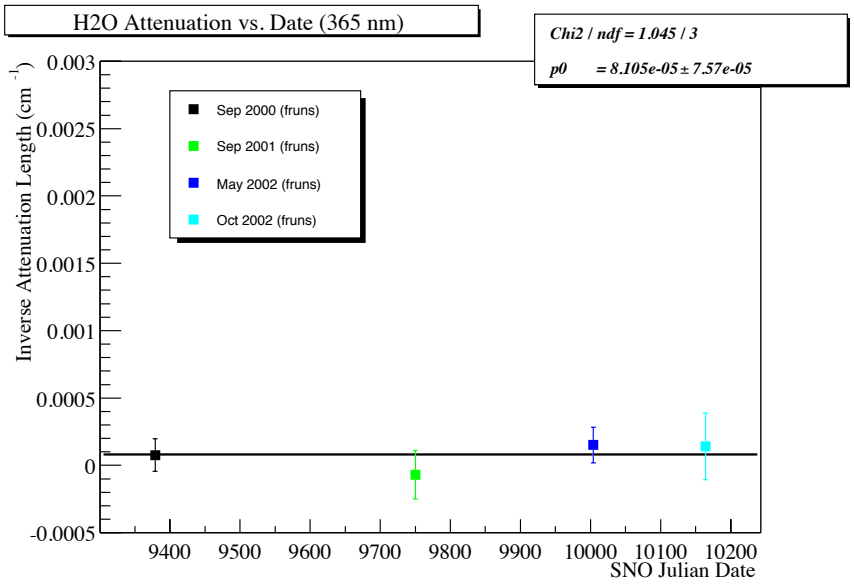

Figure A.17: A linear fit to the measured 365 nm H_2O attenuations as a function of time [20].

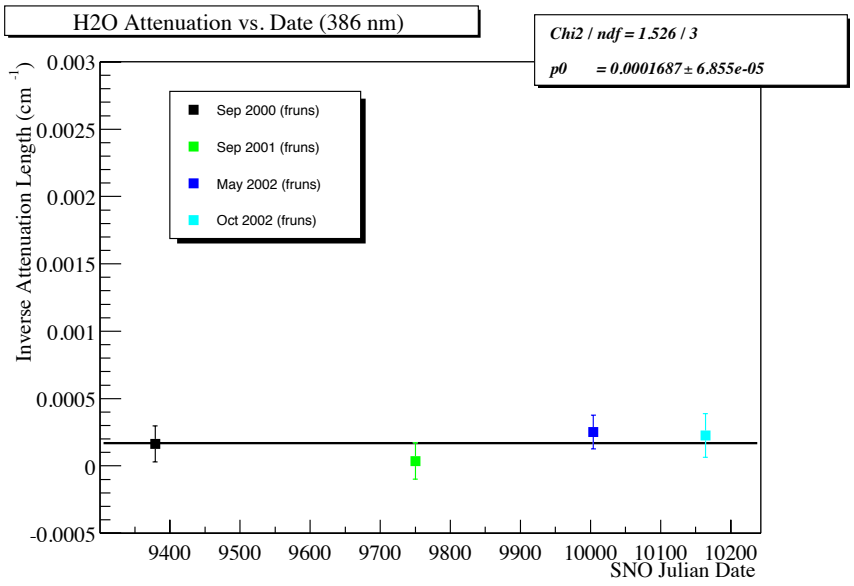

Figure A.18: A linear fit to the measured 386 nm H_2O attenuations as a function of time [20].

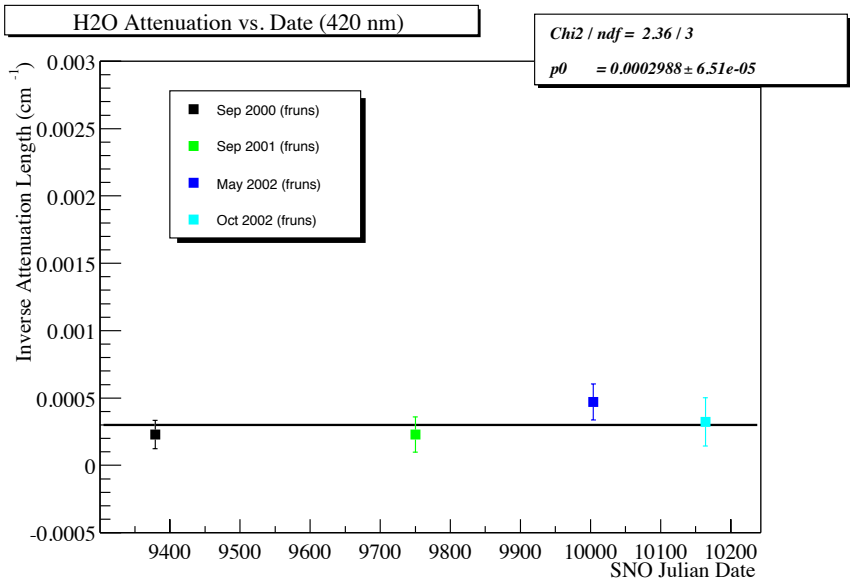

Figure A.19: A linear fit to the measured 420 nm H_2O attenuations as a function of time [20].

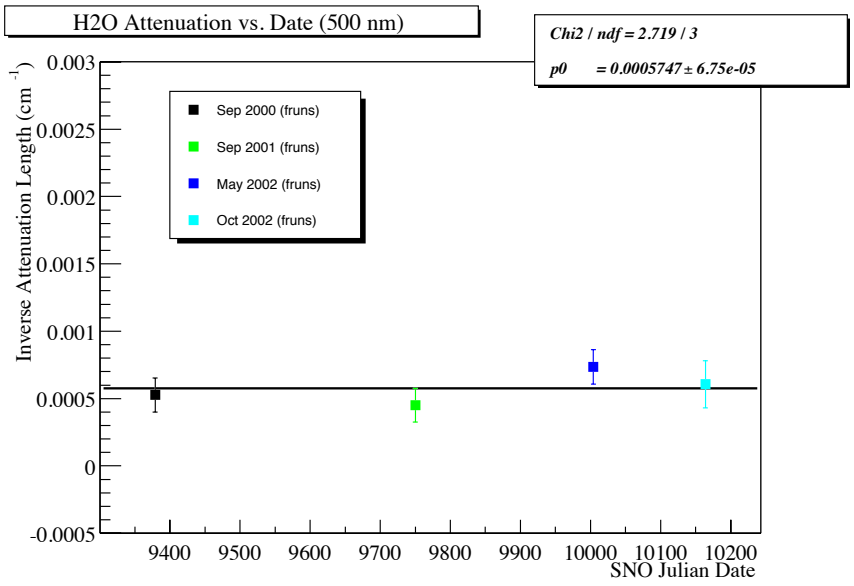

Figure A.20: A linear fit to the measured 500 nm H_2O attenuations as a function of time [20].

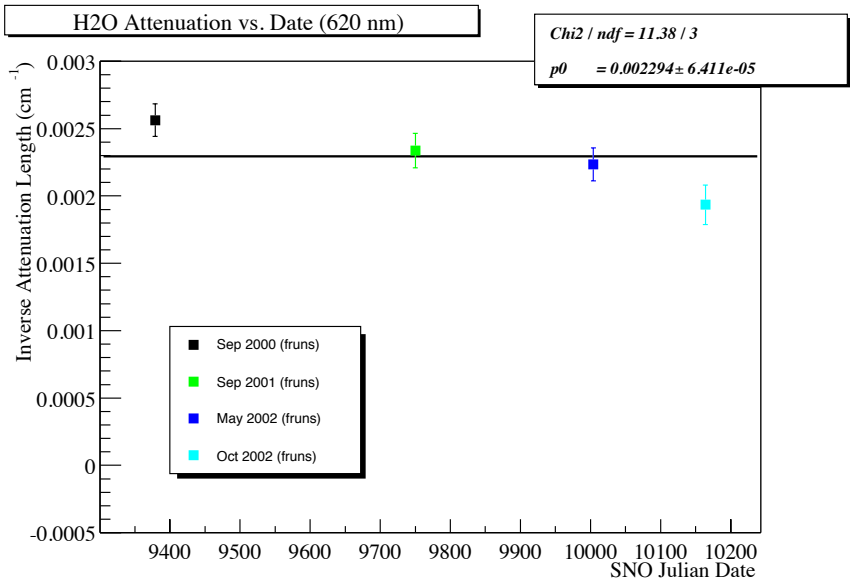

Figure A.21: A linear fit to the measured 620 nm H_2O attenuations as a function of time [20].

A.6 Measured PMT Angular Response

This section contains the plots of the PMT angular response curves for the pure D_2O and salt phase laser scans. There is a large change observed between the D_2O (September 2000) and salt phases at the low wavelengths. This change is believed to be due to a deterioration of the PMT reflector panels during the transition to the salt phase. The PMT angular response appears to be relatively constant over the period of the salt phase.

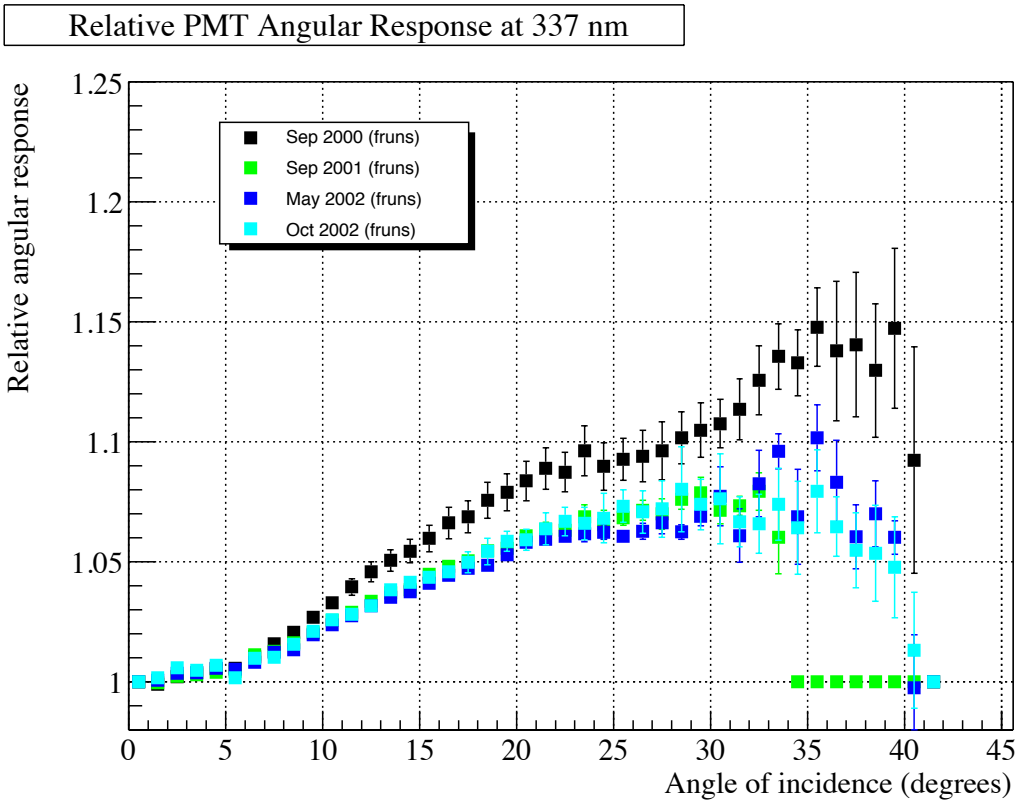

Figure A.22: The measured PMT angular response for 337 nm laser data [20].

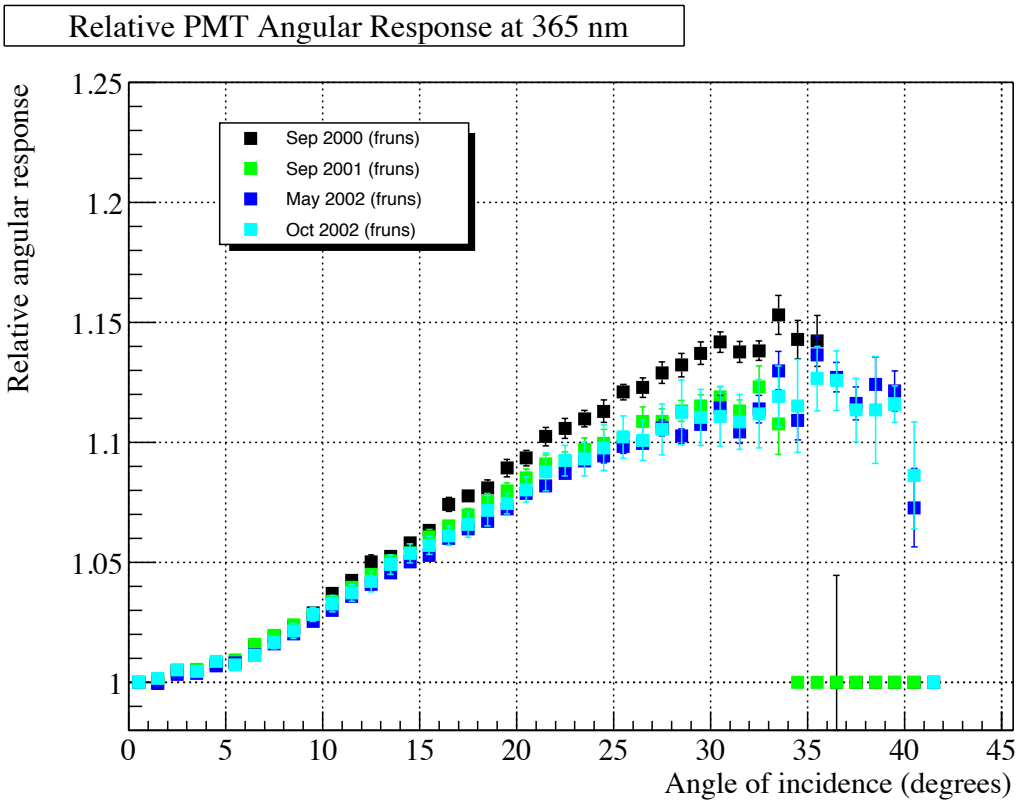

Figure A.23: The measured PMT angular response for 365 nm laser data [20].

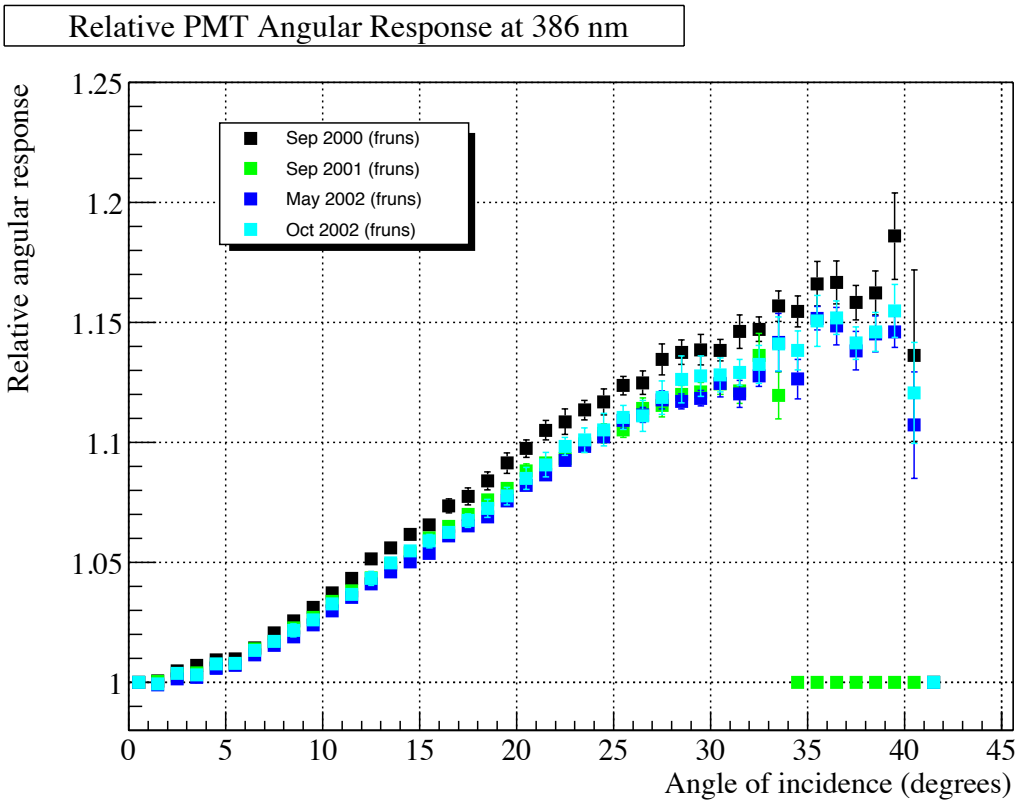

Figure A.24: The measured PMT angular response for 386 nm laser data [20].

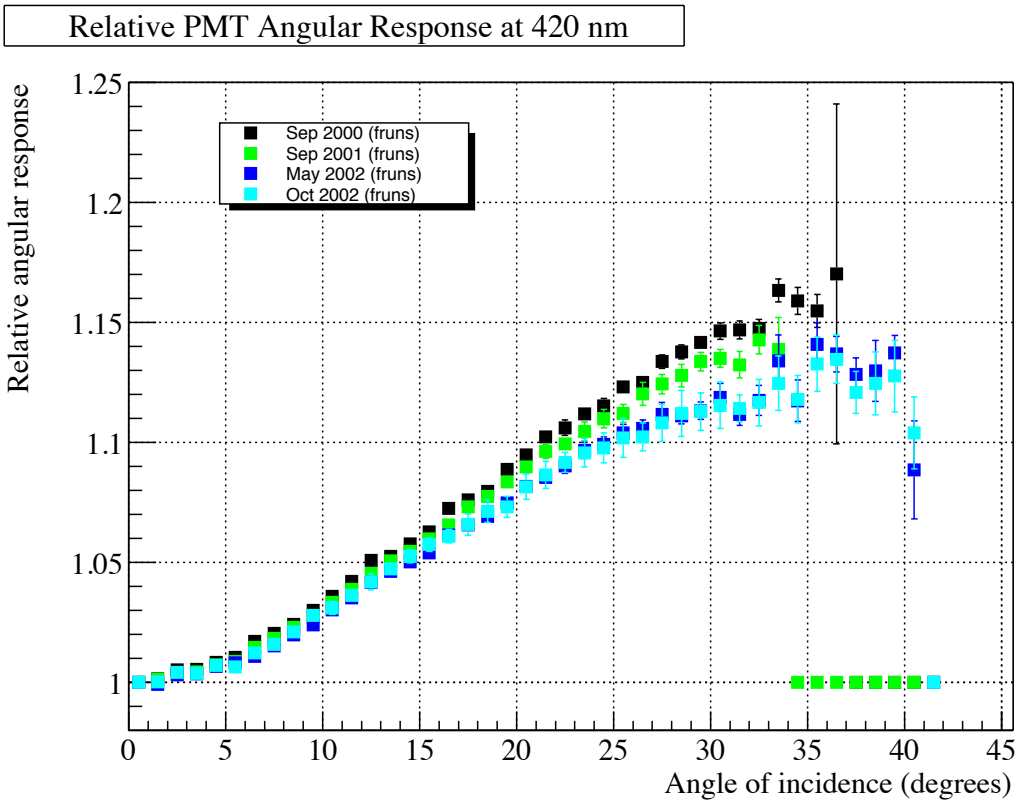

Figure A.25: The measured PMT angular response for 420 nm laser data [20].

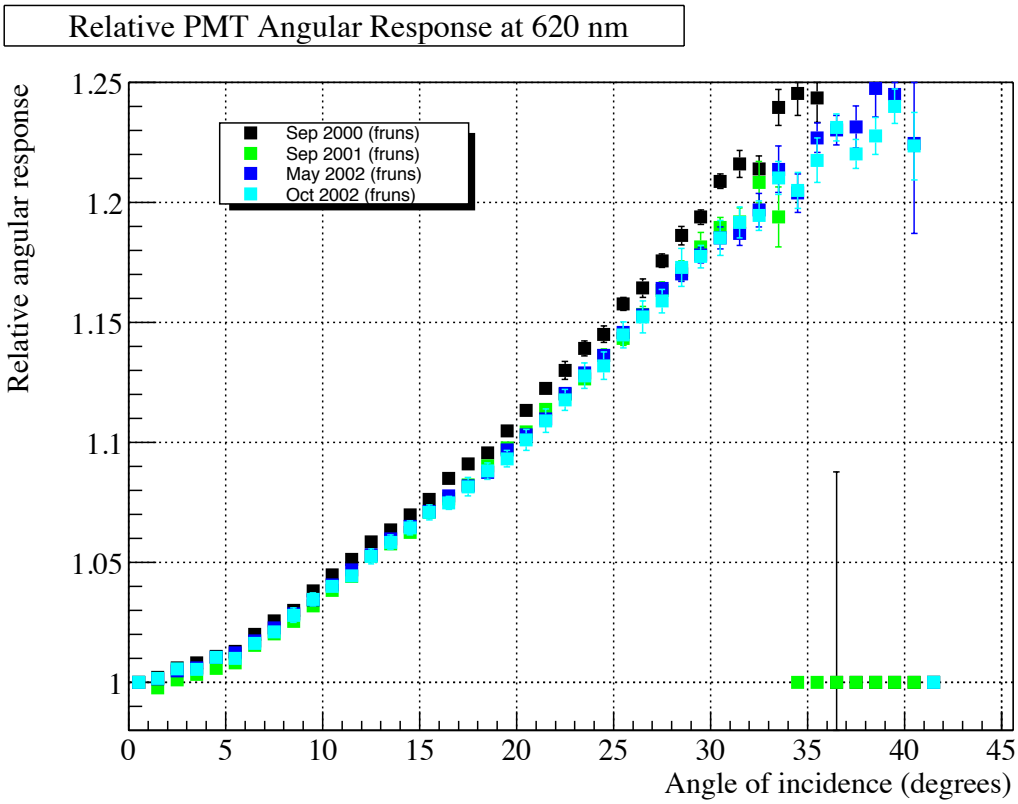

Figure A.26: The measured PMT angular response for 620 nm laser data [20].

Appendix B

PDF Development

The sections in this appendix contain information the reader may find useful to assist with understanding the methods for developing an analytic NC PDF, and the parameterized PDFs for the external background neutrons.

B.1 Development of an Analytic NC Energy PDF

B.1.1 SNOMAN command files for γ ray MC Generation

This section contains examples of the SNOMAN command files developed to generate γ ray distributions. When a neutron captures on a chlorine atom, a series of γ rays (on average 2 to 3) are released with energies ranging between 0.7 and 8.5 MeV. To develop an analytic PDF, it is necessary to understand the detector response to the γ rays in this energy range. This is accomplished by generating the γ rays with the SNOMAN MC using the command file

```
$mcdaq_hthresh 10.
$mcdaq_cthresh 5
$mcdaq_ztell off
```

```
**** Select a date for the MC, one of the primary 252Cf runs.
titles /data/data001/hepdb/titles/dqxx_0000021023.dat
$initial_date 20010909 13170700

**** Load the MC constants for optics and energy.
@/data/data003/dgrant/mc/neutron/titles/qsno_base.cmd
@/data/data003/dgrant/mc/neutron/titles/qsno_base_mc.cmd

**** The event loop-the primary processing tool of SNOMAN.
define event_loop
call mco                  **** call the MC processor
if_not_ok quit_event
call ftt                  **** call the time fitter
call ftu                  **** call the FTU fitter
call rsp(10)              **** call the RSP processor for FTU
call cln                  **** call the Classifier processor
call anl                  **** call the Analyzer processor
call qio(2)               **** call the QEvent Input/Output
end_def

$egs4_ds on               **** turns on the EGS4 data structure
$pegs_file              'pegs4_10.dat'

**** Define the output files for ntuples and ROOT trees
$hbook_file 'gamma_95mev_10000evts_numcer.ntp'
titles /data/data003/dgrant/mc/neutron/mytuples.dat
$enable_ntuple 187
FILE QIO 1 gamma_9_5mev_10000evts_nothresh_withnoise.root
FILE QIO 3 cf_21023.dat

**** Set the number of events to generate, the type of particle
**** the point of origin, distribution of the events and the energy.
$num_events  10000
$mc_interaction_type $start$$gamma$
$mc_position $pos_point      0.000000 0.000000 0.000000
$mc_direction          $dir_isotropic
$mc_energy             $en_mono 9.5
@run_snodb
```

The MC input files, qsno_base and qsno_mc_base, load the titles and command files required to define the detector properties. The file qsno_base loads the energy and optics information provided by the Energy and Optics Analysis Group:

```
@/data/data003/dgrant/mc/neutron/titles/standard_inputs.cmd
@/data/data003/dgrant/mc/neutron/titles/rsp_set_coll_eff.cmd
titles energy_calibration.dat
titles energy_control.dat
titles energy_drift.dat
titles rsp_nonline.dat
titles rsp_chcs.dat
titles rsp_rayleigh.dat
titles pmt_response_qoca_jan22.dat
@/data/data003/dgrant/mc/neutron/old_titles/bam_media_qoca_jan22.cmd
titles qio_data.dat
titles /data/data003/dgrant/mc/neutron/old_titles/laserball_dye.dat
titles /data/data003/dgrant/mc/neutron/old_titles/chfs_all.dat
titles pdf_fitter.dat
titles /data/data003/dgrant/mc/neutron/old_titles/sno_ntp_new.dat
```

The qsno_mc_base file loads the MSW information and calls a command to load the MC settings in mc_base.cmd: and command file.

```
@/data/data003/dgrant/mc/neutron/titles/mc_base.cmd
titles /data/data003/dgrant/mc/neutron/titles/unified_mc_set_msw.dat
```

The command file mc_base.cmd contains the information that can enables one to generate γ rays with different response factors. For example, in the sample mc_base.cmd file shown below, it is simple to generate γ rays with the PMT noise turned off, or to reset one of the other MC values to study possible variations within the detector.

```
$store_full_limit 1000
* $pmt_nois_rate 592.945  **** the default PMT noise rate
$pmt_nois_rate 0.         **** PMT noise rate is turned off

set bank mcdq 1 word 27 to 1

titles ccxt_but.dat
```

```
titles ncxt_but.dat
titles bopp.dat

* O17 fraction, use default
* $set_o17_d2o 0.00076
$d2o_region_01 $h2o_fraction 0.000916  **** level of light water
$d2o_region_02 $h2o_fraction 0.000916  **** in the d2o region
$set_o17_d2o   0.000485

**** Enable belly plates and tiles, disable tile variations
@geom_belly_plate_rope
@geom_acrylic_tiles
$acrylic_var $off

*dark chimney
* $geom_media $acrc_ovl $acrylic_dark

set bank tqio 1 word 1 to 0
set bank tqio 1 word 2 to 0
set bank tqio 1 word 3 to 0

*PMT time resolution is 1.5 ns
set bank PMTR 1 word 2 to 1.5

***   MC Control
$killvx                 0
$egs4_ds $on

***   Cerenkov Light generation.
$low_wave_cut          200.e-7
$high_wave_cut         720.e-7
$cerfac                0.28
$cerfac_ii             0.35
***   Particle Transport.
$fresnel_scat          $on
$rayleigh_scat         $on
$photodisintegration   $on

***  MC PMT simulation.
```

```
* $grey_disk_pmt

*below is for modified 3D

*titles pmt_geometry.dat
set bank GEDS 423 word 7 to 1
set bank GEDS 423 word 28 to 0.4
set bank GEDS 423 word 29 to 0.725
$3d_pmt
$mode_cerfac 1
```

B.1.2 MC Distributions for γ rays

The command files shown in Section B.1.1 are used to produce distributions for the γ rays in NHIT or energy. Examples of the γ ray NHIT distributions for selected energies are shown in the plots below in this section.

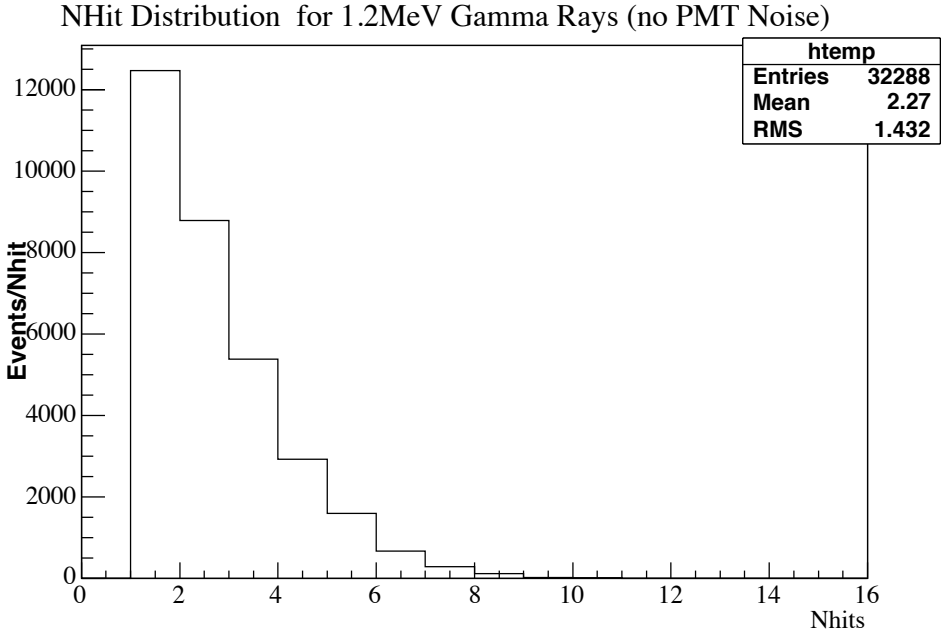

Figure B.1: The 1.2 MeV γ ray NHIT distribution, produced by the SNOMAN MC. The PMT noise rate and detector hardware threshold are set to 0 to study the structure of the NHIT distribution down to 1 NHIT.

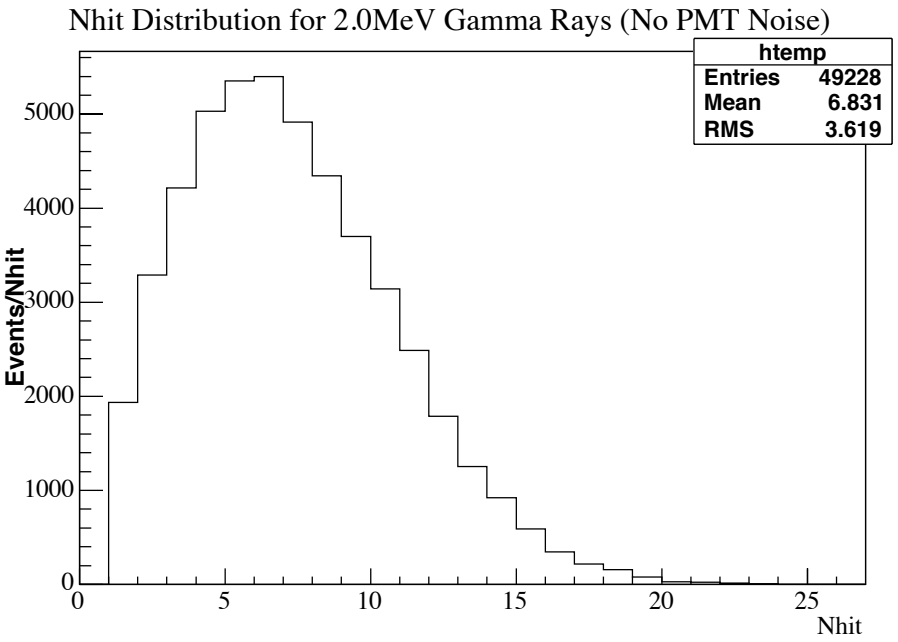

Figure B.2: The 2.0 MeV γ ray NHIT distribution, produced by the SNOMAN MC. The PMT noise rate and detector hardware threshold are set to 0 to study the structure of the NHIT distribution down to 1 NHIT.

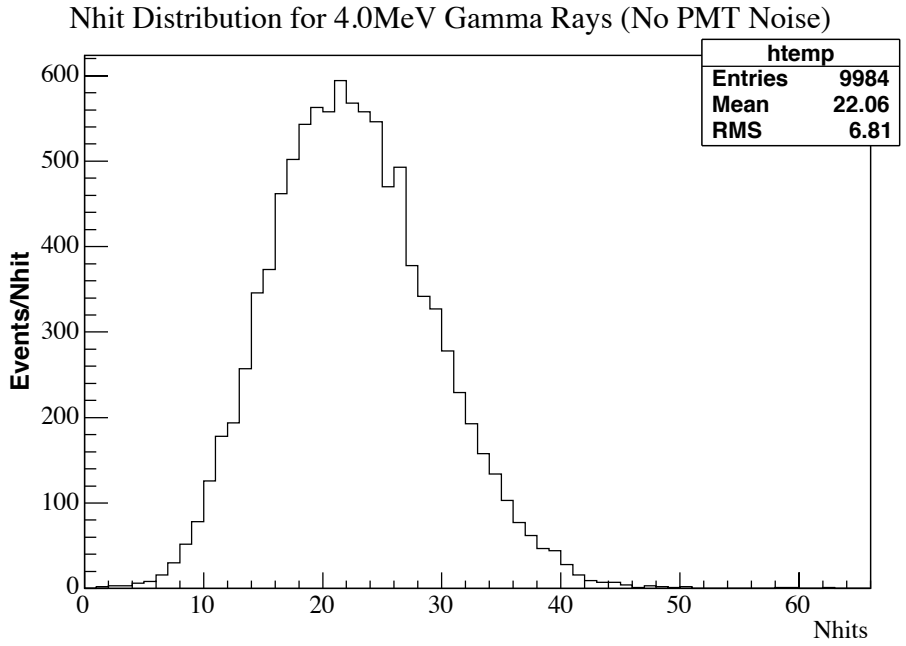

Figure B.3: The 4.0 MeV γ ray NHIT distribution, produced by the SNOMAN MC. The PMT noise rate and detector hardware threshold are set to 0 to study the structure of the NHIT distribution down to 1 NHIT.

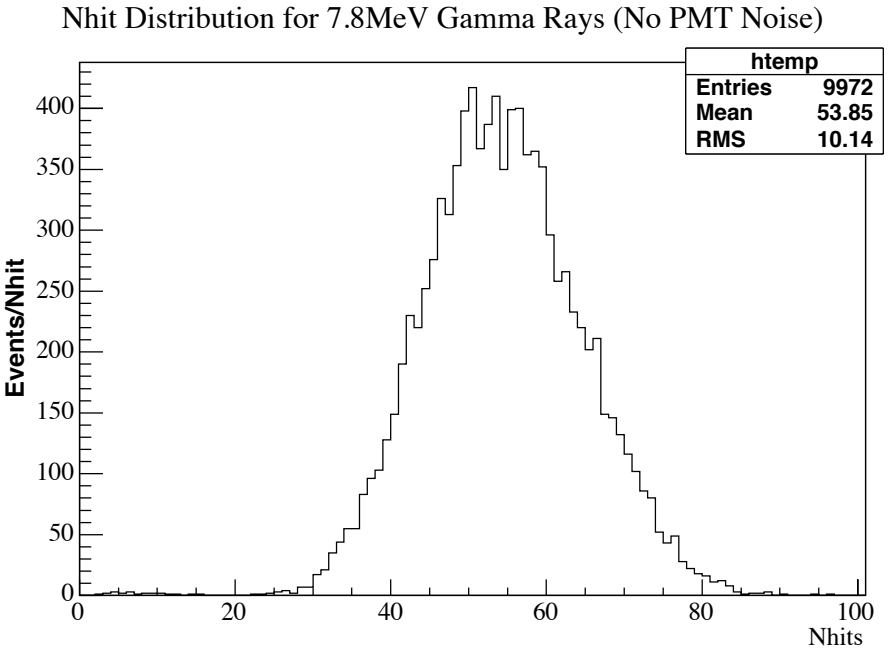

Figure B.4: The 7.8 MeV γ ray NHIT distribution, produced by the SNOMAN MC. This distribution is produced from events where the PMT noise rate and the detector threshold are set to 0.

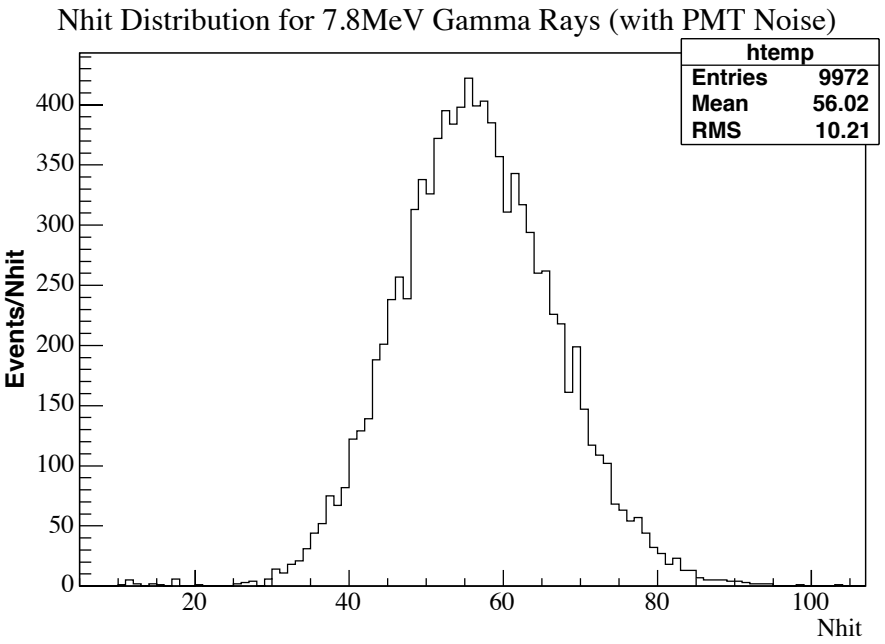

Figure B.5: The 7.8 MeV γ ray NHIT Distribution, produced by the SNOMAN MC. This distribution is produced from events where the PMT noise rate is set to the default value of 592.95 Hz and the detector hardware threshold is set at 10 NHIT. Comparing this distribution to figure B.4 shows the addition of PMT noise generates a small increase in the distribution arithmetic mean.

B.1.3 Convolution of Gaussian Functions with a Step Function

The NHIT distributions for high energy γ rays are represented well by a convolution of two Gaussian functions. However, for low energy γ rays the left tail of the NHIT distribution is truncated at the physical limit of the detector, NHIT=0. To represent these distributions, the convolution of the Gaussian functions is truncated at NHIT=1 using a step-function. This is done in the following manner. We begin with two Gaussian functions,

$$f(x) = \frac{1}{\sqrt{2\pi}\sigma_A} \exp \frac{-(x-a)^2}{2\sigma_A^2}$$

and

$$g(x) = \frac{1}{\sqrt{2\pi}\sigma_B} \exp \frac{-(x-b)^2}{2\sigma_B^2},$$

where a and b are the mean values of the two Gaussian functions. The convolution of these functions is given by

$$\begin{aligned} H(u) &= f \otimes g \\ &= \int_{-\infty}^{\infty} f(v)g(u-v)dv \\ &= \int_{-\infty}^{s} f(v)g(u-v)dv \quad + \quad \int_{s}^{\infty} f(v)g(u-v)dv, \end{aligned}$$

where s is the "turn-on" point of the step-function. Therefore, the first integral is equal to 0 by definition of the step-function. Substituting for the Gaussian functions, the convolution equation becomes

$$\begin{aligned} H(u) &= \int_{v=s}^{\infty} \frac{1}{2\pi\sigma_A} \exp \frac{-(v-a)^2}{2\sigma_A^2} \frac{1}{2\pi\sigma_B} \exp \frac{-((u-v)-b)^2}{2\sigma_B^2} \\ &= \frac{1}{2\pi\sigma_A\sigma_B} \int_{s}^{\infty} \exp\left(-\left[\frac{(v-a)^2}{2\sigma_A^2} \quad + \quad \frac{((u-v)-b)^2}{2\sigma_B^2}\right]\right) dv. \end{aligned}$$

Expanding the terms in the exponential

$$H(u) = \frac{1}{2\pi\sigma_A\sigma_B}\int_s^\infty \exp\left(\frac{-\frac{\sigma_B^2}{\sigma_A^2}(v-a)^2 \quad - \quad (u-v-b)^2}{2\sigma_B^2}\right)dv$$
$$= \frac{1}{2\pi\sigma_A\sigma_B}\int_s^\infty \exp\left(\frac{[-\frac{\sigma_B^2}{\sigma_A^2}(v-a)^2 - (u-v-b)^2][1+\frac{\sigma_A^2}{\sigma_B^2}+\frac{2\sigma_A}{\sigma_B}]}{2(\sigma_A+\sigma_B)^2}\right)dv$$
$$= \frac{1}{2\pi\sigma_A\sigma_B}\int_s^\infty \exp\left(\frac{-\frac{1}{\sigma_A^2}[\sigma_A+\sigma_B]^2(v-a)^2 - \frac{1}{\sigma_B^2}[\sigma_A+\sigma_B]^2(u-v-b)^2}{2(\sigma_A+\sigma_B)^2}\right)dv.$$

We now define $C = (\sigma_A+\sigma_B)^2$, and the numerator inside the exponential term is

$$-v^2C^2(\frac{1}{\sigma_A^2}+\frac{1}{\sigma_B^2}) + 2vC^2(\frac{a}{\sigma_A^2}+\frac{(u-b)}{\sigma_B^2}) - C^2(\frac{a^2}{\sigma_A^2}+\frac{(u-b)^2}{\sigma_B^2}).$$

The C^2 terms cancel, and the convolution equation becomes

$$H(u) = \frac{1}{2\pi\sigma_A\sigma_B}\int_s^\infty \exp\left(\frac{-v^2(\frac{1}{\sigma_A^2}+\frac{1}{\sigma_B^2}) + 2v(\frac{a}{\sigma_A^2}+\frac{(u-b)}{\sigma_B^2}) - (\frac{a^2}{\sigma_A^2}+\frac{(u-b)^2}{\sigma_B^2})}{2}\right)dv.$$

We extract the terms $-\left(\frac{1}{\sigma_A^2}+\frac{1}{sigma_B^2}\right) = -\left(\frac{\sigma_A^2+\sigma_B^2}{\sigma_A^2\sigma_B^2}\right)$. and define $Q = \frac{\sigma_A^2\sigma_B^2}{\sigma_A^2+\sigma_B^2}$. Using this in the equation above to gives

$$H(u) = \frac{1}{2\pi\sigma_A\sigma_B}\int_s^\infty \exp\left(-\frac{\frac{1}{Q}\left[v^2 - 2vQ(\frac{a}{\sigma_A^2}+\frac{(u-b)}{\sigma_B^2})\right] - (\frac{a^2}{\sigma_A^2}+\frac{(u-b)^2}{\sigma_B^2})}{2}\right)dv.$$

We define $\eta = Q\left(\frac{a}{\sigma_A^2}+\frac{u-b}{\sigma_B^2}\right)$ and this is substituted into the equation above. Isolating the v terms of the integral gives

$$H(u) = \frac{1}{2\pi\sigma_A\sigma_B}\int_s^\infty \exp\left[-\frac{1}{2Q}(v-\eta)^2\right]dv \exp\left[\frac{1}{2Q}\eta^2 - \frac{1}{2}\left(\frac{a^2}{\sigma_A^2}+\frac{(u-b)^2}{\sigma_B^2}\right)\right].$$

The second exponential in this equation reduces to a Gaussian term of the form $\exp\left(-\frac{1}{2}\frac{(a-(u-b))^2}{(\sigma_A^2+\sigma_B^2)}\right)$. The integral may be solved using a substitution of $Y = v-\eta$. This changes the integral to have the form

$$\int_{Y=S-\eta}^\infty \exp\left(-\frac{1}{2Q}Y^2\right)dY,$$

the solution of which is an Error-function. Defining $\gamma = \frac{1}{2Q}$, the solution of the integral is

$$\frac{\sqrt{\pi}}{2}\frac{\sqrt{\gamma}}{\gamma}\mathrm{erfc}\left[\sqrt{\gamma}(\mathrm{p}-\eta)\right].$$

Therefore, the initial convolution becomes

$$H(u) = \frac{1}{4\sqrt{\pi}\sqrt{\gamma}\sigma_A\sigma_B}\mathrm{erfc}(\sqrt{\gamma}(\mathrm{p}-\eta))\exp\left(-\frac{1}{2}\frac{(\mathrm{a}-(\mathrm{u}-\mathrm{b}))^2}{\sigma_\mathrm{A}^2+\sigma_\mathrm{B}^2}\right). \tag{B.1}$$

This solution is extremely useful for representing distributions which are truncated-multiple Gaussian functions. The truncation point is described by the start point (s) of the integral, and the truncation of the Gaussian functions is performed by the complementary Error-function (Erfc) term. The Gaussian term in the result is what one expects when convolving two Gaussian functions, *ie* a Gaussian function where the mean and sigmas are combined.

B.1.4 The Fit of γ ray MC Distributions using Convolved Truncated-Gaussian Functions

The MC generated γ-ray distributions are fit using equation B.1. The truncation point for the fit function is set to s=1 NHIT. As we fit the higher energy distributions, the truncation term in the equation goes to 1, and the resultant fitting function is the simple convolution of two Gaussian distributions. The plots in this section show the result of the fit for a few of the γ-ray energies. We then separate the fit results into terms for the primary and secondary Gaussian functions. We plot the fit mean, the sigma, and the constant for each the primary and secondary Gaussian functions versus the MC generated energy of the γ-ray. Polynomials are used to fit these distributions, and are used to interpolate between the energies of the generated γ-ray distributions. Using equation B.1, with the polynomial-interpolated values for the means, sigmas and constants of Gaussian functions (for a specific γ-ray energy), the detector response in NHIT (or RSP energy using a change of parameters) may be generated. These detector response distributions (for individual γ-rays) may then be combined using the experimentally measured branching ratios for the ^{35}Cl decay level to generate an analytic PDF representing neutron capture on chlorine in the SNO detector.

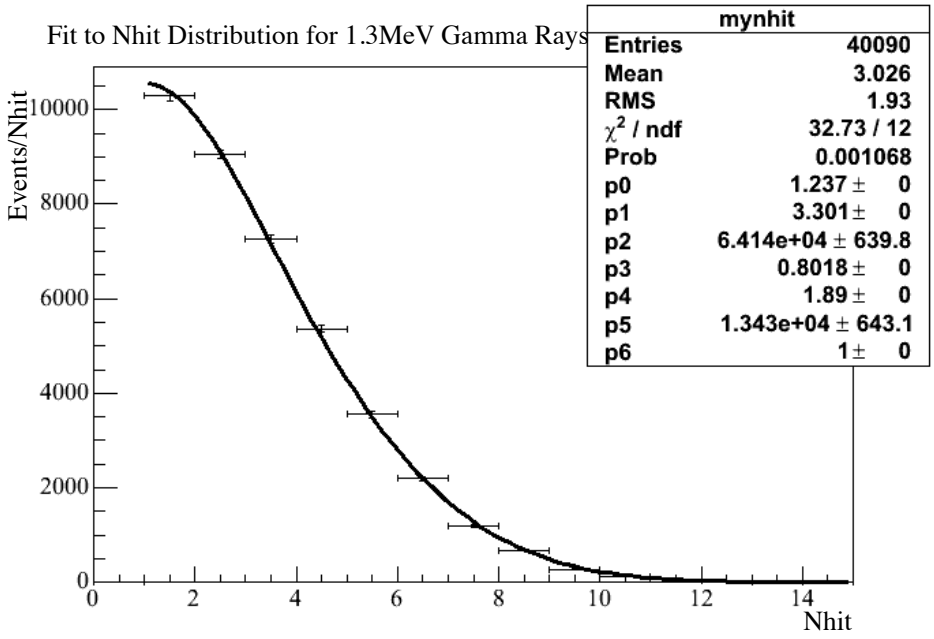

Figure B.6: A fit using equation B.1 to the 1.3 MeV γ ray NHIT distribution (with no PMT noise or detector hardware threshold included).

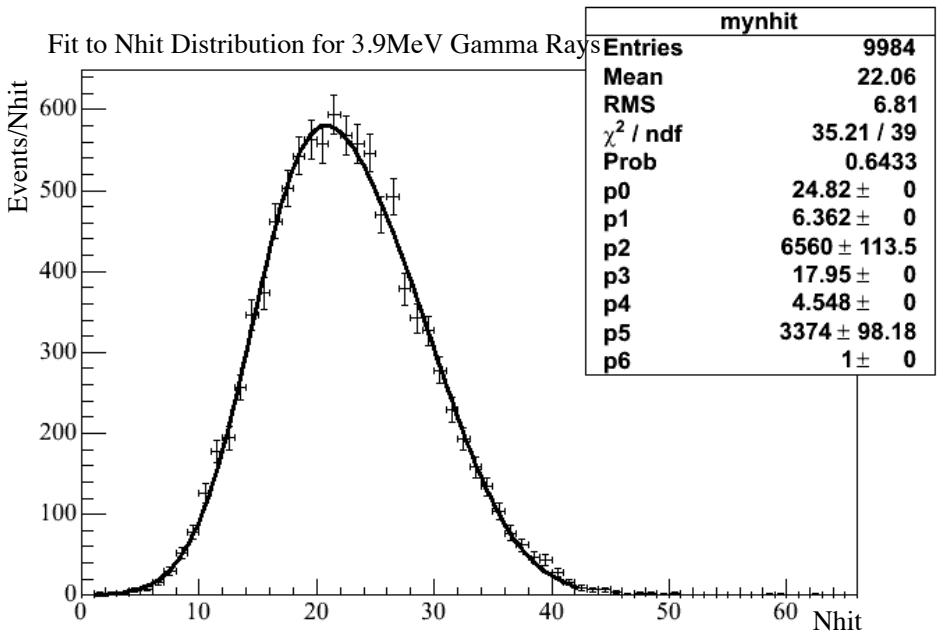

Figure B.7: A fit using equation B.1 to the 3.9 MeV γ ray NHIT distribution (with no PMT noise or detector hardware threshold included).

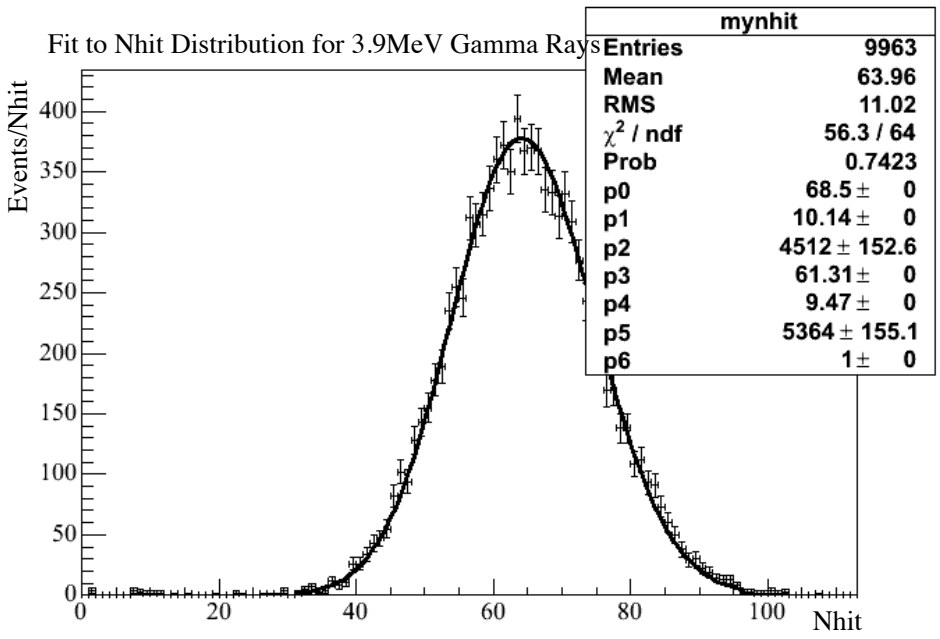

Figure B.8: A fit using equation B.1 to the 8.8 MeV γ ray NHIT distribution (with no PMT noise or detector hardware threshold included).

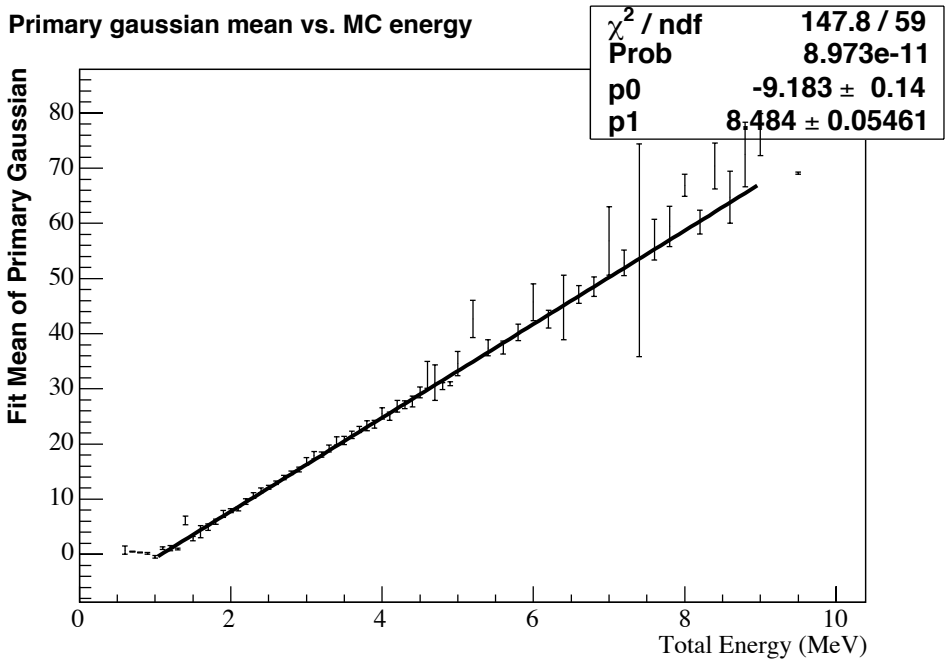

Figure B.9: A polynomial fit to the primary Gaussian mean versus energy.

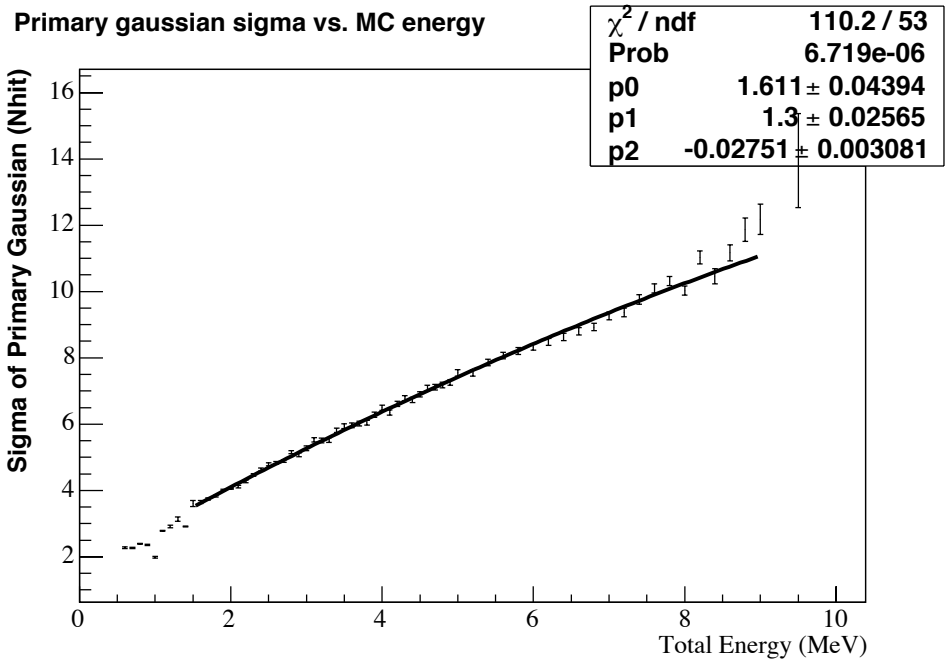

Figure B.10: A polynomial fit to the primary Gaussian sigma versus energy.

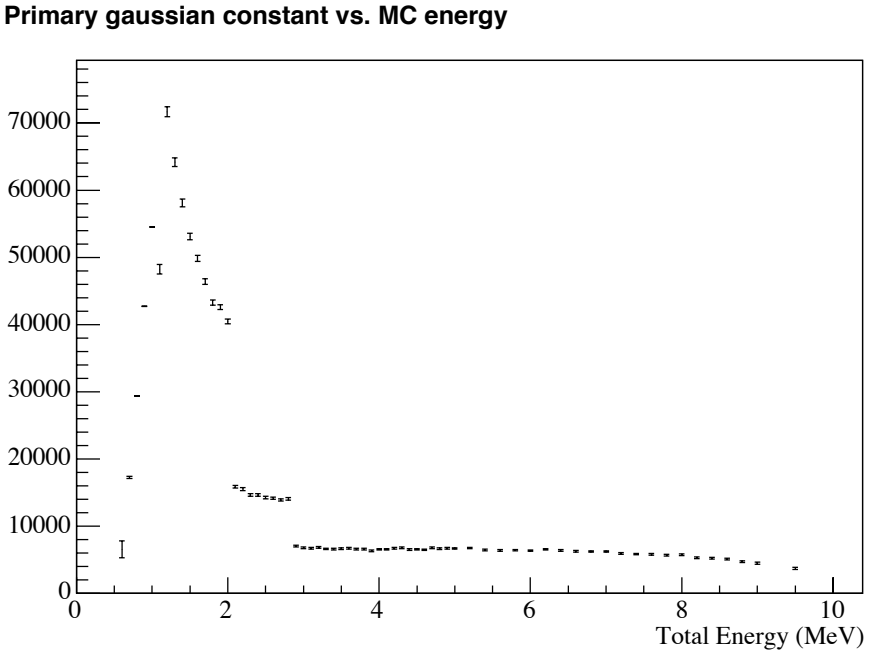

Figure B.11: The primary Gaussian constant versus energy.

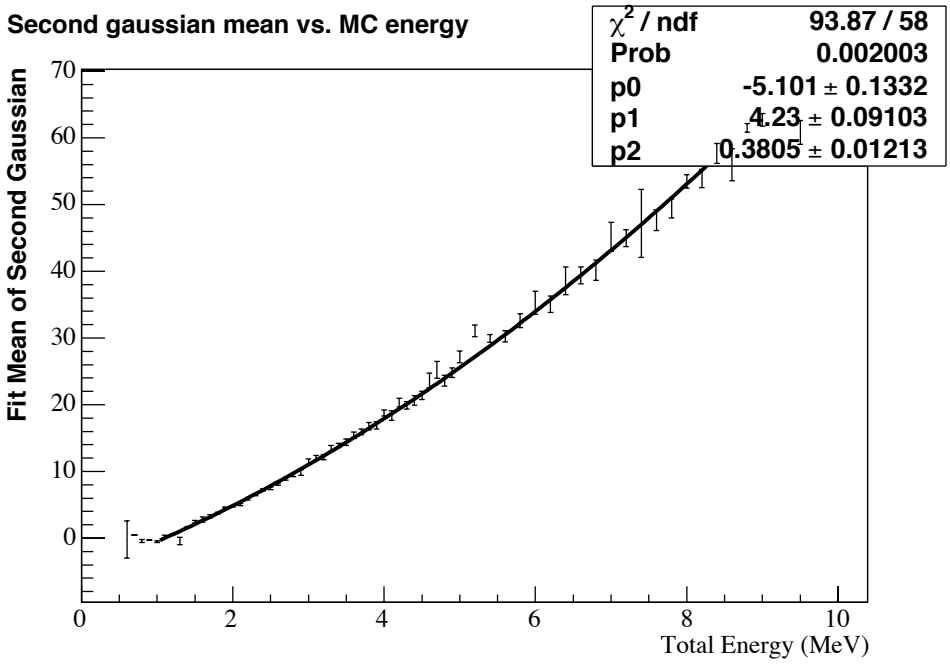

Figure B.12: A polynomial fit to the secondary Gaussian mean versus energy.

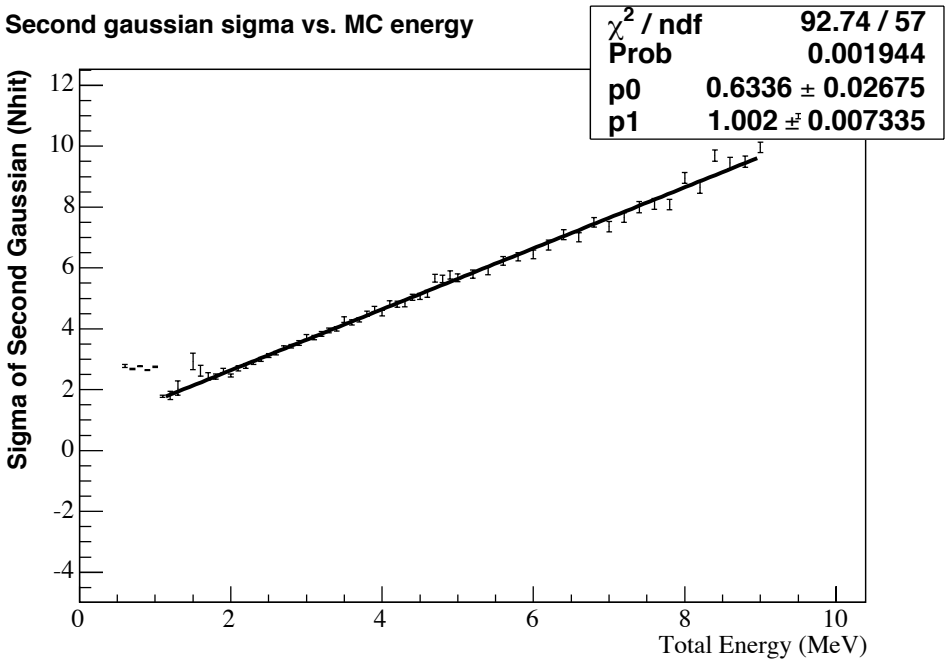

Figure B.13: A polynomial fit to the secondary Gaussian sigma versus energy.

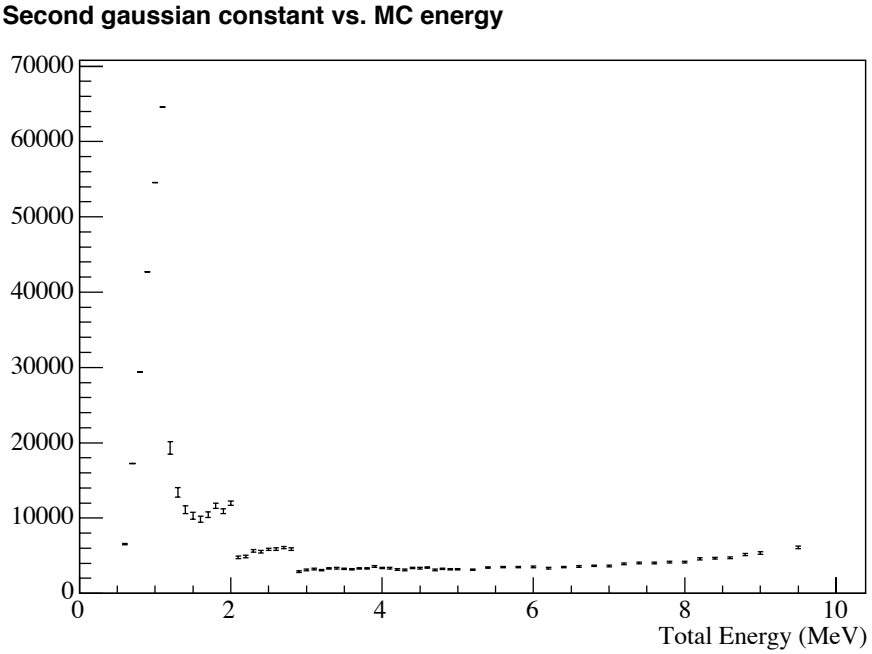

Figure B.14: The secondary Gaussian constant versus energy.

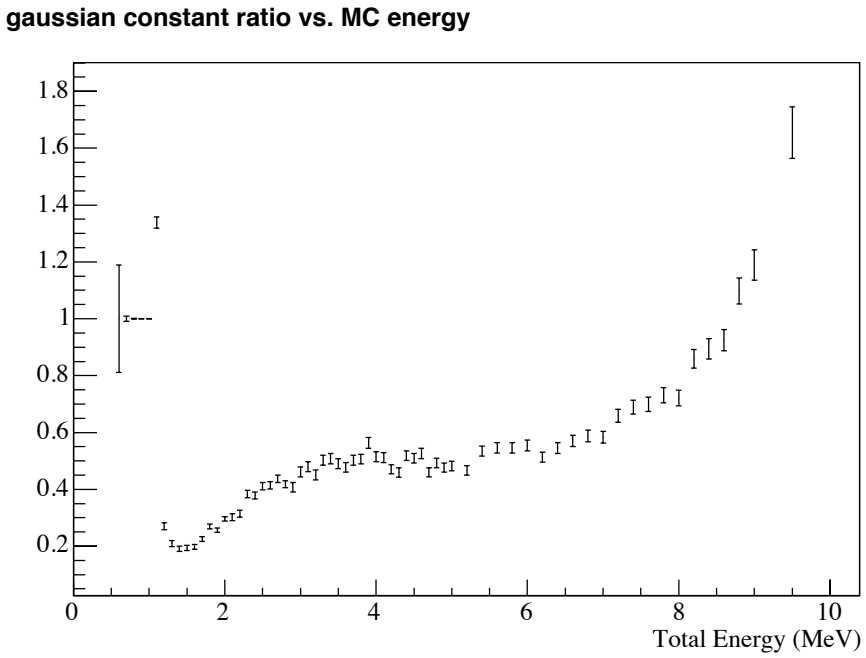

Figure B.15: The ratio of the primary and secondary Gaussian constants versus energy.

B.2 External Neutron Parameterization PDFs

This section contains the plots of the external neutron parameterized 1D PDFs for energy, isotropy (β_{14}) and angular distribution ($\cos(\theta_{Sun})$.

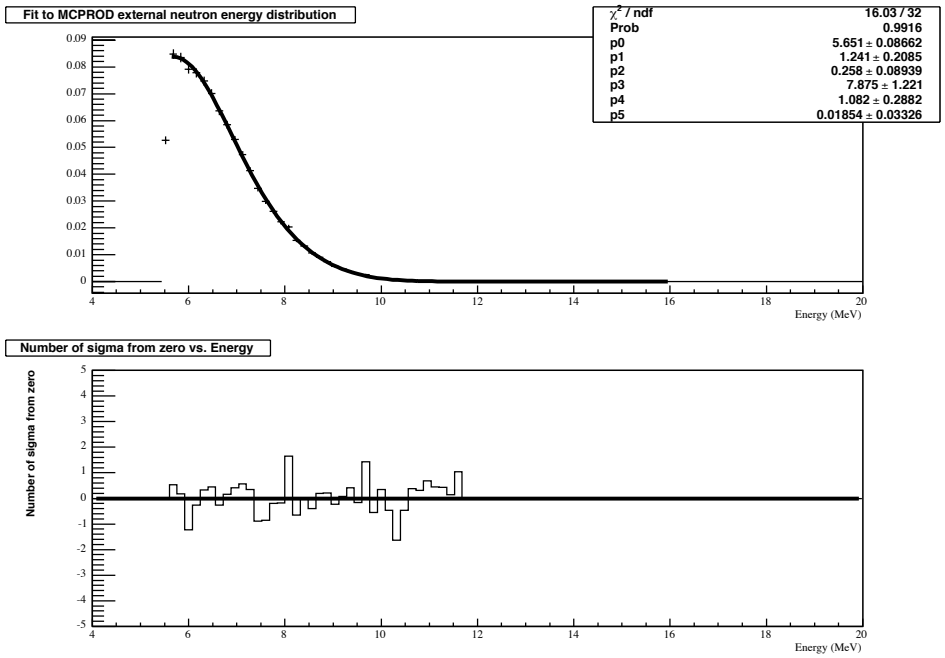

Figure B.16: The external neutron energy distribution parameterization with a double Gaussian function.

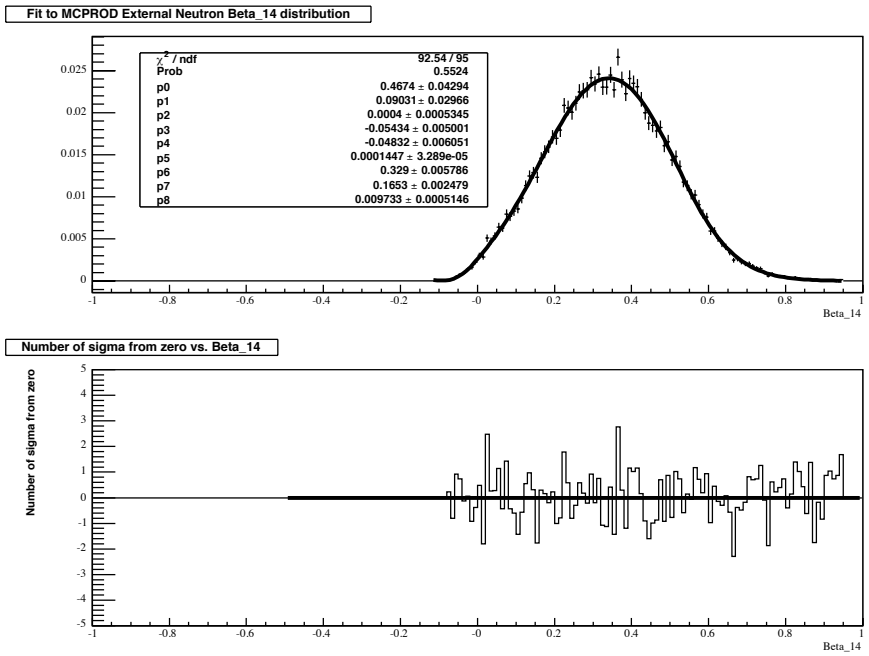

Figure B.17: The external neutron isotropy distribution parameterization using three Gaussian functions.

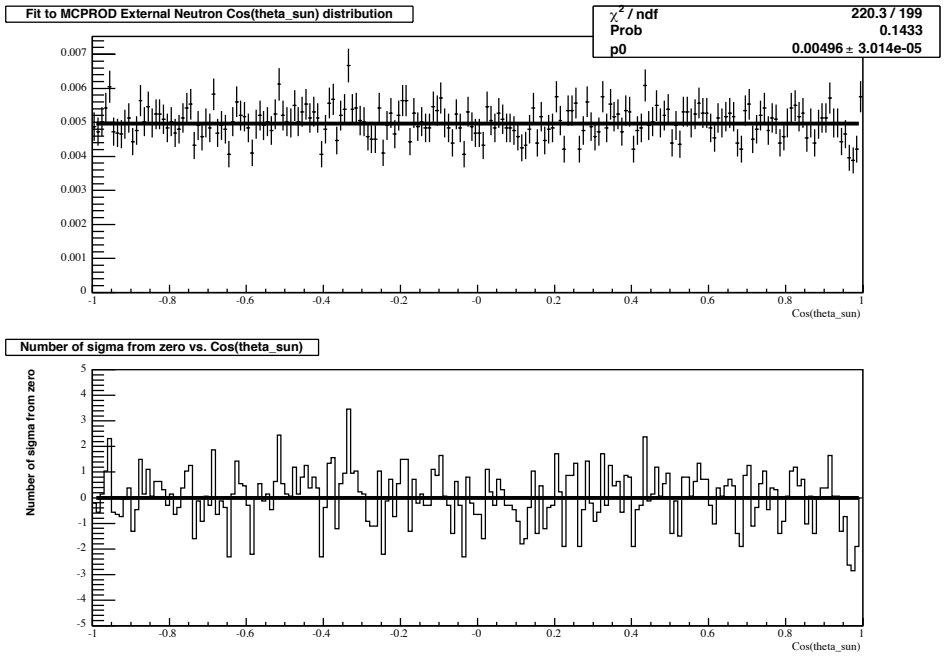

Figure B.18: The external neutron angular distribution parameterization using a zero-order polynomial.

Appendix C

Salt Phase Results

The sections of this appendix are related to issues involving the salt phase signal extraction analysis. These issues include an example of the sig-ex code card file, the covariance matrices used to create the Gaussian-correlated joint PDFs, and an example of generating systematic uncertainties associated with creating PDFs by parameterizing the CC MC event distributions.

C.1 Example of a Sig-Ex Card File

The signal extraction code used in the thesis analysis obtains all necessary information to process the salt phase data from a single card file. An example of such a card file is shown below. The card file provides the sig-ex processors with the location of where the data and the types of PDFs to use in the fit. It also contains the high-level cuts to be performed on the data, and the information of which signal types are permitted to float in the minimization routine.

```
# QNuParameters.dat - sig-ex card file
# This is the "user interface" for the QSigEx signal extraction
# package. Comment lines must begin with a pound sign.
```

```
# Inline comments are not supported and empty lines are ignored.
# Each line read from this file must begin with a "keyword" that
# designates the kind of command or input that line provides,
# followed by other inputs specific to that keyword.  Spaces, tabs,
# and punctuation characters are used to separate the fields.

DATA_FILE  data_ttree.root t

# Control Flags:
# Defines the Minuit minimization package to apply in the fit.

minimizer  MIGrad  1

# Variable Equivalencies:
# For situations where the PDF variable is a function of
# variables in the data file, one may use a formula to convert the
# two.  The formula is limited to have no more than 3 variables.
# Simple mathematical operations, such as multiplication and addition,
# are supported.

#keyword     coordinate   formula
equivalence  R3           (sqrt(FITX**2+FITY**2+FITZ**2)/600)**3
equivalence  rho          (r/600)**3

# Cut information:
# Using the ‘‘cut’’ keyword defines the high-level cuts to be
# applied to the PDFs and the data.  The cut name may be
# be assigned arbitrarily, and it is possible to change
# the value of the cut "on the fly" from within a macro.
# It is important to specify upper and lower bounds for each
# of the cuts to prevent unpredictable normalization of the PDFs.

#name    coordinate      condition
cut      emin            teff>=5.5
cut      emax            teff<=19.5
cut      cosmin          cossun>=-1
cut      cosmax          cossun<1
cut      itrmin          itr>=0.55
cut      rhomax          rho<=0.77025
cut      b14min          b14>=-0.12
```

```
cut      b14max          b14<=0.95

# PDF info:
# The information for each PDF being used in the fit is given
# here using the ‘‘pdf’’ keyword.  The PDFs can be either histograms
# (1 or multidimensional) or functions.  The data field entries
# should contain the names of the parameters from the data file.
# The "flag" field determines whether the pdf is used in a current
# fit, where 0 means it will not be used.  QSigEx has a SetPDFFlag()
# function to set the ‘‘flag’’ values while the code is running
# as an alternative to commenting out various lines in this file
# each time you want to change the pdfs in the fit.

#   flag class flux_group  dimension  name  filename      datafield
pdf  1   TTree alpha_nc    bb14       t     nc_ttree.root b14    100
pdf  1   TTree alpha_nc    ene        t     nc_ttree.root teff   100
pdf  1   TTree alpha_nc    rho        t     nc_ttree.root rho    100
pdf  1   TTree alpha_nc    cossun     t     nc_ttree.root cossun 100

pdf  1   TTree alpha_cc    bb14       t     cc_ttree.root b14    100
pdf  1   TTree alpha_cc    ene        t     cc_ttree.root teff   100
pdf  1   TTree alpha_cc    rho        t     cc_ttree.root rho    100
pdf  1   TTree alpha_cc    cossun     t     cc_ttree.root cossun 100

pdf  1   TTree alpha_es    bb14       t     es_ttree.root b14    100
pdf  1   TTree alpha_es    ene        t     es_ttree.root teff   100
pdf  1   TTree alpha_es    rho        t     es_ttree.root rho    100
pdf  1   TTree alpha_es    cossun     t     es_ttree.root cossun 100

# Flux parameters:
# Information about the flux parameters involved in the fit use the
# ‘‘flux’’ keyword.  Fluxes with an active flag equal to 1 float
# in the fit, while fluxes with an active flag equal to 0 are held
# fixed.

#    parameter_name active(1) start_val  minval   maxval   step_val
flux alpha_cc       1           500        0       100000   0.01
flux alpha_nc       1           500        0       100000   0.01
flux alpha_es       1           500        0       100000   0.01
```

	β_{14}	T_{eff}	R_{fit}	$\cos(\theta_{Sun})$
β_{14}	1.001	0.0556	-0.0235	-0.0172
T_{eff}	0.0556	1.005	-0.0138	-0.0034
R_{fit}	-0.0235	-0.0138	0.9268	0.0004
$\cos(\theta_{sun})$	-0.0172	-0.0034	0.0004	1.024

Table C.1: The covariance matrix for CC events. The matrix is generated by looking at the parameters (such as T_{eff} and R_{fit}) event-by-event from the MC. The largest correlations are observed between T_{eff} and β_{14}.

	β_{14}	T_{eff}	R_{fit}	$\cos(\theta_{Sun})$
β_{14}	1.000	0.1363	-0.0121	0.0013
T_{eff}	0.1363	1.001	-0.0085	-0.0047
R_{fit}	-0.0121	-0.0085	0.9352	-0.0008
$\cos(\theta_{sun})$	0.0013	-0.0047	-0.0008	1.038

Table C.2: The covariance matrix for NC events. The matrix is generated by looking at the parameters (such as T_{eff} and R_{fit}) event-by-event from the MC. The largest correlations are observed between T_{eff} and β_{14}.

C.2 Gaussian Correlated Joint Probabilities

The covariance matrices in this section represent the correlations between the different parameters for the event types extracted with the extended-likelihood minimization. These matrices are used to generate the Gaussian correlated joint PDFs, described in Chapter 6. Their contribution to the minimization is observed by the change to the likelihood correlation matrix 6.4.

C.3 CC PDF Systematic Uncertainties

This section contains plots that are an example of how the systematic uncertainties were determined for the parameterized PDFs used in the signal extraction. For each PDF type, the best fit of the parameterization function was adjusted using the

	β_{14}	T_{eff}	R_{fit}	$\cos(\theta_{Sun})$
β_{14}	1.575	0.0857	-0.0317	0.4230
T_{eff}	0.0857	1.013	-0.0114	0.1526
R_{fit}	-0.0317	-0.0114	0.9277	-0.0120
$\cos(\theta_{sun})$	0.4230	0.1526	-0.0120	1.798

Table C.3: The covariance matrix for ES events. The matrix is generated by looking at the parameters (such as T_{eff} and R_{fit}) event-by-event from the MC. The largest correlations are observed between β_{14} and $\cos(\theta_{Sun})$.

	β_{14}	T_{eff}	R_{fit}	$\cos(\theta_{Sun})$
β_{14}	1.007	0.1268	-0.0029	-0.0456
T_{eff}	0.1268	1.012	0.0040	-0.0042
R_{fit}	-0.0029	0.0040	1.038	-0.0059
$\cos(\theta_{sun})$	-0.0456	-0.0043	-0.0059	0.7921

Table C.4: The covariance matrix for external neutron events. The matrix is generated by looking at the parameters (such as T_{eff} and R_{fit}) event-by-event from the MC. The largest correlations are observed between T_{eff} and β_{14}.

CORSET and CORGEN routines described in chapter 5 to generate 750 "shifted" PDFs. The new PDFs are used in an ensemble test, such that the extracted CC values from sig-ex using each new PDF are binned in a histogram. The arithmetic RMS of this distribution is representative of the systematic uncertainty for the extracted flux caused by parameterizing the MC distributions to generate signal PDFs.

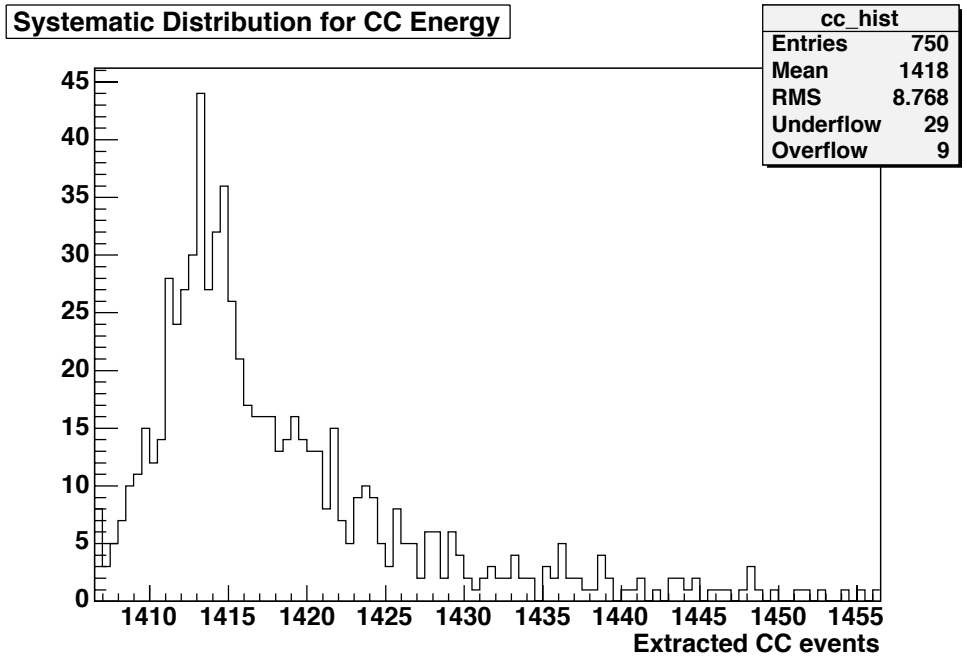

Figure C.1: The distribution for the number of extracted CC events when using systematically shifted energy PDFs. The arithmetic RMS of the distribution is the systematic error associated with parameterizing the CC MC energy distribution for use in the signal extraction process.

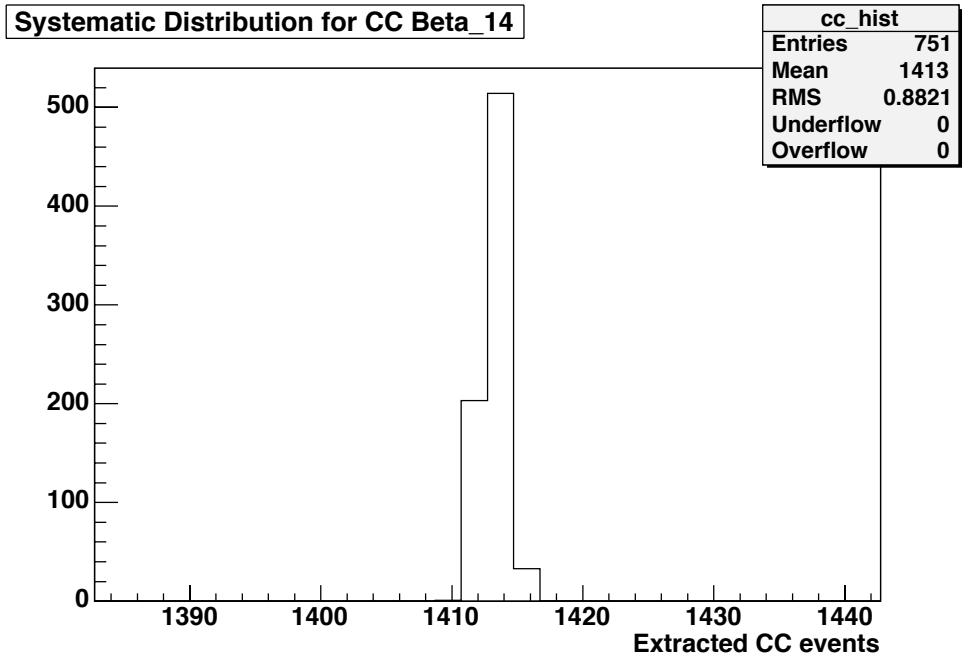

Figure C.2: The distribution for the number of extracted CC events when using systematically shifted β_{14} PDFs. The arithmetic RMS of the distribution is the systematic error associated with parameterizing the CC MC β_{14} distribution for use in the signal extraction process.

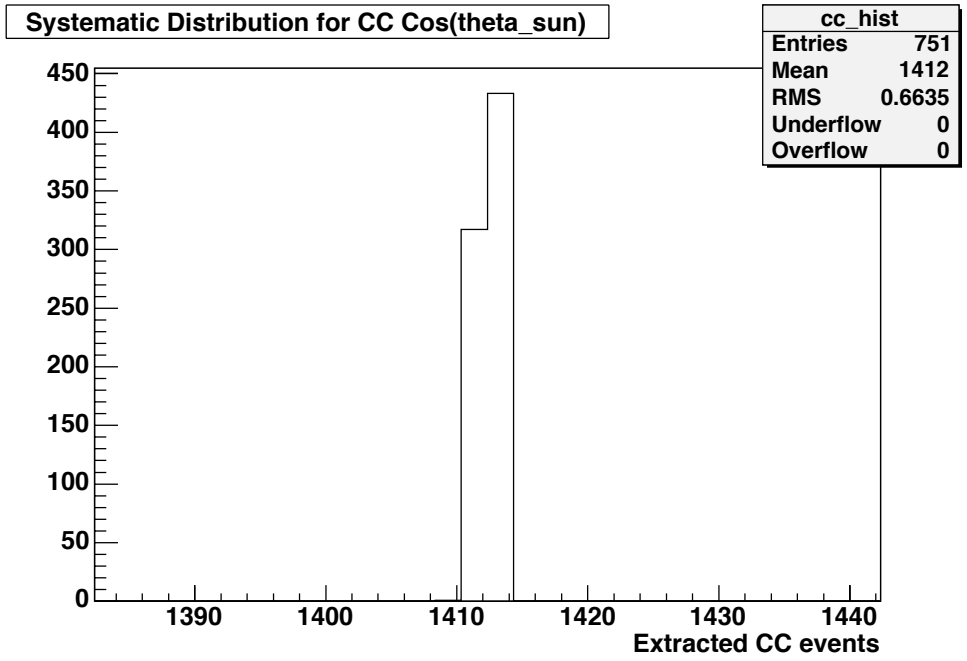

Figure C.3: The distribution for the number of extracted CC events when using systematically shifted $\cos(\theta_{Sun})$ PDFs. The arithmetic RMS of the distribution is the systematic error associated with parameterizing the CC MC $\cos(\theta_{Sun})$ distribution for use in the signal extraction process.

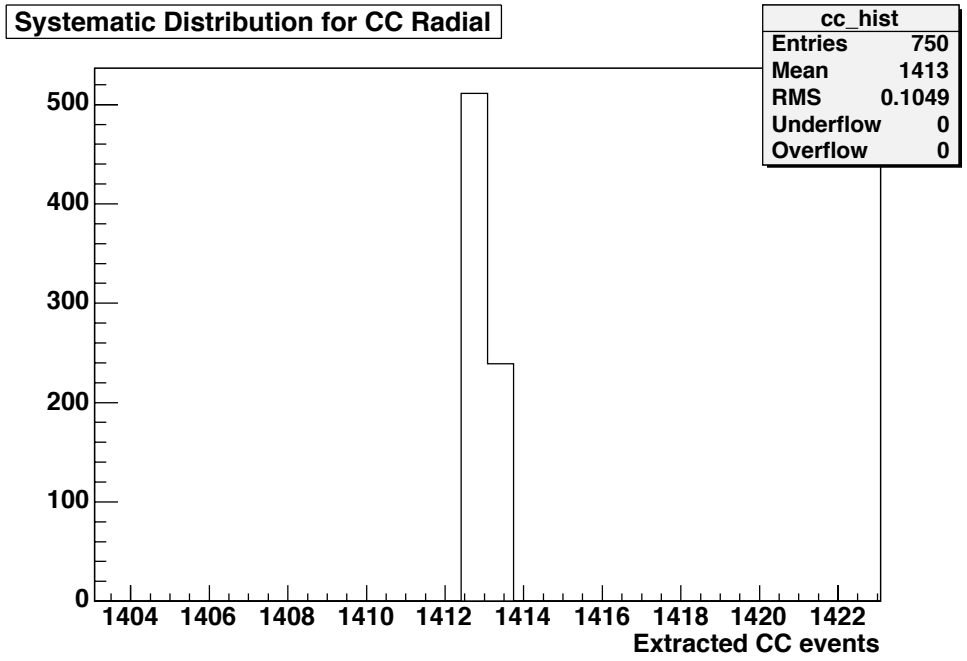

Figure C.4: The distribution for the number of extracted CC events when using systematically shifted radial PDFs. The arithmetic RMS of the distribution is the systematic error associated with parameterizing the CC MC radial distribution for use in the signal extraction process.